UNIVERSITY OF CALIFORNIA
Santa Barbara

Spin Interactions Between Conduction Electrons and Local Moments in Semiconductor Quantum Wells

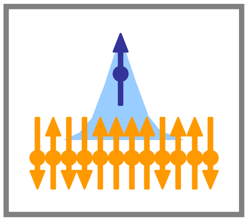

A dissertation submitted in partial satisfaction
of the requirements for the degree of

Doctor of Philosophy
in
Physics
by

Martino Poggio

Committee in charge:

Professor David D. Awschalom, Chairperson

Professor Leon Balents

Professor Andrew N. Cleland

December 2005

The dissertation of Martino Poggio is approved:

Committee Chairperson

October 2005

Spin Interactions Between Conduction Electrons and Local Moments in Semiconductor Quantum Wells

by

Martino Poggio

To my good friend and colleague,
Giovanni Bellomi

Acknowledgments

If I could choose a period in my life to repeat in perpetuity, it would certainly be my time in graduate school. I have thoroughly enjoyed my experience at UCSB and it is with considerable sadness that I prepare to leave the people and places that have made the last 5 years here in Santa Barbara so much fun. It is my great pleasure to finally thank those to whom I owe so much.

I'd like to first thank David Awschalom for his support and guidance. I am truly fortunate to have had him as my advisor. His high scientific standards and staunch support for his students have made working in his lab something I truly enjoy, as most of my friends can surely attest. I did a lot of learning in PSBS 1708 about physics, experimental science, and life in general, most of which I owe to David. He has been an ideal advisor.

I'd like to thank my colleagues and friends in the group. I am grateful to the previous generation of graduate students on whose shoulders we all stand and whose dog-eared theses were never far from my desk, especially Scott Crooker, Jay Kikkawa, and Jack Harris. In the early days I was lucky enough to work with and learn from some other Awschalom Lab All-Stars including Jay Gupta and Darron Young, who together taught me just about everything I know how to do in the lab. On top of being great friends and teachers, I think it's safe to say that those first couple of years in their Near Field Lab were some of the zaniest the group has ever seen. I owe Darron a special debt for putting up with me as a house-mate for 2 years. I also thank Zeke Johnston-Halperin for his ready advice and Irina Malajovich for being a welcoming first guide to the Awschalom lab.

I am equally fortunate to have worked with a gifted group of contemporaries including, Yui Kato, Roberto Myers, Nate Stern, Jesse Berezovsky, Hadrian

Knotz, Felix Mendoza, Vanessa Sih, Jason Stephens, Maiken Mikkelsen, and Ryan Epstein. I have especially benefited from witnessing Yui's domination of all problems tackled and from the many fruitful collaborations with Roberto. None of what is presented in the second half of this volume would have come to pass without his sample-growing brilliance. Despite our numerous disagreements and heated exchanges, he has never held a grudge and in fact, the confrontational style of our collaboration has probably been a major part of its success. Roberto's friendship outside of the lab, his prowess in a sail boat, and his knack for all things artistic have also been an integral part of many good times. Nate's assistance in the lab and his attention to detail have been invaluable to the latter half of my experiments. His patience with my odd and unpredictable schedule and his general good nature, despite endless conflict between Roberto and me, were more important than he may realize. I'm happy to leave my former corner of the optics lab in his very capable hands.

I am grateful to a number of former post-docs who have enriched my time here in one way or another, especially Ines Meinel for her true friendship; I can't imagine Santa Barbara without her. Thinking about our adventures in cooking and wine selection at the old Valerio house always makes me nostalgic for the early years. Gian Salis and his well-structured ideas were very influential to the course of my early experiments. I thank Geoff Steeves for his collaboration and enthusiasm during the "age of nuclei" and, of course, for convincing me to buy a sail boat. Many thanks to Ionel Tifrea for his interest in our work and for his patient collaborations. I am indebted to Alex Hollietner for his sound advice, his gnarly birthday present, and his poor cycling; to Florian Meier for explaining the mysteries of Faraday rotation; to Wayne Lau, Sai Ghosh, and Dave Steuerman for entertaining discussions; and to Min Ouyang, who along with Jesse and me, can't resist a late, late night in the lab.

Several professors have been extremely helpful through the years through collaborations and helpful discussions. Most notably, I'd like to thank Art Gossard, without whom my experiments would not have been possible. His MBE lab and his encouragement of interdepartmental collaboration are among the reasons which make working at UCSB a pleasure and a privilege. I also thank Daniel Loss and Michael Flatté for their friendly company at many conferences and especially for their assistance in theoretical matters.

Many thanks to the talented and good-natured guys in the physics machine shop: Mike Wrocklage, Doug Rehn, Mark Sheckherd, and Jeff Dutter. Doug bailed me out of more than one predicament, while Mike and Mark had a hand in quite a few essential parts of the experimental apparatus. The always reliable Paul Gritt and his efforts to keep the lab running smoothly are also greatly appreciated. Thanks of course to the ever cheery Holly Woo and the good people at CNSI for speed and efficiency in monetary matters. Finally, all of us in the lab are indebted to the DoD and NSF, whose dollars make our research possible.

Outside the lab, life has been rich and full of good times largely because of the friends and characters in orbit around 202 Selrose Lane (a house we never would have landed without some smooth talking from David himself). Let me first thank Jon Miller for his great friendship and for coming out to SB and forcing me to enjoy the place. His emphasis on leisure has been an invaluable foil to the more neurotic components of my personality. Ever witty and quick with his latest scheme, Jon has helped make life in SB a continuing series of funny stories. I'd like to thank my friend and former house-mate Chelsey Swanson, for her sense of humor and for bringing some So-Cal balance to temper Jon's and my Boston bombast. Thanks to Kristen Madler for her friendship and for always being game to go out for a glass of port (unless already in her PJs). Thanks also to house-mate Ryan Rassmussen and former house-mate Kristen

Morrison. Of course, I am grateful to the great friends in the extended Selrose clan: Suzanne Wilson, Steve Harding, Vanessa Silva, Aaron Gillen, Ryan Aubry, Chad Turner, Melanie Rassmussen, and Sarah Fretwell. It will be hard to leave my Santa Barbara family. Hold down the fort; I'll be back for Thanksgiving!

Running and all my runner friends have kept me sane through the years. I owe a debt first to John Orach and Mick Caruso for taking me under their wing and giving me my first taste of running up front. Thanks to Aaron for all those "Glamour Runs" and wacky phone messages and to Steve who is always a blast whether he's running or not, even on Sunday nights. Thanks too to Rusty Snow for all those workouts and to all the other guys who've hit the roads, trails, and track with me over the years: Carl Schulhof, Richard Haug, Rod Garrat, Jim Kornell, Dave Saunders, Terry Howell, Ramiro, Carl Legleiter, Steve Rider, Joe Devreese, Seth Waterfall, John Brennand, and many others. Keep running fast!

I am especially grateful to my family for their love and support; to my sister Allegra, whom I never see as much as I'd like, and who sets a constant example for me with her adventurous spirit and good nature; to my grandparents and family back in Italy who have always supported me despite the distance between us and my inability to explain what I'm doing; and finally to my parents Barbara and Tomaso. I couldn't ask for a better pair. My mother's love and support got me through all stages of my life and I only hope that some of her considerable intelligence and culture rubbed off on me in the process. My father and his stories of beautiful coeds is responsible for my landing in Santa Barbara, but more importantly he is the reason I have always wanted to be a scientist. It's convenient when your heros are also your parents. Ever supportive and always curious to hear what I'm doing, their calls and visits have been more appreciated than they may realize.

Vitæ

Education

2000	A.B., Physics, Harvard University
2003	M.A., Physics, University of California, Santa Barbara.
2005	Ph.D., Physics, University of California, Santa Barbara.

Publications

Journal Articles

“Structural, electrical, and magneto-optical characterization of paramagnetic GaMnAs quantum wells,” M. Poggio, R. C. Myers, N. P. Stern, A. C. Gossard, and D. D. Awschalom, *Phys. Rev. B* in press.

“Spin dynamics in electrochemically charged CdSe quantum dots,” N. P. Stern, M. Poggio, M. H. Bartl, E. L. Hu, G. D. Stucky, and D. D. Awschalom, *Phys. Rev. B* **72**, 161303(R) (2005).

“Antiferromagnetic s - d exchange coupling in GaMnAs,” R. C. Myers, M. Poggio, N. P. Stern, A. C. Gossard, and D. D. Awschalom, *Phys. Rev. Lett.* **95**, 017204 (2005).

“High-field optically detected nuclear magnetic resonance in GaAs,” M. Poggio and D. D. Awschalom, *Appl. Phys. Lett.* **86**, 182103 (2005).

“Spin transfer and coherence in coupled quantum wells,” M. Poggio, G. M. Steeves, R. C. Myers, N. P. Stern, A. C. Gossard, and D. D. Awschalom, *Phys. Rev. B* **70**, 121305(R) (2004).

"Local manipulation of nuclear spin in a semiconductor quantum well," M. Poggio, G. M. Steeves, R. C. Myers, Y. Kato, A. C. Gossard, and D. D. Awschalom, *Phys. Rev. Lett.* **91**, 207602 (2003).

"Quantum information processing with large nuclear spins in GaAs semiconductors," M. N. Leuenberger, D. Loss, M. Poggio, and D. D. Awschalom, *Phys. Rev. Lett.* **89**, 207601 (2002).

"Spin coherence and dephasing in GaN," B. Beschoten, E. Johnston-Halperin, D. K. Young, M. Poggio, J. E. Grimaldi, S. Keller, S. P. DenBaars, U. K. Mishra, E. L. Hu, and D. D. Awschalom, *Phys. Rev. B* **63**, 121202(R) (2001).

Other Articles

"Francis Harry Compton Crick," T. Poggio and M. Poggio, *Phys. Today* **57**, 80 (2004).

"Cooperative physics of fly swarms: an emergent behavior," M. Poggio and T. Poggio, *M.I.T. A.I. Memo* **1512** (1995).

Fields of study

Major field: Physics

Spin Interactions Between Conduction Electrons and Local Moments in Semiconductor Quantum Wells

Professor David D. Awschalom

Abstract

Spin Interactions Between Conduction Electrons and Local Moments in Semiconductor Quantum Wells

by

Martino Poggio

Spin interactions are studied between conduction band electrons in GaAs heterostructures and local moments, specifically the spins of constituent lattice nuclei and of partially filled electronic shells of impurity atoms. Nuclear spin polarizations are addressed through the contact hyperfine interaction resulting in the development of a method for high-field optically detected nuclear magnetic resonance sensitive to 10^8 nuclei. This interaction is then used to generate nuclear spin polarization profiles within a single parabolic quantum well; the position of these nanometer-scale sheets of polarized nuclei can be shifted along the growth direction using an externally applied electric field. In doped $\mathrm{Ga}_{1-x}\mathrm{Mn}_x\mathrm{As}/\mathrm{Al}_{0.4}\mathrm{Ga}_{0.6}\mathrm{As}$ quantum wells with $0.002\% < x < 0.13\%$, measurements of coherent electron spin dynamics show an antiferromagnetic exchange between s-like conduction band electrons and electrons localized in the d-shell of the Mn^{2+} impurities, which varies as a function of well width. During the course of these investigations, a wide variety of heterostructures are used to confine and control the spin of band electrons. Asymmetric coupled quantum wells have particularly interesting consequences for the spin dynamics of conduction electrons confined therein.

Contents

Chapter 3 High-field optically detected nuclear magnetic resonance 46

Chapter 4 Localized nuclear polarization in a quantum well 72

List of figures

List of tables

Chapter 1

Introduction

1.1 Perspective

The introduction of the concept of spin in the 1920's [1, 2] – the notion that elementary particles have an intrinsic angular momentum – is wholly quantum mechanical and cannot be understood in the context of classical physics [3]. Indeed, in the classical limit where $\hbar \to 0$, it disappears completely. Spin is such a fundamental part of quantum mechanics that perhaps the most compelling of the early experiments to confirm the theory, the Stern-Gerlach experiment [4], was not due to the quantization of orbital angular momentum as Stern and Gerlach originally thought, but was due to the quantization of spin [5].

While the theoretical origins of spin lie in relativistic considerations and require the application of quantum electro-dynamics, it emerges in many of the most basic quantum mechanical phenomena. From early observations of the "anomalous" Zeeman effect [6] in the spectrum of the hydrogen atom to the recent discovery of giant magneto-resistance (GMR) in metals [7, 8, 9], spin lies at the heart of the physical explanation. As we approach an age in which engineers routinely turn to quantum mechanics and its principles in the design of ever smaller and faster devices, understanding spin and its interactions becomes increasingly relevant. In this vein, this dissertation tackles a specific subset of these interactions, interactions between the spin of itinerant electrons and localized moments, in a class of materials of imminent technological relevance, GaAs-based semiconductor heterostructures.

1.2 Background

GaAs, due to its high electron mobility and direct band gap, is a critical component of today's semiconductor technology; its applications range from integrated circuits operating at microwave frequencies to light-emitting and laser diodes. As the possibility of new devices based on spin has emerged in recent years [10], researchers have turned to GaAs due to its favorable electronic properties and rich spin phenomenology. Experiments in GaAs have revealed conduction electron spin coherence on the order of 100 ns [11], over distances in excess of 100 μm [12], and even across heterointerfaces [13, 14]. Electric fields have been used in GaAs/AlGaAs parabolic quantum wells (PQWs) to control the electron spin g-factor [15, 16] and in lateral channels to generate and manipulate spins in the absence of magnetic fields [17, 18]. Similar experiments have also led to the observation of the spin Hall effect in GaAs and InGaAs epilayers [19]. Experiments in highly confined GaAs systems, known as gate-defined quantum dots, have also demonstrated long electron spin lifetimes and the ability to manipulate the spin states of single electrons [20, 21, 22].

Lest we limit ourselves to electronic spin, note that the spin of lattice nuclei is also responsible for a number of intriguing effects in GaAs which have been studied over the past 50 years [23, 24, 25]. Particularly interesting are phenomena attributable to the contact hyperfine interaction, which couples the itinerant spins in the semiconductor bands to those of the nuclei. Through this interaction, optical excitation can result in the hyperpolarization of nuclear moments [23] enabling the detection of nuclear magnetic resonance (NMR) in GaAs with a sensitivity several orders of magnitude larger than conventional methods provide [26, 27, 28, 29, 30, 31]. Recent work, aimed at developing techniques for locally manipulating nuclear polarization, have expanded our knowledge of the microscopic processes taking place between electronic and nuclear spins in low-dimensional structures [32, 33, 34, 35]. The ability to perform controlled interactions on small numbers of nuclei is critical for schemes suggesting the use of the semiconductor nuclear spins to store information; in such schemes, mobile band electrons naturally act as mediators used both to probe and modify the nuclear states [36]. GaAs structures provide a promising medium for the application of these ideas with their favorable electronic properties and long nuclear spin lifetimes (ranging up to minutes and hours).

In addition to lattice nuclei, another group of localized moments is fundamental to the physics of GaAs: the spin of shell electrons bound to magnetic dopants. The coupling of these moments to band electrons leads to a variety of phenomena, including, perhaps most importantly, carrier-mediated ferromagnetism in III-V dilute magnetic semiconductors (DMS) [37, 38]. These interactions enable striking experimental results demonstrating the external electrical control of ferromagnetism in a thin-film semiconducting alloy [39, 40]. While the ferromagnetic transition temperatures in these materials are currently below room-temperature, progress is being made towards this milestone. A material with controllable room-temperature ferromagnetism, especially an alloy of GaAs with its well-established electronic applications, would put spin-based interactions in semiconductors firmly in the realm of everyday information technology.

1.3 Results

In the context of the aforementioned work, we focus specifically on interactions of band electrons in GaAs heterostructures with both the spin of lattice nuclei and of electrons bound to impurity atoms. Particular attention is payed to the effects of carrier confinement on these interactions. Our study of the contact hyperfine interaction in quantum wells (QWs) leads to the demonstration of a technique for NMR sensitive far beyond conventional methods [41] and subsequent work in PQWs makes further use of the contact hyperfine interaction to pattern nanometer-scale profiles of nuclear polarization [42, 43]. Experiments discussed here on the *s*-*d* exchange interaction, between conduction band electrons and Mn impurities in GaMnAs QWs, yield surprising results, suggesting deficiencies in the current theoretical understanding of these materials [44, 45]. These measurements suggest that the *s*-*d* exchange energy in GaMnAs has both a strong dependence on confinement and is antiferromagnetic. The latter result may stimulate the rethinking of current theories for *sp*-*d* exchange in GaMnAs [46]. Heterostructures of GaAs play a central role throughout the presented work as a means to confine and control band electrons and their spin. The effect of confinement and band engineering on the dynamics of conduction band spins is prominent in our measurements of coupled quantum well (CQW) structures [47].

1.4 Organization

This dissertation is organized as follows. Chapter 2 contains a brief introduction to the concept of spin followed by a more detailed discussion of spin interactions in zinc-blende semiconductors. Chapters 3 and 4 focus on the contact hyperfine interaction and the spin of lattice nuclei in GaAs heterostructures; experiments are described demonstrating high field optically detected NMR and the patterning of localized nuclear polarization in a PQW, respectively. Shifting the discussion to the spin of impurity ions, chapter 5 covers measurements of the *s*-*d* exchange energy in GaAs QWs doped with Mn. Finally, chapter 6 presents measurements of the coherence and transfer of electronic spin localized in CQWs.

Chapter 2

Spin dynamics in zinc-blende semiconductors

2.1 Introduction

The crux of this dissertation lies in the concept of spin and in its interactions with other spins, with charge, and with electromagnetic fields. Specifically, these topics are addressed in experiments on heterostructures of GaAs and its alloys AlGaAs, InGaAs, and GaMnAs, all zinc-blende lattices. In order to properly interpret these experiments, in this chapter we lay the foundations in section 2.2 with a brief treatment of spin dynamics in general. Section 2.3 narrows the focus of the discussion onto the spin of mobile electronic carriers in a zinc-blende lattice. Differences between this case and the case of free electron spins, largely due to the mixing of spin and orbit degrees of freedom, become apparent in this section. Since much of the work presented in later chapters involves spins trapped in quantum wells, the effects of confinement on the electronic bands is considered in section 2.4. Section 2.5 covers the interaction of carriers with localized moments including lattice nuclei and magnetic impurities. Since we use optical methods in this work to generate and detect spin in a zinc-blende lattice, special attention is payed throughout the chapter to the optical selection rules. Finally, a brief overview of the main experimental techniques which we employ to probe spin dynamics, Faraday and Kerr rotation, is provided in section 2.6.

2.2 Free electron spin dynamics

2.2.1 Electron spin

In non-relativistic quantum mechanics, an electron can be described by a state $\psi(x,y,z,t)$ which depends on the three spatial coordinates and time [3, 48, 49]. Using only these degrees of freedom, a theory emerges which accurately describes a number of physical systems, including the hydrogen atom. When the hydrogen spectrum is examined in detail, however, discrepancies appear which this framework cannot explain. A large variety of other physical phenomena including ferromagnetism, the Zeeman effect, and most notably the behavior of silver atoms in the Stern-Gerlach experiment [4] remain outside the reach of this simple treatment. This experimental evidence coupled with the requirements made by a fully relativistic description of quantum mechanics lead to the addition of another degree of freedom to the electron, known as *spin*. The spin observable **S** is an intrinsic angular momentum of the electron in addition to its orbital angular momentum **L**. For the free electron, the **S** operator acts in a separate state space from the orbital degrees of freedom and thus commutes with all orbital observables. In quantum mechanics, angular momentum **J** is defined as an observable whose coordinates satisfy:

$$[J_\alpha, J_\beta] = i\varepsilon_{\alpha\beta\gamma}\hbar J_\gamma, \tag{2.1}$$

where $\hbar$ is Planck's constant, the quantum of angular momentum. Both **L** and **S** satisfy these commutation relations which form the basis for their properties throughout quantum mechanics. For example, the fact that the spectrum of measurable angular momentum values is bounded and discrete is fully contained in equation 2.1. Further, in order to account for experiments, the electron is designated as a spin-1/2 particle, i.e. $s = 1/2$. Therefore its spin state space is two-dimensional and measurements of **S** along a given direction can only result in $\pm\hbar/2$.

2.2.2 The intrinsic magnetic moment of an electron

The magnetic moment **M** associated with the orbital angular momentum of an electron is,

$$\mathbf{M} = -\frac{e}{2m_e}\mathbf{L} = -\frac{\mu_B}{\hbar}\mathbf{L}, \tag{2.2}$$

where $-e$ ($e > 0$) is the charge and m_e is the mass of an electron and $\mu_B = \frac{e\hbar}{2m_e}$ is the Bohr magneton. An analogous equation gives the magnetic moment of an electron associated with its intrinsic angular momentum:

$$\mathbf{M}_S = -\frac{g\mu_B}{\hbar}\mathbf{S}, \tag{2.3}$$

where g is the Landé g-factor. For a free electron $g_0 = 2.002319304386 \pm 10^{-11}$ [50], though it can be significantly different for an electron in the conduction band of a semiconductor as discussed in section 2.3.3.

2.2.3 Spin precession

In general, the Hamiltonian for a magnetic moment **M** in a uniform magnetic field **B** is,

$$H = -\mathbf{M}\cdot\mathbf{B}. \tag{2.4}$$

In the case of a free electron, we can separate spin and orbital degrees of freedom and focus on the energy associated with spin:

$$H_S = \frac{g\mu_B}{\hbar}\mathbf{B}\cdot\mathbf{S} = \frac{g\mu_B}{\hbar}BS_z, \tag{2.5}$$

where we have taken $\hat{z}$ as the direction of $\mathbf{B}$. Equation 2.5 represents a simple two-state system. The eigenstates of S_z are $|\uparrow\rangle$ and $|\downarrow\rangle$ with eigenvalues of $+\hbar/2$ and $-\hbar/2$, respectively. These states are also eigenstates of H_S, with energy eigenvalues of $+\frac{1}{2}g\mu_B B$ and $-\frac{1}{2}g\mu_B B$, respectively. Spin states parallel to $\mathbf{B}$, i.e. eigenstates of S_z, are stationary, while states perpendicular to $\mathbf{B}$ are not; the eigenstates of S_x and S_y evolve in time.

The time dependence of $\mathbf{S}$ is simply,

$$\frac{d\mathbf{S}}{dt} = \frac{i}{\hbar}[H_S, \mathbf{S}] + \frac{\partial \mathbf{S}}{\partial t}. \tag{2.6}$$

Since $\frac{\partial \mathbf{S}}{\partial t} = 0$, using equations 2.1 and 2.5, we obtain:

$$\frac{d\mathbf{S}}{dt} = \vec{\omega}_L \times \mathbf{S}, \tag{2.7}$$

where $\vec{\omega}_L = 2\pi\vec{\nu}_L = \frac{g\mu_B}{\hbar}\mathbf{B}$ is the Larmor precession vector. Trivially, the expectation value of this operator evolves as,

$$\frac{d}{dt}\langle\mathbf{S}\rangle = \vec{\omega}_L \times \langle\mathbf{S}\rangle. \tag{2.8}$$

This familiar looking equation results in the precession of $\langle\mathbf{S}\rangle$ around the axis defined by $\vec{\omega}_L$ at an angular frequency given by $|\vec{\omega}_L|$. Therefore, for an electron in an arbitrary initial spin state given by,

$$|\psi\rangle = \cos\left(\frac{\theta}{2}\right)e^{-i\phi/2}|\uparrow\rangle + \sin\left(\frac{\theta}{2}\right)e^{i\phi/2}|\downarrow\rangle, \tag{2.9}$$

$\langle\mathbf{S}\rangle$ will evolve in time according to:

$$\langle\mathbf{S}\rangle = \frac{\hbar}{2}\left(\sin\theta\cos\left(\omega_L t + \phi\right)\hat{x} + \sin\theta\sin\left(\omega_L t + \phi\right)\hat{y} + \cos\theta\hat{z}\right). \tag{2.10}$$

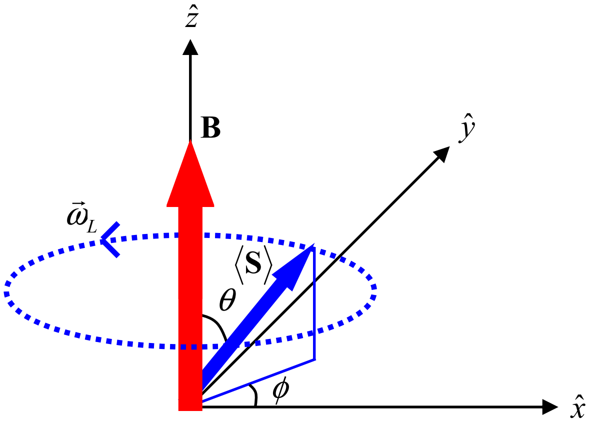

Figure 2.1: A schematic diagram depicting Larmor precession of the spin vector $\langle\mathbf{S}\rangle$ in a constant magnetic field **B** according to equation 2.10.

As an example, take an eigenstate of S_x, $|\phi\rangle = \frac{1}{\sqrt{2}}(|\uparrow\rangle + |\downarrow\rangle)$, as the initial state. In this case, it is clear from equations 2.9 and 2.10 that the expectation value of the electron spin, which was initially directed along $\hat{x}$ will precess about **B** in the xy-plane:

$$\langle\mathbf{S}\rangle = \frac{\hbar}{2}\left(\cos\left(\omega_L t\right)\hat{x} + \sin\left(\omega_L t\right)\hat{y}\right). \tag{2.11}$$

2.2.4 Spin relaxation

In real systems, the cosinusoidal spin precession described in section 2.2.3 does not go on forever. Interactions with the environment, which have not been included in our idealized Hamiltonian, contribute to the relaxation of the spin state. There are two types of spin relaxation, longitudinal relaxation characterized by a time constant T_1 and transverse relaxation characterized by a time constant T_2. The former mechanism is a process of energy relaxation and involves spin flips in the direction of **B** (equivalent to the randomization of θ in equation 2.9). As is clear from equation 2.5, these flips require or produce energy which has to be exchanged with environmental systems, such as the phonon bath. Transverse spin relaxation, on the other hand, involves decoherence of a spin state through the randomization of the phase between the two components of a superposition state (equivalent to the randomization of ϕ in equation 2.9). This process randomizes the component of the spin state perpendicular to $\mathbf{B}$. Since the perpendicular component is irrelevant to the energy of the spin, this type of relaxation neither requires nor produces energy.

Another process, known as spin dephasing, affects transverse spin lifetimes and is relevant in the measurement of ensembles of spins or in time-averaged measurements of single spins. Dephasing arises due to inhomogeneities in the system: spins at different positions or times precess at different rates. The resultant scrambling of the average spin polarization causes the measured lifetime to be limited by the inhomogeneous transverse spin lifetime ${T_2}^*$. Several methods of extracting the transverse lifetime T_2 of a single spin exist even when $T_2 > {T_2}^*$, most notably the spin-resonance method known as the Hahn spin echo [51]. Note that the difference in T_2 and ${T_2}^*$ is not a reflection of processes acting on single spins, but rather it is a manifestation of the randomization of spins in an ensemble, either in time or space, with respect to each other.

The measurements of electron spin coherence discussed in this dissertation are measurements of spin ensembles which are typically limited by inhomogeneous dephasing. Therefore to account for the effects of spin relaxation we include the phenomenological parameters T_1 and ${T_2}^*$ in the dynamical equation for an ensemble of non-interacting spins in a magnetic field. This equation represents a simple modification of equation 2.8,

$$\frac{d}{dt}\langle\mathbf{S}\rangle = \vec{\omega}_L \times \langle\mathbf{S}\rangle - \frac{(\langle\mathbf{S}\rangle \cdot \hat{\omega}_L - S_{eq})\hat{\omega}_L}{T_1} - \frac{\langle\mathbf{S}\rangle - (\langle\mathbf{S}\rangle \cdot \hat{\omega}_L)\hat{\omega}_L}{{T_2}^*}, \tag{2.12}$$

where S_{eq} is the equilibrium magnitude of $\langle\mathbf{S}\rangle$ along the direction of the applied magnetic field given by $\hat{\omega} = \vec{\omega}_L / |\vec{\omega}_L|$. Since in the experiments described in this dissertation $S_{eq} \simeq 0$, let us simplify our calculations by taking $S_{eq} = 0$. Having included the relaxation parameters in the dynamical equation, we see that the initial state shown in equation 2.9 now evolves according to:

$$\langle \mathbf{S} \rangle = \frac{\hbar}{2} \left(e^{-t/T_2{}^*} \sin\theta \left[\cos(\omega_L t + \phi)\hat{x} + \sin(\omega_L t + \phi)\hat{y} \right] + e^{-t/T_1} \cos\theta \hat{z} \right). \tag{2.13}$$

Therefore, the spin dynamics of an ensemble of non-interacting free electrons in a magnetic field are characterized by exponential decay along the quantization axis and exponentially damped cosinusoidal precession in the plane perpendicular to the quantization axis.

2.3 Carrier spin in zinc-blende semiconductors

2.3.1 Crystal structure and electronic properties

III-V compounds crystallize in the zinc-blende structure consisting of two interpenetrating, face-centered cubic (FCC) lattices. Each FCC lattice is displaced by one fourth of the main cube diagonal from the other and is formed by one of the two constituent atomic species. Therefore, given a cube side of length a, the elementary cell of the zinc-blende lattice contains one atom of each species with one atom displaced by a vector $\left(\frac{a}{4}, \frac{a}{4}, \frac{a}{4}\right)$ relative to the other. The Bravais lattice underlying the zinc-blende lattice is the FCC lattice, whose reciprocal lattice is body centered cubic (BCC).

The zinc-blende structure results in the distribution of an equal number of atoms from each of the two species, e.g. Ga and As, on a diamond lattice such that each has four of the other type as nearest neighbors. In III-V binary compounds, there are 8 outer electrons per unit cell which contribute to the chemical bonds formed between nearest neighbors. Other inner electrons, found in closed-shell configurations with wave functions closely bound to lattice nuclei do not contribute to the the transport or to the near-band-gap optical properties discussed here. In GaAs, the 8 outermost electrons, 3 from the $4s^2 4p^1$ orbital configuration of Ga and 5 from the $4s^2 4p^3$ configuration of As, hybridize to form tetrahedral bonds between nearest neighbors. Each s and p orbital hybridizes with the corresponding orbital of its nearest neighbor to form a bonding and an antibonding pair. Bonding orbitals are characterized by a high electron density between the atoms while antibonding orbitals tend to have a high density at the atomic sites. Due to the large number of unit cells, the bonding and antibonding levels broaden into bands. The bonding s levels are the most deeply bound and are always occupied by 2 electrons per unit cell. The other 6 electrons per unit cell fill the three bonding p levels, which form the valence band of the crystal. The remaining antibonding levels are unfilled with the lowest lying, the antibonding s level, forming the conduction band of the material [52].

We now consider the electronic states near the center of the Brillouin zone (Γ point) where $\mathbf{k} = 0$. In GaAs, the top of the valence band and the bottom of the conduction band occur here, forming a direct band-gap. This region of the band structure is the relevant part for most processes occurring in the semiconductor. According to the Bloch theorem, electron states can be written in the following form:

$$\psi_{n,\mathbf{k}}(\mathbf{r}) = N u_{n,\mathbf{k}}(\mathbf{r}) e^{i\mathbf{k}\cdot\mathbf{r}}, \tag{2.14}$$

where $\mathbf{r}$ is the electron position, N is a normalization coefficient, $u_{n,\mathbf{k}}(\mathbf{r})$ is a function in the n^{th} Brillouin zone periodic with the periodicity of the lattice, and $\mathbf{k}$ is the crystal wave vector. Though these functions are seldom calculated explicitly, we can use the symmetry of the crystal coupled with some standard approximations such as $\mathbf{k}\cdot\mathbf{p}$ theory [53] or the Kane model [54] to make adequate descriptions of relevant phenomena. In the absence of external fields we have the Hamiltonian (in CGS),

$$H = \frac{p^2}{2m_0} + V_0(\mathbf{r}) + \frac{1}{2m_0^2c^2}\left(\mathbf{S}\times\nabla V_0\right)\cdot\mathbf{p}, \tag{2.15}$$

where m_0 is the free electron mass, $V_0(\mathbf{r})$ is the periodic potential of the lattice, and c is the speed of light. By solving the Schödinger equation for the set of eigenstates and energy eigenvalues at the Γ point ($\mathbf{k}=0$), we find Bloch functions of the form $\psi_{n,0}(\mathbf{r}) = Nu_{n,0}(\mathbf{r})$. These functions are orthonormal, $(1/\Omega)\left\langle u_{m',0}|u_{m,0}\right\rangle = \delta_{m',m}$, where Ω is volume of the unit cell and they form a complete basis with respect to functions with the lattice periodicity such that, $u_{n,\mathbf{k}} = \sum\limits_m c_m(\mathbf{k})u_{m,0}(\mathbf{r})$. We can then expand the solutions for $\mathbf{k}\neq 0$:

$$\psi_{n,\mathbf{k}}(\mathbf{r}) = Ne^{i\mathbf{k}\cdot\mathbf{r}}\sum_m c_m(\mathbf{k})u_{m,0}(\mathbf{r}). \tag{2.16}$$

A minimal set of $\{u_{m,0}(\mathbf{r})\}$ includes only states on either side of the band gap: in this case, an s-like conduction band wave function denoted by $|S\rangle$ and three p-like valence band wave functions denoted by $|X\rangle$, $|Y\rangle$, and $|Z\rangle$. These states have the same symmetry as the atomic s, p_x, p_y, and p_z orbitals from which they are formed. By simply adding the spin degree of freedom as a tensor product, we have a basis of 2 conduction band states and 6 valence band states: $\{|S\uparrow\rangle, |X\uparrow\rangle, |Y\uparrow\rangle, |Z\uparrow\rangle, |S\downarrow\rangle, |X\downarrow\rangle, |Y\downarrow\rangle, |Z\downarrow\rangle\}$. Even with such a limited basis, we can calculate many of the most important electronic and optical properties of III-V semiconductors. Naturally, more bands can be included in order to refine the approximation.

Since the III-V Hamiltonian involves a non-zero spin-orbit coupling term proportional to $\mathbf{L}\cdot\mathbf{S} = \frac{1}{2}\left(\mathbf{J}^2 - \mathbf{L}^2 - \mathbf{S}^2\right)$, it is natural to use a basis in which this term is diagonal, the basis of total angular momentum $\mathbf{J} = \mathbf{L}+\mathbf{S}$. In order to do so, we will first express the orbital component of the Bloch functions

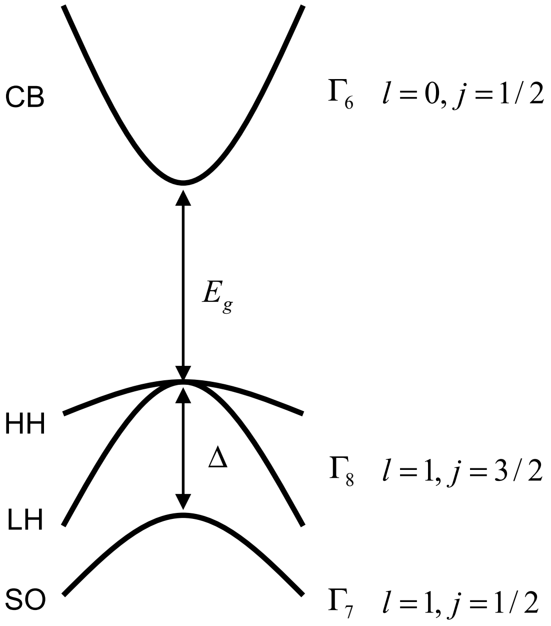

Figure 2.2: Band structure diagram near the Γ point in zinc-blende crystals.

in terms of eigenstates of $\mathbf{L}$, $|l,m_l\rangle$: $|0,0\rangle = i|S\rangle$, $|1,0\rangle = |Z\rangle$, and $|1,\pm1\rangle = \sqrt{\frac{1}{2}}(|X\rangle \pm i|Y\rangle)$. Combining with spin, we can write our basis in terms of eigenstates of total angular momentum, $|j,m_j\rangle$, shown in table 2.1. For the conduction band edge, $l=0$ and $s=\frac{1}{2}$, giving $j=\frac{1}{2}$. Meanwhile for the valence band edge, $l=1$ and $s=\frac{1}{2}$, giving $j=\frac{3}{2},\frac{1}{2}$. Since $\langle \mathbf{L}\cdot\mathbf{S}\rangle = \frac{\hbar^2}{2}(j(j+1) - l(l+1) - s(s+1))$, the $j=\frac{1}{2}$ hole band is split off in energy from the $j=\frac{3}{2}$ bands. This band is known as the split off (SO) hole band while the other two valence bands are degenerate at $\mathbf{k}=0$ and are known as the heavy hole (HH) and light hole (LH) bands for $m_j = \pm\frac{3}{2}$ and $m_j = \pm\frac{1}{2}$, respectively, because of differences in their effective masses.

Table 2.1: The conduction and valence band states at the Γ point in zinc-blende crystals.

Band	u_i	$\left\|j,m_j\right\rangle$	E_i
CB	u_1	$\left\|\frac{1}{2},+\frac{1}{2}\right\rangle_{\mathrm{CB}} = \|0,0\rangle\|\uparrow\rangle$	E_{c}
	u_2	$\left\|\frac{1}{2},-\frac{1}{2}\right\rangle_{\mathrm{CB}} = \|0,0\rangle\|\downarrow\rangle$	E_{c}
HH	u_3	$\left\|\frac{3}{2},+\frac{3}{2}\right\rangle_{\mathrm{HH}} = \|1,+1\rangle\|\uparrow\rangle$	E_{v}
	u_4	$\left\|\frac{3}{2},-\frac{3}{2}\right\rangle_{\mathrm{HH}} = \|1,-1\rangle\|\downarrow\rangle$	E_{v}
LH	u_5	$\left\|\frac{3}{2},-\frac{1}{2}\right\rangle_{\mathrm{LH}} = -\sqrt{\frac{1}{3}}\|1,-1\rangle\|\uparrow\rangle-\sqrt{\frac{2}{3}}\|1,0\rangle\|\downarrow\rangle$	E_{v}
	u_6	$\left\|\frac{3}{2},+\frac{1}{2}\right\rangle_{\mathrm{LH}} = \sqrt{\frac{1}{3}}\|1,+1\rangle\|\downarrow\rangle-\sqrt{\frac{2}{3}}\|1,0\rangle\|\uparrow\rangle$	E_{v}
SO	u_7	$\left\|\frac{1}{2},-\frac{1}{2}\right\rangle_{\mathrm{SO}} = -\sqrt{\frac{2}{3}}\|1,-1\rangle\|\uparrow\rangle+\sqrt{\frac{1}{3}}\|1,0\rangle\|\downarrow\rangle$	$E_{\mathrm{v}}-\Delta$
	u_8	$\left\|\frac{1}{2},+\frac{1}{2}\right\rangle_{\mathrm{SO}} = \sqrt{\frac{2}{3}}\|1,+1\rangle\|\downarrow\rangle+\sqrt{\frac{1}{3}}\|1,0\rangle\|\uparrow\rangle$	$E_{\mathrm{v}}-\Delta$

2.3.2 Interband transitions and optical orientation

Due to the direct nature of the band gap, photons can induce electronic transitions between valence and conduction band states near the Γ point. In the electric dipole approximation the rate of transition from an initial state $|\psi_i\rangle$ to a final state $|\psi_f\rangle$ is given by Fermi's Golden Rule as $\frac{2\pi}{\hbar}\left|\langle\psi_f|e\mathbf{r}\cdot\mathbf{E}|\psi_i\rangle\right|^2\delta(E_f - E_i - h\nu)$, where $\mathbf{E}$ is the electric field of the incident radiation, ν is the frequency of the radiation, and E_f and E_i are the energies of the final and initial states. Since we have previously taken $\hat{z}$ as the quantization axis for angular momentum, σ^+ and σ^- polarized radiation (defined in figure 2.3) are given by $E(t)\left(-\frac{1}{\sqrt{2}}[\hat{x}+i\hat{y}]\right)$ and $E(t)\left(\frac{1}{\sqrt{2}}[\hat{x}-i\hat{y}]\right)$, respectively. Note that due to the cubic symmetry in the zinc-blende structure, the $\hat{z}$ axis can be taken along either the [100], [010], or [001] axes without loss of generality.

In order to easily calculate the optical transition rates between the valence and conduction band states, note that our basis states, shown in table 2.1 are in the form of spherical harmonics. Since the dipole term $e\mathbf{r}\cdot\mathbf{E}$ can also be expressed as a spherical harmonic, we can take advantage of the orthonormality

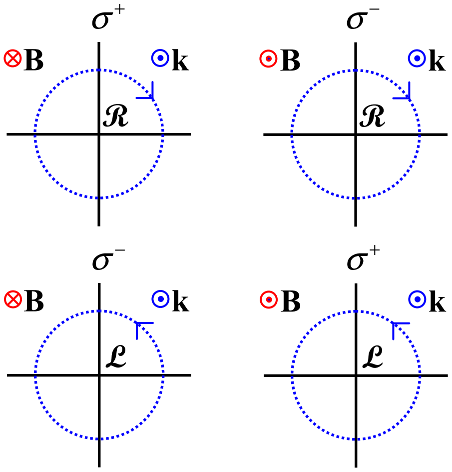

Figure 2.3: Schematic diagrams illustrating the definitions of $\mathscr{R}$, $\mathscr{L}$,σ^+, and σ^- polarized light. $\mathscr{R}$ and $\mathscr{L}$ are defined in terms of the angular momentum carried by the light and its propagation direction **k**, whereas σ^+ and σ^- are defined in terms of the angular momentum and an external applied magnetic field **B**. Arrow heads on the dotted-line circles indicate the direction of rotation of the light's electric field vector [55].

of this basis to simplify our calculations:

$$e\mathbf{r}\cdot\mathbf{E}_{\sigma^+} \quad \propto \quad \langle 1,-1|\mathbf{r}\rangle\,, \tag{2.17}$$

$$e\mathbf{r}\cdot\mathbf{E}_{\sigma^-} \quad \propto \quad \langle 1,+1|\mathbf{r}\rangle\,, \tag{2.18}$$

The orbital portion of both conduction band states is the spherically symmetric function $|0,0\rangle$ and thus can be ignored in our calculations. Therefore, using table 2.1, the above equations, and the orthonormality of the spin eigenstates, we can solve for all of the matrix elements required to determine transition rates up to an arbitrary constant γ as shown in table 2.2.

For the transition rate to be non-zero, Fermi's Golden Rule also requires a photon energy resonant with the energy gap between the valence and conduction band states. As evident in table 2.1, the SO band is shifted down from the other valence bands by an energy Δ due to the spin-orbit coupling. The magnitude of Δ goes roughly as Z^4 where Z is the atomic number. In GaAs, $\Delta = 0.34$ eV and thus cannot be ignored. Therefore in considering optical excitation resonant with the band-gap ($E_\mathrm{c} - E_\mathrm{v}$), we will consider only transitions from the HH and LH bands to the conduction band (CB).

The results of table 2.2 are combined with Fermi's Golden Rule to produce the transition rates summarized in figure 2.4. The inequality of various transition rates for a given circular polarization results in a spin imbalance in the conduction band. 100% circularly polarized illumination resonant with the band-gap energy results in a 50% polarized population of excited electrons in the conduction band. This convenient property of the system's electronic structure is critical for the optical studies of electron spin dynamics presented in this dissertation and relies entirely on the system having a large enough spin-orbit coupling to push the SO band out of resonance with the optical excitation. Careful inspection of table 2.2 and figure 2.4 show that if Δ is smaller that the energy width of the optical excitation, no spin polarization is created in the conduction band. In addition to providing a means by which to optically inject polarized carriers in these semiconductors, the selection rules discussed here also aid in the detection of electron and hole spin polarization through measurements of the polarization of recombinant radiation.

2.3.3 Deviation from the free electron g-factor

As mentioned at the end of section 2.2.2, the g-factor of conduction band electrons can be significantly different from the free electron value. In various zinc-blende semiconductors it can vary from -50 to 2 [56]. This large change in g_e is due to spin-orbit term in the Hamiltonian of the system leading to a coupling between the conduction and valence bands linear in the magnetic field B. Though

Table 2.2: Optical matrix elements up to an arbitrary constant γ near the zone center of a zinc-blende lattice.

Pol.	CB spin	$\lvert\langle\psi_{cb}\vert e\mathbf{r}\cdot\mathbf{E}\vert\psi_{vb}\rangle\rvert^2$	
σ^+	↑	$\big\lvert {}_{\mathrm{CB}}\langle \frac{1}{2},+\frac{1}{2} \vert e\mathbf{r}\cdot\mathbf{E} \vert \frac{3}{2},+\frac{1}{2}\rangle_{\mathrm{LH}} \big\rvert^2 \propto \frac{2}{3}\lvert\langle 1,-1\vert 1,0\rangle\rvert^2$	$=0$
		$\big\lvert {}_{\mathrm{CB}}\langle \frac{1}{2},+\frac{1}{2} \vert e\mathbf{r}\cdot\mathbf{E} \vert \frac{3}{2},-\frac{1}{2}\rangle_{\mathrm{LH}} \big\rvert^2 \propto \frac{1}{3}\lvert\langle 1,-1\vert 1,-1\rangle\rvert^2$	$=\frac{1}{3}\gamma$
		$\big\lvert {}_{\mathrm{CB}}\langle \frac{1}{2},+\frac{1}{2} \vert e\mathbf{r}\cdot\mathbf{E} \vert \frac{3}{2},+\frac{3}{2}\rangle_{\mathrm{HH}} \big\rvert^2 \propto \frac{1}{3}\lvert\langle 1,-1\vert 1,+1\rangle\rvert^2$	$=0$
		$\big\lvert {}_{\mathrm{CB}}\langle \frac{1}{2},+\frac{1}{2} \vert e\mathbf{r}\cdot\mathbf{E} \vert \frac{3}{2},-\frac{3}{2}\rangle_{\mathrm{HH}} \big\rvert^2$	$=0$
		$\big\lvert {}_{\mathrm{CB}}\langle \frac{1}{2},+\frac{1}{2} \vert e\mathbf{r}\cdot\mathbf{E} \vert \frac{1}{2},+\frac{1}{2}\rangle_{\mathrm{SO}} \big\rvert^2 \propto \frac{1}{3}\lvert\langle 1,-1\vert 1,0\rangle\rvert^2$	$=0$
		$\big\lvert {}_{\mathrm{CB}}\langle \frac{1}{2},+\frac{1}{2} \vert e\mathbf{r}\cdot\mathbf{E} \vert \frac{1}{2},-\frac{1}{2}\rangle_{\mathrm{SO}} \big\rvert^2 \propto \frac{2}{3}\lvert\langle 1,-1\vert 1,-1\rangle\rvert^2$	$=\frac{2}{3}\gamma$
σ^+	↓	$\big\lvert {}_{\mathrm{CB}}\langle \frac{1}{2},-\frac{1}{2} \vert e\mathbf{r}\cdot\mathbf{E} \vert \frac{3}{2},+\frac{1}{2}\rangle_{\mathrm{LH}} \big\rvert^2 \propto \frac{1}{3}\lvert\langle 1,-1\vert 1,+1\rangle\rvert^2$	$=0$
		$\big\lvert {}_{\mathrm{CB}}\langle \frac{1}{2},-\frac{1}{2} \vert e\mathbf{r}\cdot\mathbf{E} \vert \frac{3}{2},-\frac{1}{2}\rangle_{\mathrm{LH}} \big\rvert^2 \propto \frac{2}{3}\lvert\langle 1,-1\vert 1,0\rangle\rvert^2$	$=0$
		$\big\lvert {}_{\mathrm{CB}}\langle \frac{1}{2},-\frac{1}{2} \vert e\mathbf{r}\cdot\mathbf{E} \vert \frac{3}{2},+\frac{3}{2}\rangle_{\mathrm{HH}} \big\rvert^2$	$=0$
		$\big\lvert {}_{\mathrm{CB}}\langle \frac{1}{2},-\frac{1}{2} \vert e\mathbf{r}\cdot\mathbf{E} \vert \frac{3}{2},-\frac{3}{2}\rangle_{\mathrm{HH}} \big\rvert^2 \propto \lvert\langle 1,-1\vert 1,-1\rangle\rvert^2$	$=\gamma$
		$\big\lvert {}_{\mathrm{CB}}\langle \frac{1}{2},-\frac{1}{2} \vert e\mathbf{r}\cdot\mathbf{E} \vert \frac{1}{2},+\frac{1}{2}\rangle_{\mathrm{SO}} \big\rvert^2 \propto \frac{2}{3}\lvert\langle 1,-1\vert 1,+1\rangle\rvert^2$	$=0$
		$\big\lvert {}_{\mathrm{CB}}\langle \frac{1}{2},-\frac{1}{2} \vert e\mathbf{r}\cdot\mathbf{E} \vert \frac{1}{2},-\frac{1}{2}\rangle_{\mathrm{SO}} \big\rvert^2 \propto \frac{1}{3}\lvert\langle 1,-1\vert 1,0\rangle\rvert^2$	$=0$
σ^-	↑	$\big\lvert {}_{\mathrm{CB}}\langle \frac{1}{2},+\frac{1}{2} \vert e\mathbf{r}\cdot\mathbf{E} \vert \frac{3}{2},+\frac{1}{2}\rangle_{\mathrm{LH}} \big\rvert^2 \propto \frac{2}{3}\lvert\langle 1,+1\vert 1,0\rangle\rvert^2$	$=0$
		$\big\lvert {}_{\mathrm{CB}}\langle \frac{1}{2},+\frac{1}{2} \vert e\mathbf{r}\cdot\mathbf{E} \vert \frac{3}{2},-\frac{1}{2}\rangle_{\mathrm{LH}} \big\rvert^2 \propto \frac{1}{3}\lvert\langle 1,+1\vert 1,-1\rangle\rvert^2$	$=0$
		$\big\lvert {}_{\mathrm{CB}}\langle \frac{1}{2},+\frac{1}{2} \vert e\mathbf{r}\cdot\mathbf{E} \vert \frac{3}{2},+\frac{3}{2}\rangle_{\mathrm{HH}} \big\rvert^2 \propto \lvert\langle 1,+1\vert 1,+1\rangle\rvert^2$	$=\gamma$
		$\big\lvert {}_{\mathrm{CB}}\langle \frac{1}{2},+\frac{1}{2} \vert e\mathbf{r}\cdot\mathbf{E} \vert \frac{3}{2},-\frac{3}{2}\rangle_{\mathrm{HH}} \big\rvert^2$	$=0$
		$\big\lvert {}_{\mathrm{CB}}\langle \frac{1}{2},+\frac{1}{2} \vert e\mathbf{r}\cdot\mathbf{E} \vert \frac{1}{2},+\frac{1}{2}\rangle_{\mathrm{SO}} \big\rvert^2 \propto \frac{1}{3}\lvert\langle 1,+1\vert 1,0\rangle\rvert^2$	$=0$
		$\big\lvert {}_{\mathrm{CB}}\langle \frac{1}{2},+\frac{1}{2} \vert e\mathbf{r}\cdot\mathbf{E} \vert \frac{1}{2},-\frac{1}{2}\rangle_{\mathrm{SO}} \big\rvert^2 \propto \frac{2}{3}\lvert\langle 1,+1\vert 1,-1\rangle\rvert^2$	$=0$
σ^-	↓	$\big\lvert {}_{\mathrm{CB}}\langle \frac{1}{2},-\frac{1}{2} \vert e\mathbf{r}\cdot\mathbf{E} \vert \frac{3}{2},+\frac{1}{2}\rangle_{\mathrm{LH}} \big\rvert^2 \propto \frac{1}{3}\lvert\langle 1,+1\vert 1,+1\rangle\rvert^2$	$=\frac{1}{3}\gamma$
		$\big\lvert {}_{\mathrm{CB}}\langle \frac{1}{2},-\frac{1}{2} \vert e\mathbf{r}\cdot\mathbf{E} \vert \frac{3}{2},-\frac{1}{2}\rangle_{\mathrm{LH}} \big\rvert^2 \propto \frac{2}{3}\lvert\langle 1,+1\vert 1,0\rangle\rvert^2$	$=0$
		$\big\lvert {}_{\mathrm{CB}}\langle \frac{1}{2},-\frac{1}{2} \vert e\mathbf{r}\cdot\mathbf{E} \vert \frac{3}{2},+\frac{3}{2}\rangle_{\mathrm{HH}} \big\rvert^2$	$=0$
		$\big\lvert {}_{\mathrm{CB}}\langle \frac{1}{2},-\frac{1}{2} \vert e\mathbf{r}\cdot\mathbf{E} \vert \frac{3}{2},-\frac{3}{2}\rangle_{\mathrm{HH}} \big\rvert^2 \propto \lvert\langle 1,+1\vert 1,-1\rangle\rvert^2$	$=0$
		$\big\lvert {}_{\mathrm{CB}}\langle \frac{1}{2},-\frac{1}{2} \vert e\mathbf{r}\cdot\mathbf{E} \vert \frac{1}{2},+\frac{1}{2}\rangle_{\mathrm{SO}} \big\rvert^2 \propto \frac{2}{3}\lvert\langle 1,+1\vert 1,+1\rangle\rvert^2$	$=\frac{2}{3}\gamma$
		$\big\lvert {}_{\mathrm{CB}}\langle \frac{1}{2},-\frac{1}{2} \vert e\mathbf{r}\cdot\mathbf{E} \vert \frac{1}{2},-\frac{1}{2}\rangle_{\mathrm{SO}} \big\rvert^2 \propto \frac{1}{3}\lvert\langle 1,+1\vert 1,0\rangle\rvert^2$	$=0$

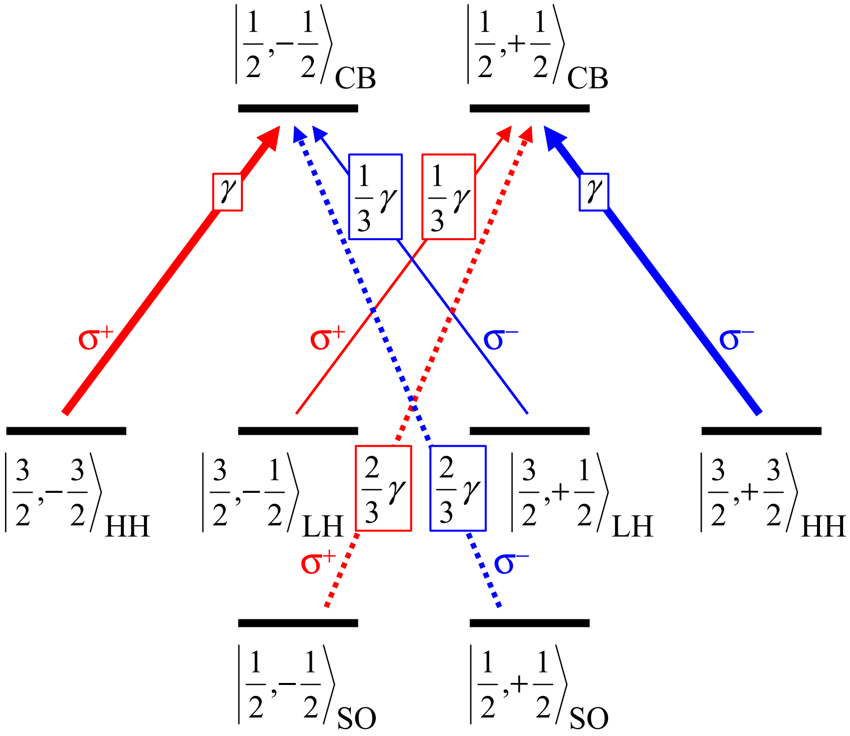

Figure 2.4: A schematic diagram illustrating the optical selection rules for σ^+ and σ^- polarized light in a zinc-blende lattice. Note that since the SO band is at a lower energy than the other valence bands, its transitions are not typically excited (dotted arrows). As a result circular polarized irradiation creates a 50% ($\uparrow$:$\downarrow = 3:1$) polarization in the conduction band.

a concise discussion of the conduction band g-factor in zinc-blende materials is given in a previous dissertation [57], a similar treatment will be given here for completeness.

We take the Hamiltonian in equation 2.15 and modify it to account for the presence of a magnetic field **B** [58, 59]:

$$H = \frac{P^2}{2m_0} + V_0(\mathbf{r}) + \frac{1}{2m_0^2c^2}(\mathbf{S}\times\nabla V_0)\cdot\mathbf{P} + \frac{g_0\mu_\mathrm{B}}{\hbar}\mathbf{B}\cdot\mathbf{S}, \tag{2.19}$$

where $\mathbf{P} = \mathbf{p} + \frac{e}{c}\mathbf{A}$ is the kinetic momentum and $\mathbf{A}$ is the vector potential of $\mathbf{B}$.

We now look for solutions to the Schrödinger equation $H\psi = \varepsilon\psi$ in the form,

$$\psi(\mathbf{r}) = \sum_m \Psi_m(\mathbf{r}) u_{m,0}(\mathbf{r}), \tag{2.20}$$

where the summation runs over the energy bands. The non-zero magnetic field makes the eigenvalue problem non-periodic resulting in the envelope functions $\Psi_m(\mathbf{r})$, which along with $\mathbf{A}$, we assume to be slowly varying and essentially constant over the unit cell. Recall from section 2.3.1 that $u_{m,0}(\mathbf{r})$ are the periodic parts of the Bloch function at $\mathbf{k} = 0$ satisfying the eigenvalue equation:

$$\left(\frac{p^2}{2m_0} + V_0(\mathbf{r}) + \frac{1}{2m_0^2c^2}\left(\mathbf{S} \times \nabla V_0\right) \cdot \mathbf{p}\right) u_{m0}(\mathbf{r}) = \varepsilon_m u_{m0}(\mathbf{r}), \tag{2.21}$$

where ε_m denotes the band-edge energies at the Γ point. Combining equations 2.19, 2.20, and 2.21 with the Schrödinger equation and integrating over the unit cell we obtain:

$$\sum_m \left[\left(\frac{P^2}{2m_0} + \varepsilon_m - \varepsilon\right)\delta_{m'm} + \frac{1}{m_0}\kappa_{m'm} \cdot \mathbf{P} + \frac{g_0\mu_{\mathrm{B}}}{\hbar}\mathbf{B} \cdot \mathbf{S}_{m'm}\right]\Psi_m(\mathbf{r}) = 0, \tag{2.22}$$

where,

$$\vec{\kappa}_{m'm} = (1/\Omega)\left\langle u_{m'0}\right| \mathbf{p} + \frac{1}{2m_0^2c^2}\left(\mathbf{S} \times \nabla V_0\right)\left|u_{m0}\right\rangle, \tag{2.23}$$

and,

$$\mathbf{S}_{m'm} = (1/\Omega)\left\langle u_{m'0}\right| \mathbf{S} \left|u_{m0}\right\rangle. \tag{2.24}$$

In this calculation we have taken the slowly varying functions $\Psi_m(\mathbf{r})$ and $\mathbf{A}$ out of the integration. The first term in equation 2.22 contains the kinetic energy of a free electron in a constant magnetic field. The last term is the bare Zeeman splitting due to the free electron g-factor g_0 and the term proportional to $\vec{\kappa}_{m'm}$ gives rise to the change of the g-factor.

Since in this dissertation we are principally concerned with spin dynamics in the conduction band of III-V compounds, we focus on matrix elements involving the conduction band states, i.e. $m' = 1,2$. Since spin is a good quantum

Table 2.3: Interband matrix elements $\vec{\kappa}_{m'm} \cdot \mathbf{P}$ for the conduction band.

	u_3	u_4	u_5	u_6	u_7	u_8
u_1	κP_+	0	$-\sqrt{\frac{1}{3}}\kappa P_-$	$-\sqrt{\frac{2}{3}}\kappa P_z$	$-\sqrt{\frac{2}{3}}\kappa P_-$	$\sqrt{\frac{1}{3}}\kappa P_z$
u_2	0	κP_-	$-\sqrt{\frac{2}{3}}\kappa P_z$	$\sqrt{\frac{1}{3}}\kappa P_+$	$\sqrt{\frac{1}{3}}\kappa P_z$	$\sqrt{\frac{2}{3}}\kappa P_+$

number for these states, we are left only with diagonal elements of the Zeeman term, $\mathbf{S}_{1,m} = \frac{\hbar}{2}\delta_{1,m}$ and $\mathbf{S}_{2,m} = \frac{\hbar}{2}\delta_{2,m}$. $\vec{\kappa}_{m',m}$ is somewhat more complicated; in order to simplify, we ignore the small spin-orbit contribution in this interband matrix element and set $\vec{\kappa}_{m',m} = (1/\Omega)\left\langle u_{m',0}\right| \mathbf{p} \left|u_{m,0}\right\rangle$ [60]. Though it looks as if we have wiped away the spin-orbit interaction from consideration, its effect on the system persists in the form of the zero-order functions $u_{m,0}$ of table 2.1, which include the spin-orbit effect (specifically in the energy shift of the SO band, Δ). Using these functions and the identity,

$$\vec{\kappa} \cdot \mathbf{P} = \kappa_+ P_- + \kappa_- P_+ + \kappa_z P_z, \tag{2.25}$$

where $\kappa_\pm = (1/\sqrt{2})(\kappa_x \pm i\kappa_y)$ and $P_\pm = (1/\sqrt{2})(P_x \pm iP_y)$ we solve for $\vec{\kappa}_{m'm} \cdot \mathbf{P}$. We define $\kappa = -(i/\Omega)\langle S|\, p_x \,|X\rangle = -(i/\Omega)\langle S|\, p_y \,|Y\rangle = -(i/\Omega)\langle S|\, p_z \,|Z\rangle$, and list only the interband matrix elements in table 2.3 since the diagonal terms vanish.

Armed with these matrix elements, we now turn our attention to the envelope functions. Taking $\mathbf{B} = B\hat{z}$ and $\mathbf{A} = -By\hat{x}$ (the Landau gauge), the eigenfunctions of the first diagonal term in equation 2.22 are $e^{(ik_x x + ik_z z)}\chi_n(y)$, where $\chi_n(y)$ is the harmonic oscillator function for the n^{th} level. Since we are interested in solutions near the Γ point, we set $k_x = k_z = 0$, making the envelope functions equal to linear combinations of the harmonic oscillator functions: $\Psi_m(\mathbf{r}) = \sum\limits_n c_n \chi_n(y)$. Since $k_z = 0$, P_z vanishes, so we only need to consider matrix elements containing P_+ and P_-. Using the definitions of the oscillator raising and lowering operators we find,

$$P_+\chi_n(y) = -\sqrt{\hbar eB}a_y^\dagger\chi_n(y) = -\sqrt{\hbar eB(n+1)}\chi_{n+1}(y) \tag{2.26}$$

$$P_-\chi_n(y) = -\sqrt{\hbar eB}a_y\chi_n(y) = -\sqrt{\hbar eBn}\chi_{n-1}(y). \tag{2.27}$$

Therefore the $\vec{\kappa}_{m',m}\cdot\mathbf{P}$ term only couples conduction band states to valence band states in neighboring Landau levels. Finally we can solve for the energy of the $\Psi_m(\mathbf{r})$ states by treating $\vec{\kappa}_{m'm}\cdot\mathbf{P}$ as a perturbation in equation 2.19. Again, since we are limiting ourselves to the conduction band ($m = 1,2$), the Zeeman term containing the free electron g-factor is diagonal and is included in the unperturbed energy. Since the diagonal matrix elements of $\vec{\kappa}_{m'm}\cdot\mathbf{P}$ vanish, there is no first order correction to the energy and we go straight to second order perturbation theory. The spin-up conduction band state in the n^{th} Landau level, $\Psi_{1,n}(\mathbf{r})$, couples to the valence band states $\Psi_{3,n-1}(\mathbf{r})$, $\Psi_{5,n+1}(\mathbf{r})$, $\Psi_{7,n+1}(\mathbf{r})$, resulting in the following second order energy correction:

$$\begin{aligned}\sum_m \frac{|H_{1,m}|^2}{E_c - E_m} &= \frac{e\hbar\kappa^2}{m_0^2}B\left[\frac{2}{3}(n+1)\frac{1}{E_\text{g}+\Delta} + n\frac{1}{E_\text{g}} + \frac{1}{3}(n+1)\frac{1}{E_\text{g}}\right] \\ &= \frac{e\hbar\kappa^2}{m_0^2}B\left(\frac{4n+1}{3}\frac{1}{E_\text{g}} + \frac{2n+2}{3}\frac{1}{E_\text{g}+\Delta}\right).\end{aligned} \tag{2.28}$$

The spin-down conduction band state, $\Psi_{2,n}(\mathbf{r})$, couples to the valence band states $\Psi_{4,n+1}(\mathbf{r})$, $\Psi_{6,n-1}(\mathbf{r})$, $\Psi_{8,n-1}(\mathbf{r})$, resulting in a different correction:

$$\begin{aligned}\sum_m \frac{|H_{2,m}|^2}{E_c - E_m} &= \frac{e\hbar\kappa^2}{m_0^2}B\left[\frac{2}{3}n\frac{1}{E_\text{g}+\Delta} + \frac{1}{3}n\frac{1}{E_\text{g}} + (n+1)\frac{1}{E_\text{g}}\right] \\ &= \frac{e\hbar\kappa^2}{m_0^2}B\left(\frac{4n+3}{3}\frac{1}{E_\text{g}} + \frac{2n}{3}\frac{1}{E_\text{g}+\Delta}\right).\end{aligned} \tag{2.29}$$

The additional spin splitting from this perturbation is the difference in energies between the spin-up and -down bands:

$$\begin{aligned}\sum_m \frac{|H_{1,m}|^2}{E_c - E_m} - \sum_m \frac{|H_{2,m}|^2}{E_c - E_m} &= \frac{e\hbar\kappa^2}{m_0^2} B \left(-\frac{2}{3}\frac{1}{E_\mathrm{g}} + \frac{2}{3}\frac{1}{E_\mathrm{g} + \Delta} \right) \\ &= -\frac{2}{3}\left(\frac{2\kappa^2}{m_0}\right)\left(\frac{1}{E_\mathrm{g}} - \frac{1}{E_\mathrm{g}+\Delta}\right)\mu_\mathrm{B} B. \qquad (2.30)\end{aligned}$$

Since this energy shift is proportional to B and otherwise contains only constant material-specific parameters, it can be written as a correction to the g-factor. Therefore, we write an effective g-factor for the conduction band,

$$g_e = g_0 - \frac{2}{3}\left(\frac{2\kappa^2}{m_0}\right)\left(\frac{1}{E_\mathrm{g}} - \frac{1}{E_\mathrm{g}+\Delta}\right) = g_0 - \frac{2}{3}\left(\frac{2\kappa^2}{m_0}\right)\frac{\Delta}{E_\mathrm{g}\left(E_\mathrm{g}+\Delta\right)}. \qquad (2.31)$$

From this analysis it is clear that both spin-up and spin-down conduction bands are pushed up in energy due to the $\vec{\kappa}_{m'm} \cdot \mathbf{P}$ perturbation, however, an asymmetry in the coupling of spin states to the valence band leads to a spin dependent energy shift. The deviation of the effective g-factor from g_0 in equation 2.31 is proportional to the spin-orbit splitting Δ and is inversely proportional to the square of the band gap $E_g = E_c - E_v$ when $E_g \gg \Delta$. The term $2\kappa^2/m_0$ has the unit of energy and is often quoted in the literature as a standard parameter. For GaAs, $2\kappa^2/m_0 = 27.86$ eV, $E_\mathrm{g} = 1.519$ eV, and $\Delta = 0.341$ eV [58, 61].

This simple model begins to fail as E_g becomes comparable to the energy difference from the s-like conduction band considered here to higher conduction bands. These upper conduction bands couple to the s-like conduction band in the same manner as the valence bands, necessitating further corrections to the g-factor [56].

2.4 Quantum wells and the effects of confinement

2.4.1 Bands in a quantum well

Until this point, we have discussed the band structure for bulk zinc-blende materials. Much of this dissertation, however, deals with quasi two-dimensional electrons trapped in quantum wells (QWs). In particular we study QWs made from heterostructures of GaAs and AlGaAs or GaAs and InGaAs. In comparison to electrons in a bulk system, electrons confined in these quantum structures have significantly different electronic properties. The reduction in dimensionality breaks a number of symmetries present in bulk causing changes in the band structure. Confinement along one axis results in quantized energy levels and envelope functions characteristic of QWs along one direction, while the other directions are characterized by the continuous energy dispersion of the bulk. In the band structure, subbands emerge centered around each QW energy level with a quasi two-dimensional densities of states. Some of these features are illustrated in figure 2.5 depicting electrons in an idealized QW with parabolic bands.

The most obvious difference between bulk and QW properties in optical experiments is the enhanced band-gap energy of the QWs. This increase in the separation of the conduction and valence bands is due to the non-zero energy of the QW ground state which shifts the lowest electron and hole subbands further from each other in energy (see figure 2.5). Note that in the following discussion we assume that the QW heterojunctions are ideal and we treat them as simple steps in potential energy, ignoring the effects of strain and dislocations. Uniaxial strain in particular, can strongly affect the valence band structure [62].

In the most basic terms, confinement alters the valence band by breaking the symmetry of the crystal. The bulk HH states $\left|\frac{3}{2}, \pm\frac{3}{2}\right\rangle$ are linear combinations

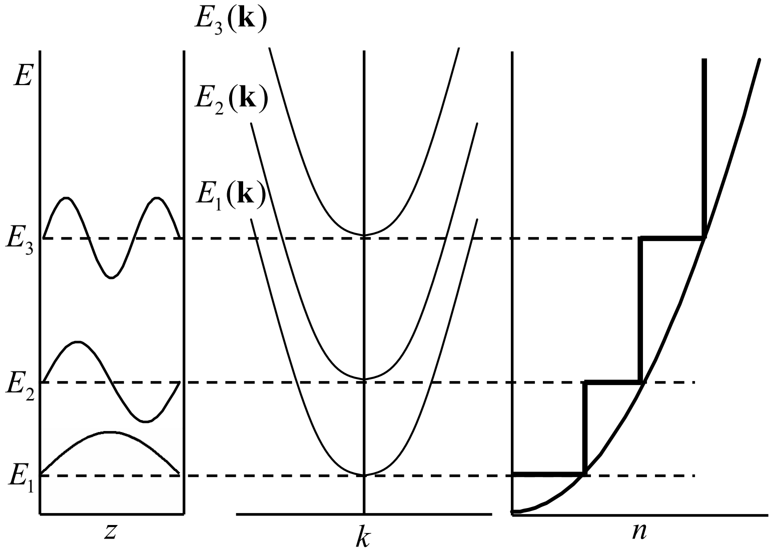

Figure 2.5: A schematic diagram illustrating the envelope functions, subbands, and density of states of a typical square QW. Note that the density of states n is step-like (bold line) and thus quasi-two-dimensional. It follows the countour of the three-dimensional density of states (normal line) [62].

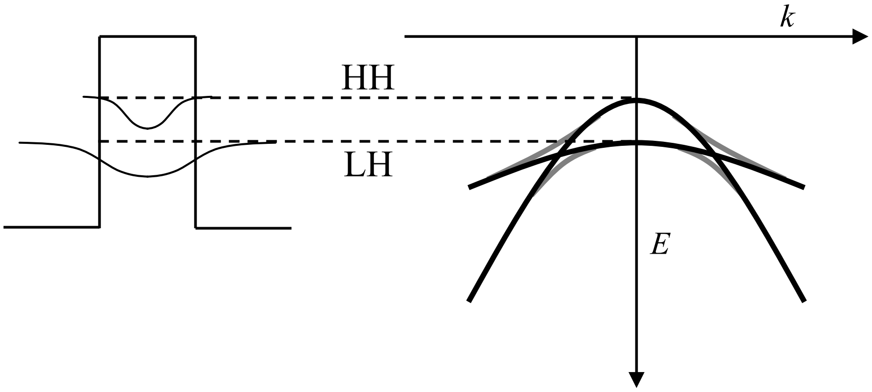

Figure 2.6: A simple energy diagram for heavy and light holes in a QW. The HH have the lower energy at $\mathbf{k} = 0$, but their energy rises more rapidly with $\mathbf{k}$ such that the HH and LH bands cross. Coupling between the bands leads to an anticrossing (shown in gray) and a mixing of the HH and LH bands [62].

of the $|X\rangle$ and $|Y\rangle$ orbitals. These p orbitals are highly anisotropic and overlap strongly along the $\hat{x}$ and $\hat{y}$ directions, respectively. Both are oriented perpendicular to $\hat{z}$, which we take as the confinement direction of our QW (in this case the axis of angular momentum quantization coincides with the confinement direction). As a result, for heavy holes, propagation at a particular velocity along $\hat{z}$ requires more energy than it does along $\hat{x}$ or $\hat{y}$, i.e. the effective mass is larger (heavier) for $\hat{z}$ than for the other directions. The opposite effect occurs for the LH states $\left|\frac{3}{2}, \pm\frac{1}{2}\right\rangle$ which are made up of $|X\rangle$, $|Y\rangle$, and $|Z\rangle$ orbitals, with larger relative amplitudes of $|Z\rangle$. Thus the effective mass of the light holes along $\hat{z}$ is smaller (lighter) than along other directions. The heavy and light effective masses of the HH and LH states, respectively, along $\hat{z}$ result in the HH bound state being more deeply bound that the LH state. In addition, in the xy-plane, in which the propagation in the QW must occur, HH subbands have a lighter effective mass than LH subbands, reversing the order relative to bulk. The results of this analysis are shown in figure 2.6; the degeneracy in the bulk of the HH and LH states at $\mathbf{k} = 0$ is lifted in QWs and the heavy and light character of the two bands is strongly mixed. This simplified treatment of the effects of confinement on the electronic band structure touches on some general trends, but is far from rigorous. The valence band in QWs is complicated and few analytical solutions exist; treatments based on the Kane or Luttinger models result in realistic band structures though such detailed calculations will not be reproduced here.

2.4.2 Interband transitions in a quantum well

In a QW, transition rates from valence band to conduction band states are modified relative to the bulk case both by the changes in the bands discussed in section 2.4.1 and by the relative parity of the QW envelope functions. If the splitting of HH and LH bands induced by confinement is large enough (e.g. this splitting is ~ 30 meV in an 8-nm GaAs/Al$_{0.4}$Ga$_{0.6}$As QW) compared to the energy width of the optical excitation, only the HH band needs to be considered in valence to conduction band transitions. According to figure 2.4, such a situation leads to large optically oriented spin polarizations in the conduction band.

Transition rates are also affected by the envelope functions of the QW. In a QW system, the electron states are no longer the same states shown in equation 2.14. Rather, these states are a product of the envelope function, which is quantized in one direction ($\hat{z}$ here), and the appropriate Bloch function. The envelope functions of a QW are separable and are a product of a plane wave in the xy plane and of a bound state along $\hat{z}$:

$$\Psi_{b,m_z\mathbf{k}_\perp}(\mathbf{r}) = N e^{i(\mathbf{k}_\perp\cdot\mathbf{r})}\phi_{b,m_z}(z), \tag{2.32}$$

where N is a normalization constant, $\mathbf{k}_\perp$ is the wave vector perpendicular to the confinement direction $\hat{z}$, b is an index referring to the band (e.g. CB, HH, LH, and SO), and $\phi_{b,m_z}(z)$ is the eigenstate of the m_z^{th} level in the QW. While Bloch functions $u_{n,0}(\mathbf{r})$ vary on the length scale of the unit cell, the envelope functions $\Psi_{b,m_z\mathbf{k}_\perp}(\mathbf{r})$ vary on much larger spatial scales and are nearly constant over one unit cell. For this reason, when calculating matrix elements for QWs analogous to those calculated for bulk in table 2.2, we can separate out the integral involving the envelope functions. As a result the QW valence to conduction band transition rates are proportional to the bulk rates multiplied by the square of the inner product of the valence and conduction band QW eigenstates:

$$|\langle\psi_{\mathrm{cb}}|e\mathbf{r}\cdot\mathbf{E}|\psi_{\mathrm{vb}}\rangle|^2 = |\langle u_{\mathrm{cb}}|e\mathbf{r}\cdot\mathbf{E}|u_{\mathrm{vb}}\rangle|^2 \left|\int \phi^*_{\mathrm{cb}\,n_z}(z)\phi_{\mathrm{vb}\,m_z}(z)dz\right|^2 . \tag{2.33}$$

While in the idealized case of an infinitely deep QW, $\int \phi^*_{\mathrm{cb}\,n_z}(z)\phi_{\mathrm{vb}\,m_z}(z)dz = \delta_{n_z,m_z}$, in real QWs this orthonormality does not survive. Transitions where $n_z =$

m_z, however, are still the strongest. In addition it is clear from equation 2.33, that transition rates between QW subbands will vanish unless both envelope functions have the same parity.

While there are several important differences in the electronic structure and optical selection rules of QWs compared to bulk systems, the general features remain intact. While the band structure is somewhat more complicated in QWs, spin polarized conduction electrons can still be excited by resonant circularly polarized illumination. The strong relation between luminescence polarization and spin polarization in the bands also persists. In this dissertation, QW structures are designed to have subband levels which are separated by energies much larger than the energy width of our excitation laser; in this way our experiments are usually confined to the dynamics of the lowest conduction subband only.

2.4.3 The g-factor in a quantum well

The confinement of conduction electrons in a QW also has an effect on their g-factor. The results of section 2.3.3, specifically equation 2.31, show that the effective g-factor of conduction band states depends on both the the band-gap energy E_g and on the spin-orbit splitting Δ. As discussed in section 2.4.1, the conduction and valence bands in a QW are pulled further apart in energy by the effects of confinement, enhancing E_g. At $\mathbf{k}_\perp = 0$, the n^{th} subband is shifted from the bulk band-edge by an energy E_n^b where b labels the band of interest (CB, HH, LH, or SO). E_n^b, sometimes referred to as the confinement energy, is simply the energy of the n^{th} level of a one-dimensional QW. It has been shown, to first approximation, that the conduction band g-factor in square QWs has the same value as for electrons in the conduction band of a bulk system at an energy above the band-edge equal to the confinement energy E_n^b [63]. In this approximation the hole confinement energy is ignored as it is typically much smaller than the electron confinement energy. Several experiments confirm that the enhanced band-gap due to quantum confinement is the dominant effect in determining the g-factor in GaAs/AlGaAs and GaAs/InGaAs QWs [44, 47, 64, 65, 66, 67]. The effect of penetration of the electron wave function into the barrier is found to be small as are the effects of other differences between the QW band structure and the bulk structure [63].

Therefore an approximate expression for the g-factor in the lowest subband of a quantum well is,

$$g_e = g_0 - \frac{2}{3}\left(\frac{2\kappa^2}{m_0}\right)\frac{\Delta}{\left(E_\mathrm{g}+E_0^\mathrm{cb}+E_0^\mathrm{vb}\right)\left[\left(E_\mathrm{g}+E_0^\mathrm{cb}+E_0^\mathrm{vb}\right)+\Delta\right]}, \tag{2.34}$$

where electron and hole confinement energies E_0^cb and E_0^vb depend on the parameters of the QW such as the width and the barrier height. E_g, the bulk value of the band-gap for the material used in the QW region, depends strongly on the type of material used (e.g. pure GaAs, $\mathrm{Al}_x\mathrm{Ga}_{1-x}\mathrm{As}$, or $\mathrm{In}_x\mathrm{Ga}_{1-x}\mathrm{As}$). It should be clear from equation 2.34 that quantum structures can be engineered with a wide variety of values for g_e. In GaAs/AlGaAs QWs, depending on the parameters, the g-factor can be made positive or negative roughly within the range $-0.4 < g_e < 0.2$.

Note also, that the symmetries broken by the confinement of carriers in a QW result in anisotropic conduction band g-factors. While in bulk g_e can be considered a scalar valid in any quantization direction, in QWs the g-factor is a tensor $\overleftrightarrow{g_e}$ which can have drastically different values along different crystalline directions [68].

Up until this point we have been discussing conventional square QWs, however, some specialized heterostructures have been developed, such as parabolic quantum wells (PQWs) and coupled quantum wells (CQWs), in which g_e can be controlled using applied electric fields [15, 47]. The g-factors in these structures have different, more complex dependences and such devices will be discussed in detail in chapters 4 and 6.

2.5 Electron spin interactions with local moments

2.5.1 Coupling to nuclear spins in the crystal lattice

Electron spins in a semiconductor are coupled to the nuclear spins in the crystal lattice. In this section we will lay the foundation for our understanding of this coupling, though these interactions will be covered in greater theoretical and experimental detail in chapters 3 and 4.

Recall our definition of the magnetic moment of an electron due to its intrinsic angular momentum in equation 2.3. An analogous equation can be written for the nucleus:

$$\mathbf{M}_I = \gamma_N \mathbf{I}, \tag{2.35}$$

where $\mathbf{I}$ is the spin of the nucleus and γ_N is its gyromagnetic ratio. The vector potential associated with this moment at a position $\mathbf{r}$ from the nucleus is (in CGS) [69],

$$\mathbf{A} = \frac{\mathbf{M}_I \times \mathbf{r}}{r^3} = \nabla \times \frac{\mathbf{M}_I}{r} = \nabla \times \frac{\gamma_N \mathbf{I}}{r}. \tag{2.36}$$

Recalling the Hamiltonian for a semiconductor in the presence of a magnetic field expressed in equation 2.19, we rewrite it for $\mathbf{B} = \nabla \times \mathbf{A}$ and ignore the spin-orbit coupling and the periodic potential $V_0(\mathbf{r})$, which is irrelevant in this discussion:

$$H = \frac{1}{2m_0}\left(\mathbf{p} + \frac{e}{c}\mathbf{A}\right)^2 + \frac{g_0 \mu_\mathrm{B}}{\hbar} \mathbf{S} \cdot \nabla \times \mathbf{A}. \tag{2.37}$$

Keeping terms up to first order in **A** we have,

$$\begin{aligned} H &= \frac{1}{2m_0}\left(p^2+\frac{e}{c}\mathbf{p}\cdot\mathbf{A}+\frac{e}{c}\mathbf{A}\cdot\mathbf{p}\right)+\frac{g_0\mu_\mathrm{B}}{\hbar}\mathbf{S}\cdot\nabla\times\mathbf{A} \\ &= \frac{p^2}{2m_0}+2\mu_\mathrm{B}\frac{\mathbf{L}\cdot\mathbf{M}_I}{r^3}+\frac{g_0\mu_\mathrm{B}}{\hbar}\mathbf{S}\cdot\left(\nabla\times\left(\nabla\times\frac{\mathbf{M}_I}{r}\right)\right), \end{aligned} \tag{2.38}$$

where $\mathbf{L}=\mathbf{r}\times\mathbf{p}$ is the orbital angular momentum of the electron. Since we are concerned with dynamics in the conduction band, whose states have angular momentum $l=0$, the magnetic moment of the nucleus affects the electronic system through the last, spin-dependent term in equation 2.38. This term contains the expression for the magnetic field due to an ideal magnetic dipole [70]:

$$\left(\nabla\times\left(\nabla\times\frac{\mathbf{M}_I}{r}\right)\right)=\frac{1}{r^3}\left[3(\mathbf{M}_I\cdot\hat{r})\hat{r}-\mathbf{M}_I\right]+\frac{8\pi}{3}\mathbf{M}_I\delta^3(\mathbf{r}). \tag{2.39}$$

The spin-dependent part of the Hamiltonian then becomes,

$$H_S=\frac{g\mu_\mathrm{B}\gamma_N}{\hbar}\left(\frac{1}{r^3}\left[3(\mathbf{I}\cdot\hat{r})(\mathbf{S}\cdot\hat{r})-(\mathbf{I}\cdot\mathbf{S})\right]+\frac{8\pi}{3}(\mathbf{I}\cdot\mathbf{S})\delta^3(\mathbf{r})\right). \tag{2.40}$$

This is the coupling Hamiltonian for two ideal magnetic moments, where the term in brackets describes simple magnetic dipole-dipole coupling and the last term is a contact hyperfine coupling. Calculating the mean value of this energy $\langle H_S\rangle$ over the unit cell using solutions in the form of equation 2.20, we find that for the *s*-like conduction band states, in which the spherically symmetric electron density is concentrated on the nuclear sites, the dipole-dipole term vanishes and the contact term dominates. On the other hand, for the *p*-like valence band states, whose electron density is concentrated away from the nuclear sites, the contact term vanishes leaving a dipole-dipole coupling which nevertheless remains considerably weaker than the conduction band contact term. Therefore, we ignore the valence band dipole-dipole coupling, considering only the large contribution of the contact term in the conduction band.

We can now write the coupling Hamiltonian between zinc-blende conduction band spins and lattice nuclear spins:

$$H_{\mathrm{hf}} = \frac{8\pi}{3}\frac{g\mu_{\mathrm{B}}}{\hbar}\gamma_N(\mathbf{I}\cdot\mathbf{S})\delta^3(\mathbf{r}-\mathbf{R}), \tag{2.41}$$

known as the contact hyperfine coupling where $\mathbf{R}$ is the position of the nucleus. Note that to transfer this equation into SI units, we simply replace the leading term $\frac{8\pi}{3}$ with $\frac{2\mu_0}{3}$ [50]. Integrating over the unit cell we find,

$$H_{\mathrm{hf}} = \frac{8\pi}{3}\frac{g\mu_{\mathrm{B}}}{\hbar}\gamma_N\eta\,|\Psi(\mathbf{R})|^2\,\mathbf{I}\cdot\mathbf{S}, \tag{2.42}$$

where $\Psi(\mathbf{R})$ is the envelope wave function and $\eta = (1/\Omega)\,|u_{\mathrm{cb}}(\mathbf{R})|^2$ is the Bloch amplitude at the site of the nucleus normalized by the volume of the unit cell. It is clear from equation 2.42 that the nuclear hyperfine coupling goes as the overlap of the electron density with the nuclear site. Averaging over the whole crystal of volume Ω or for an isotropic envelope function, as in a bulk system, equation 2.42 simplifies to,

$$H_{\mathrm{hf}} = \frac{1}{\Omega}\frac{8\pi}{3}\frac{g\mu_{\mathrm{B}}}{\hbar}\gamma_N\eta\,\mathbf{I}\cdot\mathbf{S}. \tag{2.43}$$

The contact hyperfine coupling leads to a variety of phenomena in zinc-blende semiconductors including the Overhauser and Knight shifts in electron and nuclear magnetic resonance experiments, respectively. Furthermore, in semiconductors H_{hf} leads to the dynamic polarization of lattice nuclei by optically oriented electrons and also contributes to electron spin relaxation is these materials. These topics will be discussed in detail in chapter 4.

Fundamentally, H_{hf} serves as a conduit between itinerant carriers (conduction electrons) and stationary moments (lattice nuclei). It is for this reason, and for the prospect of using the electronic and nuclear spins in semiconductors to store quantum information, that recent interest in this coupling has been so strong.

2.5.2 Coupling to localized impurity spins

In a semiconductor with impurities, the spin of partially filled electronic shells of impurity atoms can couple to the spin of mobile band electrons. This interaction between carriers and localized electrons can be represented by a Heisenberg-like Hamiltonian [71],

$$H_{\text{ex}} = -\frac{1}{\hbar^2}\sum_n J(\mathbf{r}-\mathbf{R}_n)\mathbf{S}\cdot\Xi_n, \tag{2.44}$$

where $\mathbf{S}$ is the spin operator of a band electron at position $\mathbf{r}$, Ξ_n is the total spin operator for the shell (usually $3d$ or $4f$) of the impurity atom at $\mathbf{R}_n$, $J(\mathbf{r}-\mathbf{R}_n)$ is the exchange coupling, and the sum is carried out over all impurities in the volume of interest. Note that equation 2.44 is not rooted in the magnetization of particles and their vector potentials as was our treatment of the the electronic-nuclear coupling in section 2.5.1. The critical difference is that this coupling involves interactions between electrons, which are identical particles. For them, the mutual Coulomb repulsion energy far outweighs any magnetic coupling between their spin-related magnetizations. Therefore the dominant spin-dependent energy arises not from the relative orientation of magnetizations but from Fermi-Dirac statistics [72]. Indeed, exchange interactions of the form of equation 2.44 are derived by considering only the Coulomb interaction between electrons in conjunction with their Fermi-Dirac statistics. Such couplings explain phenomena from the spin dependence of the atomic energy levels of helium to physical origin of ferromagnetism.

The early development of the model summarized in equation 2.5.2 was driven by the mysterious magnetic properties of rare-earth metals with the ideas of Zener [73, 74, 75] and Vonsoviskii and Turov [76]. Since the magnetic behavior could not be explained in terms of direct exchange between electronic wave functions on neighboring atoms, the indirect coupling of localized moments via conduction electrons was invoked [76, 77, 78, 79, 80]. A pair of important assumptions are made in the adoption of equation 2.44. First, we associate a constant number of electrons with the electronic shell of the impurity atom, i.e. the magnitude of the localized spin is taken to be constant. Second, we assume that the localized moments can be described in terms of spin eigenvalues rather than total angular momentum. We justify these simplifying assumptions since the resulting model is consistent with a wide variety of experimental data in II-VI and III-V semiconductors. Our interest in this coupling is focused on III-V compounds; in chapter 5 of this volume, we apply equation 2.44 to describe the spin dynamics of carriers and Mn impurities in $\mathrm{Ga}_{(1-x)}\mathrm{Mn}_x\mathrm{As}$ and $\mathrm{In}_y\mathrm{Ga}_{(1-x-y)}\mathrm{Mn}_x\mathrm{As}$ heterostructures.

We can further simplify H_{ex} by making a mean-field approximation. The wave functions of conduction and valence band electrons extend throughout the crystal; therefore we can assume that they interact with a large number of magnetic moments in the sample. As a result, the band electrons are subject to the average spin value of the localized moments. Thus it is permissible to average over all possible spin states of the magnetic moments at the level of the Hamiltonian. We now have,

$$H_{\mathrm{ex}} = -\frac{1}{\hbar^2}\mathbf{S}\cdot\langle\Xi_z\rangle\,\hat{z}\sum_n J(\mathbf{r}-\mathbf{R}_n), \tag{2.45}$$

where $\langle\Xi_z\rangle$ is the average spin state of a magnetic impurity, which for paramagnetic spins lies exclusively along the direction of the applied magnetic field $\hat{z}$ (in this dissertation we focus on paramagnetic Mn impurities). In addition, let us make a virtual crystal approximation in which we assume that the exchange interaction occurs with one average value at all sites in the crystal rather than only at specific impurity sites:

$$H_{\text{ex}} = -\frac{1}{\hbar^2} S_z \langle \Xi_z \rangle x \sum_{\mathbf{R}} J(\mathbf{r}-\mathbf{R}), \tag{2.46}$$

where x is the fraction of magnetic impurities per crystal site, and the sum runs over all crystal sites $\mathbf{R}$ in a given volume.

Since electron spin is a good quantum number in the conduction band, we proceed as we did in section 2.5.1 with the hyperfine coupling: we integrate over the unit cell using solutions in the form of equation 2.20. Therefore for the conduction band states u_1 and u_2,

$$\begin{aligned} H_{\text{ex}} &= -\frac{1}{\hbar^2} S_z \langle \Xi_z \rangle x \frac{1}{\Omega} \left\langle S \left| \sum_{\mathbf{R}} J(\mathbf{r}-\mathbf{R}) \right| S \right\rangle |\Psi(\mathbf{r})|^2 \\ &= -\frac{1}{\hbar^2} x N_0 \alpha |\Psi(\mathbf{r})|^2 \langle \Xi_z \rangle S_z, \end{aligned} \tag{2.47}$$

where Ω is the volume of the unit cell, N_0 is the number of crystal sites in the unit cell, and $\alpha = \frac{1}{\Omega} \left\langle S \left| \sum_{\mathbf{R}} J(\mathbf{r}-\mathbf{R}) \right| S \right\rangle$ or more simply, $\alpha = (1/\Omega) \langle S|J|S \rangle$. Averaging over the whole crystal or for an isotropic envelope function, as in a bulk system, equation 2.47 simplifies to,

$$H_{\text{ex}} = -\frac{1}{\hbar^2} x N_0 \alpha \langle \Xi_z \rangle S_z. \tag{2.48}$$

Now, remembering the Zeeman term, we write the spin-dependent Hamiltonian for the conduction band as,

$$H_S^{\text{cb}} = \frac{g_e \mu_{\text{B}}}{\hbar} B S_z - \frac{1}{\hbar^2} x N_0 \alpha \langle \Xi_z \rangle S_z. \tag{2.49}$$

The problem is not quite so simple for the valence band states because these states are not eigenstates of spin (see table 2.1). We first note that the only non-zero matrix elements between band states are [71]:

$$\alpha = (1/\Omega) \langle S|J|S \rangle, \tag{2.50}$$

$$\beta = (1/\Omega) \langle X|J|X \rangle = (1/\Omega) \langle Y|J|Y \rangle = (1/\Omega) \langle Z|J|Z \rangle. \tag{2.51}$$

Now consider H_{ex} in the basis of table 2.1, once again averaging over the whole crystal or for an isotropic envelope function,

$$H_{\text{ex}} = -\frac{1}{\hbar^2} x N_0 \langle \Xi_z \rangle (1/\Omega) \langle u_m | S_z J | u_n \rangle . \tag{2.52}$$

Calculating the individual matrix elements and writing the Hamiltonian in matrix form where the sequence of basis functions in our notation is u_1, u_2, u_3, u_4, u_5, u_6, u_7,u_8, we obtain:

$$H_{\text{ex}} = -\frac{1}{\hbar} x N_0 \langle \Xi_z \rangle \begin{pmatrix} \frac{1}{2}\alpha & 0 & 0 & 0 & 0 & 0 & 0 & 0 \\ 0 & -\frac{1}{2}\alpha & 0 & 0 & 0 & 0 & 0 & 0 \\ 0 & 0 & \frac{1}{2}\beta & 0 & 0 & 0 & 0 & 0 \\ 0 & 0 & 0 & -\frac{1}{2}\beta & 0 & 0 & 0 & 0 \\ 0 & 0 & 0 & 0 & -\frac{1}{6}\beta & 0 & \frac{\sqrt{2}}{3}\beta & 0 \\ 0 & 0 & 0 & 0 & 0 & \frac{1}{6}\beta & 0 & -\frac{\sqrt{2}}{3}\beta \\ 0 & 0 & 0 & 0 & \frac{\sqrt{2}}{3}\beta & 0 & \frac{1}{6}\beta & 0 \\ 0 & 0 & 0 & 0 & 0 & -\frac{\sqrt{2}}{3}\beta & 0 & -\frac{1}{6}\beta \end{pmatrix} .$$

Since the SO holes, u_7 and u_8, whose energy in GaAs is shifted from the other hole bands by $\Delta = 0.34$ eV, are largely irrelevant to resonant optical experiments, we consider only the HH and LH states. In this case the above matrix is diagonal and we can write the exchange Hamiltonian together with the Zeeman term in a similar form as for the conduction band (equation 2.49). Total angular momentum J_z and not spin is a good quantum number in the valence band, therefore we write the Hamiltonian as,

$$H_J^{\text{vb}} = \frac{g_{\text{h}} \mu_{\text{B}}}{3\hbar} B J_z - \frac{1}{3\hbar^2} x N_0 \beta \langle \Xi_z \rangle J_z, \tag{2.53}$$

where g_h is the hole g-factor.

Equations 2.49 and 2.53 illustrate the dependence of the conduction and valence band spin splittings on the the spin polarization of the magnetic impurities present in the crystal. In the case of Mn doping in GaAs, at low concentrations, the impurities are isolated from each other and act as spin-5/2 paramagnets. Their magnetization along the applied field, and thus their average spin value $\langle \Xi_z \rangle$ goes as,

$$M_z \propto \langle \Xi_z \rangle \propto B_{5/2}\left(\frac{5 g_{Mn} \mu_{\mathrm{B}} B}{2 k_B (T - \theta_P)} \right), \tag{2.54}$$

where $B_S(\eta) = \frac{2S+1}{2S} \coth\left(\frac{2S+1}{2S}\eta\right) - \frac{1}{2S}\coth\left(\frac{1}{2S}\eta\right)$ is the Brillouin function for spin S, g_{Mn} is the g-factor for Mn^{2+}, k_B is the Boltzmann constant, T is the temperature, and θ_P is the paramagnetic Curie temperature. Section 5.3.2 includes a derivation of equation 2.54. For a sufficiently large Mn concentration x and exchange couplings α and β, this magnetization will significantly alter the otherwise linear dependence of spin-splitting on magnetic field. In chapter 5, we explore the physics of equations 2.49 and 2.53 in greater detail.

2.6 Time-resolved Faraday and Kerr rotation

2.6.1 The Faraday effect

Optical techniques are particularly convenient for measuring electron spin dynamics in zinc-blende semiconductors. Due to the optical selection rules discussed in section 2.3.2, it is straightforward to inject spin-polarized carrier spins into the electronic bands; one simply irradiates the sample with circularly polarized photons at the band-gap energy. Probing these spin states and measuring their dynamics can be achieved using several methods. Photoluminescence (PL), both polarization-resolved and time-resolved, is a useful tool for detecting the spin state of recombining carriers. Due to the complicated structure of the valence band in many heterostructures, however, these measurements can be difficult to interpret unambiguously. The recombination process, by nature, reflects the dynamics of both the conduction and valence bands and since it involves carriers near the band extrema, it is disproportionately sensitive to shallow donors, acceptors, and impurities. Moreover, PL only provides information for the duration of the carrier lifetime, which can often be shorter than the electron spin lifetime. While we rely on PL for a number of measurements, in most experiments the method of time-resolved Faraday or Kerr rotation is used to probe spin dynamics.

In 1845, Michael Faraday discovered that the polarization axis of linearly polarized light passing through a piece of glass rotates by an angle proportional to the magnetic field applied along the propagation direction [81]. The Faraday effect is a result of a magnetic field-dependent circular birefringence, i.e. a difference in the index of refraction between right- and left-circularly polarized ($\mathscr{R}$ and $\mathscr{L}$) light dependent on magnetic field. The difference in index is a result of the magnetization induced in a material by the applied magnetic field. A difference in the index of $\mathscr{R}$ and $\mathscr{L}$ will cause a phase shift between $\mathscr{R}$ and $\mathscr{L}$ light passing through a material; since linearly polarized light is a superposition of $\mathscr{R}$ and $\mathscr{L}$, a phase shift between these components results in the rotation of its polarization axis by an angle known as the Faraday rotation (FR) angle. Therefore, in the case of magnetized materials, the the FR angle is proportional to the component of the magnetization along the direction of propagation. The Kerr effect and Kerr rotation (KR) refer to the analogous effect on light reflected off of rather than transmitted through a material. The underlying mechanism behind the KR and FR is the same and either method can be used depending on the experimental conditions.

A full treatment of the Faraday effect involves taking into account the consequences of applying a magnetic field on atomic and molecular orbitals in a material and is beyond the scope of this dissertation. We focus on using the

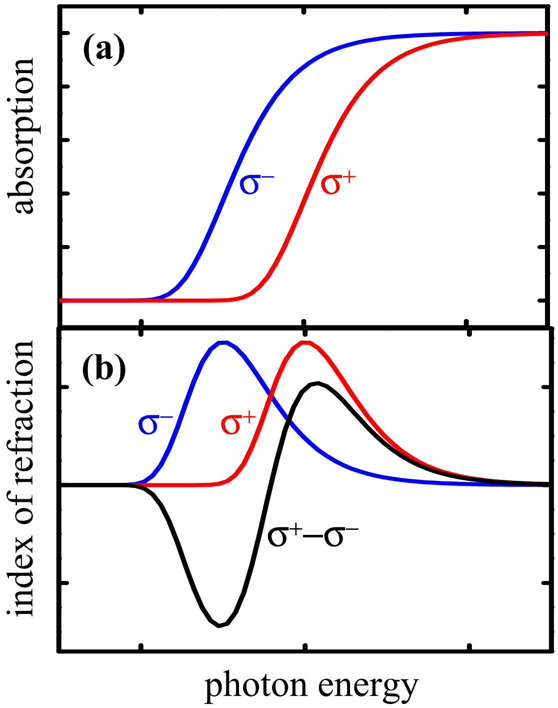

Figure 2.7: Absorption and index of refraction for σ^+ and σ^- in the presence of a spin splitting. The black line represents the index of refraction of linearly polarized light and shows the typical spectral dependence of the Faraday rotation angle.

FR angle as a sensitive probe of the magnetization due to electron spins in the conduction band of a semiconductor. The sensitivity of the FR angle to conduction band spin polarization is greatly enhanced near corresponding absorption resonances. Absorption due to transitions from the valence to the conduction band for σ^+ and σ^- polarized light has the qualitative shape shown in figure 2.7a. In a magnetic field, these two absorption resonances are split by the average Zeeman energy of the electrons and holes, which in turn is proportional to the ensemble polarization of electron and hole spins. While the optical orientation process described in section 2.3.2 creates both spin-polarized electrons and holes, in general we can ignore hole spins in the experiments discussed in this dissertation due to their short lifetime in these systems [82]. Therefore we consider the splitting to depend on the electron spin polarization only. We also ignore exciton spins, as their lifetime is limited by the hole spin lifetime [83].

Using the standard Kramers-Kronig relations, we use the absorption resonances to obtain the indices of refraction corresponding to σ^+ and σ^- light, shown qualitatively in figure 2.7b. The difference in the two indices is peaked around the absorption resonance, resulting in a spectral region of resonant FR, where the FR angle is proportional to the energy splitting between the two conduction spin absorption energies. The proportionality is linear as long as the characteristic spectral width of the absorption resonance is large compared with the spin splitting.

The splitting of the absorption spectra is a sum of the average Zeeman splitting of the electron spins, $\frac{g_e \mu_B}{\hbar} \mathbf{B} \cdot \langle \mathbf{S} \rangle$, and the energy splitting due to the relative population of the spin subbands (both effects are illustrated in figure 2.8). In the latter effect, the presence of carriers in a spin subband blocks absorption at low energies due to phase space filling, resulting in an enhanced absorption energy. Both of these effects, and thus the FR angle, are proportional to the ensemble electron spin polarization in the conduction band. While it is difficult to separate the two contributions to the FR angle, the non-linear dependence of FR on pump power suggests that the state filling effect dominates in measurements of carrier spin polarization [84].

2.6.2 Time-resolved measurements

Measurements of FR and KR provide such a sensitive probe of conduction band spin in semiconductors that a detection sensitivity of several spins has been recently reported [19]. Since the underlying process behind the technique is absorption rather than luminescence, it probes spin dynamics in the system long

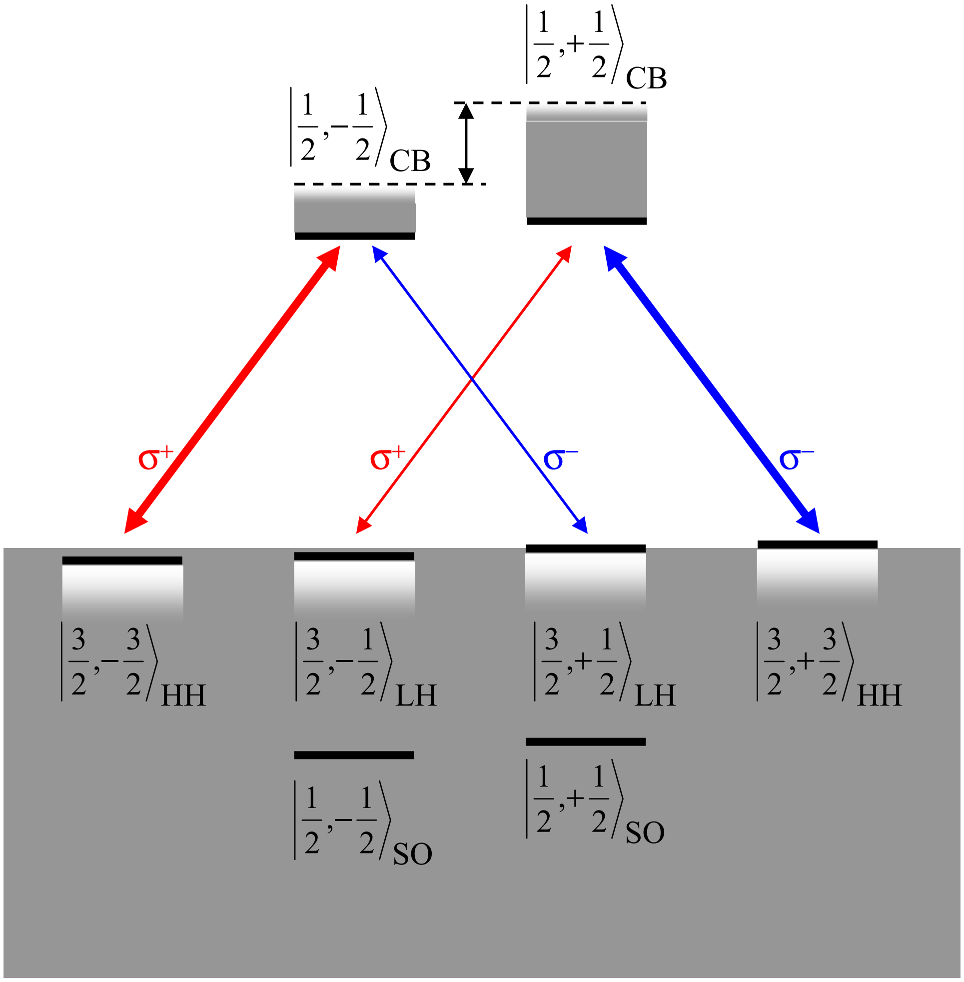

Figure 2.8: A schematic diagram showing the effects of the Zeeman splitting and state filling of electron spin subbands. The splitting in the absorption of σ^+ and σ^- shown in figure 2.7 is a result of both of these effects. Here, the state filling effect is shown to dominate. Since hole spin lifetimes are short in the systems discussed in this dissertation, we ignore their effects.

after carriers have recombined. It is the ability to probe the dynamics of electron spins in time, however, which makes the FR measurement especially powerful.

In a typical experiment, light from a pulsed laser tuned to the absorption energy of the relevant conduction band state is split into a beams of circularly polarized pump and linearly polarized probe pulses. The pump, which is focused onto the surface of the sample, injects spin polarized electrons into the conduction band as discussed in section 2.3.2. After a time Δt, which is set using a mechanical delay line, the probe beam, which is focused onto the same spot on the surface and is nearly collinear with the pump, transmits or reflects off of the sample. The probe beam's axis of polarization is then rotated by the FR or KR angle $\theta(\Delta t)$ which is proportional to the average electron spin polarization along its propagation direction. $\theta(\Delta t)$ is detected using a balanced photodiode bridge [85] and a series of lock-in amplifiers. If the laser propagation direction is perpendicular to the applied magnetic field (the Voigt geometry), the FR angle is well described by and exponentially decaying cosine:

$$\theta_{\perp}(\Delta t) = \theta_0 e^{-\frac{\Delta t}{T_2^*}} \cos(2\pi \nu_L \Delta t), \tag{2.55}$$

where θ_0 is the initial amplitude, T_2^* is the inhomogeneous transverse spin lifetime, and $\nu_L = g\mu_{\mathrm{B}}B/h$ is the Larmor frequency. When the laser propagation is parallel to the applied magnetic field (the Faraday geometry), it is well-described by an exponential decay:

$$\theta_{||}(\Delta t) = \theta_0 e^{-\frac{\Delta t}{T_1}}, \tag{2.56}$$

where T_1 is the longitudinal spin lifetime. At intermediate angles of incidence, we observe a combination of these signals. Equations 2.55 and 2.56 represent idealized cases; in real systems further complications must often be considered, including multiple decay time constants, multiple g-factors, anisotropic

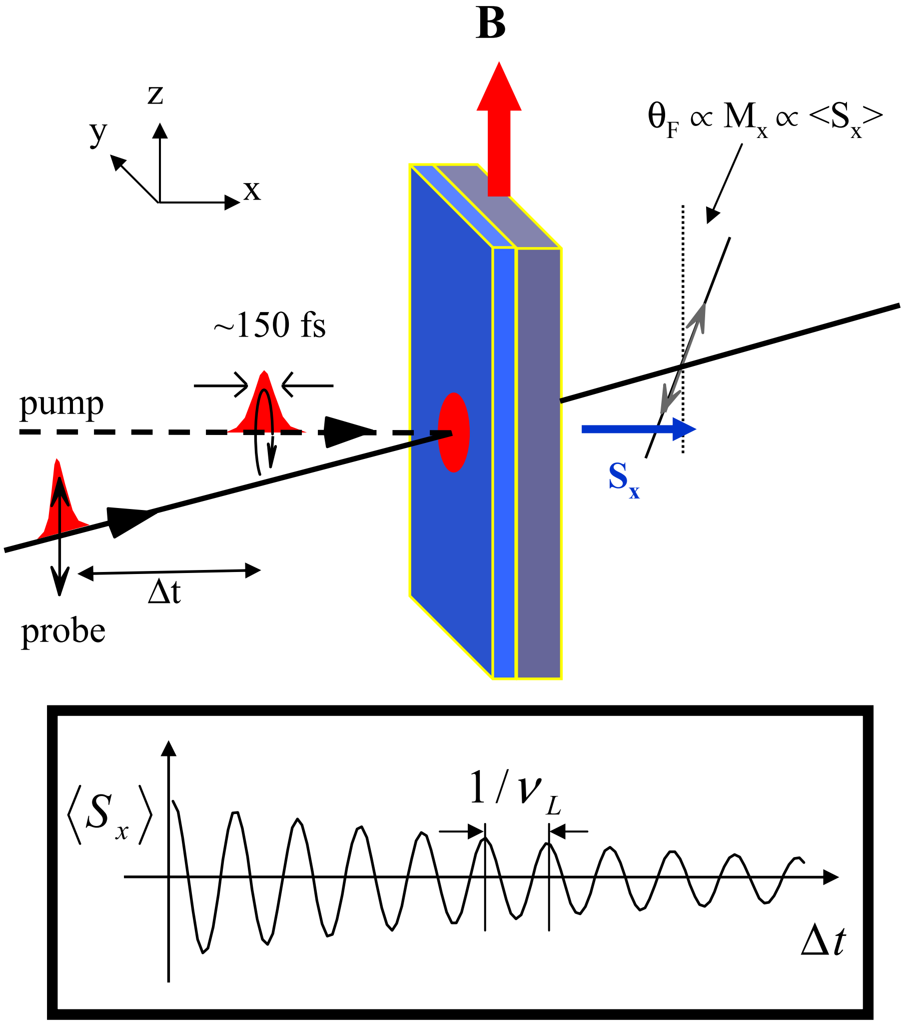

Figure 2.9: A schematic diagram showing a typical experimental setup of a time-resolved Faraday rotation measurement. The inset is a representation of typical data.

g-factors, and other considerations. A complete description of the experimental details involved in this measurement technique is provided in a previous dissertation [57].

Chapter 3

High-field optically detected nuclear magnetic resonance

3.1 Introduction

The contact hyperfine interaction, which was introduced in section 2.5.1, couples the spin of conduction band electrons in a semiconductor to nuclear spins in the crystalline lattice. Among the many consequences of this coupling are the dynamic spin polarization of the lattice nuclei by optically oriented electron spins and the Overhauser shift in the electron spin resonance frequency. Used together, these effects allow for the optical detection of nuclear magnetic resonance (NMR). The detection sensitivity of this technique is several orders of magnitude better than conventional NMR methods allowing for the measurement of nuclear spin phenomena in certain semiconductor nanostructures containing too few spins for conventional detection. The fundamental reason behind the enhancement in sensitivity is that under optical pumping conditions, conduction electron spins are strongly out of equilibrium; through the hyperfine coupling this strong imbalance leads to an anomalously large nuclear spin polarization.

In this chapter we will briefly introduce NMR and magnetic resonance in general in section 3.3. Section 3.4 focuses on the mechanism behind the dynamic optical orientation of nuclear spins. How polarized nuclear spins affect conduction electrons, particularly through the Overhauser effect, is also discussed in this section. The final two sections of the chapter, 3.5 and 3.6, describe optically detected NMR (ODNMR) experiments using detection schemes based on Faraday rotation (FR) and luminescence polarization, respectively. The former measurement technique represents an improvement in sensitivity of several orders of magnitude with respect to typical ODNMR.

3.2 Background

The small number of nuclear spins in quantum wells (QWs) and quantum dots makes conventional NMR experiments difficult in these semiconductor nanostructures. The enhancement in nuclear spin polarization achieved through optical pumping [23] can increase the detection sensitivity of typical radio frequency (RF) probes from a minimum of 10^{17} nuclear spins to 10^{12}. As a result, RF detection of optically pumped GaAs multiple QWs has been achieved [26]. Detection of NMR has also been demonstrated through optical measurements of recombination polarization, either by exciting NMR transitions with a conventional coil [27, 86], or by purely optical means [28, 29, 30, 31]. In the latter case, an optical field is modulated at the nuclear Larmor frequency resulting in an oscillating electron magnetization. This magnetization interacts with nuclear spins through the contact hyperfine coupling and induces NMR transitions in lieu of an external RF field. While ODNMR provides the high sensitivity typical of optical techniques, it has several limitations. For electron g-factors and spin lifetimes typical of GaAs structures, ODNMR is only possible at low magnetic fields (< 1 T). In addition, the reliance on radiative recombination for detection makes ODNMR disproportionately sensitive to nuclei located near shallow donors and impurities [87].

Another type of ODNMR is possible using time-resolved FR [85] to probe nuclear spin polarization. In this detection scheme, FR measures the spin precession frequency of electrons in the conduction band. Nuclear spins act on electron spins through the contact hyperfine interaction altering this frequency and allowing for the precise measurement of nuclear polarization. All-optical versions of this method have been demonstrated in bulk GaAs and in GaAs QWs [32, 68, 88]. These measurements can be made at high applied magnetic fields and, unlike measurements of time- and polarization-resolved photoluminescence, they are not limited by the charge recombination time.

Here we present an extension of this technique utilizing a radio frequency (RF) coil for the excitation of NMR transitions. The use of an external RF field allows for the future application of well-developed pulsed-NMR techniques for noise reduction while at the same time exploiting the high sensitivity of FR detection. In addition, the conventional magnetic excitation of nuclear transitions circumvents the complex interactions between electrons and nuclei which take place in schemes involving optical excitation. Unlike conventional RF magnetic fields, which induce only dipole transitions, modulated optical fields induce both magnetic dipole transitions and electric quadrupole transitions [31, 42, 68, 88]. Electric quadrupole transitions are discussed in further detail in section 4.5.3.

3.3 Magnetic resonance

Magnetic resonance is a powerful and well-established spectroscopic tool for both electrons and atomic nuclei. Its far-reaching impact on disciplines ranging from physics, to chemistry, to medicine is based on its fundamental ability to reveal detailed information about the magnetic environment immediately surrounding resonant spins. Magnetic resonance imaging in particular, which is based on proton spin resonance in water molecules, has given medical doctors and neuroscientists a non-invasive technique for looking inside the human body. NMR techniques also allow us to probe processes at the atomic level. Recent advances in the detection of fewer and fewer spins through magnetic resonance, including the recent detection of the electron spin resonance (ESR) of a single electron in SiO_2 [89], suggest the possibility of imaging techniques able to map the electronic structure of single molecules [90, 91].

Standard magnetic resonance experiments involve the application of a static longitudinal magnetic field $\mathbf{B} = B\hat{z}$ and an oscillating transverse magnetic $\mathbf{B}_1 = B_1 \sin(\omega_1 t)\hat{y}$ field perpendicular to it. Recalling equation 2.8 for the motion of a spin in a magnetic field, we can write,

$$\frac{d}{dt}\langle \mathbf{S} \rangle = \frac{g\mu_{\mathrm{B}}}{\hbar}(\mathbf{B} + \mathbf{B_1}) \times \langle \mathbf{S} \rangle \,. \tag{3.1}$$

Let us define a coordinate system which rotates about $\hat{z}$ at the angular frequency ω_1 of $\mathbf{B_1}$:

$$\hat{x}'' = \hat{x}\cos\omega_1 t + \hat{y}\sin\omega_1 t \tag{3.2}$$

$$\hat{y}'' = -\hat{x}\sin\omega_1 t + \hat{y}\cos\omega_1 t \tag{3.3}$$

$$\hat{z}'' = \hat{z}. \tag{3.4}$$

In this frame, the derivative of an arbitrary vector **v** can be expressed as,

$$\frac{d\mathbf{v}}{dt} = \left.\frac{\partial \mathbf{v}}{\partial t}\right|_{\text{rotating frame}} + \omega_1 \times \mathbf{v}. \tag{3.5}$$

In the rotating frame we can express $\mathbf{B_1}$, which can be decomposed into co- and counter-rotating magnetic fields, as,

$$\mathbf{B}_1 = \frac{B_1}{2}\hat{x}'' - \frac{B_1}{2}\left[\cos(2\omega_1 t)\hat{x}'' - \sin(2\omega_1 t)\hat{y}''\right]. \tag{3.6}$$

Under normal conditions, where $B \gg B_1$, the spin vector precesses about the $\hat{z}$ axis at an angular frequency $\omega = \frac{g\mu_\mathrm{B}}{\hbar}B$. It is therefore stationary in a rotating frame defined by $\omega\hat{z}$. The spin vector is only sensitive to the effects of transverse oscillating fields which are stationary in its frame or whose relative periods are longer than the transverse spin lifetime ($1/|\omega_1 - \omega| > T_2$); all other fields average to zero over time. Therefore we only need to consider the first co-rotating term of equation 3.6 in a spectral region defined by $|\omega_1 - \omega| < 1/T_2$, i.e. around the resonance condition $\omega_1 = \omega$. We take $\mathbf{B}_1 = \frac{B_1}{2}\hat{x}''$ and by combining equations 3.1 and 3.5 we write the equation of motion in the rotating frame as,

$$\left.\frac{\partial \langle \mathbf{S} \rangle}{\partial t}\right|_{\text{rotating frame}} = \left[(\omega - \omega_1)\hat{z}'' + \Omega_n \hat{x}''\right] \times \langle \mathbf{S} \rangle, \tag{3.7}$$

where $\Omega_n = \frac{g\mu_\mathrm{B}B_1}{2\hbar}$ is commonly known as the angular nutation frequency. In the rotating frame, $\langle \mathbf{S} \rangle$ will precess around the angular frequency vector $(\omega - \omega_1)\hat{z}'' + \Omega_n\hat{x}''$. On resonance, the precession is purely around $\hat{x}''$ at an angular frequency Ω_n. Given a spin vector initially aligned along the static field, $\langle \mathbf{S} \rangle = \frac{\hbar}{2}\hat{z}$, in a resonant transverse field it will precess and nutate according to,

$$\langle \mathbf{S}(t) \rangle = \frac{\hbar}{2}(-\sin(\Omega_n t)\hat{y}'' + \cos(\Omega_n t)\hat{z}''). \tag{3.8}$$

As is clear from equation 3.8, the nutation frequency Ω_n depends on the strength of $\mathbf{B}_1$. The final state of $\langle \mathbf{S} \rangle$ depends both on Ω_n and the amount of time $\mathbf{B}_1$ is applied. In typical NMR and ESR experiments, pulses of resonant $\mathbf{B}_1$ of fixed amplitude and varying duration are used to manipulate the spin state of the system. Though the protocols and pulse sequences used in modern NMR and ESR can often seem impenetrably complex, the technique is based on the simple principles outlined in this section.

The discussion in this section can naturally be extended to any driven two-state system in quantum mechanics, e.g. a laser driving two isolated states in an atom. In this case the Larmor frequency ω corresponds to the energy difference between the energy states and the nutation rate Ω_n corresponds to the Rabi oscillation between the states. In a driven atomic transition, the oscillating magnetic field $\mathbf{B}_1$ corresponds to a resonant laser field. Both cases are mathematically identical.

Note that in ESR, for the free electron ($g = g_0 = 2$) the resonant frequency $\nu = \omega/(2\pi) = \frac{g\mu_\mathrm{B}}{h}B \simeq 28$ GHz at $B = 1$ T. Nuclear gyromagnetic ratios, which depend on the isotope in question, are about 10^3 times smaller due to the much larger mass of the proton in comparison with the mass of the electron: $\mu_\mathrm{B} = \frac{e\hbar}{2m_e}$ and $\mu_N = \frac{e\hbar}{2m_p}$ where $m_e = 9.109 \times 10^{-31}$ kg and $m_p = 1.673 \times 10^{-27}$ kg. Therefore the resonance frequencies for the nuclei discussed in this dissertation tend to be around $\nu \simeq 10$ MHz at $B = 1$ T (see appendix E for a list of nuclear gyromagnetic ratios). Note also that since the nuclear spin number I can be larger than $1/2$, many of these nuclear spins are not two-state systems and do not exactly map to the simple Bloch-sphere model of this section. A more complex model must be used to predict the nuclear spin dynamics [92], though the simple picture discussed here is sufficient for our purposes.

3.4 Dynamic Nuclear Polarization

3.4.1 Polarization of nuclei by oriented electrons

Illumination with resonant circularly polarized light polarizes electronic spins in the conduction band of a zinc-blende semiconductor, as discussed in section 2.3.2, bringing them far out of equilibrium. Through the contact hyperfine interaction, this polarization imbalance is shared with nuclear spins in the crystal lattice, resulting in nuclear spin polarization. The contact hyperfine term, which is proportional to $\mathbf{I}\cdot\mathbf{S}$ is the conduit through which the polarized reservoir of electronic spins cools the nuclear spins. By expressing this coupling in terms of standard raising and lowering operators for spin we have,

$$\mathbf{I}\cdot\mathbf{S} = \frac{1}{2}(I^+S^- + I^-S^+) + I_zS_z. \tag{3.9}$$

In this form it is clear that the contact hyperfine interaction conserves the total spin of the electronic-nuclear system and that through mutual spin flips, or “flip-flop” interactions, angular momentum can be transferred from the electronic to the nuclear reservoirs and vice-versa. The nuclear polarization along the applied magnetic field arises as a result of the establishment of thermal equilibrium between these two reservoirs. In a magnetic field, the nuclear spin system is well-isolated from the lattice since the spin-lattice relaxation time $T_{\text{s-l}}$, which can be as long as seconds to days, is much longer than the dipolar spin-spin relaxation time between neighboring nuclei $T_{\text{s-s}}$, which is around 100 μs [25]. The nuclear spin bath can therefore be characterized by a spin temperature Θ_n.

As long as the external applied field is much larger than the local field due to dipole coupling between nuclei ($B \gg B_L$), the effect of these spin-spin interactions can be neglected and the interaction of each nuclear spin with the electrons can be considered separately. Note that $T_{\text{s-s}} = 1/(\gamma_N B_L)$ such that in these systems $B_L \simeq 1$ mT. As shown in equation 3.9, the total spin of the electron-nuclear system is conserved and therefore we can write a balance equation,

$$W_{m,m-1} N_m n_{\downarrow} = W_{m-1,m} N_{m-1} n_{\uparrow}, \tag{3.10}$$

where N_m represents the population of the level with nuclear spin $\hbar m$, $W_{m-1,m}$ and $W_{m,m-1}$ are the transition probabilities to and from this level, and $n_{\uparrow\downarrow} = 1/2 \pm \langle S \rangle$ are the relative populations of the spin-up and spin-down electrons. The transition rates are related by thermodynamics,

$$W_{m,m-1} = W_{m-1,m} e^{\frac{g\mu_{\mathrm{B}} B}{k_B T}}, \tag{3.11}$$

where in the energy difference $g\mu_{\mathrm{B}}B$ between states of the electron and nuclear spin, we have neglected the Zeeman energy of the nucleus ($g\mu_{\mathrm{B}} \gg \hbar\gamma_N$). The energy required for each transition is taken from the lattice, which is represented as a reservoir of temperature T. Combining equations 3.10 and 3.11, we find,

$$\frac{N_m}{N_{m-1}} = \frac{(1+2\langle S \rangle)}{(1-2\langle S \rangle)} \frac{(1-2S_T)}{(1-2S_T)}, \tag{3.12}$$

where $\langle S \rangle$ is the average electron spin and $S_T = -\frac{1}{2} \tanh\left(\frac{g\mu_{\mathrm{B}} B}{2k_B T}\right)$ is the equilibrium value of electron spin in the absence of optical pumping. Using this relation we can express the average nuclear spin $\langle I \rangle = \sum\limits_{m=-I}^{I} \hbar m N_m$ as a Brillouin function:

$$\langle I \rangle = \hbar I B_I \left(\ln \left(\frac{(1+2\langle S \rangle)}{(1-2\langle S \rangle)} \frac{(1-2S_T)}{(1-2S_T)} \right) \right). \tag{3.13}$$

Typically in the case of optical pumping $\langle S \rangle \gg S_T$, therefore we can neglect S_T and retain the first term in the expansion of the Brillouin function, so that,

$$\langle I \rangle = \frac{4}{3} \hbar I (I+1) \langle S \rangle. \tag{3.14}$$

Recalling that the quantization axis in this treatment was determined in equation 3.9 along the static magnetic field **B**, we generalize equation 3.14 into vector form,

$$\langle \mathbf{I} \rangle = \frac{4}{3}\hbar I(I+1)\frac{(\langle \mathbf{S} \rangle \cdot \mathbf{B})\,\mathbf{B}}{B^2}. \tag{3.15}$$

The gist of the preceding discussion is that dynamic nuclear polarization (DNP) [23] is caused by the component of electron spin along the applied field direction and that the subsequent nuclear polarization is proportional to the electron spin polarization achieved by optical orientation. Note also, that DNP is most efficient in semiconductors at liquid helium temperatures disappearing for $T > 20$ K [68].

3.4.2 The Overhauser shift

As discussed in section 3.4.1, the presence of optically oriented electrons in a semiconductor can act to polarize nuclear spins. The contact hyperfine term, however, plays a dual role. It also allows polarized nuclear spins to act on electron spins. This inherent feedback in the Hamiltonian leads to bistability and hysteresis in the electron-nuclear spin system at very low applied magnetic fields ($B \sim B_L$) as shown in figure 3.6. Though we will not discuss this low-field bistability here [25], this section will cover the effect of nuclear polarization on conduction band spin dynamics.

Recall the form of the contact hyperfine interaction given in equation 2.42. For the moment we absorb the multiplicative terms into a constant:

$$A_H = \frac{8\pi}{3}\frac{g\mu_\mathrm{B}}{\hbar}\gamma_N \eta \left|\Psi(\mathbf{R})\right|^2. \tag{3.16}$$

Writing the Hamiltonian of our system pertaining to the electron and nuclear spin we have,

$$H_\mathrm{spin} = \frac{g\mu_\mathrm{B}}{\hbar}\mathbf{B}\cdot\mathbf{S} + \gamma_N \mathbf{B}\cdot\mathbf{I} + A_H \mathbf{I}\cdot\mathbf{S} + H_Q, \tag{3.17}$$

where H_Q is nuclear electric quadrupolar interaction, which we ignore for the moment. From this equation we see that the Larmor precession and NMR resonance frequencies for the electron and nuclear spins, respectively, are modified by the contact hyperfine term:

$$\nu_L = \frac{g\mu_B B}{h} + \frac{A_H}{2\pi}\langle I\rangle = \frac{g\mu_B B}{h} + \nu_n, \tag{3.18}$$

$$\nu_{NMR} = \frac{\gamma_N B}{2\pi} + \frac{A_H}{2\pi}\langle S\rangle = \frac{\gamma_N B}{2\pi} + \nu_e, \tag{3.19}$$

where ν_n and ν_e are known as the Overhauser shift and the Knight shift, respectively. In the literature, this additional energy due to the hyperfine term, written in both cases here as a frequency shift, is often expressed in terms of an effective magnetic field: either as an effective nuclear field $\mathbf{B}_n = \frac{\hbar A_H}{g\mu_B}\langle \mathbf{I}\rangle$ or as an effective electronic field $\mathbf{B}_e = \frac{A_H}{\gamma_N}\langle \mathbf{S}\rangle$. In order to avoid confusion in materials with differing gyromagnetic ratios and with variable and anisotropic g-factors, we will refer to the Overhauser shift frequency $\nu_n = \frac{A_H}{2\pi}\langle I\rangle$ and the Knight shift frequency as $\nu_e = \frac{A_H}{2\pi}\langle S\rangle$.

The Knight shift is observed in conventional NMR as a shift in the resonant frequency of a nuclear isotope. The Overhauser shift is similarly seen as a shift of a resonance in ESR. In this dissertation, the Overhauser shift is detected in time-resolved FR measurements as a change in the electron precession frequency ν_L. Measurements of ν_n provide a sensitive probe of $\langle \mathbf{I}\rangle$. Taking into account the natural abundance of isotopes, for 100% polarized lattice nuclei in GaAs ($\langle I\rangle/I = 1$) we can make an estimate originally given by Paget [25, 86]:

$$\nu_n(^{75}\mathrm{As}) = 17.0\ \mathrm{GHz}, \tag{3.20}$$

$$\nu_n(^{71}\mathrm{Ga}) = 7.2\ \mathrm{GHz}, \tag{3.21}$$

$$\nu_n(^{69}\mathrm{Ga}) = 8.4\ \mathrm{GHz}. \tag{3.22}$$

We sum these values and obtain for a fully polarized lattice, $\nu_n = 32.6$ GHz.

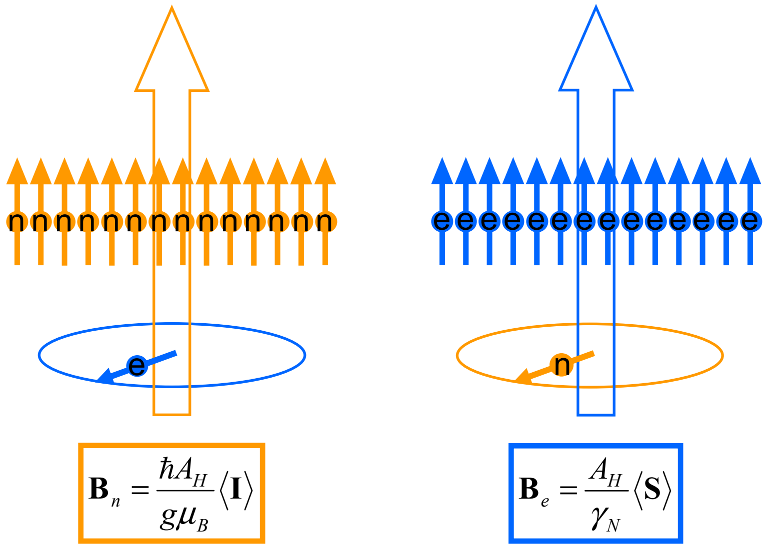

Figure 3.1: A representation of $\mathbf{B}_n$ and $\mathbf{B}_e$.

3.5 NMR detected by Faraday rotation

3.5.1 Experimental details

As shown in figure 3.2, a semiconductor sample is cooled to $T = 5$ K in a magneto-optical cryostat with an applied magnetic field $\mathbf{B}$ along $\hat{z}$ and is mounted in the center of a 10 mm $\times$ 5 mm Helmholtz coil wound from 22 AWG magnet wire. RF radiation is coupled to the coil from the top of the cryostat through an impedance-matched semi-rigid coaxial transmission line producing an RF magnetic field $\mathbf{B}_1$ along $\hat{y}$. The sample growth direction $\hat{x}'$ lies in the xz-plane and can be rotated to adjust the angle θ between the growth direction and the laser propagation direction along $\hat{x}$. Unless otherwise specified, $\theta = 10^\circ$.

Tilting the sample by a non-zero angle θ as shown in figure 3.2 redirects the electron spin polarization along the growth direction $\hat{x}'$, resulting in a component of electron spin along the magnetic field axis $\hat{z}$. This pinning of the

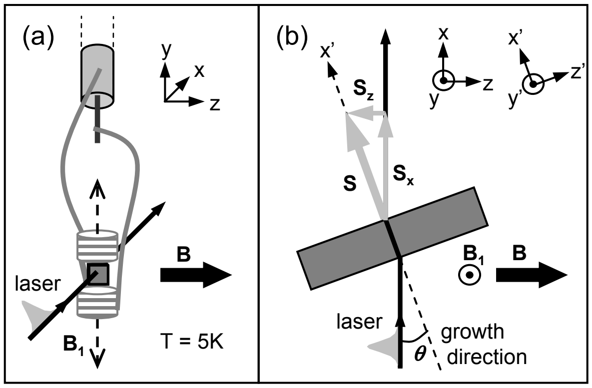

Figure 3.2: Schematic of the experimental geometry. (a) Side view of the apparatus within a magneto-optical cryostat. (b) Top view of the sample at the center of the Helmholtz coil. The xyz coordinate system is defined by the applied magnetic field while the $x'y'z'$ coordinate system is tied to the sample's crystal axes and is defined by the growth direction.

initial electron spin polarization along $\hat{x}'$ relies on the fact that pump pulses couple predominantly to HH states, which are split from the LH states in a QW [68, 93]. This component of electron spin polarization S_z injected along the magnetic field depends on θ. This dependence can be non-trivial if the g-factor is not isotropic and is characterized by a tensor $\overleftrightarrow{g}$, as is the case in QWs.

We measure time-resolved FR in a modulation doped 7.5-nm wide (110) GaAs/AlGaAs QW with a mobility of 1700 cm^2 V^{-1} s^{-1} and an electron density of 9×10^{10} cm^{-2} at $T = 300$ K. Confinement along the (110) crystal direction suppresses D'yakonov-Perel spin scattering resulting in spin lifetimes longer than 1 ns from $T = 5$ K to room temperature [38]. A 250-fs 76-MHz Ti:Sapphire laser tuned near the exciton absorption energy (1.572 eV) produces pulses which are split into pump and probe with a full width at half maximum (FWHM) of 8 meV and an average power of 2.0 mW and 100 μW, respectively. The linearly (circularly) polarized probe (pump) is modulated by an optical chopper at $f_1 = 940$ Hz ($f_2 = 3.12$ kHz). Both beams are focused on the sample surface to an overlapping spot 50 μm in diameter with the pump beam injecting polarized electron spins along the sample growth direction $\hat{x}'$ as shown in figure 3.2b. Small rotations in the linear polarization of the transmitted probe are measured and are proportional to the component of electron spin polarization in the conduction band along the growth direction. Variation of the pump-probe time delay Δt reveals the time evolution of this spin polarization. In the absence of nuclear polarization, electron spins precess about an axis and at a frequency defined by the Larmor precession vector $\vec{\nu}_L = \overleftrightarrow{g} \cdot \mathbf{B}\mu_B/h$, where $\overleftrightarrow{g}$ is the Landé g-factor expressed as a tensor, μ_B is the Bohr magneton, and h is Planck's constant. GaAs QWs grown in the (110) direction exhibit strong anisotropy in $\overleftrightarrow{g}$ resulting in both the dependence of ν_L on the orientation of $\mathbf{B}$ with respect to the sample's crystal axes and in a difference between the precession axis $\vec{\nu}_L$ and the direction of $\mathbf{B}$ [68].

At $T = 5$ K, spin-polarized photo-excited electrons generate nuclear spin polarization within the QW through DNP. This "flip-flop" process results in an average nuclear spin $\langle \mathbf{I} \rangle$ along $\mathbf{B}$ and is driven by the component of electron spin S_z in that direction. The sign and magnitude of $\langle \mathbf{I} \rangle$ depend on the angle θ.

The presence of a non-zero $\langle \mathbf{I} \rangle$ in turn acts on the electron spin dynamics through an Overhauser shift of the precession vector: $\vec{\nu}_L = \overleftrightarrow{g} \cdot \mathbf{B}\mu_B/h + \vec{\nu}_n$, where $\vec{\nu}_n = A_H \langle \mathbf{I} \rangle / h$. The measurement of ν_L and the knowledge of $\overleftrightarrow{g}$ and $\vec{B}$ yield the Overhauser frequency shift ν_n. Changes in the average nuclear polarization $\langle I \rangle / I$ within the QW can be measured directly as changes in the precession frequency $\Delta\nu_L$.

3.5.2 Isotopic resonances

FR is plotted in figure 3.3a as a function of Δt at $B = 5.3$ T with the coil driven continuously at a frequency ν_1 set to the ^{69}Ga resonance at 54.0000 MHz and at

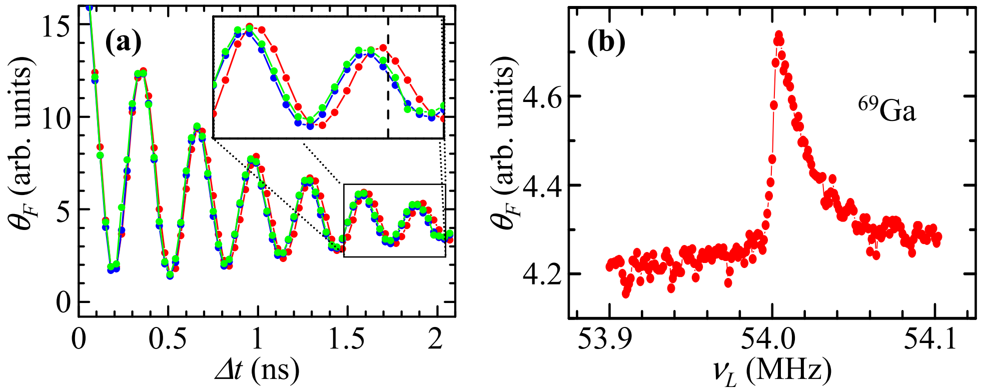

Figure 3.3: NMR detected by time-resolved FR in a (110) GaAs/AlGaAs QW. (a) FR data taken at $B = 5.3$ T with B_1 driven at 54.0000 MHz, 54.0400 MHz, and 53.9800 MHz for the red, blue, and green points, respectively. Lines connect the data to guide the eye. (b) FR shown as a function of ν_1 for fixed $\Delta t = 1932$ ps as indicated by the dashed line in the inset to (a).

two frequencies slightly detuned from resonance. The inset clarifies the reduction of ν_L for the resonant scan in which nuclear spin transitions induced by B_1 decrease $\langle I \rangle$. Scans with an off-resonant ν_1, show the same $\langle I \rangle$ established by DNP without any applied B_1. Figure 3.3b shows FR data taken under the same conditions as in figure 3.3a while sweeping ν_1 across the ^{69}Ga resonance at a fixed $\Delta t = 1932$ ps. Here, the resonant depolarization of $\langle I \rangle$ and the change in ν_L appear as a peak in the FR signal. The asymmetry of the resonance reflects the fast rate of the frequency sweep with respect to the time required to polarize the nuclei $T_{DNP} \sim 90$ s. In order to investigate the true form of the peak, ν_1 is swept across the full nuclear resonance in a time $T_{sweep} >> T_{DNP}$. This condition is satisfied for the data shown in figure 3.4a where the resonances due to the three isotopes present in the QW, ^{69}Ga, ^{71}Ga, and ^{75}As, appear at the expected frequencies.

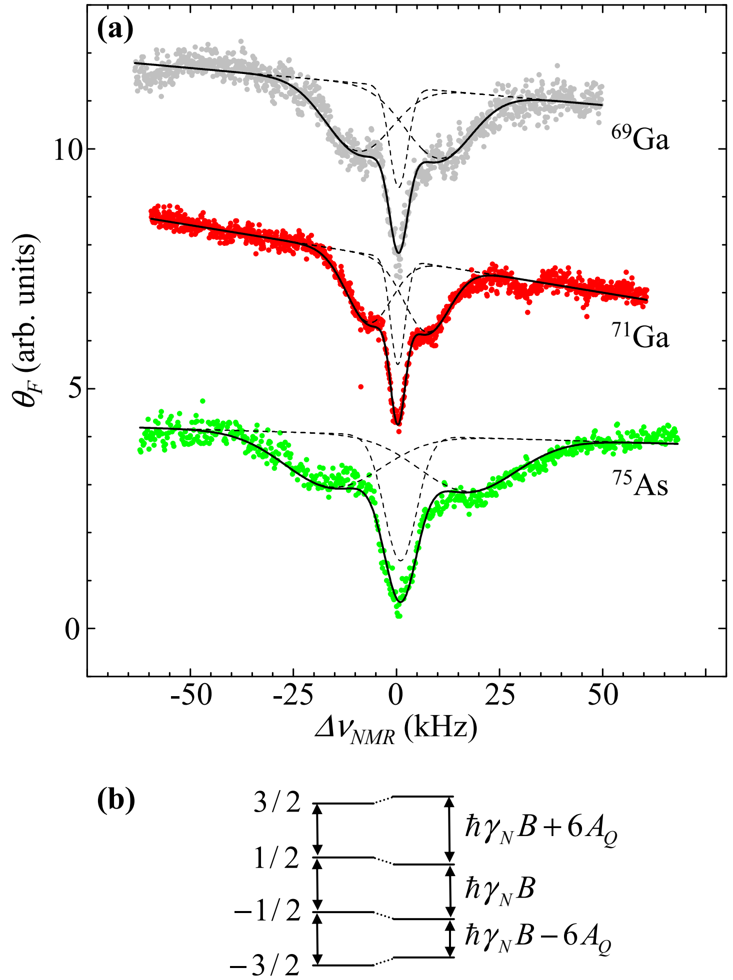

Figure 3.4: NMR detected by time-resolved FR in a (110) GaAs/AlGaAs QW. (a) FR plotted as a function of detuning $\Delta\nu_{NMR}$ from the ^{69}Ga resonance of 52.9539 MHz at $B = 5.2$ T, from the ^{71}Ga resonance of 67.2898 MHz at $B = 5.2$ T, and from the ^{75}As resonance of 54.4992 MHz at $B = 7.5$ T for the gray, red, and green points, respectively. Solid black lines are fits to the data while dashed lines show the three peaks included in those fits. A schematic diagram of the relevant level structure is included in (b).

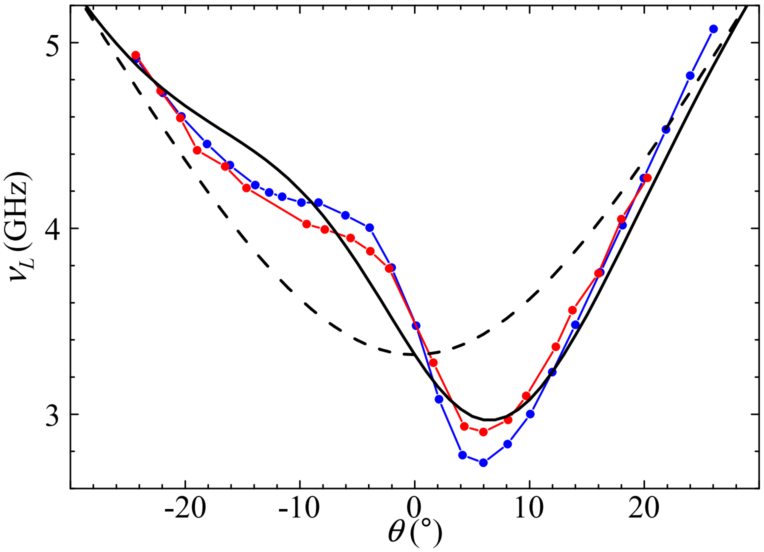

Figure 3.5: ν_L shown as a function of θ at $B = 5.5$ T for no RF voltage applied to the coil and for -15 dBm applied at the ^{69}Ga resonance at 56.0070 MHz for the blue and red points, respectively. The solid black line is a fit to the angular dependence of ν_L in the presence of a non-zero $\langle I \rangle$. The dashed black line shows the same dependence with $\langle I \rangle = 0$.

In addition, we observe satellite peaks for each resonance due to the nuclear electric quadrupolar splitting $6A_Q$. Since this splitting is typically small in these systems compared to the nuclear Zeeman energy (for $B > 1$ mT), we treat it as a perturbation. For a moment let us skip ahead to follow the derivation of the quadrupolar coupling in section 4.5.3. Solving for the first order energy correction in perturbation theory using the the expression for the quadrupolar term in equation 4.25, we have:

$$E^{(1)} = \langle I,m|H_Q|I,m\rangle = A_Q(3m^2 - I(I+1)), \tag{3.23}$$

since only the diagonal terms survive. Here $|I,m\rangle$ are the eigenstates of nuclear spin I and $I_z = \hbar m$ and we have absorbed all constants into the energy A_Q.

Since ^{69}Ga, ^{71}Ga, and ^{75}As all have $I = 3/2$, the $m = \pm 3/2$ states are shifted by $E^{(1)} = 3A_Q$ and the $m = \pm 1/2$ states are shifted by $E^{(1)} = -3A_Q$. As a result the levels are shifted as shown by the level diagram in figure 3.4b, giving rise to satellite peaks split by $6A_Q$.

By fitting each resonance to a Gaussian peak and two symmetric satellites, the splittings $6A_Q/h$ are measured to be 9.7 kHz, 7.0 kHz, and 16.3 kHz for the ^{69}Ga, ^{71}Ga, and ^{75}As isotopes. These values are similar to previously reported measurements and indicate the presence of a small amount of strain on the crystal likely due the wax used in mounting the sample [94]. The line-width (FWHM) of the main resonance is 2.6 kHz, 2.1 kHz, and 4.6 kHz for the ^{69}Ga, ^{71}Ga, and ^{75}As isotopes, respectively. The line-widths of the satellite peaks are broader at 9.4 kHz, 6.5 kHz, and 13.8 kHz probably because of inhomogeneous strain in the sample. As noted elsewhere [94], methods such as ours for accurately measuring A_Q are useful in the determination of built-in strain in semiconductor heterostructures.

The dependence of ν_L on θ is shown in figure 3.5 in the case of no RF voltage applied to the transmission line and in the case of -15 dBm applied at the ^{69}Ga resonance $\nu_1 = 56.0070$ MHz for $B = 5.5$ T. The solid black line is an angle dependence calculated according the simple model described by Salis et al. [68]. We take into account an anisotropic $\overleftrightarrow{g}$ and a 9% nuclear spin polarization. The calculation reproduces the qualitative features of the data and confirms the dependence of DNP on θ. This analysis also leads to the conclusion that the curve taken with the coil resonantly depolarizing the ^{69}Ga nuclei has a nuclear polarization of $6 - 7\%$. Since the natural abundance of ^{69}Ga in GaAs is 0.3, we can say that the RF coil is close to achieving full depolarization of the resonant isotope within the QW.

3.5.3 Sensitivity to 10^8 nuclear spins

The sensitivity of the FR-based ODNMR represents one of its main advantages over conventional luminescence-based methods. In the measurement described in section 3.5.2, analysis of the signal-to-noise ratio and the nuclear polarizations detected, reveals our ability to distinguish changes in polarizations as small as, $\langle I \rangle / I \sim 0.015\%$, corresponding to a sensitivity of 10^8 nuclear spins. In total, the measurement probes the polarization of the $\sim 10^{12}$ nuclear spins in the QW.

Let us examine the dependence of the measurement's sensitivity on the experimental parameters. The sensitivity of the FR angle to the nuclear polarization is given by,

$$\begin{aligned} \frac{d\theta_F}{d\langle I \rangle} &\propto \frac{d}{d\langle I \rangle}\left[e^{-\Delta t/T_2^*}\cos\left(A_H\langle I \rangle \Delta t + \frac{g\mu_{\mathrm{B}}B}{\hbar}\Delta t\right)\right] \\ &\propto A_H \Delta t e^{-\Delta t/T_2^*}\sin\left(A_H\langle I \rangle \Delta t + \frac{g\mu_{\mathrm{B}}B}{\hbar}\Delta t\right). \end{aligned} \tag{3.24}$$

Since the time-scale in the experiment is set by the inhomogeneous transverse spin lifetime T_2^*, we set $\Delta t \simeq T_2^*$. We further assume that the relevant frequencies are large enough compared $1/T_2^*$ that we can ignore the effects of the rapidly varying sinusoidal term. As a result,

$$\frac{d\theta_F}{d\langle I \rangle} \propto A_H T_2^*. \tag{3.25}$$

Therefore, the sensitivity of the FR-based ODNMR increases proportional to the electron spin lifetime in a given sample and with the strength of its hyperfine interaction. Moreover, the sensitivity is independent of both magnetic field and g-factor, making this technique well-suited for applications at high magnetic field and high g-factor. As discussed in section 3.6.4, conventional ODNMR is not sensitive in these regimes.

3.6 NMR detected by luminescence polarization

3.6.1 The Hanle effect

The Hanle effect describes the depolarization of luminescence by a transverse magnetic field. It was first observed in the resonance fluorescence of gases by Hanle in 1924 [95], and was subsequently applied in experiments on optical orientation in semiconductors by Parsons in 1969 [96]. Here, and in conventional ODNMR, the effect is used to monitor the lattice nuclear polarization through its effects on conduction band spins.

In optical orientation experiments, photoexcited electron spins will precess around an applied magnetic field $\mathbf{B} = B\hat{z}$ according to the form of equation 2.12. Suppose carriers are excited along $\hat{x}'$ using circularly polarized light and their recombinant luminescence is collected along the same axis. Since the circular polarization of the luminescence is proportional to the average electron spin along the axis of collection, $\mathscr{P}_{x'} \propto \langle S_{x'} \rangle$ [25], we focus on the dynamics of the spin component along $\hat{x}'$,

$$\langle S_{x'}(t) \rangle = \langle S_{x'}(0) \rangle \left(\sin^2 \theta e^{-t/T_2^*} \cos(2\pi \nu_L t) + \cos^2 \theta e^{-t/T_1} \right), \tag{3.26}$$

where, in this case, θ is the angle between $\hat{z}$ and $\hat{x}'$. To obtain a steady state polarization, we average over the distribution of lifetimes $(1/T_{\text{e-h}})e^{-t/T_{\text{e-h}}}$, where $T_{\text{e-h}}$ is the electron-hole recombination time, and find,

$$\begin{aligned} \mathscr{P}_{x'} \propto & \int_0^\infty \langle S_{x'}(t) \rangle (1/T_{\text{e-h}}) e^{-t/T_{\text{e-h}}} dt \\ & = \frac{\langle S_{x'}(0) \rangle}{T_{\text{e-h}}} \left(\frac{T_2^{*'} \sin^2 \theta}{1 + \left(2\pi \nu_L T_2^{*'}\right)^2} + T_1^{'} \cos^2 \theta \right), \end{aligned} \tag{3.27}$$

where $1/T_2^{*'} = 1/T_2^* + 1/T_{\text{e-h}}$ and $1/T_1^{'} = 1/T_1 + 1/T_{\text{e-h}}$ are the spin relaxation rates modified by the recombination time. In the absence of nuclear polarization, $\nu_L = \frac{g\mu_B B}{h}$ and therefore the polarization is a Lorentzian as a function of field with a characteristic width proportional to the recombination-limited spin lifetime $T_2^{*'}$ and the g-factor.

In the presence of a nuclear polarization, which we know from equation 3.15 is collinear with the applied field, ν_L changes by the Overhauser shift frequency ν_n. The Hanle polarization curve reflects this change with its peak shifting by B_n. Recall, however, that while for $B \gg B_L$, $\langle \mathbf{I} \rangle \propto \frac{(\langle \mathbf{S} \rangle \cdot \mathbf{B})\mathbf{B}}{B^2}$, when $B \sim B_L$, the effect of nuclear spin-spin interactions scrambles $\langle \mathbf{I} \rangle$. This consideration modifies equation 3.15 for the steady state nuclear polarization at low fields such that,

$$\langle \mathbf{I} \rangle = \frac{4}{3}\hbar I(I+1)\frac{(\langle \mathbf{S} \rangle \cdot \mathbf{B})\mathbf{B}}{B^2}\frac{1}{1+(\gamma_N B T_{\text{s-s}})^2}, \tag{3.28}$$

where we have proceeded in a similar vein with the nuclear spin as we did for the electron spin in equation 3.27. We now have a polarization dependence,

$$\mathscr{P}_z \propto \frac{T_2^{*'}}{T_{\text{e-h}}}\left(\frac{\sin^2\theta}{1+\left(\frac{g\mu_B T_2^{*'}}{\hbar}\right)^2 (B+B_n)^2}\right) + \frac{T_1^{'}}{T_{\text{e-h}}}\cos^2\theta, \tag{3.29}$$

where,

$$B_n \propto \frac{\cos\theta}{1+(\gamma_N B T_{\text{s-s}})^2}. \tag{3.30}$$

The results of this analysis are summarized in figure 3.6a where we show the form of typical Hanle curves with and without the effects of nuclear polarization. From the figure, one can see that the Hanle effect reveals both the steady state nuclear polarization from the position of the offset peak, and the relevant time scales of the system, from the peak widths. Furthermore, consideration of the polarization asymmetry with field can also be used to calibrate the sign of the g-factor of the material in question [97]. As a method for measuring ODNMR, the sensitivity of the polarization to B_n makes it a natural choice.

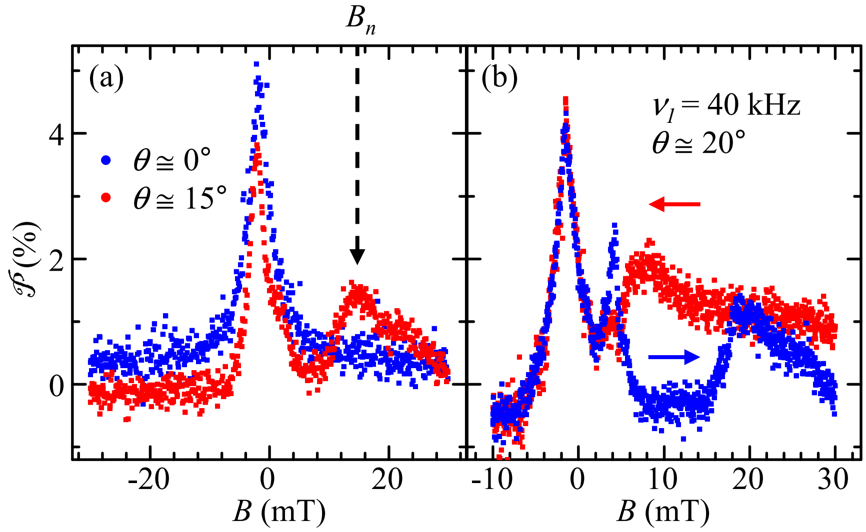

Figure 3.6: Hanle effect data showing the effects of nuclear polarization. (a) shows two sets of Hanle data one with $\theta \simeq 0°$ which is symmetric since $\langle \mathbf{I} \rangle = 0$. The other set with $\theta \simeq 15°$ has a non-zero $\langle \mathbf{I} \rangle$ and we can see $B_n \simeq 15$ mT. In both cases lifetimes can be extracted from the peak widths. No RF field is applied. (b) shows two field scans in the presence of an RF field: one from -10 mT to 30 mT and the other from 30 mT to -10 mT; other parameters are identical. The hysteresis apparent in the data is direct evidence of the system's low field bistability when $B \sim B_L$.

As an aside, note that a phenomenon similar to the Hanle effect can be observed by measuring the steady-state FR angle due to photoexcited spins [19]. In this case, the data will have a similar functional form and will reveal analogous information. One advantage of this technique in comparison with the luminescence-based Hanle effect is that the characteristic Lorentzian linewidths will not be limited by the recombination time $T_{\text{e-h}}$ in n-type systems.

3.6.2 Experimental details

A conventional ODNMR measurement is made in order to compare its sensitivity to the FR-based scheme. In this case, a sample of bulk semi-insulating (100)

GaAs is used instead of a QW due to the lower expected sensitivity of the photoluminescence (PL) technique. 5 mW of circularly polarized light from a CW Ti:Sapphire laser tuned to 1.570 eV is focused to a 100-μm diameter spot on the sample surface. For this experiment, the sample geometry is the same as shown in figure 3.2 with $\theta = 20^\circ$. Instead of collecting a transmitted probe beam, here the polarization of the PL $\mathscr{P}_{x'}$ emitted by the sample along the growth direction $\hat{x}'$ is measured using a 40-kHz photo-elastic modulator, followed by a linear polarizer, and a spectrometer coupled to a photo-multiplier tube. Emission from the excitonic peak at 1.514 eV is collected at 5 K as a function of B.

3.6.3 Isotopic resonances

Figure 3.7a shows $\mathscr{P}_{x'}$ as a function of B with B_1 driven at ν_1. The Hanle effect data shown here is typical of GaAs in the presence of DNP [25] and clearly illustrates the resonant depolarization at the isotopic NMR frequencies. Electron spin precession causes the time-averaged spin vector, and thus $\mathscr{P}_{x'}$, to decrease in an increasing transverse magnetic field. By the same reasoning, $\mathscr{P}_{x'}$ is sensitive to the effective transverse magnetic field B_n due to $\langle I \rangle$. The broad peaks seen around 20 mT in figure 3.7 are a result of B_n directly opposing and compensating B. The narrow peaks shown to shift as a function of ν_1 are due to a decrease in B_n under the resonant depolarization of $\langle I \rangle$. The 10 kHz/mT shift in the resonance for small ν_1 is close to the gyromagnetic ratio of the three relevant isotopes. As ν_1 increases, the splitting between resonances increases until at $\nu_1 = 100$ kHz and $\nu_1 = 120$ kHz, the three resonances (^{69}Ga, ^{71}Ga, and ^{75}As) are clearly distinguishable.

A calculation of the Hanle effect based on typical bulk GaAs parameters and the three NMR resonances is shown in figure 3.7b. There is good qualita-

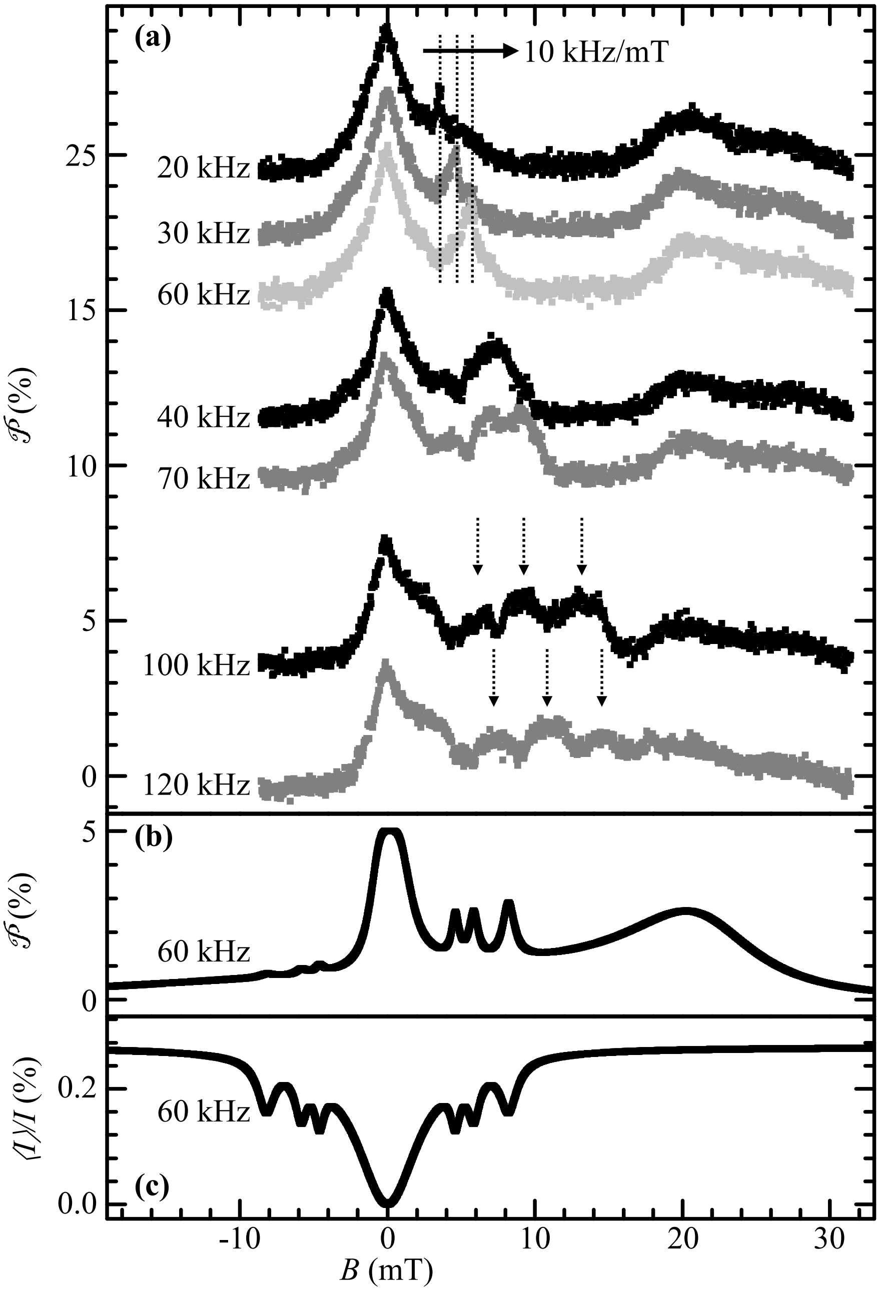

Figure 3.7: NMR detected by time-averaged PL polarization in semi-insulating (100) bulk GaAs. (a) $\mathscr{P}_{x'}$ taken as B is swept from -10 mT to 30 mT at 2 mT/min for different values of ν_1. (b) A calculation of $\mathscr{P}_{x'}$ as a function of B is shown along with the corresponding (c) dependence of $\langle I \rangle / I$ on B. The dip around $B = 0$ T is due to the emergence of nuclear spin-spin coupling at low fields.

tive agreement between the model and the data allowing us to estimate $\langle I \rangle / I \sim 0.25\%$ as shown in the dependence of $\langle I \rangle$ on B predicted by the model in figure 3.7c.

3.6.4 Sensitivity to 10^{12} nuclear spins

The signal-to-noise in the data indicates that we are sensitive to changes down to 0.05%. Since the region from which we are collecting PL contains $\sim 10^{16}$ nuclei, we estimate a sensitivity of 10^{12} nuclear spins for this ODNMR technique. In the FR measurement, which was done in a QW, we probed many fewer nuclei: $\sim 10^{12}$. There we could distinguish nuclear polarizations as small as 0.015% corresponding to a sensitivity of 10^8 nuclear spins.

We now examine how the sensitivity of the PL polarization-based ODNMR technique depends on the experimental parameters. In particular, we are interested in its behavior as we increase the magnetic field. The sensitivity of the the PL polarization on the nuclear polarization is,

$$\begin{aligned} \frac{d\mathscr{P}_{x'}}{d\langle I \rangle} &\propto \frac{d}{d\langle I \rangle}\left[\frac{T_2^{*'}}{T_{\text{e-h}}}\left(\frac{\sin^2\theta}{1+T_2^{*'2}\left(\frac{g\mu_{\text{B}}B}{\hbar}+A_H\langle I \rangle\right)^2}\right)\right] \\ &\propto \frac{-2A_H T_2^{*'3}\left(\frac{g\mu_{\text{B}}B}{\hbar}+A_H\langle I \rangle\right)\sin^2\theta}{T_{\text{e-h}}\left(1+T_2^{*'2}\left(\frac{g\mu_{\text{B}}B}{\hbar}+A_H\langle I \rangle\right)^2\right)^2}. \end{aligned} \tag{3.31}$$

While this looks extraordinarily messy, we can make some approximations in some useful limits. For typical experimental parameters of bulk GaAs and GaAs-based heterostructures, in high magnetic fields ($B > 1$ T), $\frac{1}{T_2^{*'}} \ll \frac{g\mu_{\text{B}}B}{\hbar} + A_H\langle I \rangle$. This simplifies equation 3.31 considerably in the high field regime:

$$\frac{d\mathscr{P}_{x'}}{d\langle I \rangle} \propto \frac{-2A_H\sin^2\theta}{T_{\text{e-h}}T_2^{*'}\left(\frac{g\mu_{\text{B}}B}{\hbar}+A_H\langle I \rangle\right)^3}. \tag{3.32}$$

At high fields, it is also generally true that $\frac{g\mu_{\mathrm{B}}B}{\hbar} > A_H \langle I \rangle$, allowing us to estimate further that as a function of salient parameters, the polarization has the following proportionality:

$$\frac{d\mathscr{P}_{x'}}{d\langle I \rangle} \propto \frac{1}{T_{\text{e-h}}^2 g^3 B^3} \tag{3.33}$$

Here we have made the assumption that $T_2^{*'} \simeq T_{\text{e-h}}$, which is reasonable in GaAs systems since $T_2^{*'}$ is usually limited by $T_{\text{e-h}}$ as in typical cases $T_2^* \gg T_{\text{e-h}}$.

The general result of this analysis is that for high magnetic fields, over 1 T, the Hanle effect becomes very insensitive to nuclear polarization. While this conclusion is fairly obvious from the data shown in figures 3.6 and 3.7 from bulk GaAs, we have shown this deficiency to be rooted in the nature of the measurement. The sensitivity gets worse at higher fields, and it also degrades for samples with long recombination lifetimes and large g-factors. In these regimes the FR-based ODNMR is far more sensitive. In a limited, low-field regime, however, equation 3.33 is invalid and the PL-based ODNMR can actually be quite sensitive (e.g. in figures 3.6 and 3.7 we have a sensitivity of 10^{12} for $B \sim 10$ mT).

3.7 Conclusion

In conclusion, ODNMR detected by time-resolved FR is an extremely sensitive probe of nuclear polarization capable of resolving small numbers of nuclear spins and distinguishing quadrupolar splittings in the kHz range. It may find use in the determination of built-in strain in GaAs heterostructures and provides an excellent way to perform ODNMR measurements at high magnetic fields, impossible by conventional techniques based on PL polarization. The fundamental difference of the FR technique versus techniques based on the Hanle effect is that the Hanle measurement is a measurement of time-averaged spin rather than of spin dynamics. The information lost in this averaging procedure makes this measurement fundamentally less powerful.

Chapter 4

Localized nuclear polarization in a quantum well

4.1 Introduction

A central theme of this work is the exploration of the contact hyperfine interaction in GaAs-based semiconductors. Up to this point, however, we have not discussed the local character of the coupling. It is local by its very nature, as expressed in equation 2.41: the coupling is non-zero at the locus of each nucleus and vanishes everywhere else. In semiconductor heterostructures, the electron envelope function plays a direct role in determining the spatial extent of the interaction as is evident from equation 2.42. Under optical orientation, this coupling produces a nuclear polarization profile whose extent is similarly determined [98]. As a result, this interaction affords us the unique ability to pattern nuclear polarization profiles in the image of the envelope functions of polarized conduction band electrons. Depending on the type of heterostructure used, nanometer-scale polarization profiles should be achieved. This chapter covers some of the first experiments performed in this vein, as well as discussing the physical origin of electrically induced resonant nuclear spin transitions in these same experimental systems.

Section 4.2 introduces the fundamental idea behind the experiments presented in this chapter. Section 4.3 covers the means by which we shape and translate the electron envelope function, while in section 4.4 we discuss and present data demonstrating the creation of nanometer-scale profiles of dynamically polarized nuclear spins. Finally, electrically induced nuclear spin transitions and their origins are explained in section 4.5.

4.2 Motivation

4.2.1 Background

Nuclear spin has been proposed as a robust medium for quantum information processing [99] in the solid state [36]. Due to the ease with which charge can be controlled in semiconductors, it is natural to use conduction electrons as intermediaries in manipulating nuclear spin. One approach is to tune the population and energy distribution of the electrons [35, 100]; our approach is to directly vary the spatial overlap of spin-polarized electrons with lattice nuclei. The ability to create nanometer-sized nuclear spin distributions combined with long solid-state nuclear spin lifetimes has important implications for the future of dense information storage, both classical and quantum. In addition, control over highly localized interactions between conduction electrons and lattice nuclei may provide a means to manipulate such information.

Here, we use gate voltages to electrically position $\sim$ 23 nm wide distributions of polarized nuclei over a $\sim$ 20 nm range in a single parabolic quantum well (PQW). Using optically-injected spin-polarized carriers, we exploit the contact hyperfine interaction to produce nuclear polarization in the vicinity of their confined envelope functions [98]. The thin sheets of polarized nuclei are laterally defined by the diameter of a focused laser spot. The application of resonant radio frequency (RF) voltages to the gates provides additional electrical control over nuclear spin. In this case, nuclear depolarization is observed and is attributed to a local charge mediated quadrupolar interaction in contrast to a spin dependent coupling.

Of course, manipulation of nuclear spins is nothing new; nuclear magnetic resonance (NMR) has been around for over a half-century. The innovation here is the ability to address small numbers of nuclei, relative to typical NMR techniques (10^{12} vs. 10^{16}), in solid state systems using largely conventional electronics. NMR techniques using coils and magnetic field gradients are difficult to implement on nanometer scales; for this reason we look to spin interactions between electrons and nuclei to act as effective magnetic fields, i.e. our goal is to use these interactions to polarize and manipulate nuclear spin. The exquisite control over electrons developed in modern semiconductor technology aids us in this endeavor.

4.2.2 Implementation

As discussed in section 3.4.2 the effect of spin polarized electrons on nearby lattice nuclear spins can be expressed in terms of an effective magnetic field $\mathbf{B}_e$. This field, which is a manifestation of the contact hyperfine interaction, acts to polarize nuclear spins as discussed in section 3.4.1. Dynamic nuclear polarization (DNP), however, depends on the strength of the hyperfine interaction, which goes as,

$$H_{\mathrm{hf}} \propto |\Psi(\mathbf{R})|^2 \mathbf{I} \cdot \mathbf{S}, \tag{4.1}$$

where $\Psi(\mathbf{R})$ is the electron envelope function and $\mathbf{R}$ is the position of the relevant nucleus. The nuclear polarization profile which develops as a result has a similar spatial extent: it will be confined to the immediate vicinity of the electron probability density. Therefore, we can imagine controlling the position of a confined envelope function of polarized electron spins and thereby polarizing different regions of the crystal. Furthermore, note that since $\mathbf{B}_e$ goes as $|\Psi(\mathbf{R})|^2$, we can vary this effective field at a nuclear site by controlling the position of the electron envelope function. At resonant drive frequencies we may thus expect to induce nuclear spin transitions in the immediate vicinity of the electron probability density. These concepts are illustrated in figure 4.1 and make up the basis for the experiments presented in the rest of this section.

4.3 Translation of the electron envelope function

4.3.1 The parabolic potential

A parabolic potential is the ideal confining potential for achieving distortion-free translation of an electron. With the application of a uniform electric field across such a potential we induce a spatial shift of the parabolic potential and have,

$$U(x') = \frac{1}{2}m_e\omega^2 x'^2 + \frac{e}{d}(U_g - U_0)x', \tag{4.2}$$

where $\hat{x}'$ is the confinement direction (the sample growth direction), m_e is the effective electron mass, e is its charge, ω is characteristic angular frequency of the potential, U_g is the voltage applied across two electrodes a distance d apart across the potential, and U_0 is an offset voltage known as the built-in potential which often appears in real semiconductor systems. By changing the voltage applied across the potential, we shift the energy minimum and thus the center

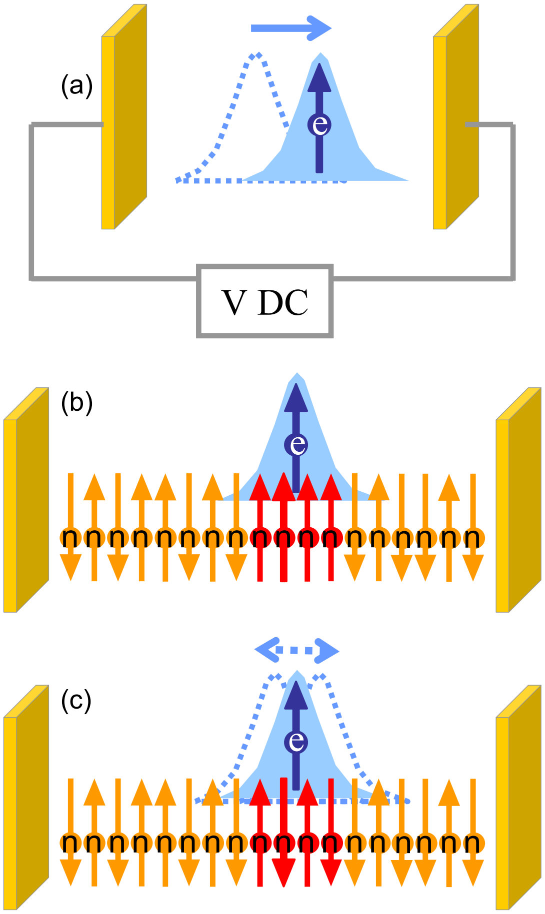

Figure 4.1: We want to build a device in which we can control the local interactions between electronic and nuclear spin with an applied voltage by (a) moving the electron envelope function using a pair of external gates, (b) locally polarizing the spin of lattice nuclei, and (c) resonantly inducing nuclear spin transitions.

of the eigenstate wave functions to,

$$x_0' = \frac{e}{m_e \omega^2 d}(U_g - U_0), \tag{4.3}$$

while retaining the parabolic shape of the potential profile. In an idealized system, with an infinite parabolic potential, the electron eigenstates translate a distance proportional to U_g without distortion. In realistic systems, where the harmonic potential is finite, this description remains correct to first order. In contrast, electric fields applied across a standard square potential well distort the electronic eigenstates and result in negligible wave function translation due to the sharpness of the well's barriers [57].

4.3.2 Parabolic quantum wells

In order to realize this scenario in a real system, we grow a GaAs/AlGaAs heterostructure by molecular beam epitaxy (MBE) (see appendix A for the exact structure) which we subsequently process using standard semiconductor techniques (see appendix B for the exact processing techniques). The sample [16] is an undoped 100-nm (100) $\mathrm{Al}_x\mathrm{Ga}_{1-x}\mathrm{As}$ PQW [101], schematically shown in figure 4.3. The aluminum concentration x is varied from 7% at the center of the well to 40% in the barriers to create a parabolic confinement potential in the conduction band. Directly below the PQW is a 450-nm $\mathrm{Al}_{0.4}\mathrm{Ga}_{0.6}\mathrm{As}$ barrier, then a 500-nm of layer of low temperature-grown GaAs serving as a conduction barrier [102], and finally a 50-nm n-GaAs back gate contacted using annealed AuGe/Ni. Above the PQW is a 50-nm $\mathrm{Al}_{0.4}\mathrm{Ga}_{0.6}\mathrm{As}$ barrier followed by a transparent front gate consisting of 5 nm of titanium and 5 nm of gold which was evaporated on the sample surface. A voltage U_g applied across the front gate and the grounded back gate produces a constant electric field across the PQW and results in a negligible leakage current ($< 10\mu$A). Experiments are performed at

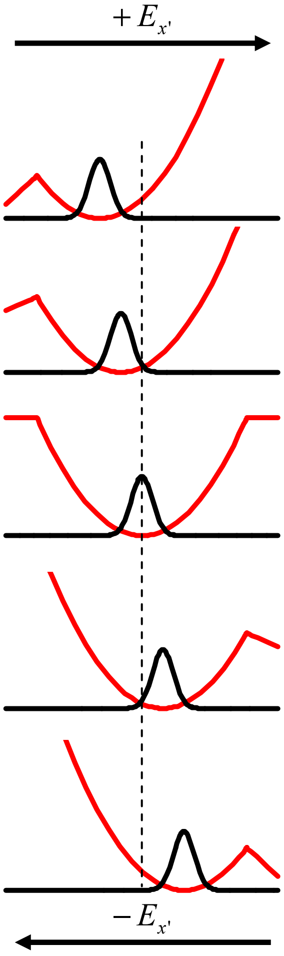

Figure 4.2: A series of energy diagrams showing a parabolic potential with its ground state electron envelope function. The constant electric field $E_{x'}$ applied across the potential goes from positive to negative scanning the diagrams from top to bottom. The peak position of the electron ground state x'_0 is proportional to $E_{x'}$.

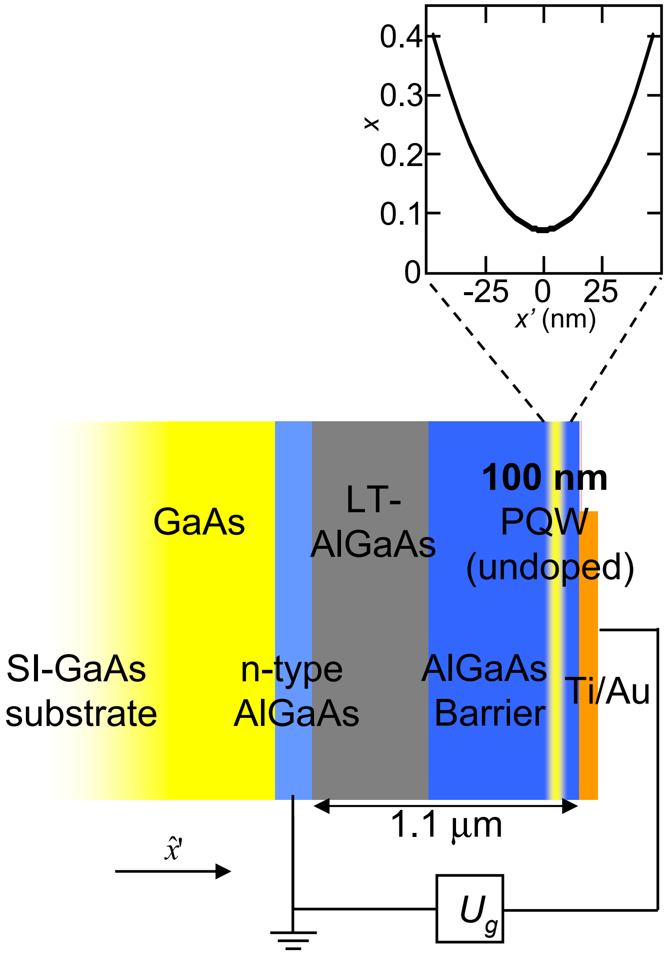

Figure 4.3: A schematic diagram of the gated $Al_xGa_{1-x}As$ PQW with $x(x')$ in the inset.

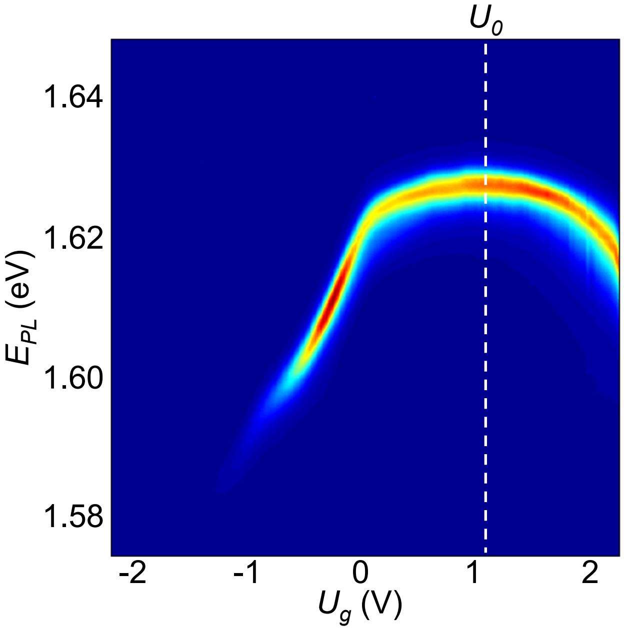

Figure 4.4: PL from a 100-nm PQW as a function of U_g and detection energy E_{PL} at $T = 5$ K with counts plotted in a color-scale.

5 K in a magneto-optical cryostat with a semi-rigid coaxial cable coupling DC and RF voltages to the sample gates.

Figure 4.4 shows the energy of photoluminescence (PL) as a function of U_g at T = 5 K excited by a pulsed laser at 1.676 eV with and average intensity of ~ 1 W/cm^2. The PL energy is highest at the built in potential U_0 = 1.1 ± 0.1 V and decreases as U_g is tuned away from that value. Such behavior is consistent with the quantum-confined Stark effect [103] and shows that the application of U_g affects the band-structure as expected. The observed shift is 6.8 ±1.0 meV/V^2 compared with a theoretical value of 5.0 meV/V^2 calculated using conduction and valence band offsets from the literature [104] and neglecting changes in the exciton binding energy, which are of the order of 4 meV [105]. Such agreement gives us confidence in our ability to produce a constant and homogeneous electric field across the PQW proportional to U_g. The decrease of the PL intensity away from U_0 arises from the reduced wave function overlap between photoexcited electrons and holes with increasing electric field, leading to the dissociation of the exciton.

4.3.3 Measuring electron translation

As discussed in section 4.3.1, electric fields applied across the gated PQW structure result, to first order, in the distortion-free displacement of the center of the electron envelope function x'_0 along the growth direction. In order to determine the exact dependence of x'_0 on U_g we do a series of measurements of the conduction band Landé g-factor. Recall from equation 2.31 that g_e depends on the band-gap energy E_g. The Al concentration in our PQW is graded along $\hat{x}'$ in such a way that the confinement energy, and thus E_g, vary parabolically as a function of x'. Therefore g_e is also a function of x'. As a result we use measurements of g_e to track the center position x'_0 of the electron envelope function along the confinement direction in the PQW.

Given that in our experiments the density of the optically excited electrons and holes is $\sim 10^{10}$ cm^{-2}, only the lowest subband is occupied and screening effects can be neglected. We can then use the ground state wave function for a parabolic potential as our electron envelope function,

$$\Psi(x' - x'_0) = l^{-1/2}\pi^{-1/4}e^{-\frac{(x'-x'_0)^2}{2l^2}}, \tag{4.4}$$

where $l = \sqrt{\hbar/(m_e\omega)}$ is the characteristic length. A fit to published experimental data relating g_e to the Al concentration x in bulk [106], shown in figure 4.5, gives us the relation $g_e(x)$. From the design of the structure, we know $x(x')$ (see the inset in figure 4.3), allowing us to convert from position to g-factor through

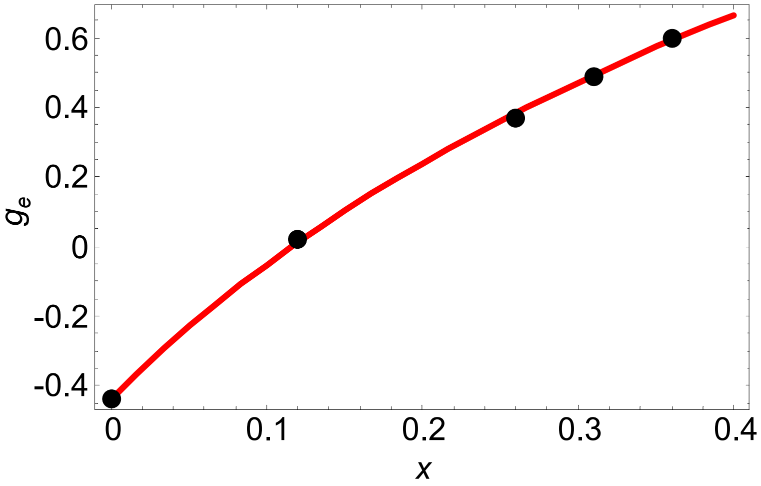

Figure 4.5: Dependence of g_e on x in bulk Al$_x$Ga$_{1-x}$As. The points are data from Weisbuch et al. [106] and the red line is a non-linear fit $g_e(x)$.

$g_e(x(x'))$. Note, however, that the electrons trapped in the PQW are not perfectly two-dimensional; their extent along $\hat{x}'$ is described by $|\Psi(x'-x'_0)|^2$. The g-factor we measure for electrons in the PQW is therefore an average over the electron probability density,

$$\bar{g}_e(x'_0) = \int g_e(x(x'))|\Psi(x'-x'_0)|^2 dx' + \Delta g_c, \tag{4.5}$$

where Δg_c is a phenomenological constant due to confinement effects not included in our simple model [15]. We set $\Delta g_c = 0.024$ such that our measured g-factor at $U_g = U_0$ corresponds to expected value for $x = 0.07$, i.e. $x'_0 = 0$. We now have the g-factor as a function of envelope function position, which through a numerical procedure we invert, resulting in $x'_0(\bar{g}_e)$. The functions $g_e(x')$, $\bar{g}_e(x'_0)$, and $x'_0(\bar{g}_e)$ are plotted in figure 4.6.

Having built up the machinery for determining the position of the electron envelope function based on the knowledge of $\bar{g}_e$, we proceed to the measurement of $\bar{g}_e$. Time-resolved Faraday rotation (FR) measurements [85] are per-

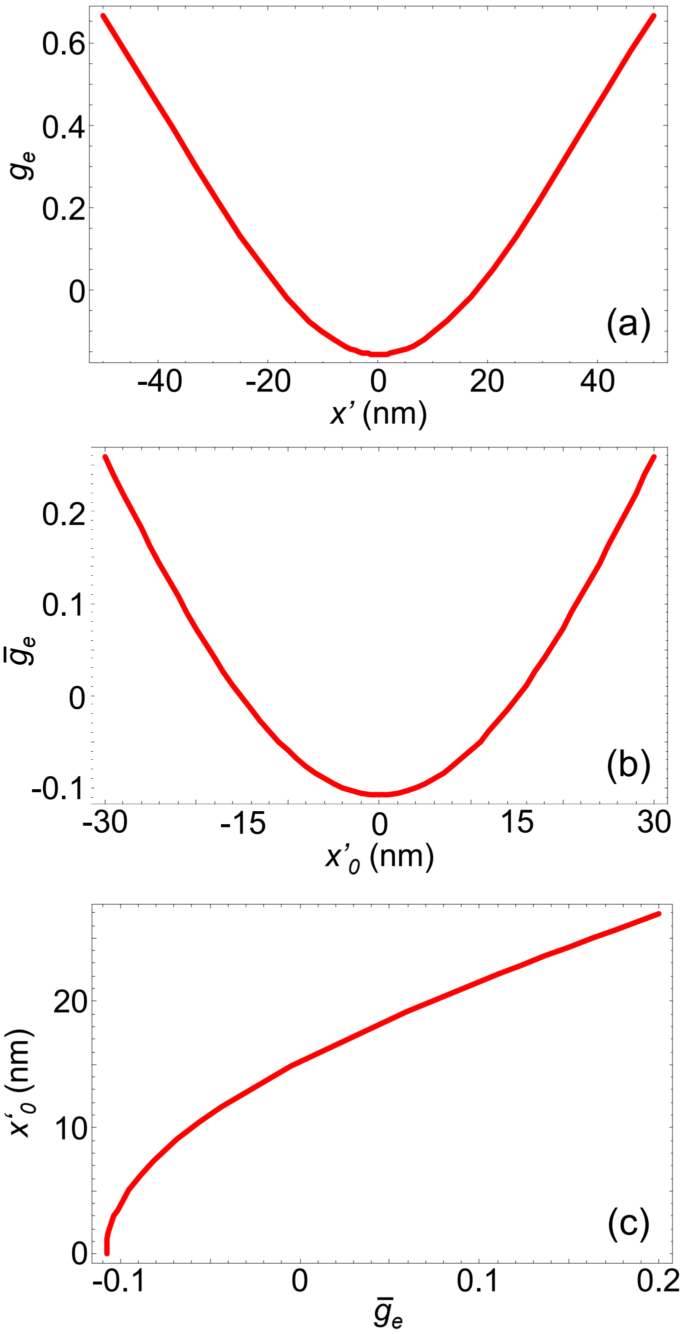

Figure 4.6: The functions $g_e(x')$, $\bar{g}_e(x'_0)$, and $x'_0(\bar{g}_e)$ are plotted in (a), (b), and (c), respectively.

formed using a 76-MHz femtosecond Ti:Sapphire laser tuned near the absorption edge of the PQW (1.62 eV). Laser pulses are split into circularly (linearly) polarized pump (probe) pulses with an average power of 2.5 mW (250 μW). Pulses are modulated by optical choppers at f_1= 3.3 kHz and f_2= 1.0 kHz, respectively, and are focused to an overlapping spot ($\sim$30 μm in diameter) on the semitransparent front-gate. Electron spin precession is well described by an equation of the form discussed in section 2.6.2,

$$\theta_F(\Delta t) = \theta_\perp e^{\frac{-\Delta t}{T_2^*}} \cos(2\pi\nu_L\Delta t + \phi) + \theta_{||} e^{\frac{-\Delta t}{T_1}}, \tag{4.6}$$

where $\theta_\perp$ is proportional to the spin injected perpendicular to the applied field, $\theta_{||}$ is proportional to the spin injected parallel to the applied field, T_2^* is the inhomogeneous transverse spin lifetime, T_1 is the longitudinal spin lifetime, ϕ is the phase, and the Larmor frequency ν_L, which in the absence of nuclear polarization is given by $\nu_L = \bar{g}_e\mu_\mathrm{B}B/h$. B is an externally applied magnetic field applied according to the diagram in figure 3.2b; we adopt the same definition of the angle θ and the same coordinate systems as shown in that figure. To avoid polarization of the nuclear spins, no electron spins are to be injected along the field direction: $\theta_{||} = 0$ must be true. This condition forces the laser excitation to be perpendicular to the applied field ($\theta = 0$).

Typical time-resolved data in the absence of nuclear polarization are shown in figure 4.7 for different U_g and are fit to equation 4.6. From these fits we extract T_2^*, which is plotted in figure 4.8 as a function of U_g and reaches a minimum near U_0. This behavior reflects the formation of excitons in the flat-band condition due to the spatial proximity of the confined electrons and holes. The concurrent reduction of T_2^* near U_0 can be attributed to the enhanced charge recombination rate of bound electrons and holes or to electron-hole exchange which may also limit the electron spin lifetime at low temperature [107]. We

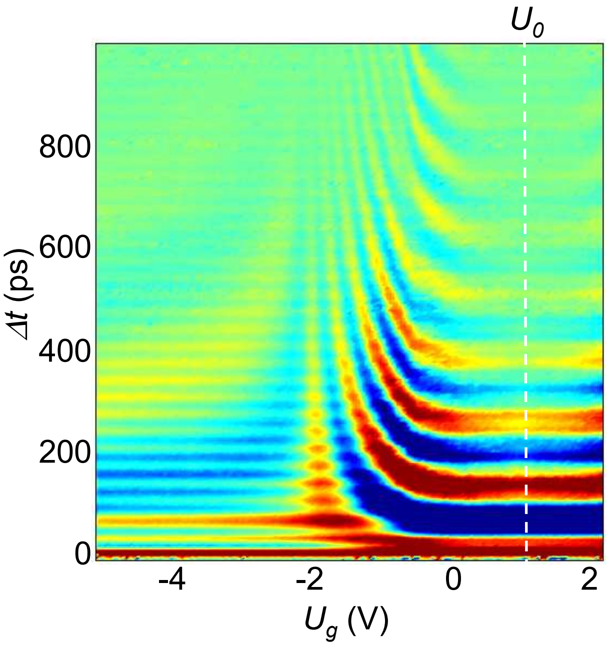

Figure 4.7: Typical FR data from a PQW as a function of Δt and U_g. The high frequency oscillations in the signal background are due to unintentional injection of spin polarized carriers into the GaAs substrate of this sample.

also extract $\bar{g}$ and plot it as a function of U_g in figure 4.8. In figure 4.9, we apply our conversion function $x_0'(\bar{g})$ and plot x_0' as a function of U_g for a different but structurally identical 100-nm PQW sample to the one discussed to this point. The small differences in the form of the g-factor tuning curve as a function of U_g are likely due to device specific differences in processing each individual sample.

For small voltages away from U_0, the electron and hole form an exciton and the electron wave function position varies little with gate voltage. Once this binding energy is overcome, the data show an electron displacement of 5 nm/V over a $\sim$ 20 nm range (the corresponding calculated hole displacement is -7.5 nm/V). The dependence is nearly linear as expected from equation 4.3. In order to put the tuning range in perspective, note that calculations of the

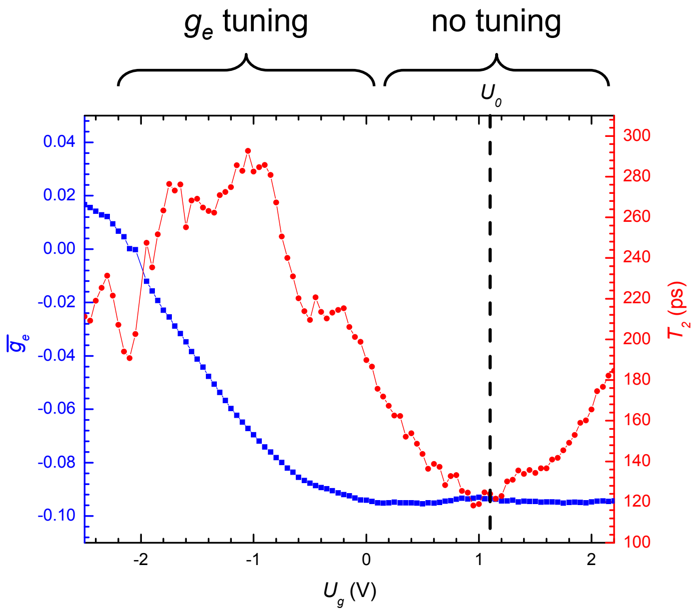

Figure 4.8: $\bar{g}_e$ and T_2^* plotted as functions of U_g. These parameters are extracted from fits of time-resolved FR data using equation 4.6.

ground state envelope function yield a full-width at half-maximum (FWHM) of the electronic probability distribution, $|\Psi(z-z_0)|^2$, $2l\sqrt{\ln 2} = 16$ nm.

In addition to translating the electron envelope function within the PQW, we can also modulate its position at RF at least as high as 100 MHz. Work in similar samples achieved modulation as high as 4 GHz [16]. A RF voltage applied to U_g causes the periodic displacement of the electron envelope function within the PQW sampling a range of $\bar{g}_e$ and therefore introducing a distribution of frequency components into the electron Larmor precession. The upper curve of figure 4.10a shows spin dynamics described by equation 4.6 of an electron at a fixed position x_0' with no RF modulation applied to U_g. Contrasting those dynamics are the more complex dynamics of the lower trace measured with RF

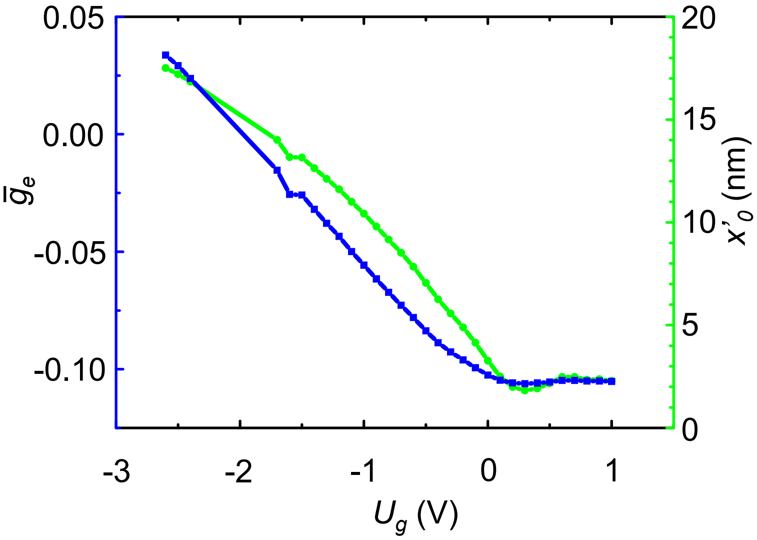

Figure 4.9: $\bar{g}_e$ plotted as a function of U_g along with x'_0 as a function of U_g. The $x'_0(U_g)$ curve is generated by applying our conversion $x'_0(\bar{g}_e)$ to the $\bar{g}_e(U_g)$ curve.

modulation applied to U_g. We derive a simple model to explain the additional frequency components introduced by RF modulation.

For each pump-probe delay time Δt, a single FR measurement consists of an average in lab-time of the instantaneous FR angle. Since the laser repetition rate is not synchronized with the RF modulation applied to U_g, under the influence of an RF modulation on U_g, a typical spin precession decay shown in equation 4.6, must be averaged over a full cycle of the envelope function's motion along $\hat{x}'$. In other words, it must be averaged over a range of sampled Larmor frequencies defined by the maximum and minimum x'_0 positions in a cycle:

$$\begin{aligned}\theta_F(\Delta t) &= \frac{1}{2\pi}\int_0^{2\pi} \theta_\perp e^{\frac{-\Delta t}{T_2^*}} \cos\left[\frac{\mu_B B}{\hbar}\left(\bar{g}_{\text{avg}}+\bar{g}_{\text{diff}}\sin t'\right)\Delta t+\phi\right] dt' + \theta_{||} e^{\frac{-\Delta t}{T_1}} \\ &= \theta_\perp e^{\frac{-\Delta t}{T_2^*}} J_0\left[\frac{\mu_B B}{\hbar}\bar{g}_{\text{diff}}\Delta t\right] \cos\left[\frac{\mu_B B}{\hbar}\bar{g}_{\text{avg}}\Delta t+\phi\right] + \theta_{||} e^{\frac{-\Delta t}{T_1}}, \qquad (4.7)\end{aligned}$$

where $J_0(x)$ is a Bessel function of the first kind, $\bar{g}_{\text{avg}} = \frac{\bar{g}_e(x'_{\text{max}})+\bar{g}_e(x'_{\text{min}})}{2}$, and

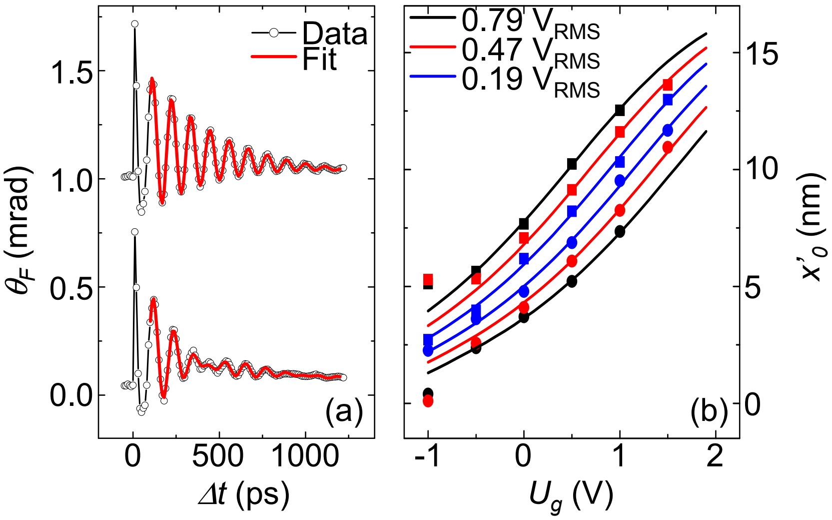

Figure 4.10: (a) Upper curve: θ_F as a function of Δt with no applied RF voltage (offset 1 mrad for clarity), $B = 6$ T, U_g= -0.1 V (fit to equation 4.6 red). Lower curve: θ_F as a function of Δt at the same B and U_g with an off-resonant RF voltage of 0.785 V$_{RMS}$ at 28.5 MHz corresponding to a peak-to-peak oscillation of x'_0 of $\sim$ 4 nm (fit to equation 4.7 red). (b) Maximum (x'_{max}) and minimum (x'_{min}) wave function positions plotted as a function of U_g for different RMS RF voltages. Square (circular) data points represent the upper (lower) bound of wave function displacement x'_{max} (x'_{min}). Solid lines are fits to x'_{max} and x'_{min}. Nuclear polarization is constant in (a) and (b); observed effects are explained by electron dynamics alone.

$\bar{g}_{\text{diff}} = \frac{\bar{g}_e(x'_{\text{max}})-\bar{g}_e(x'_{\text{min}})}{2}$. x'_{max} and x'_{min} are the maximum and minimum positions in the PQW sampled by the center of the oscillating electron envelope function. Though the full equation for θ_F looks complex, its behavior is simple. An oscillating U_g modifies the unperturbed decaying cosine by changing its precession frequency to an average over a range of frequencies. In addition, the cosinusoidal oscillations are modulated by a Bessel function. As is evident from the lower curve in figure 4.10a, the data is well fit by this model. Furthermore, by fitting the data with equation 4.7 we can determine x'_{max} and x'_{min} as a function

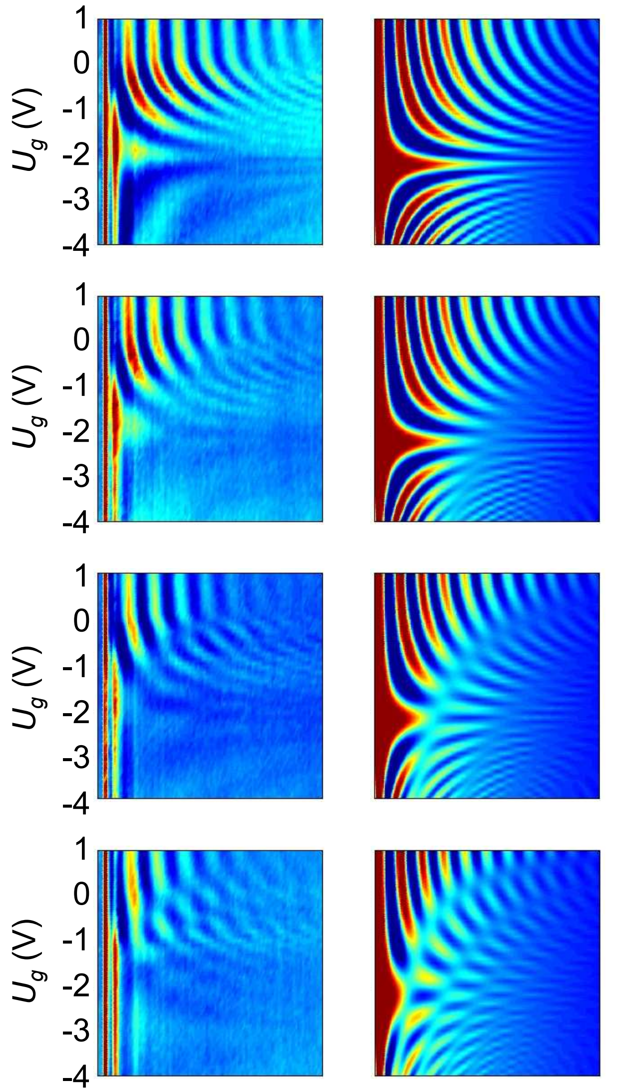

Figure 4.11: A comparison of FR data and simulations as a function of increasing RF power on U_g. The FR data are shown in a color-scale in the left column while the simulations are in the right column. Applied RF power is increasing from top to bottom.

of U_g for a range of RF powers as shown in figure 4.10b. Fits to the data are calculated assuming the wave function displacement is governed by the relationship given in figure 4.9. The only free fitting parameter is the amplitude of RF power across the gates, which, as expected, is found to scale linearly with power applied to the device. The data show that modulation amplitude of x_0', $\Delta x' = x'_{\mathrm{max}} - x'_{\mathrm{min}}$, varies with U_g at a fixed RF power; $\Delta x'$ increases for voltage ranges where the electron moves more easily. This result combined with the excellent agreement of our fitting function 4.7 with the time-resolved FR data demonstrates our ability to displace the electron wave function over nanometer length scales and on nanosecond time scales. As further evidence, see figure 4.11, in which we compare FR data taken as a function of Δt and U_g for different RF powers on U_g with simulations using the model based on equation 4.7.

4.4 Nuclear polarization profiles

4.4.1 Experimental details

Spin-polarized photo-excited electrons generate nuclear spin polarization within the PQW through DNP. The contact hyperfine coupling $A_H \propto |\Psi(\mathbf{R})|^2$ is responsible for this transfer in polarization. We now describe experiments investigating the spatial dependence of the polarization profile. In order to optically induce a nuclear polarization, we simply adjust the angle θ between the sample and the magnetic field as discussed in section 3.5.1. DNP is driven by the longitudinal component of electron spin, which is suppressed in the measurements described in section 4.3.

The average nuclear polarization $\langle I \rangle$ can be extracted from time-resolved FR measurements of ν_L as discussed in section 3.4.2. Through the measurements discussed in section 4.3.3 we know the dependence $\bar{g}$ on U_g. Once the PQW undergoes DNP, an Overhauser frequency $\nu_n = \frac{A_H}{2\pi} \langle I \rangle$ shifts ν_L with respect to the unpolarized case. We can therefore map out ν_n for all U_g. Recall from section 3.4.2 that for GaAs calculations show $\nu_n = 32.6$ GHz for the 100% nuclear polarization of all three constituent isotopes; after DNP, ν_n is measured up to 1 GHz in the PQW corresponding to $\sim 2.5\%$ nuclear polarization.

In the measurement of nuclear polarization profiles we begin with an unpolarized nuclear lattice; optically pumping the PQW at constant $U_g = U_{\text{pol}}$ fixes the location of spin-polarized electrons at x'_{pol}. After 20 minutes of DNP (we measure $T_{DNP} \simeq 17$ minutes), time-resolved FR data is taken to determine ν_L as a function of U_g. Scans of θ_F are taken as a function of U_g at each value of Δt and then the data are fit to extract ν_L. Scans take 7 s after which U_g is reset to U_{pol} for 120 s (well above the observed minimum time necessary to maintain the original nuclear polarization profile). This process ensures that the initial nuclear polarization profile is maintained and remains undisturbed by the measurement process. Comparing Larmor frequencies of the polarized and unpolarized states, we determine ν_n vs. U_g, as shown in figure 4.12. Given our conversion between U_g and x'_0 shown in figure 4.9, we can also plot the spatial distribution of ν_n, also shown in figure 4.12.

4.4.2 Experimental results

The data show localization of the nuclear polarization around the electron envelope function's polarizing position x'_{pol}. As expected the maximum ν_n is obtained when U_g applied during the measurement phase matches U_{pol} used during the polarization phase. The spatial distribution of ν_n can be created at selected

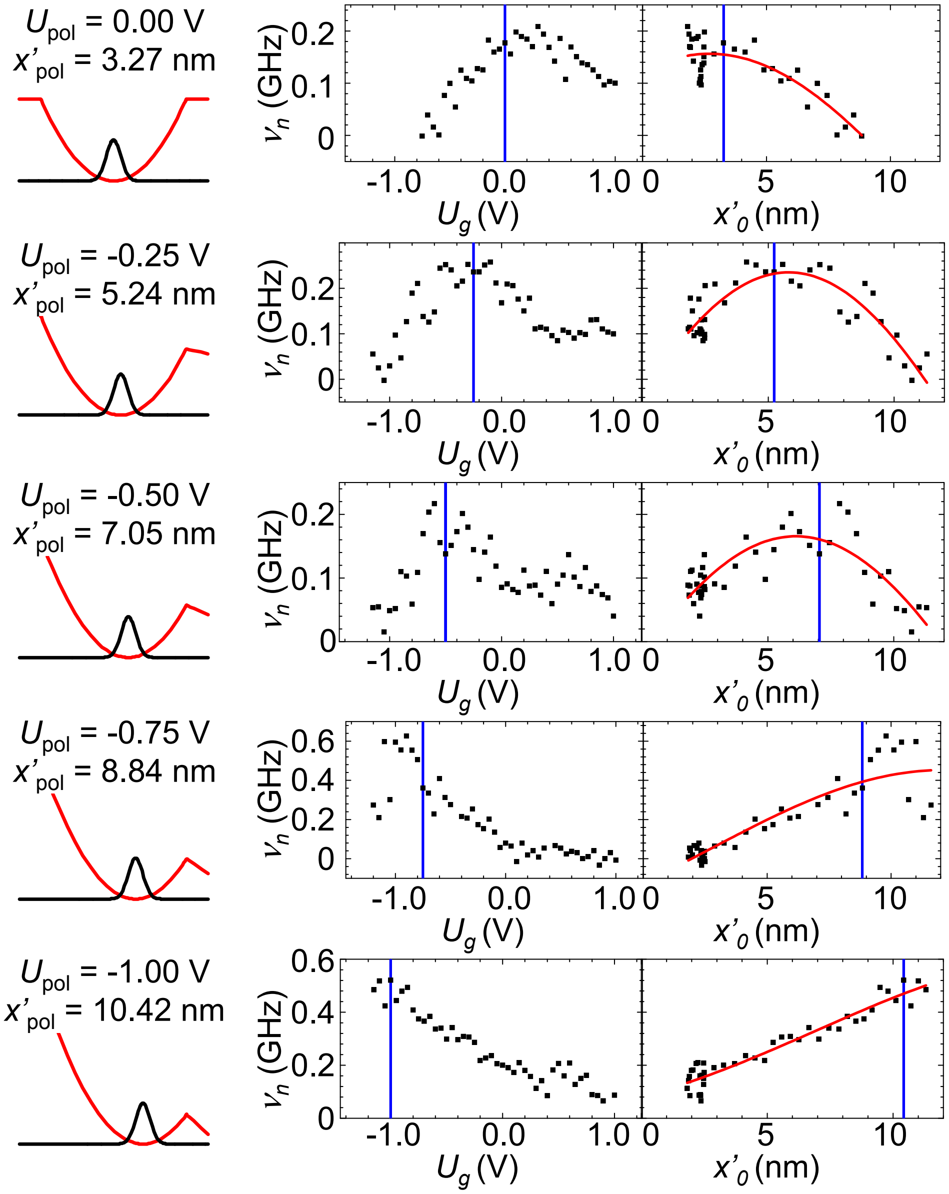

Figure 4.12: Measurements of the nuclear polarization distribution within the PQW. In the left-most column the electron envelope function is shown schematically, centered at different U_{pol} (x'_{pol}). Corresponding nuclear polarization distributions are created at $B = 3.98$ T by polarizing nuclei for 20 minutes at voltage U_{pol} or equivalently position x'_{pol} (blue line). Nuclear polarization is measured as an Overhauser shift ν_n and is plotted as a function of U_g and x'_0 (solid points). Red curves are Gaussian fits to the data with a fixed FWHM of 23 nm. Centers of the Gaussian fits are 2.7 nm, 5.8 nm, and 6.1 nm, 12.1 nm, and 16.6 nm from top to bottom.

positions within our 100-nm quantum well simply by tuning the voltage U_g before the polarization process. The steady-state width of these distributions, set by the range of the contact hyperfine interaction, is broadened by nuclear spin diffusion at a rate of 10 nm^2 s^{-1} [98].

4.4.3 Theoretical analysis

As discussed in section 3.4.2,

$$\nu_n(\mathbf{R}) = \frac{4g\mu_\mathrm{B}}{3\hbar}\gamma_N\eta\,|\Psi(\mathbf{R})|^2\,\langle I(\mathbf{R})\rangle\,, \tag{4.8}$$

where $\mathbf{R}$ is a position in the crystal. Since during the measurement the envelope function is centered on x'_0 and the confinement is along $\hat{x}'$, $\Psi(\mathbf{R}) = \Psi(x' - x'_0)$. Furthermore, after DNP through optically polarized conduction electrons with the envelope function fixed at $x' = x'_\mathrm{pol}$,

$$\langle I(\mathbf{R})\rangle = \left\langle I(x' - x'_\mathrm{pol})\right\rangle = \frac{4}{3}\hbar I(I+1)\left\langle S_{||}\right\rangle|\Psi(x' - x'_\mathrm{pol})|^2, \tag{4.9}$$

as discussed in section 3.4.1. Since the Overhauser frequency actually measured constitutes a response from the whole PQW, for each combination of x'_0 and x'_pol, i.e. for each combination of U_g and U_{pol}, we integrate $\nu_n(\mathbf{R})$ over the structure:

$$\nu_n(x'_0, x'_\mathrm{pol}) = \int_\mathrm{structure} C|\Psi(x' - x'_0)|^2|\Psi(x' - x'_\mathrm{pol})|^2 dx', \tag{4.10}$$

where we have absorbed all the spatially constant terms into C. Given our parabolic potential and the form of $\Psi(x')$ given in equation 4.4 we have,

$$\nu_n(x'_0, x'_\mathrm{pol}) = \frac{C}{l\sqrt{2\pi}}e^{-\frac{(x'_0 - x'_\mathrm{pol})^2}{2l^2}}, \tag{4.11}$$

which has the same form and FWHM as $\Psi(x')$ (see section 4.3.3). Therefore, from these theoretical considerations, we expect to measure a FWHM of

$2l\sqrt{2\ln 2} = 23$ nm. Fitting the measured nuclear polarization profiles shown in figure 4.12 to a Gaussian with a 23-nm FWHM, we obtain a reasonable agreement between the polarizing position x'_{pol} and the center of the Gaussian fit as discussed in the caption of figure 4.12.

There are a number of possible explanations for the small discrepancies between x'_{pol} and the center of the fits. Most prominent is that we are only able to measure the distribution of ν_n over a 20-nm range because of the limitations of our device (specifically leakage current). Such a range is too small to capture the full Gaussian distribution. It is also likely that there is a systematic error in the determination of x'_0 as a function of U_g due to the many layers involved in that conversion. The approximation of our PQW as an idealized well, with a Gaussian ground state envelope function introduces minimal error as shown in a more realistic theoretical treatment of similar PQWs [108].

A detailed theoretical analysis [109] has been pursued for this system resulting in calculations which qualitatively match the $\nu_n(x'_0, x'_{\text{pol}})$ profiles shown in figure 4.12. The magnitudes of $\nu_n(x'_0, x'_{\text{pol}})$ predicted in those calculations are very similar to the measured values. The analysis essentially involves treating the PQW more realistically and calculating the constant η for ^{69}Ga, ^{71}Ga, ^{75}As, and ^{27}Al, which depends on the Bloch function overlap with each different isotopes. A numerical $\mathbf{k} \cdot \mathbf{p}$ calculation is undertaken [108] and the abundances of the different isotopes in different regions of the sample are taken into account.

4.5 Resonant nuclear depolarization

4.5.1 Experimental details and results

Applying a resonant RF voltage to U_g induces nuclear spin transitions among the polarized nuclei in the PQW. The continuous induction of these transitions results in a drop in the time averaged nuclear spin polarization $\langle I \rangle$. As shown in figure 4.13, a decrease in $\langle I \rangle$ leads to a change in ν_n and thus in θ_F at a fixed delay, whose sign and amplitude depend on our choice of Δt and the magnitude of the change in $\langle I \rangle$. Just as in chapter 3, nuclear depolarization resonances are apparent for the three most abundant isotopes in the sample, ^{75}As ($\gamma_N/(2\pi) = 7.317$ MHz/T), ^{71}Ga ($\gamma_N/(2\pi) = 10.257$ MHz/T), and ^{69}Ga ($\gamma_N/(2\pi) = 13.032$ MHz/T), at the expected NMR frequencies. We do not observe resonances for ^{27}Al ($\gamma_N/(2\pi) = 11.135$ MHz/T), possibly due to the low Al concentrations within the PQW (7% at the center). The asymmetry of the resonance peaks is due to the long time scales on which DNP acts in this sample compared to the scan times; the induction of resonant spin transitions quickly depolarizes $\langle I \rangle$, however, full re-polarization through DNP takes much longer ($T_{DNP} \simeq 17$ minutes). Measurements also reveal resonances for each of these isotopes at 1/2, 2/3 and 2 times the nuclear resonance frequencies. The change in θ_F, approximately proportional to the change in ν_n is strongest for the $2\nu_{NMR}$ transition, followed in strength by the ν_{NMR}, $\frac{1}{2}\nu_{NMR}$ and finally the $\frac{2}{3}\nu_{NMR}$ transition. Resonances at $2\nu_{NMR}$ indicate the presence of $\Delta m = \pm 2$ transitions in addition to $\Delta m = \pm 1$ transitions (where m is the nuclear spin number along the applied field). The fractional resonances at $\frac{1}{2}\nu_{NMR}$ and $\frac{2}{3}\nu_{NMR}$ on the other hand, are likely the result of these same $\Delta m = \pm 1, \pm 2$ spin transitions induced by harmonics of the RF modulation frequency, which may arise due to nonlinearities in the depolarization mechanism.

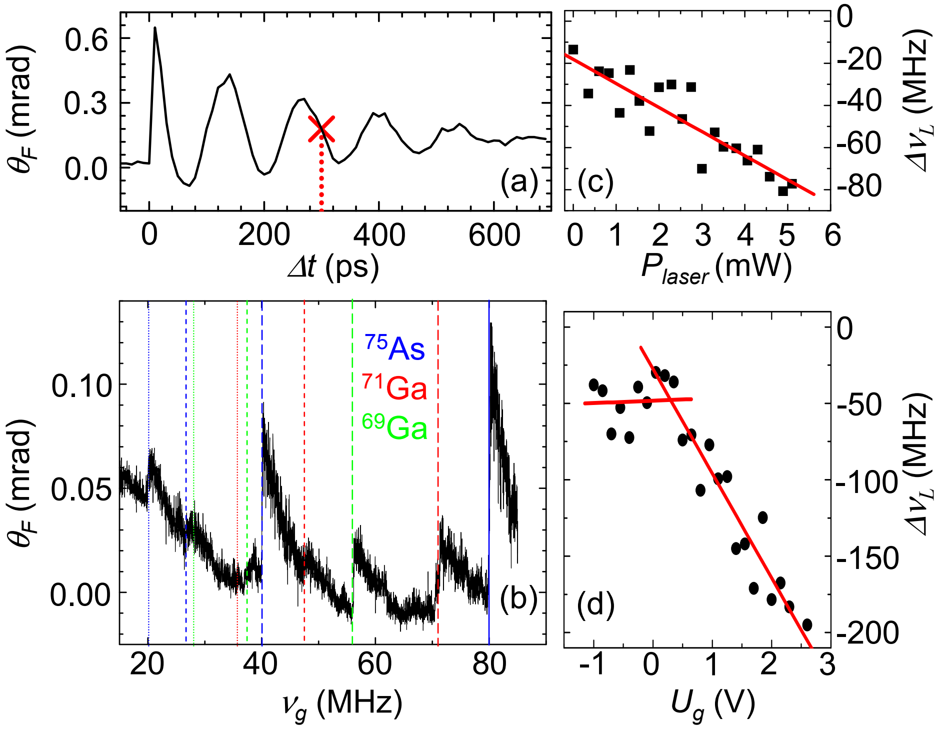

Figure 4.13: (a) θ_F as a function of time delay Δt. The red "x" indicates $\Delta t = 300$ ps used for scan (b) showing θ_F as a function of applied gate frequency ν_g ((a) and (b): $B = 5.46$ T, RF voltage is 0.14 V_{RMS}). Dotted, dashed, long-dashed, and solid vertical lines indicate literature values for $\frac{1}{2}\nu_{NMR}$, $\frac{2}{3}\nu_{NMR}$, ν_{NMR}, and $2\nu_{NMR}$, respectively, for each color-coded isotope. (c) Larmor frequency shift $\Delta\nu_L$ for different laser powers during RF irradiation ((c) and (d): $B = 3.98$ T, RF voltage is 0.286 V_{RMS}, at 29.113MHz for 20 seconds, depolarizing ^{75}As). (d) $\Delta\nu_L$ as a function of transient offset voltage where the RF modulation is applied. Bias voltage U_g is always reset to 0.0 V when measuring $\Delta\nu_L$.

In addition to the possibility of spurious time-varying magnetic fields inducing $\Delta m = \pm 1$ transitions, it is known that $\Delta m = \pm 1, \pm 2$ transitions can occur from interactions of the nuclear quadrupole moment with time-varying applied electric fields [24]. Though RF voltages applied across the gates of our sample result in unintentional fields which could induce both NMR and nuclear quadrupolar resonance (NQR), these effects should persist regardless of the presence of laser-injected carriers in the undoped PQW. In contrast, we find that the application of resonant RF voltage modulation in the absence of laser excitation leads to a greatly reduced $\Delta \nu_n$ ($\sim 20\%$ of $\Delta \nu_n$ at 2.5 mW of average pump power). Additional data shown in figure 4.13c show that as laser power increases and more carriers are injected into the PQW, $\Delta \nu_n$ increases, suggesting the central role of carriers trapped in the PQW in the depolarization mechanism. Therefore spurious time-varying electric and magnetic fields are ruled out as a dominant depolarizing mechanism, probably due to the low leakage and displacement currents between front and back gates. As a result we turn to interactions occurring within the PQW to explain the observed depolarization resonances. As an aside, note that $\Delta m = \pm 2$ resonances at $2\nu_{NMR}$ are unique to the NQR mechanism and can only be induced by time-varying electric rather than magnetic fields. In our experiments described in chapter 3 where an external time-varying magnetic field induces nuclear spin transitions, resonances at $2\nu_{NMR}$ are not observed.

To investigate the spatial dependence of the depolarization mechanism within the PQW, resonant RF oscillations are applied with the electron wave function centered at different positions along x'. Nuclei are initially polarized at $U_{\mathrm{pol}} =$ 0.0 V, then U_g is adjusted to an offset voltage and the electron wave function is oscillated for 20 seconds depolarizing the ^{75}As nuclei. The RF modulation is then turned off, U_g is restored to its initial value U_{pol}, and $\Delta \nu_n$ is measured.

Figure 4.13d shows RF depolarization data where the depolarization amplitude seems to correlate with the displacement of the electron wave function shown in figure 4.9.

4.5.2 The contact hyperfine interaction

There are two main interactions between carriers in the PQW and lattice nuclear spins which could lead to resonant nuclear depolarization. The first is the contact hyperfine interaction, which has already been discussed in detail in section 2.5.1. The modulation of the electron envelope function position at the NMR frequency causes an effective field $\mathbf{B}_e = \frac{A_H}{\gamma_N} \langle \mathbf{S} \rangle$, to oscillate at each nuclear site. In analogy to the induction of nuclear transitions due to a conventional magnetic field, this effective field could also excite transitions and therefore depolarize nuclear spins. Here we investigate, whether this mechanism could be responsible for the resonances observed upon sweeping the frequency ν_g of the voltage applied across the PQW sample.

In conventional NMR, a magnetic field oscillating at the resonance frequency causes nuclear spin transitions through the nuclear Zeeman term in the Hamiltonian,

$$H_N = \gamma_N \mathbf{B} \cdot \mathbf{I}. \tag{4.12}$$

Here, the co-rotating component of the resonant oscillating field B_1, which is perpendicular to a constant applied magnetic field B, leads to spin transitions, just as shown for electrons in section 3.3. Ignoring the counter-rotating field whose effect averages to zero, the total applied field is,

$$\mathbf{B}(t) = B_1 \cos(2\pi\nu_{NMR}t)\hat{x} + B_1 \sin(2\pi\nu_{NMR}t)\hat{y} + B\hat{z}, \tag{4.13}$$

where ν_{NMR} is the resonant frequency for the isotope of interest.

The hyperfine interaction looks very similar to the Hamiltonian of equation 4.12:

$$H_{hf} = A_H \mathbf{S} \cdot \mathbf{I}. \tag{4.14}$$

In order to induce nuclear spin transitions, **S** must take on an equivalent form to the co-rotating field proportional to B_1 in equation 4.13. In our experimental geometry, however, we know that the component of electron spin parallel to the applied field is decaying with a time-constant T_1 and the perpendicular component is oscillating about the field and decaying with a time-constant T_2^* (e.g. see equation 4.6). In addition, because of the modulation of the electron envelope function's position, $\langle \mathbf{S} \rangle$ at each nuclear site is also oscillating at the modulation frequency ν_g applied to the gate voltage U_g. With the static magnetic field applied along $\hat{z}$ we can roughly approximate,

$$\begin{aligned}
\langle \mathbf{S}(t) \rangle &= S_\perp e^{-t/T_2^*} \cos(2\pi\nu_g t)\left[\cos(2\pi\nu_L t)\hat{x} + \sin(2\pi\nu_L t)\hat{y}\right] \\
&\qquad + S_{||} e^{-t/T_1} \cos(2\pi\nu_g t)\hat{z} \\
&= \frac{S_\perp}{2} e^{-t/T_2^*} \left[(\cos(2\pi(\nu_L + \nu_g)t) + \cos(2\pi(\nu_L - \nu_g)t))\,\hat{x}\right. \\
&\qquad \left. + (\sin(2\pi(\nu_L + \nu_g)t) + \sin(2\pi(\nu_L - \nu_g)t))\,\hat{y}\right] \\
&\qquad + S_{||} e^{-t/T_1} \cos(2\pi\nu_g t)\hat{z}.
\end{aligned} \tag{4.15}$$

In the induction of spin transitions, the final term along $\hat{z}$ is irrelevant. Nuclear spin transitions can only be excited around $\nu_g = \nu_L \pm \nu_{NMR}$; since $\nu_L \gg \nu_{NMR}$, $\langle \mathbf{S}(t) \rangle$ cannot induce the transitions. Therefore, the depolarization resonances observed in sweeping ν_g across $2\nu_{NMR}$, ν_{NMR}, and fractional values of ν_{NMR} cannot be explained in terms of the contact hyperfine interaction. We must look to other possible mechanisms to explain the observed behavior.

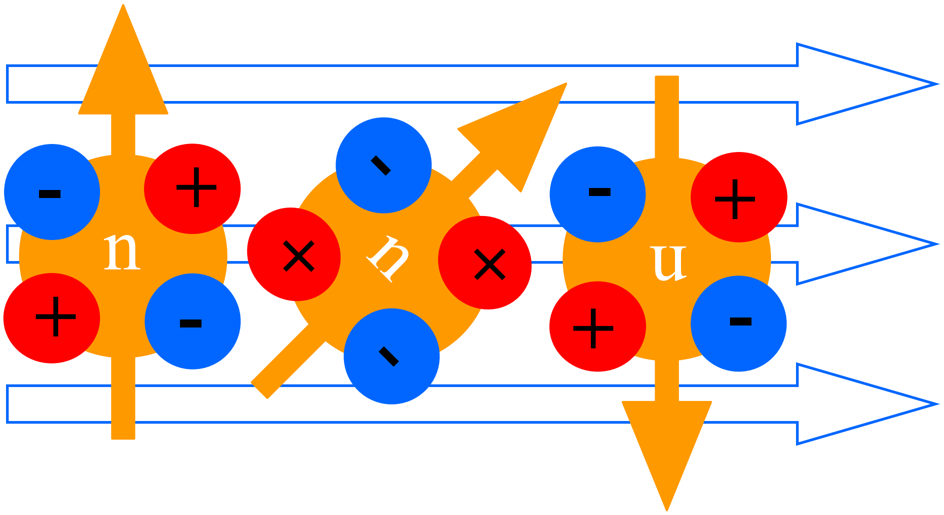

Figure 4.14: A schematic showing different orientations of the electric quadrupole moment of a nucleus in an electric field gradient, represented by the blue arrows.

4.5.3 The nuclear electric quadrupole interaction

As mentioned in section 4.5.1 time-varying electric fields can induce nuclear spin transitions through NQR. In general, the nuclear charge density is not spherically symmetric and thus has a non-zero electric quadrupolar moment. This moment causes the electrostatic energy of the nucleus to vary as a function of the orientation of the nucleus in an electric field gradient. Due to the connection between nuclear spin orientation and nuclear charge distribution, the electric quadrupolar term in the Hamiltonian can lead to spin transitions. Note from the schematic in figure 4.14 that nuclear rotations through π radians result in the same quadrupolar charge distributions; spin $\hbar m$ and spin $-\hbar m$ have degenerate quadrupolar energies.

In order to discuss NQR in more detail, we will derive the origin of this term in the nuclear spin Hamiltonian. Starting with the energy of the nuclear charge distribution $\rho(\mathbf{r})$ in a potential $U(\mathbf{r})$ we have [110],

$$E = \int \rho(\mathbf{r})U(\mathbf{r})dV. \tag{4.16}$$

Expanding the potential in a Taylor's series about the origin:

$$U(\mathbf{r}) = U(0) + \sum_{\alpha} x_\alpha \left.\frac{\partial U}{\partial x_\alpha}\right|_{r=0} + \frac{1}{2!}\sum_{\alpha,\beta} x_\alpha x_\beta \left.\frac{\partial^2 U}{\partial x_\alpha \partial x_\beta}\right|_{r=0} + \ldots, \tag{4.17}$$

where x_1, x_2, and x_3 correspond to x, y, and z, respectively. We now have,

$$E = U(0)\int \rho dV + \sum_{\alpha} U_\alpha \int x_\alpha \rho dV + \frac{1}{2!}\sum_{\alpha,\beta} U_{\alpha,\beta}\int x_\alpha x_\beta \rho dV + \ldots, \tag{4.18}$$

where we have defined $U_\alpha = \left.\frac{\partial U}{\partial x_\alpha}\right|_{r=0}$ and $U_{\alpha,\beta} = \left.\frac{\partial^2 U}{\partial x_\alpha \partial x_\beta}\right|_{r=0}$. The first term in this expansion represents the electrostatic energy of the nucleus taken as a point charge, which does not depend on nuclear orientation. By choosing the origin to coincide with the center of the nucleus, the second term, involving the electric dipole moment, vanishes. The next non-vanishing term is the electric quadrupole term. We can rewrite this term as,

$$E^{(2)} = \frac{1}{6}\sum_{\alpha,\beta}\left(U_{\alpha,\beta}Q_{\alpha,\beta} + U_{\alpha,\beta}\delta_{\alpha,\beta}\int r^2 \rho dV\right), \tag{4.19}$$

where,

$$Q_{\alpha,\beta} = \int \left(3x_\alpha x_\beta - \delta_{\alpha,\beta} r^2\right)\rho dV, \tag{4.20}$$

and $\delta_{\alpha,\beta}$ is the Kronecker delta. In the absence of electronic charge at the nucleus, U satisfies Laplace's equation $\nabla^2 U = \sum_\alpha U_{\alpha,\alpha} = 0$ and the second term in equation 4.19 vanishes. In the PQW, where the electron envelope function can be non-zero at the nuclear site, Poisson's equation applies instead: $\nabla^2 U = \sum_\alpha U_{\alpha,\alpha} = -4\pi e|\Psi(0)|^2$. Since we are only concerned with the energy dependent on the *orientation* of the nuclear charge distribution (and thus the orientation of its spin), we can ignore this term proportional to $\int r^2 \rho dV$ just as we ignored the first term in equation 4.18. We thus write the orientation-dependent energy as,

$$E^{(2)} = \frac{1}{6}\sum_{\alpha,\beta} U_{\alpha,\beta} Q_{\alpha,\beta}. \tag{4.21}$$

In order to obtain a quantum mechanical expression for the quadrupolar moment we consider the constituent particles of the nucleus. Rather than treating the nuclear charge distribution as a continuous function ρ, we take it as a sum over protons and write the quadrupolar moment as:

$$Q_{\alpha,\beta} = e \sum_{\text{protons}} \left(3x_{\alpha,k}x_{\beta,k} - \delta_{\alpha,\beta} r_k^2\right), \tag{4.22}$$

where the index k corresponds to each constituent proton. Calling upon the Wigner-Eckart theorem [110], which can be used to relate angular momentum operators to coordinate operators through common commutation relations, we find an alternate expression for the operator corresponding to the quadrupolar moment:

$$Q_{\alpha,\beta} = \frac{eQ}{\hbar^2 I(2I-I)} \left(\frac{3}{2}\left(I_\alpha I_\beta + I_\beta I_\alpha\right) - \delta_{\alpha,\beta} I^2\right), \tag{4.23}$$

where Q is the quadrupole moment of the nucleus, and I_α and I_β are operators corresponding to the angular momentum components of the nucleus. The quadrupolar contribution to the Hamiltonian is then,

$$H_Q = \frac{eQ}{6\hbar^2 I(2I-I)} \sum_{\alpha,\beta} U_{\alpha,\beta} \left(\frac{3}{2}\left(I_\alpha I_\beta + I_\beta I_\alpha\right) - \delta_{\alpha,\beta} I^2\right). \tag{4.24}$$

Choosing principle axes along which the symmetric tensor $U_{\alpha,\beta} = 0$ for $\alpha \neq \beta$ and after some algebraic manipulations, we find,

$$\begin{aligned} H_Q \quad = \quad & \frac{eQ}{4\hbar^2 I(2I-I)} \left[U_0(3I_z^2 - I^2) + U_{+1}(I^- I_z + I_z I^-)\right. \\ & \left. + U_{-1}(I^+ I_z + I_z I^+) + U_{+2}(I^-)^2 + U_{-2}(I^+)^2\right], \end{aligned} \tag{4.25}$$

where we define,

$$\begin{aligned} U_0 &= U_{zz} \\ U_{\pm 1} &= U_{zx} \pm iU_{xy} \\ U_{\pm 2} &= \frac{1}{2}(U_{xx} - U_{yy}) \pm iU_{xy}. \end{aligned} \tag{4.26}$$

4.5.4 Theoretical interpretation

The expression for the quadrupolar coupling in equation 4.25 is particularly illuminating in discussing the induction of nuclear spin transitions. The Hamiltonians for the other spin-flip processes in our system, the coupling of an external field to the nuclear spin and the contact hyperfine coupling, involve terms proportional to $BI^{\pm}$ and $S^{\pm}I^{\mp}$, respectively; these interactions can induce $\Delta m = \pm 1$ transitions at energies of $h\nu_{NMR}$. As is clear from equation 4.25, H_Q can induce $\Delta m = \pm 1$ and $\Delta m = \pm 2$ transitions at energies of $h\nu_{NMR}$ and $2h\nu_{NMR}$, respectively. Unlike NMR transitions which require the application of resonant time-varying magnetic fields, NQR transitions require resonant time-varying electric field gradients (EFGs): $U_{\alpha,\beta}$.

In our PQW system, electrons and holes moving along $\hat{x}'$ with the action of U_g produce these time-varying EFGs at the nuclear sites. In GaAs, the nuclear quadrupole moment is also sensitive to time-varying electric fields: the nuclei lie at positions lacking inversion symmetry causing electric fields to generate EFGs [31]. Calculations of the time-varying fields induced around the electron and hole charge distributions within the well indicate the presence of electric fields and EFGs on the order of 10^6 V/m, and 10^{14} V/m^2, respectively. Therefore carriers oscillating at ν_{NMR} and $2\nu_{NMR}$ in the quantum well will certainly excite nuclear spin transitions.

As mentioned in section 4.5.1 the weak fractional resonances observed at

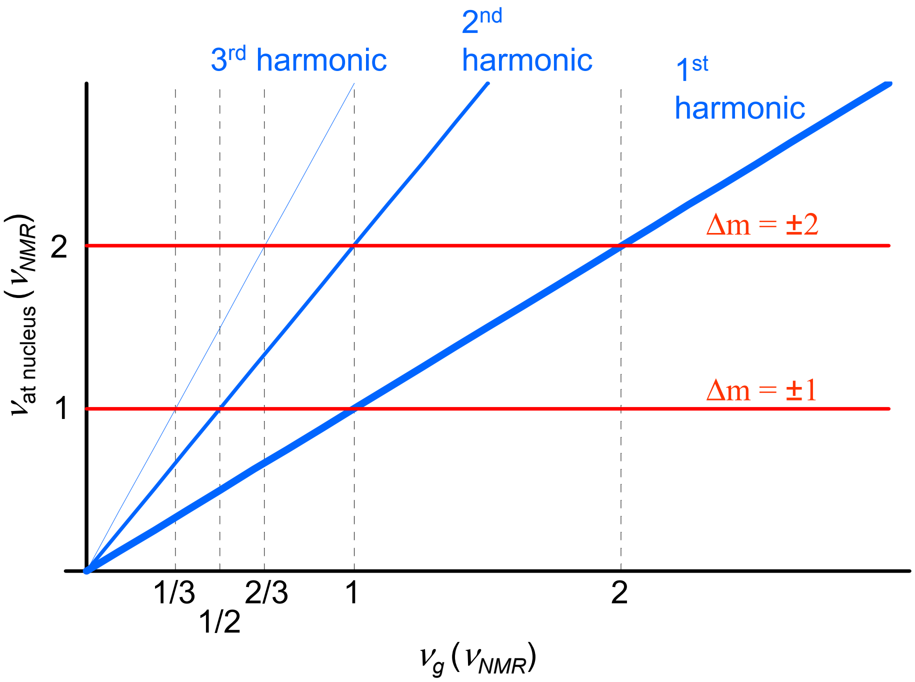

Figure 4.15: The effect of higher harmonics of ν_g on nuclei in the PQW. Here we plot the electric field modulation frequency at each nuclear site $\nu_{\text{at nucleus}}$ as a function of the drive frequency ν_g. All axes are plotted in units of the NMR resonance frequency ν_{NMR}. The first three harmonics of ν_g are shown as blue lines of decreasing thickness representing their fading amplitude. Their intersection with the red lines showing the nuclear resonance frequencies represents the fulfillment of the resonance condition. At these values of ν_g, indicated by dotted lines, nuclear spin transitions should be induced by NQR. Higher harmonics than the 3rd may also be present, but are not considered here.

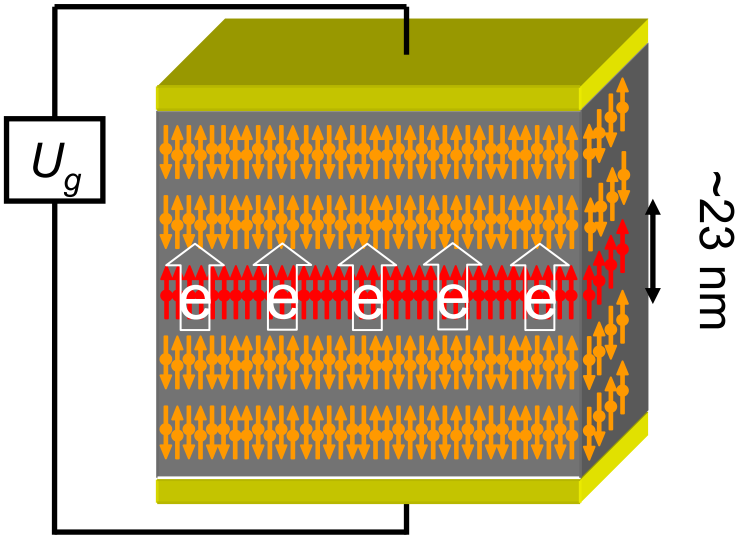

Figure 4.16: A schematic representation of the creation of a nanometer-scale nuclear spin polarization profile.

$\frac{1}{2}\nu_{NMR}$ and $\frac{2}{3}\nu_{NMR}$ are likely induced by higher harmonics of the drive frequency applied to U_g. Since the amplitude of electric fields and EFGs at the nuclear sites is in general not a linear function of the position of electrons and holes in the PQW, the time-dependence of electric fields and EFGs at the nuclear sites contains harmonics of the modulation frequency ν_g: $2\nu_g$, $3\nu_g$, etc. These higher harmonics, though weaker in amplitude than the drive frequency field induce resonant transitions at fractions of ν_{NMR} as shown in figure 4.15.

Having applied a simple model considering NQR transitions induced by moving carriers in the PQW, we have accounted for all of the resonances present in figure 4.13. It is therefore likely that this brand of local NQR is responsible for the observed resonant nuclear depolarization.

4.6 Conclusion

The measurement of a position dependent $\nu_n(x'_0, x'_{\mathrm{pol}})$ and its qualitative agreement with theoretical predictions point to our ability to to use localized spin-polarized electrons to orient nanometer-scale profiles of nuclear spin, as shown schematically in figure 4.16. Extending such techniques from systems with one-dimensional confinement (quantum wells) to systems with higher degrees of confinement (quantum wires and quantum dots) may allow for the controllable polarization of drastically fewer nuclear spins.

The experimental data show our ability to control local interactions between electrons and nuclear spin in a PQW with an externally applied gate voltage. Quasi-static bias voltages allow the patterning of nanometer-size nuclear spin distributions and RF voltages periodically displace carriers in the PQW inducing NQR. These depolarization resonances can be controlled both electrically and optically yielding a great degree of flexibility in techniques for coherent nuclear control. The ability to electronically control nuclear spin may be advantageous in quantum information processing [111] and in spintronic devices where nuclei can produce large and localized effective magnetic fields in otherwise non-magnetic materials.

Chapter 5

The *s*-*d* exchange coupling in GaMnAs quantum wells

5.1 Introduction

The introduction of magnetic dopants into semiconductors allows for the study of interactions between itinerant and localized spins. Dilute magnetic semiconductors (DMS) are semiconducting alloys in which a fraction of the cation sites are occupied by magnetic ions. The spin of electrons localized in the partially filled shells of the substitutional impurities couples to the spin of carriers in both the conduction and valence bands as discussed in section 2.5.2. As a result, electronic Zeeman splittings are enhanced leading to dramatic spin-dependent properties including giant Faraday rotation, the magnetic-field-induced metal-insulator transition, and the formation of magnetic polarons. Most importantly, however, the discovery of ferromagnetism in zinc-blende III-V and II-VI Mn-based compounds and the realization that this collective magnetic behavior is mediated by delocalized or weakly localized holes, has given a technological impetus for developing a clear picture of the carrier-shell exchange couplings.

In these systems the exchange between the *s*-like conduction band or *p*-like valence band and the *d* shell of the Mn^{2+} are known as the *s*-*d* and *p*-*d* exchange parameters, respectively (*sp*-*d* collectively). In addition to offering an ideal system in which to study the interactions between localized and delocalized spin, DMS offer the prospect of a room-temperature ferromagnetic semiconductor whose ferromagnetic state can be switched on or off by changes in carrier concentration. Such a material would have far-reaching implications on the semiconductor industry and would propel spintronics into the mainstream of computing technology.

This chapter treats the development of GaMnAs quantum wells (QWs) and the measurement of their *s*-*d* and *p*-*d* exchange couplings. Surprising results regarding the size and sign of the interaction point to deficiencies in the current theory which has successfully described experiments in II-VI DMS within a higher regime of doping. A new model may be required to describe Mn-based III-V compounds.

We first give a brief background in section 5.2 followed by an analysis in section 5.3 of the effect of *sp*-*d* exchange on semiconductor band structure. Section 5.4 follows and includes the growth of GaMnAs QWs and the analysis of the Mn-doping profile using secondary ion mass spectroscopy (SIMS). We then present time-resolved Kerr rotation (KR) measurements of the *s*-*d* exchange coupling in sections 5.5 and 5.6. Section 5.7 describes our attempts at determining the *p*-*d* coupling. Finally section 5.8 covers some possible theoretical interpretations for our experimental results.

5.2 Background

In II-VI DMS, the *s*-*d* and *p*-*d* exchange energies are readily measurable and have been characterized in detail through magneto-optical spectroscopy. These materials benefit from high Mn solubility and the electrical neutrality of Mn impurities upon incorporating into the lattice. High concentrations of Mn-doping are achievable, making the effects of *s*-*d* and *p*-*d* exchange large and easily measurable.

The situation in the III-V alloy GaMnAs is more complex. The presence of Coulomb potentials centered on the magnetic ions as well as on compensating donors introduces an additional obstacle to the interpretation of measurements. More importantly, as a consequence of the low solubility of Mn in GaAs, molecular beam epitaxy (MBE) growth is typically performed at low substrate temperatures ($\sim 250°$C) and high arsenic overpressures. This is a regime of growth in which defects, chiefly excess As and Mn interstitials, are incorporated into the epilayers at concentrations that quench sensitive optical properties, such as photoluminescence (PL) and absorption. Therefore characterization of the exchange parameters through optical techniques is problematic in these materials. Despite this constraint, several estimates of the *p*-*d* exchange constant have been published from modeling of transport [112], core-level photoemission [113], and cyclotron resonance measurements [114]. A previous study on highly dilute $Ga_{1-x}Mn_xAs$ ($x < 0.2\%$) crystals grown by the Czochralski method reports polarized magnetoreflectance data from which the total exciton spin splitting is determined to within 600 meV [115]. This measurement of the collective *sp*-*d* energy, however, includes no independent measurements of the *s*-*d* and *p*-*d* exchange constants ($N_0\alpha$ and $N_0\beta$, respectively); the reported estimation of $N_0\beta$ depends on an assumed positive value of $N_0\alpha$ based on work in

II-VI DMS.

In our work, MBE growth conditions are optimized in order to produce GaMnAs in which coherent spin dynamics can be observed optically, while at the same time incorporating enough Mn to make the effects of *s*-*d* and *p*-*d* couplings observable. Two types of QW structures are studied, GaMnAs/AlGaAs and InGaMnAs/GaAs. Both the sign and magnitude of the *s*-*d* coupling are determined for QWs of several different widths revealing the dependence of this energy on the carrier confinement. Since a limited understanding of the exchange coupling exists for GaMnAs relative to II-VI systems, the measurements presented in this chapter have been met with broad interest in the DMS community.

5.3 The effect of *s*-*d* and *p*-*d* exchange on band structure

5.3.1 Incorporation of the Mn impurity in GaAs

As discussed in section 2.3.2 and shown in figure 2.4, the band structure of zincblende semiconductors provides convenient selection rules for the excitation and probing of carrier spin dynamics. In the presence of *s*-*d* and *p*-*d* exchange, this structure changes reflecting the coupling between carriers and magnetic impurities.

A large volume of work exists in II-VI DMS in which the spin-spin coupling expressed in equation 2.44 plays a central role in the magnetic behavior. Some examples of these materials include $\mathrm{Zn}_{(1-x)}\mathrm{Mn}_x\mathrm{Se}$, $\mathrm{Cd}_{(1-x)}\mathrm{Mn}_x\mathrm{S}$, and $\mathrm{Hg}_{(1-x)}\mathrm{Mn}_x\mathrm{Te}$. Growth of II-VI DMS by MBE is well-established, including the growth of complex heterostructures [85, 116]. These semiconductors have direct-gaps and grow in the familiar zinc-blende crystal structure, giving them qualitatively identical band structures and optical selection rules as the III-V compounds discussed in this dissertation.

Here we tap into this broad understanding of the effect of *s-d* and *p-d* exchange couplings on the bands of zinc-blende semiconductors and develop a detailed picture of these effects for Mn impurities in GaAs-based materials specifically. We begin with the specific incorporation behavior of Mn in GaAs.

The most natural incorporation site for Mn impurities found in GaAs is the Ga site. Such substitutional incorporation is important in retaining the crystallinity of the the host semiconductor. Interstitial incorporation of Mn can also occur under certain crystal growth conditions [117]. Interstitial Mn centers are generally undesirable as they constitute crystalline defects and introduce defect states into the band structure. In high enough concentrations they can severely limit the material's mobility, optical quality, and magnetic properties [118]. In the growth of the GaMnAs QWs discussed here, considerable care is taken to achieve the highest $Mn_{\text{sub}}/Mn_{\text{int}}$ ratio possible, where Mn_{sub} is the concentration of substitutional Mn and Mn_{int} is the concentration of interstitial Mn.

Atomic Mn has an $[\text{Ar}].3d^5.4s^2$ ground state electron configuration. The completion of bonds to the nearest neighbor As atoms requires three electrons from each atom occupying a Ga site. Therefore, we could infer a $3d^4$ (Mn^{3+}) configuration for the substitutional Mn as found in GaP [119]. Electron paramagnetic resonance (EPR) and microwave circular dichroism experiments, however, do not support this model suggesting instead that substitutional Mn is incorporated in a $3d^4$ configuration with a tightly bound electron and a weakly bound hole [120, 121]. This neutral complex A^0 can be viewed as being in the $3d^5$ (Mn^{2+}) with a shallow hole in orbit. A^0 is observed in EPR experiments for bulk GaAs doped with Mn ($x < 0.001$), but is missing in more concentrated

Mn epilayers ($x > 0.002$) [120, 122, 123]. At higher Mn concentrations, the increased screening of the Coulomb potential due to the $3d^5$ core by the delocalized holes may make the holes ionize easily, resulting in the dissociation of A^0 centers. The ionization energy of A^0 is determined spectroscopically to be $E_{\text{vb}} + 113.0$ meV [120]. Ionized A^0 centers, A^-, are acceptors whose configuration is simply $3d^5$ and their presence in GaAs was confirmed in EPR spectra from both bulk and epilayers samples [124, 125]. Both A^0 and A^- are likely present in the $Ga_{1-x}Mn_xAs$ QWs discussed here where $x < .001$.

5.3.2 Spin of the Mn impurities

In the A^0 centers, the hole and the $3d^5$ core essentially retain their electronic structure. The core has a g-factor $g_{Mn} = 2$ and $S = 5/2$; the loosely bound hole, which is antiferromagnetically coupled to the core has $S = 3/2$. For the entire complex $g_{A^0} = 2.77$ and $J = 1$ [120]. A^0 and A^- have different angular momentum states and thus give rise to different bulk magnetizations as measured with a superconducting quantum interference device (SQUID), for instance. They also may result in different *sp*-*d* exchange couplings. The spin state of the $3d^5$ shell ($S = 5/2$), however, remains unchanged. Since the *s*-*d* interaction is a one-center potential exchange between *s* electrons in the conduction band and *d* electrons of the Mn shell, this exchange should remain unaltered by the presence of the loosely bound hole [122]. In contrast, *p*-*d* exchange is strongly modified by this hole. The presence of a loosely bound hole in A^0 opens a ferromagnetic exchange path whereas the A^- acceptor offers only antiferromagnetic channels. In the literature, such a dependence on the nature of the Mn acceptor core is offered as an explanation for the apparent sign flip of the *p*-*d* term as the Mn concentration is increased from the very dilute limit (paramagnetic) to the high doping regime (ferromagnetic). It may also explain the widely varying values of $N_0\beta$ measured in our PL experiments (section 5.7.2).

We emphasize that our exchange splitting model takes $g_{Mn} = 2$ and thus neglects any effect of the loosely bound hole on the core state g-factor since the exchange interaction between the hole and the core is expected to be small [126]. Measurements in III-V DMS support this assumption by consistently showing g_{Mn} = 2.0. As a result of these considerations, we conclude that the relative concentration of A^- and A^0 centers in our samples should have a negligible effect on both $N_0\alpha$ and g_{Mn}, allowing us to ignore this detail in our extraction of $N_0\alpha$ from the data. Measurements of $N_0\beta$, however, are complicated by the effects of this relative concentration.

The five *d* shell electrons in the $3d^5$ Mn cores arrange according to Hund's Rules: $(\uparrow\uparrow\uparrow\uparrow\uparrow)$. The total orbital angular momentum of this state is $L = 0$ and the total angular momentum is $J = L + S = 5/2$. For the samples studied in this dissertation, the concentration of Mn impurities is low enough that we are always in a regime in which Mn spins do not interact with each other, i.e. the Mn spins are paramagnetic and their average spin is a thermal average of the occupation of spin states for a single core:

$$\langle \Xi_z \rangle = \frac{\sum\limits_{S_z=-S}^{S_z=+S} \hbar S_z e^{\frac{-g_{Mn}\mu_\mathrm{B} B S_z}{k_B(T+\theta_P)}}}{\sum\limits_{S_z=-S}^{S_z=+S} e^{\frac{-g_{Mn}\mu_\mathrm{B} B S_z}{k_B(T+\theta_P)}}}, \tag{5.1}$$

where the magnetic field B points along $\hat{z}$, k_B is the Boltzmann constant, T is the temperature, θ_P is the paramagnetic Curie temperature, and the summation yields,

$$\langle \Xi_z \rangle = -\hbar \frac{5}{2} B_{5/2} \left(\frac{5 g_{Mn} \mu_\mathrm{B} B}{2 k_B (T - \theta_P)} \right), \tag{5.2}$$

where,

$$B_S(\eta) = \frac{2S+1}{2S}\coth\left(\frac{2S+1}{2S}\eta\right) - \frac{1}{2S}\coth\left(\frac{1}{2S}\eta\right), \tag{5.3}$$

is the thermodynamic Brillouin function for a spin S. The average spin $\langle \Xi_z \rangle$ appears in the *s*-*d* and *p*-*d* couplings, as discussed in section 2.5.2, and determines the form of their dependence on magnetic field and temperature.

5.3.3 GaMnAs band structure

Through the *s*-*d* and *p*-*d* couplings, Mn impurities alter the conduction and valence bands of GaMnAs with respect to the bands of pure GaAs. As derived in section 2.5.2, the Hamiltonians for conduction and valence bands are:

$$\begin{aligned} H_S^{\mathrm{cb}} &= \frac{g_e \mu_{\mathrm{B}}}{\hbar} B S_z - \frac{1}{\hbar^2} x N_0 \alpha \langle \Xi_z \rangle S_z & (5.4) \\ H_J^{\mathrm{vb}} &= \frac{g_{\mathrm{h}} \mu_{\mathrm{B}}}{3\hbar} B J_z - \frac{1}{3\hbar^2} x N_0 \beta \langle \Xi_z \rangle J_z. & (5.5) \end{aligned}$$

The effect on the bands is shown schematically in figures 5.1. Optical experiments sensitive to the band splittings discussed in later sections, including KR and PL, reveal behavior consistent with this schematic representation.

5.4 Growth of optical quality GaMnAs quantum wells

5.4.1 Motivation and background

In this section we describe the development of the capability to grow GaMnAs quantum structures by MBE in which coherent spin dynamics can be observed optically. An upcoming dissertation includes, in exhaustive detail, further discussion of this subject [127]. Initially, our growth effort focused on achieving stoichiometric GaMnAs grown at a typical low temperature of 250°C, at

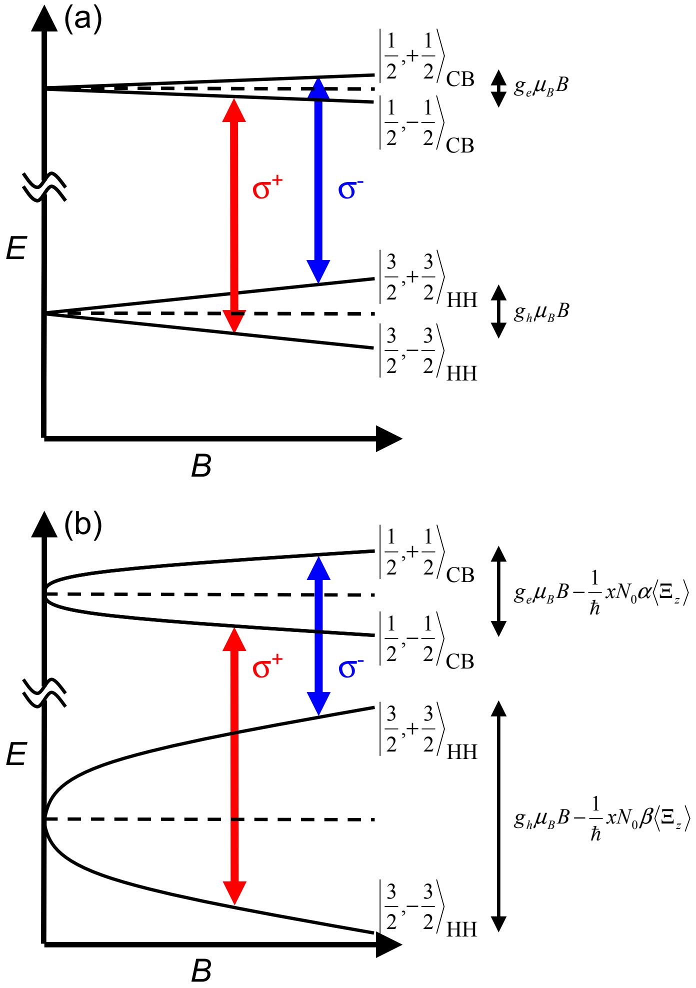

Figure 5.1: A diagram depicting the effect of Mn impurity spins on the GaAs band structure. Only the HH band is considered here since the experiments discussed in this chapter are in QWs, in which the HH band is split from both the LH band and the SO band. (a) represents the dependence of the bands on magnetic field *B* in undoped GaAs QWs, while (b) represents this dependence in Mn doped GaAs QWs.

which the use of As overpressures leads to large concentrations of excess As. Stoichiometric growth can be achieved at low substrate temperatures by digital growth techniques, such as atomic layer epitaxy (ALE) in which the As flux is shutter controlled [128], or analog growth in which the As flux is controlled by source temperature and/or valve position. The former technique has enabled digital ferromagnetic heterostructures made up of sub-monolayers of MnAs with independent control of charge carriers in the non-magnetic GaAs spacer layers, while hybrid growths using both high temperature MBE (optical layer) and low temperature ALE (magnetic layer) have been developed to enable optical quality in GaAs/AlGaAs QWs with a ferromagnetic barrier [129]. Although polarization-resolved PL from these QWs demonstrates a spin coupling between the magnetic layer and carriers in the QWs, time-resolved KR measurements are unable to resolve electron spin dynamics. In previous work using the As-valve for flux control, it was found that stoichiometric GaAs grown at 250°C could be achieved as indicated by the low charge compensation of doped carriers (1×10^{16} cm^{-3}); however, the incorporation of Mn at levels required for ferromagnetism could only be achieved by using an As overpressure. The resulting defects quenched both PL and time-resolved KR signals [130]. In the following sections we investigate MBE grown GaMnAs/AlGaAs QWs with low Mn-doping levels ($x < 0.1\%$). At these Mn concentrations the substrate temperature can be increased to 400°C while allowing substitutional incorporation of Mn. In contrast to low temperature stoichiometric growth, at the increased growth temperatures used here, an As overpressure does not result in excess As incorporation preserving the optical properties of the crystal and enabling the observation of PL and time-resolved electron spin dynamics in GaMnAs QWs.

5.4.2 MBE Growth Details

Samples are grown on GaAs substrates in a Varian GEN-II MBE system manufactured by Veeco Instruments, Inc. In corroboration with the recent findings of Wagenhuber et al. [131], we find that the inclusion of Mn growth capability in the MBE system does not preclude the growth of high mobility samples. We measure low-temperature mobilities greater than 1.7×10^6 cm^{2}V^{-1}s^{-1} in typical modulation Si-doped AlGaAs/GaAs two-dimensional electron gas structures grown in our chamber at 630°C . For Mn-doped QWs, however, we use a lower growth temperature to enable the substitutional incorporation of Mn. Samples are grown at 400°C as monitored and controlled during growth by absorption band edge spectroscopy (ABES) using white-light transmission spectroscopy through the substrate, providing a typical substrate temperature stability of ±2°C. The growth rate of GaAs is ~ 0.7 ML s^{-1} and of Al$_{0.4}$Ga$_{0.6}$As is $\sim$ 1 ML s^{-1} as calibrated by reflection high energy electron diffraction (RHEED) intensity oscillations of the specular spot. The As$_2$:Ga beam flux ratio for all samples is 19:1 as measured by the beam equivalent pressure of each species using a bare ion gauge in the substrate position. Mn cell temperatures for doping were extrapolated from growth rate calibrations of MnAs measured at much higher growth rates using RHEED oscillations; the actual, measured, value of Mn concentrations is discussed in detail in section 5.4.3.

The QWs, shown schematically in figure 5.2a, are grown on (001) semi-insulating GaAs wafers using the following procedure. The substrate is heated to 635°C under an As overpressure for oxide desorption and then cooled to 585°C . With the substrate rotating at 10 RPM throughout the growth, a 300-nm GaAs buffer layer is first grown using 5-s growth interrupts every 15 nm for smoothing, which results in a streaky 2×4 surface reconstruction pattern as observed by RHEED. A 500-nm layer of $Al_{0.4}Ga_{0.6}As$ is grown followed by a 20-period digital superlattice of 1-nm AlAs and 1.5-nm GaAs. The sample is then cooled to the growth temperature (usually 400°C, but also 350°C and 325°C) during which the RHEED pattern changes to a 4×4 reconstruction. The first QW barrier consists of a 50-nm $Al_{0.4}Ga_{0.6}As$ layer; during its growth the 4×4 pattern becomes faint and changes to 1×1. Before the QW layer, a 10-s growth interrupt is performed to smooth the interface; during this wait the RHEED partially recovers a 4×4 reconstruction pattern. The GaMnAs QW layer deposition causes the 4×4 to again become faint leading to 1×1, but during the next 10-s wait on the top side of the QW, a 4×4 partially recovers. Increased Mn-doping leads to surface roughening as evidenced by the development of a spotty RHEED pattern during and after the QW growth. In contrast, lower-doped samples, which emit PL and show time-resolved KR signal, display a streaky two-dimensional RHEED pattern throughout their growth. The QW structure is completed on top by a barrier of 100-nm $Al_{0.4}Ga_{0.6}As$ and a 7.5-nm GaAs cap after which a streaky 4×4 reconstruction pattern is observed.

5.4.3 Mn doping profiles

The Mn concentration profile for each sample is measured using SIMS [132, 133, 134] and is plotted in figure 5.2b for a set of four 7.5-nm QWs grown on the same day at 400°C with different Mn cell temperatures. The primary beam in the SIMS measurement consists of Cs^+ ions with an impact energy of 2 keV providing a depth resolution of 3.25 nm e^{-1}, as calibrated using the atomically sharp AlGaAs/GaAs interface as a reference. The secondary ion used to measure the Mn concentration is $CsMn^+$, which is resilient to changes in ionization yield at the AlGaAs/GaAs interface. The calibration of the Mn concentration

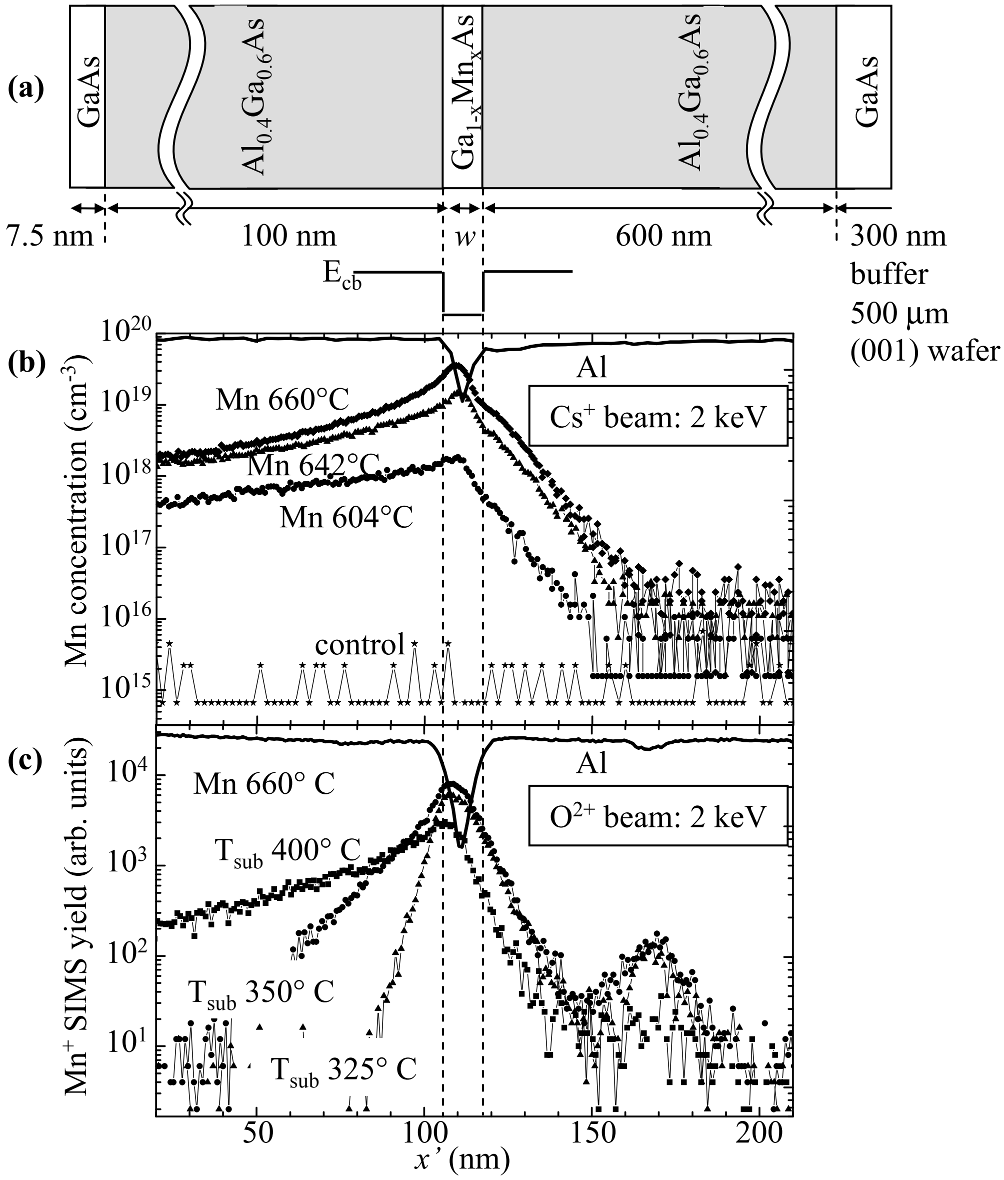

Figure 5.2: (a) Schematic of the sample structure and conduction band energy profile along the growth axis $\hat{x}'$. (b) The Mn concentration profile measured by SIMS is plotted for four 7.5-nm QWs with varying Mn effusion cell temperatures as marked in the figure, and (c) for QWs with the same Mn cell temperatures but varying substrate temperatures (marked in the figure). The uncalibrated Al SIMS signals (plotted as black lines) serve as markers for the QW region.

signal in our SIMS measurement was performed using Mn-ion implanted GaAs as a reference, while the change in the ionization yield of CsMn^+ between AlGaAs and GaAs was checked using Mn-ion implanted AlGaAs reference samples. The x'-axis calibration for the SIMS scans was performed using the Al signal as a reference for the QW region as well as the lower edge of the barrier, both layers grown at low temperature. The depth of the crater could not be used to calibrate the x'-axis since it was found that the low temperature grown layers sputter faster than the high temperature grown buffer layers.

The Mn concentration peaks near the center of the QW region, as expected; however, the surface side of the QW shows a large residual concentration of Mn which incorporates into the structure even after the Mn shutter has closed. Such behavior is not unexpected, even if the Mn-doping concentration is below the equilibrium solubility limit, since the growing surface is not at equilibrium. This behavior has previously been reported for similar structures in which Mn δ-doped GaAs grown at 400°C showed large surface segregation [135]. We note that our results do not agree quantitatively with those of Nazmul et al., and we attribute this discrepancy to the different methods used for substrate temperature measurement in these two studies, noting that Mn incorporation is highly sensitive to this growth parameter. In our MBE system, the substrate temperature is measured directly by ABES, while an indirect temperature reading from a radiatively coupled thermocouple is used by Nazmul et al. Such measurements can be more than 50°C from the actual substrate temperature.

Mn surface segregation during growth may lead to Mn clustering in our samples and allow second phase magnetic precipitates, such as MnAs, to form. We note however that though these impurities are likely present in our samples, the Schottky barrier around such precipitates prevents their detection in the electrical or optical signal of free carriers in the QWs. Hole conductivity and carrier densities measured in these samples indicate, in comparison with the SIMS data, that most of the Mn impurities present in the sample are substitutionally incorporated [45]. Thus Mn surface segregation and related growth defects have a negligible effect on our optical studies of the exchange splittings.

Below the QW, the Mn concentration decreases toward the substrate reaching a minimum point ~ 100 nm below the QW. The Mn profile is broader than the Al depth profile indicating either a SIMS measurement artifact, such as poor depth resolution or preferential Mn sputtering, i.e. knock-on effects [136, 137], or that Mn diffuses into the barrier. The lack of any dependence on substrate temperature or doping level for the Mn profile below the QW, as shown in figure 5.2, eliminates the latter possibility. The Mn knock-on effect, however, has been reported in similar structure grown by Nazmul et al. To test for this effect, we run SIMS scans on the same sample (C) at two different beam energies, 2 keV and 8 keV, shown in figure 5.3. Indeed, the Mn profile on the substrate side of the QW changes with beam energy: we observe a decay of 17 nm e^{-1} for 8 keV and 10nm e^{-1} at 2 keV. The Mn tail on the surface-side of the QW, where Mn incorporates as it floats along the surface, does not show any significant dependence on the beam energy. As a further test, we use an atomic force microscope (AFM) to measure the roughness of the SIMS craters created by the 2 keV and 8 keV beams to be 0.32 nm RMS and 0.30 nm RMS, respectively, while the roughness of the starting surface is 0.14 nm RMS. Since the crater roughness does not depend on beam energy, we conclude that the sample is uniformly sputtered at these two beam energies. Therefore, the observed difference in decay of the Mn profile is a result of the knock-on effect, which is an artifact of the SIMS measurement. The Mn profiles on the substrate side of the QW are therefore sharper than the SIMS data show.

After the lower Mn tail, ~ 100 nm below the QW, the Mn profile becomes

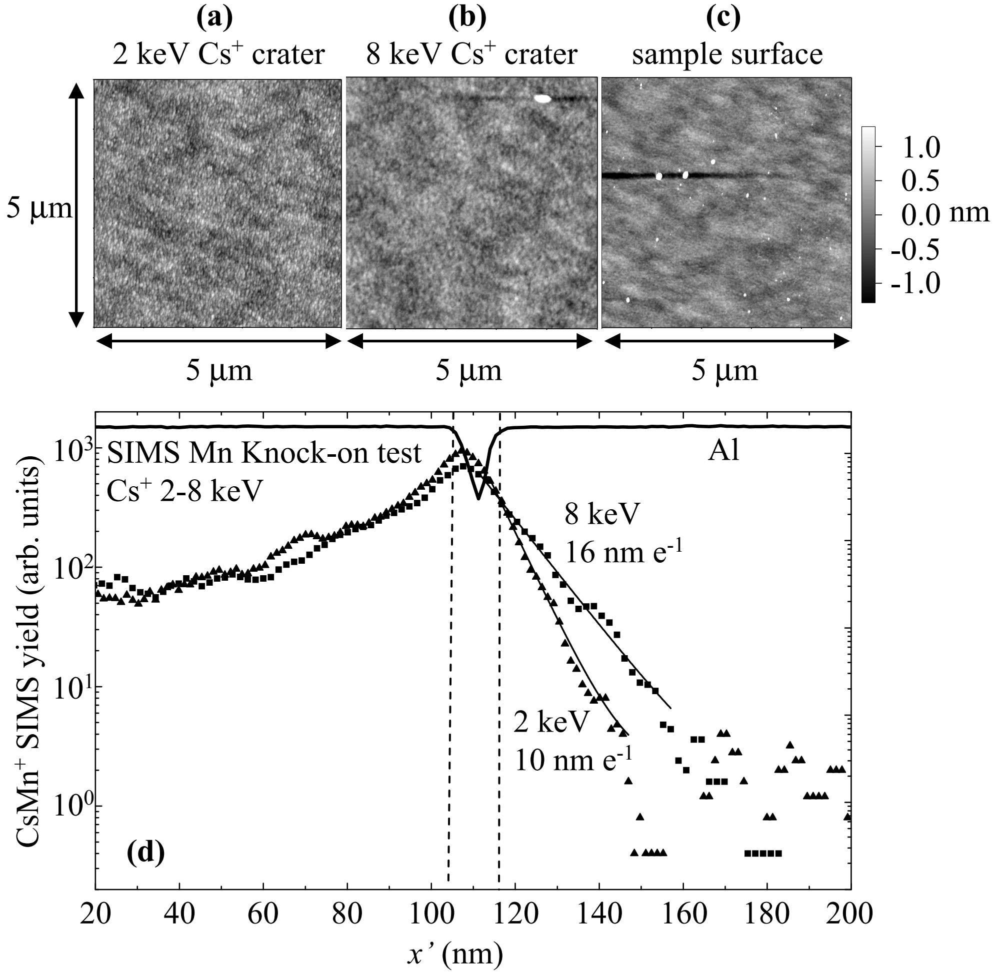

Figure 5.3: Beam energy test for preferential Mn sputtering (knock-on). (a) and (b) show AFM images of the sample morphology in the center of SIMS craters formed by a 2 keV and 8 keV Cs^+ beam, respectively. (c) shows an AFM image of the bare sample surface. (d) The Mn profiles in sample C measured at two different beam energies as labeled. Solid lines are exponential fits to the Mn profile tail below the QW.

constant for all samples. Though the value of this background Mn concentration is near the detection limit of SIMS, it is seen to scale with Mn cell temperature as seen in figure 5.2b. This behavior suggests that Mn flux escapes from the hot Mn cell and incorporates into the substrate even with the shutter closed. The Mn background for the control sample, grown with a cold Mn cell, is well below the SIMS detection limit.

5.4.4 Dependence of incorporation on substrate temperature

In figure 5.2c, the Mn SIMS profiles are plotted for three 7.5-nm wide QWs grown with the same Mn cell temperature (i.e. the same Mn beam flux), but different substrate temperatures. These SIMS scans were performed using an O^{2+} 2 keV beam. Note that the Mn profiles measured with the O^{2+} beam show a large sensitivity to AlGaAs/GaAs interfaces, probably due to oxygen impurities incorporated during growth in the AlGaAs layers, thus the vertical axis of these scans is uncalibrated (arbitrary units). The data, however, are qualitatively meaningful in the interface free regions, e.g. in the AlGaAs barrier above the QW.

As the substrate temperature is decreased, the Mn concentration profiles become dramatically sharper, the surface tail is eliminated, and the peaks become taller, indicating that, as expected, the Mn incorporation is energetically more favorable at lower temperature. Sharp Mn profiles, particularly on the surface side of the QW, are desirable for the engineering of more complex magnetic quantum structures in which precise spatial control of the magnetic doping is required. Optical signals quench, however, at the relatively high growth temperatures of 325°C and 350°C [138], due to increased defect densities even in the non-magnetic control samples. Preliminary work shows that optical quality non-magnetic and magnetically doped InGaAs/GaAs QWs can be grown at 350°C, suggesting that the loss in signal for the GaAs/AlGaAs QWs is related to Al, well-known for its impurity gettering of oxygen defects during MBE growth [139, 140]. Also noteworthy is a secondary peak in the Mn concentration 50 nm below the QW which occurs only in the 325°C and 350°C grown samples. This Mn peak corresponds to the interface between QW barrier material grown at high temperature and at low temperature, a point at which a long growth pause takes place. The peak indicates that the closed-shutter Mn flux, which scales with Mn cell temperature as discussed previously, may accumulate on the surface during the substrate cooling period before low temperature growth begins, and may subsequently incorporate once growth resumes, effectively delta doping the sample at this point. In the 400°C grown sample, grown on the same day and with the same Mn cell temperature, this effective delta doping does not occur, exemplifying the strong temperature dependence of Mn solubility in GaAs. Another possible explanation for this peak is that background impurities, such as oxygen, may incorporate during the long growth pause leading to a change in the SIMS ionization yield. This explanation is supported by the fact that the Al signal also shows a change in intensity in this same region even though the Al concentration should be constant.

5.4.5 The effective Mn concentration

Since we probe carrier spin splittings at the band edges of the QWs, the presence of Mn in the AlGaAs barriers does not directly interfere with our measurements. The leakage of Mn into the barriers, however, makes the determination of the exchange interaction in the QWs non-trivial. Recall from equation 2.47 that the *s*-*d* exchange goes as the square of the electron envelope function. If the concentration x is not homogeneous, but rather has a position dependence as we saw in section 5.4.3, then we cannot pull it out of the integration as we did in equation 2.48. The same argument applies to the *p*-*d* exchange. Therefore, we rewrite the Hamiltonians allowing for a Mn concentration profile along $\hat{x}'$:

$$\begin{aligned} H_S^{\mathrm{cb}} &= \frac{g_e \mu_{\mathrm{B}}}{\hbar} B S_z - \frac{1}{\hbar^2} \bar{x}_e N_0 \alpha \left\langle \Xi_z \right\rangle S_z & (5.6) \\ H_J^{\mathrm{vb}} &= \frac{g_h \mu_{\mathrm{B}}}{3\hbar} B J_z - \frac{1}{3\hbar^2} \bar{x}_h N_0 \beta \left\langle \Xi_z \right\rangle J_z, & (5.7) \end{aligned}$$

where,

$$\begin{aligned} \bar{x}_e &= \int x(x') \left| \Psi_e(x') \right|^2 dx' & (5.8) \\ \bar{x}_h &= \int x(x') \left| \Psi_h(x') \right|^2 dx', & (5.9) \end{aligned}$$

and $x(x')$ is the Mn fraction profile corresponding to the Mn concentration profile $Mn(x')$ measured using the SIMS technique and shown in figure 5.2. $\Psi_e(x')$ and $\Psi_h(x')$ are the ground state envelope functions in the QW for the conduction and valence band, respectively. We calculate these functions using a one-dimensional Poisson-Schroedinger solver [141] and calculate $\bar{x}_e$ and $\bar{x}_h$ numerically. These values are used in section 5.6 to extract $N_0\alpha$ and in section 5.7 in attempts to extract $N_0\beta$ from time-resolved KR and polarized PL measurements [44]. In practice, since calculations for our QWs show that $\bar{x}_h \simeq \bar{x}_e$ and because the extraction of exchange parameters proves more fruitful for the conduction band, we simply use $\bar{x}_e$ throughout. We then drop the subscript and set $\bar{x} = \bar{x}_e$ (note that $\bar{M}n$ is the average concentration corresponding to $\bar{x}$).

As discussed previously, the decay of the Mn profiles on the substrate side of the QW is due to the knock-on effect, which is an artifact of the SIMS measurement. Therefore, the calculation of $\bar{x}$ as discussed above contains this error. We estimate the uncertainty of $\bar{x}$ by calculating the effective concentration assuming that the Mn profile on the substrate side of the QW is either exactly as

Table 5.1: Temperature of the substrate during growth (T_{sub}), width of the QW (w), effective Mn concentration ($\bar{Mn}$), and effective Mn fraction $\bar{x}$ for four sets of Mn-doped GaAs/Al$_{0.4}$Ga$_{0.6}$As QWs with different w. Control samples, with no Mn-doping, are not shown here, though they are grown for each set of QW width w under identical conditions.

Sample	T_{sub} (°C)	w (nm)	$\bar{Mn}$ (cm^{-3})	$\bar{x}$ (%)
A	400	7.5	1.44×10^{18}	0.0065
B	400	7.5	1.19×10^{19}	0.0537
C	400	7.5	2.80×10^{19}	0.1266
D	400	3	5.50×10^{17}	0.0025
E	400	3	2.60×10^{18}	0.0117
F	400	3	6.06×10^{18}	0.0274
G	400	10	2.97×10^{18}	0.0134
H	400	10	6.87×10^{18}	0.0310
I	400	10	1.78×10^{19}	0.0804
J	400	10	2.82×10^{19}	0.1274
K	400	5	9.65×10^{17}	0.0044
L	400	5	2.43×10^{18}	0.0110
M	400	5	7.03×10^{18}	0.0318
N	400	5	1.27×10^{19}	0.0574

given by the SIMS measurement or is atomically sharp. Thus two values of $\bar{x}$ are calculated for each sample from which we calculate an error in $\bar{x}$. These errors are generally $< 3\%$ of $\bar{x}$, except for the QW set with $w = 3$ nm in which the error reaches 15%. The $\bar{x}$ errors lead to variations in our calculation of the *s-d* exchange parameter, which are included in the error bars of these parameters (see section 5.6).

5.4.6 Substitutional vs. interstitial Mn incorporation

An estimate of the fraction of Mn which is substitutionally incorporated can be made by assuming that each substitutional Mn donates one free hole and each interstitial Mn compensates two holes [142]. This calculation has recently been used in ferromagnetic $\mathrm{Ga}_{x-1}\mathrm{Mn}_x\mathrm{As}$ ($x \sim 1\%$) to estimate the concentrations Mn_{sub} and Mn_{int} with respect to the crystal structure [143]. Measurements of carrier concentration carried out at $T = 300$ K on samples prepared in the Van der Pauw geometry allow us to estimate that the Mn incorporation in all of our samples is more than 70% substitutional. Real values of of this fraction are expected to be larger since our simplistic treatment ignores surface depletion and the incomplete thermal activation of impurity bound holes at $T = 300$ K. For increased Mn-doping, our estimate of the fraction of substitutional Mn decreases, indicating that incorporation of growth defects, interstitial Mn or Mn containing second phases such as MnAs, is becoming significant. Precipitates remove Mn from the lattice leading to a reduction in hole concentration relative to the purely substitutional case. Other forms of hole compensation such as interstitial-substitutional pairs [117] and dimers of two nearest neighbor substitutional Mn [144] are unlikely to be present in our samples due to the low doping concentrations.

5.5 Conduction electron spin dynamics

5.5.1 Time-resolved Kerr rotation measurements

Electron spin dynamics are measured by time-resolved KR with the optical axis $\hat{x}$ perpendicular to the applied magnetic field $\mathbf{B} = B\hat{z}$ (Voigt geometry) and parallel to the growth direction $\hat{x}'$; once again we adopt the coordinate system defined in figure 3.2b with $\theta = 0$. The measurement, which monitors small rotations in the linear polarization of laser light reflected off of the sample, is sensitive to the spin polarization of electrons in the conduction band of the QW [145]. A mode-locked Ti:Sapphire laser with a 76-MHz repetition rate and 250-fs pulse width tuned to a laser energy E_L near the QW absorption energy is split into a pump (probe) beam with an average power of 2 mW (0.1 mW). The helicity of the pump beam polarization is modulated at 40 kHz by a photo-elastic modulator, while the intensity of the linearly polarized probe beam is modulated by an optical chopper at 1 kHz for lock-in detection. Both beams are focused to an overlapping 50-μm diameter spot on the sample which is mounted within a magneto-optical cryostat. The time delay Δt between pump and probe pulses is controlled using a mechanical delay line. The pump injects electron spins polarized perpendicular to $\mathbf{B}$ into the conduction band of the QW. The change in the probe polarization angle, $\theta_K(\Delta t)$ is proportional to the average electron spin polarization in the QW and is well fit to a single decaying cosine, $\theta_K(\Delta t) = \theta_\perp e^{-\Delta t/T_2^*} \cos(2\pi \nu_L \Delta t + \phi)$, where $\theta_\perp$ is proportional to the total spin injected, T_2^* is the inhomogeneous transverse spin lifetime, ν_L is the electron spin precession (Larmor) frequency, and ϕ is a phase offset. No evidence of Mn^{2+} spin precession, which occurs in II-VI magnetically doped QWs [145], has been observed in the samples studied here. The order of magnitude smaller $\bar{x}$ in our III-V QWs compared to the II-VI QWs puts any Mn^{2+} spin precession signal below the experimental detection limit.

Figure 5.4a shows typical time-resolved KR data measured at $B = 8$ T for a Mn-doped QW ($w = 7.5$ nm and $\bar{x} \sim 0.05\%$) together with a fit to $\theta_K(\Delta t)$, as described above, demonstrating electron spin coherence in the GaMnAs system. KR data showing electron spin precession was observed to quench in all samples for $\bar{x} > 0.13\%$.

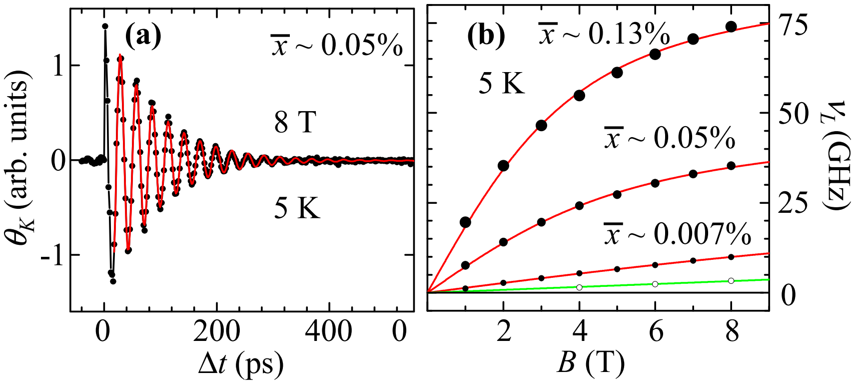

Figure 5.4: Time-resolved electron spin dynamics in $w = 7.5$ nm GaMnAs QWs. (a) An example of KR data (points) together with fit (line). (b) ν_L as a function of B for different $\bar{x}$ values (solid points); larger points indicate increasing $\bar{x}$. Open data points are for the $\bar{x} = 0$ sample. Red lines in (b) are fits to equation 5.12.

5.5.2 The transverse electron spin lifetime

The transverse electron spin lifetime (T_2^*) is plotted in figure 5.5 as a function of the percentage of Mn in four QW sample sets. In all samples measured, we observe an initial increase in T_2^* in the samples with the lowest Mn-doping as compared to the undoped control samples. This increase is consistent with the D'Yakonov-Perel (DP) spin relaxation mechanism since an increasing impurity concentration makes the process of motional narrowing more efficient by providing additional momentum scatters [146]. After reaching a maximum at very low Mn-doping ($\bar{x} \sim 0.01\%$), T_2^* then drops off as a function of $\bar{x}$ as shown in figure 5.5. This behavior suggests that for $\bar{x} > 0.01\%$, the DP mechanism is no longer dominant. In this regime either the Elliot-Yafet (EY) or the Bir-Aronov-Pikus (BAP) relaxation mechanisms may limit conduction electron spin lifetimes, since both should increase in strength with increasing $\bar{x}$ [25]. EY relaxation, due to the spin-orbit interaction, grows stronger with larger impurity

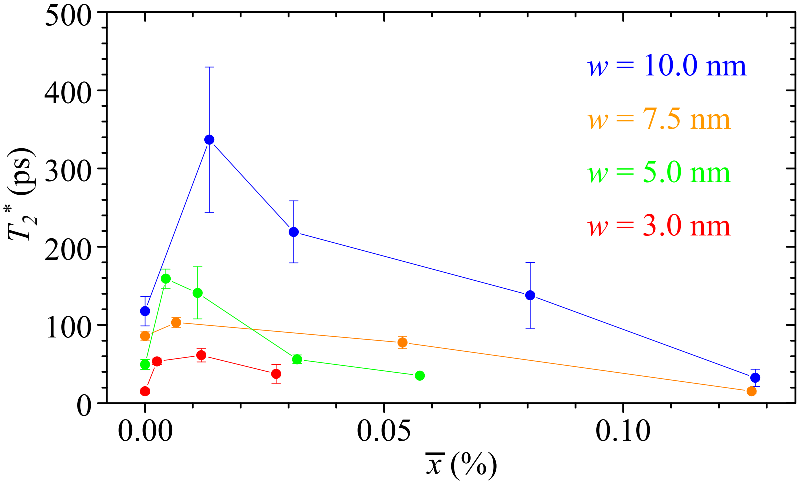

Figure 5.5: The transverse electron spin lifetime (T_2^*) at $T = 5$ K versus the percentage of Mn for four quantum well sample sets of varies width. The plotted values of T_2^* are the mean values from 0 to 8 T and the error bars represent the standard deviations.

concentrations while, the BAP process, based on the electron-hole exchange interaction, increases with increasing hole doping.

In this discussion we have so far ignored the effects of the *s*-*d* exchange interaction on the electron spin relaxation process. In II-VI DMS, the presence of magnetic impurities leads to large relaxation rates limiting the conduction electron spin lifetime [145]. Magnetic impurity doping in these materials results in relaxation through spin-flip scattering arising from the *s*-*d* exchange interaction. While the samples discussed in this report have *s*-*d* exchange energies which are several orders of magnitude smaller than in typical II-VI DMS, the effect of magnetic interactions on T_2^* cannot be totally ruled out. Several experiments can be carried out in order to examine the role of exchange interactions in the decoherence of electron spin including a finer dependence of T_2^* on $\bar{x}$ and on the sample temperature. A detailed study of changes in T_2^* as a function of QW width also may discern between the DP and the exchange scattering mechanism [147]. Such detailed studies will be the subject of future work. Preliminary results suggest that *s*-*d* exchange does not significantly contribute to spin decoherence in the conduction band [138]. Finally, we note that a qualitatively similar dependence of T_2^* on $\bar{x}$ as shown in figure 5.5 has recently been observed in InGaMnAs/GaAs QWs [138].

5.5.3 The Larmor precession frequency

ν_L is proportional to the total conduction band spin splitting between spin-up and spin-down electrons ($\Delta E = E\uparrow - E\downarrow$) and can be expressed in terms of the Zeeman splitting (ΔE_g), and the $s-d$ exchange splitting (ΔE_{s-d}):

$$h\nu_L = \Delta E = \Delta E_g + \Delta E_{s-d} = g_e \mu_B B - \frac{1}{\hbar}\bar{x} N_0 \alpha \langle \Xi_z \rangle. \tag{5.10}$$

Here h is Planck's constant, g_e is the in-plane electron g-factor, μ_B is the Bohr magneton, and $\langle \Xi_z \rangle$ is the component of Mn^{2+} spin along B where,

$$\langle \Xi_z \rangle = -\hbar \frac{5}{2} B_{5/2} \left(\frac{5 g_{Mn} \mu_B B}{2 k_B (T - \theta_P)} \right), \tag{5.11}$$

and where where $B_{5/2}$ is the spin-5/2 Brillouin function, g_{Mn} is the g-factor for Mn^{2+}, k_B is Boltzmann's constant, and θ_P is the paramagnetic Curie temperature. Note that since the g-factor for Mn^{2+} ($g_{Mn} = 2$) is positive, for $B > 0$, then $\langle \Xi_z \rangle < 0$. We emphasize that a measurement of ν_L alone, because of phase ambiguity, does not determine the sign of ΔE.

In figure 5.4b, ν_L is plotted as a function of B for a set of four samples with $w = 7.5$ nm and varying $\bar{x}$. The non-magnetic ($\bar{x} = 0$) sample shows a linear field dependence of ν_L, from which we extract values of g_e as described in equation 5.10. As the Mn doping concentration is increased, ν_L increases and its B dependence becomes non-linear. Further, this field dependence shows the same Brillouin function behavior that is expected for the magnetization of paramagnetic GaMnAs, equation 5.11. The dependence of ν_L on B and T for the sample with $w = 7.5$ nm and $\bar{x} \sim 0.007\%$ is plotted in figure 5.6a and b together with values for the control sample, $\bar{x} = 0$ and $w = 7.5$ nm. For the magnetic sample, as T is increased, ν_L decreases asymptotically toward the control sample value $g_e\mu_B B/h$ without crossing zero (figure 5.6a). Thus, it follows from equation 5.10 and from the sign of $\langle \Xi_z \rangle$ that for $w = 7.5$ nm, $N_0\alpha$ has the same sign as g_e. For $w = 7.5$ nm, $g_e < 0$ [63], and thus $N_0\alpha < 0$. This conclusion is also supported by the QW width dependence discussed below.

Using g_e extracted from the $\bar{x} = 0$ sample (green line) and equation 5.10 we fit ν_L data as a function of B and T to,

$$\nu_L = \frac{g_e\mu_B B}{h} + \frac{5A}{2h} B_{5/2}\left(\frac{5\mu_B B}{k_B(T-\theta_P)}\right), \tag{5.12}$$

which has only two fit parameters, A and θ_P. Comparing equations 5.12 to 5.10, it is clear that $A = \bar{x}N_0\alpha$. The data in figure 5.4b and figure 5.6 are fit to equation 5.12, with fits shown as red lines. A large negative θ_P (-24 K) is extracted from the fits for the sample with the lowest Mn doping (figure 5.6), which may be explained by an increased spin temperature of Mn^{2+} due to photoexcitation. This effect has been reported in II-VI DMS for low magnetic doping levels [148]. Also supporting this hypothesis, we find smaller values of $|\theta_P|$ (< 7 K) in samples with larger $\bar{x}$.

$N_0\alpha$ is examined in detail for QWs of varying w. For this analysis, we examine four sets of samples with various $\bar{x}$ (including $\bar{x} = 0$) for $w = 3, 5, 7.5$ and 10 nm. Note that each sample set of constant w was grown on the same day, which we have observed to reduce QW thickness variations between samples within each set from $\sim 3\%$ to $< 1\%$. Variations in QW thickness can affect the electron g-factor and therefore result in errors in the determination of $\bar{x}N_0\alpha$.

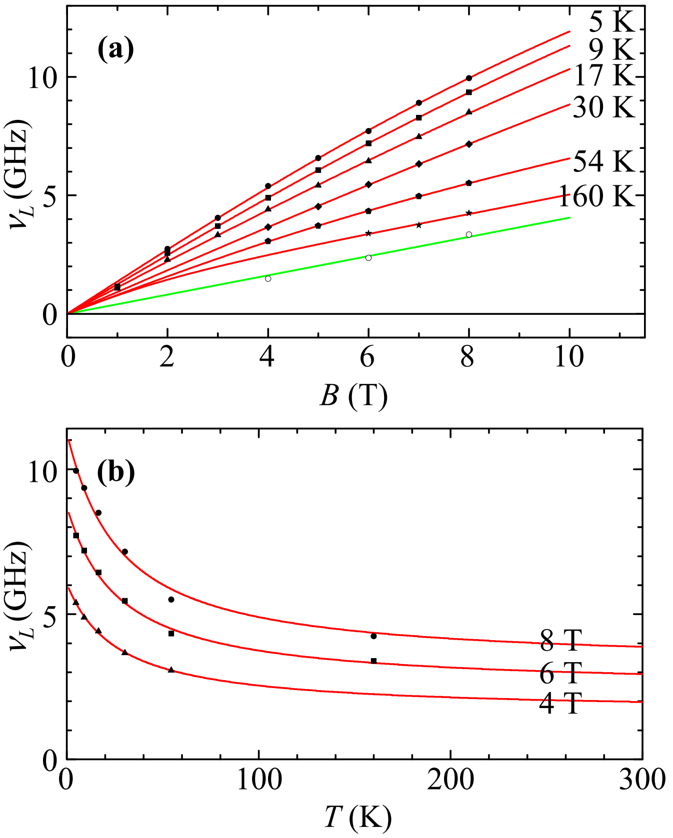

Figure 5.6: Temperature dependence of ν_L for 7.5-nm quantum wells. (a) The effect of increasing T on the B dependence of ν_L for the sample with $\bar{x} \sim 0.007\%$ (solid points) and for the $\bar{x} = 0$ sample (open points). (b) T dependence of ν_L at constant B for the $\bar{x} \sim 0.007\%$ sample. Red lines in (a) and (b) are fits to equation 5.12.

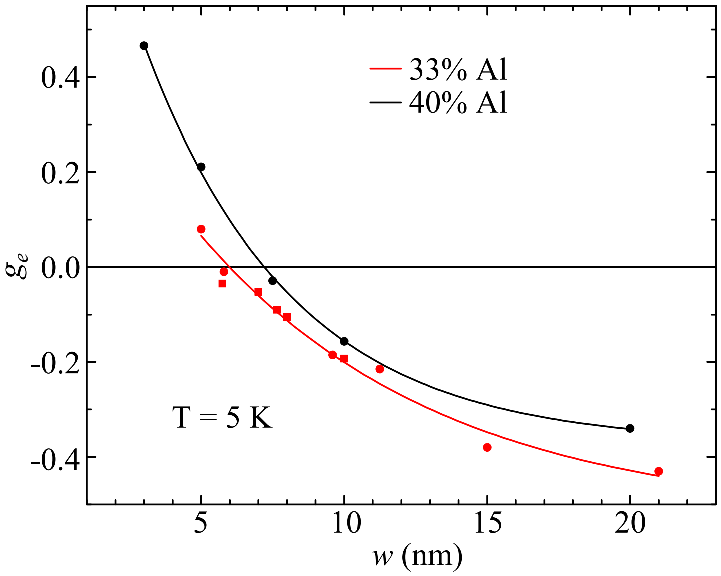

Figure 5.7: g_e as a function of QW width w. Black points are from control ($\bar{x} = 0$) samples of this study, red circles and squares are from Snelling et al. and Poggio et al., respectively [47, 63]. Lines guide the eye.

By growing samples on the same day, the error in the determination of $\bar{x}N_0\alpha$ is reduced from 10% to less than 3% as compared with samples grown on different days. In figure 5.7, g_e in the non-magnetic ($\bar{x} = 0$) QWs is plotted as a function of w together with data from two other publications [47, 63]. Our data track the thickness dependence of the QW g-factor as previously reported with a slight positive shift in g_e. The larger Al concentration (40%) in the QW barriers used in our samples versus the concentration (33%) used in the other two references [47, 63] accounts for this discrepancy [106]. Knowing the absolute sign of g_e for QWs of any width, we determine the sign of $N_0\alpha$ for each w in the manner described previously. With a calibrated sign, $\Delta E = h\nu_L$ is plotted in figure 5.8 as a function of B for all four QW sample sets with varying w. As shown in figure 5.8, for any given w, ΔE decreases as $\bar{x}$ increases.

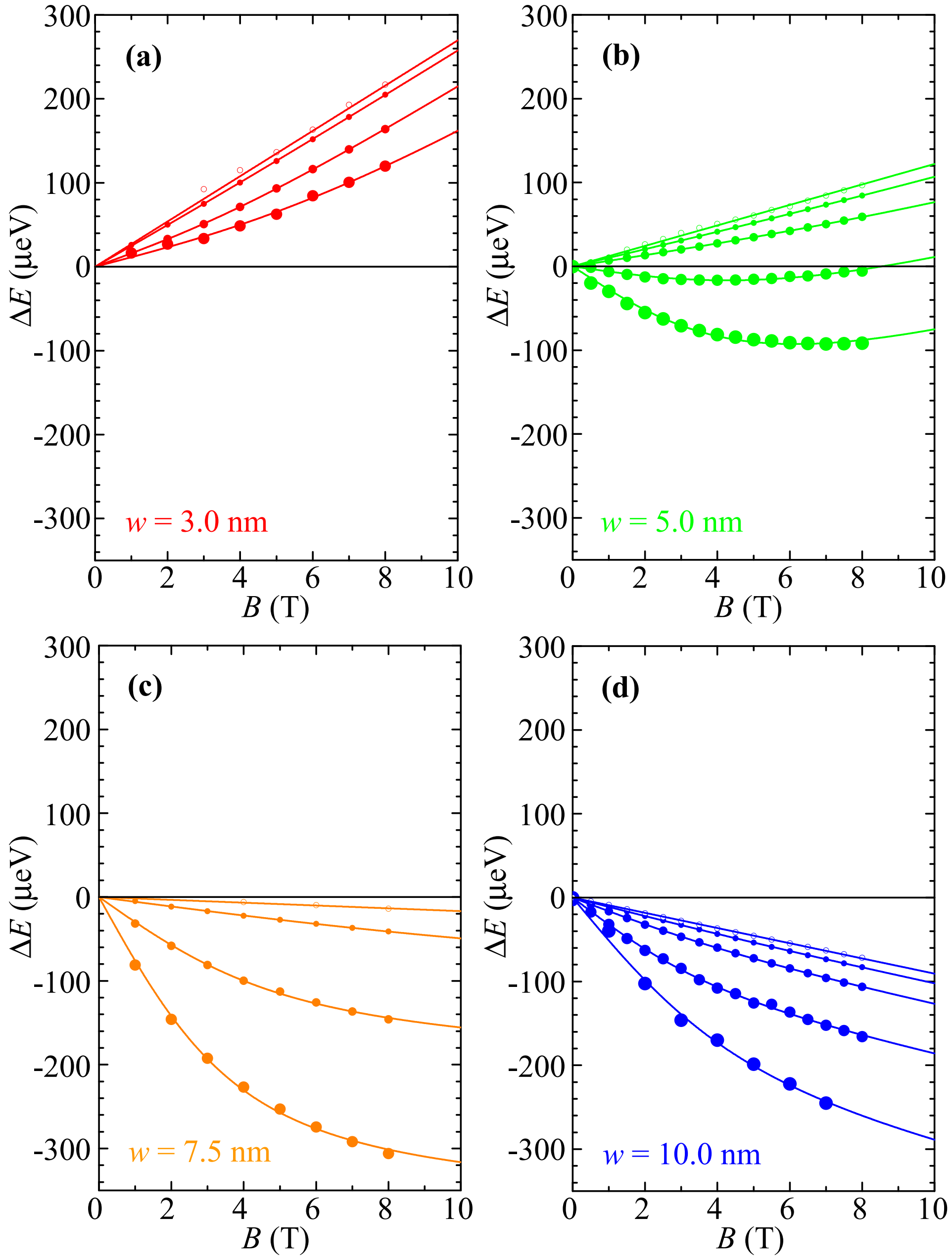

Figure 5.8: ΔE as a function of B at $T = 5$ K for QWs with and without Mn doping (solid and open circles, respectively); larger points indicate increasing $\bar{x}$. Fits to equation 5.12 are shown as lines.

Following from equation 5.10 and from the sign of $\langle \Xi_z \rangle$, this demonstrates that $N_0\alpha$ is negative, i.e. antiferromagnetic, which has been reproduced unambiguously in over 20 additional samples. A negative $N_0\alpha$ has also been measured in recent time-resolved FR measurements in InGaMnAs/GaAs QWs and in GaMnAs/AlGaAs QW with different AlGaAs barrier heights (e.g. 10% or 20% Al instead of 40%) [138].

The effect of increasing temperature on the B dependence of ΔE for the $w = 5$ nm and $\bar{x} \sim 0.032\%$ sample is shown in figure 5.9, which dramatically illustrates the negative *s*-*d* constant. For $d = 5$ nm, g_e is weakly positive, thus for $B > 0$ and at high temperature $\Delta E > 0$. As the temperature decreases, ΔE_{s-d} becomes more negative as the paramagnetic susceptibility increases. At $T = 10$ K and $B = 7$ T, $\Delta E = 0$ since the *s*-*d* exchange splitting is equal and opposite to the Zeeman splitting. For lower temperature, $\Delta E < 0$ since $|\Delta E_{s-d}| > |\Delta E_g|$. We note that the data are well fit to equation 5.12 despite their highly non-linear nature. We contrast our observation of antiferromagnetic *s*-*d* exchange in III-V GaMnAs, with the ferromagnetic *s*-*d* exchange ubiquitous in II-VI DMS. In those systems symmetry forbids hybridization of *s* and *d* orbitals, such that only direct (ferromagnetic) *s*-*d* exchange is possible [149]. The antiferromagnetic *s*-*d* exchange in GaMnAs may be due to the narrower band gap of this material compared with II-VI, such that the conduction band has partial *p* character thus allowing hybridization with the *d* orbitals localized on the Mn^{2+} impurities.

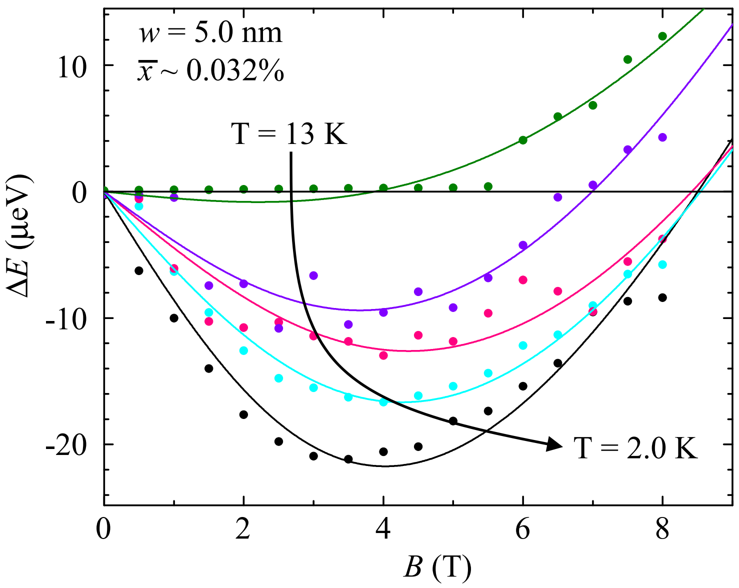

Figure 5.9: ΔE for the sample with $w = 5$ nm and $\bar{x} \sim 0.032\%$ at various temperatures. Fits to equation 5.12 are shown as lines.

5.6 Determination of the *s*-*d* exchange coupling

5.6.1 Dependence of *s*-*d* on confinement

In figure 5.10, the fit parameter $A = \bar{x}N_0\alpha$ is plotted as a function of $\bar{x}$ together with linear fits for each sample set of constant w. The finite values of $\bar{x}N_0\alpha$ at $\bar{x} = 0$, extrapolated from the linear fits, are attributed to either the experimental error in the determination of g_e in the non-magnetic QWs or error in the measurement of $\bar{x}$, both of which have a negligible effect on the slope. These linear fits demonstrate that $N_0\alpha$ is constant over the measured doping range for QWs with the same width, though it varies with w as plotted in figure 5.11a. $N_0\alpha$ is more negative the narrower the QW, while it appears to saturate for wide QWs. In II-VI DMS QWs, a negative change in $N_0\alpha$ as large as -170 meV was

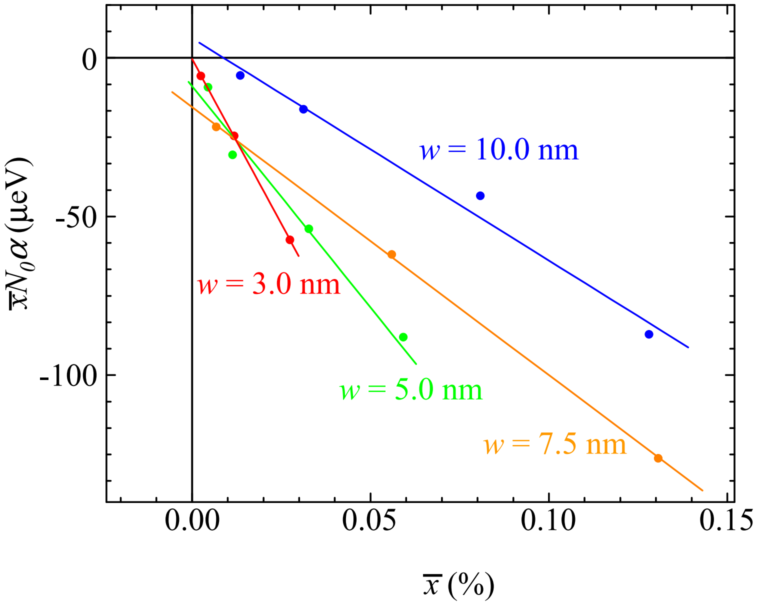

Figure 5.10: $\bar{x}N_0\alpha$ as a function of $\bar{x}$ from fits shown in figure 5.8; error bars are the size of the points. Linear fits are shown for each sample set of constant w.

previously reported for increasing confinement and was attributed to a kinetic exchange coupling due to the admixture of valence and conduction band wave functions [150].

We plot $N_0\alpha$ as a function of the electron kinetic energy (E_e) in figure 5.11b, and the data are linear. Here, E_e is defined as the energy between the bottom of the conduction band in the GaAs QW and the ground state energy (see figure 5.12), which is calculated using a one-dimensional Poisson-Schroedinger solver and the material and structural parameters of the QWs [141]. Extrapolating to $E_e = 0$ we obtain a bulk value of $N_0\alpha = -22 \pm 8$ meV for GaMnAs. A change in $N_0\alpha$ as large as -185 meV, relative to the extrapolated value for $E_e = 0$, is observed in the narrowest wells measured ($w = 3$ nm) and the slope of $N_0\alpha(E_e)$

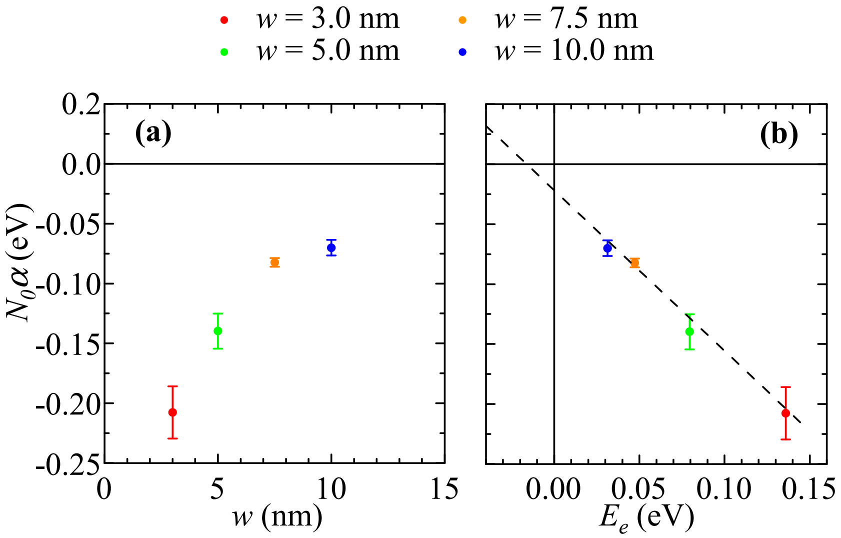

Figure 5.11: The effect of confinement on the measured $s-d$ exchange coupling. (a) $N_0\alpha$ extracted from fits in figure 5.10 and plotted as a function of w. (b) $N_0\alpha$ as a function of electron kinetic energy for GaMnAs.

is roughly the same as reported by Merkulov et al. in II-VI DMS. Since $N_0\alpha > 0$ in bulk II-VI DMS, the kinetic exchange effect appears as a reduction of $|N_0\alpha|$, and is expected to cross through zero for very large confinement. Rather than a reduction, we observe an increase in $|N_0\alpha|$ in GaMnAs QWs. This observation is consistent with the negative contribution of the kinetic exchange predicted by Merkulov et al., since we measure $N_0\alpha < 0$ in our samples.

θ_P is observed to be negative for all the samples studied here indicating that either long range Mn-Mn coupling is antiferromagnetic or the Mn^{2+} spin temperature is larger than the lattice temperature. Preliminary studies on modulation p-doped structures indicate that the negative θ_P is due to a combination of Mn^{2+} spin heating by photoexcitation, as previously discussed, and the lack of strong hole-mediated ferromagnetic Mn-Mn interaction, which occurs for much larger $\bar{x}$. In our samples the mean Mn-Mn distance may be too large for

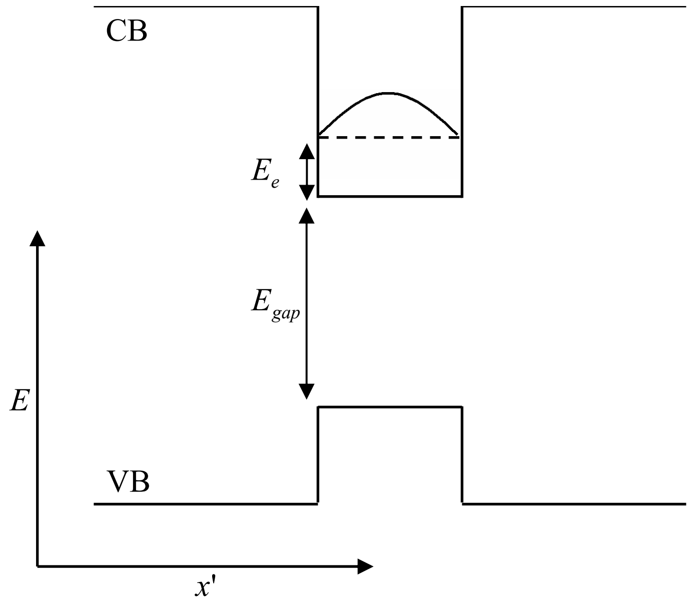

Figure 5.12: The definition of electron kinetic energy E_e in a QW.

hole-spin coherence to be maintained, thus precluding long-range ferromagnetic coupling.

5.6.2 An isotropic *s*-*d* coupling

As mentioned in section 2.4.3, the conduction band g-factor in a QW is anisotropic and must be expressed as a tensor $\overset{\leftrightarrow}{g_e}$. In order to determine whether $N_0\alpha$ also has some dependence on crystal orientation, we measure the *s*-*d* exchange energy as a function of the sample angle θ with respect to the applied magnetic field **B**. We do these measurements in a similar system to the $Al_{0.4}Ga_{0.6}As$/GaAs QWs doped with Mn of earlier sections: GaAs/$In_{0.2}Ga_{.8}As$ QWs doped with Mn.

These samples show the same qualitative behavior as the $Al_{0.4}Ga_{0.6}As$/GaAs QWs including a negative (antiferromagnetic) *s*-*d* interaction and have similar lifetimes and g-factors. They have a lower band-gap energy with $E_{gap} = 1.38$

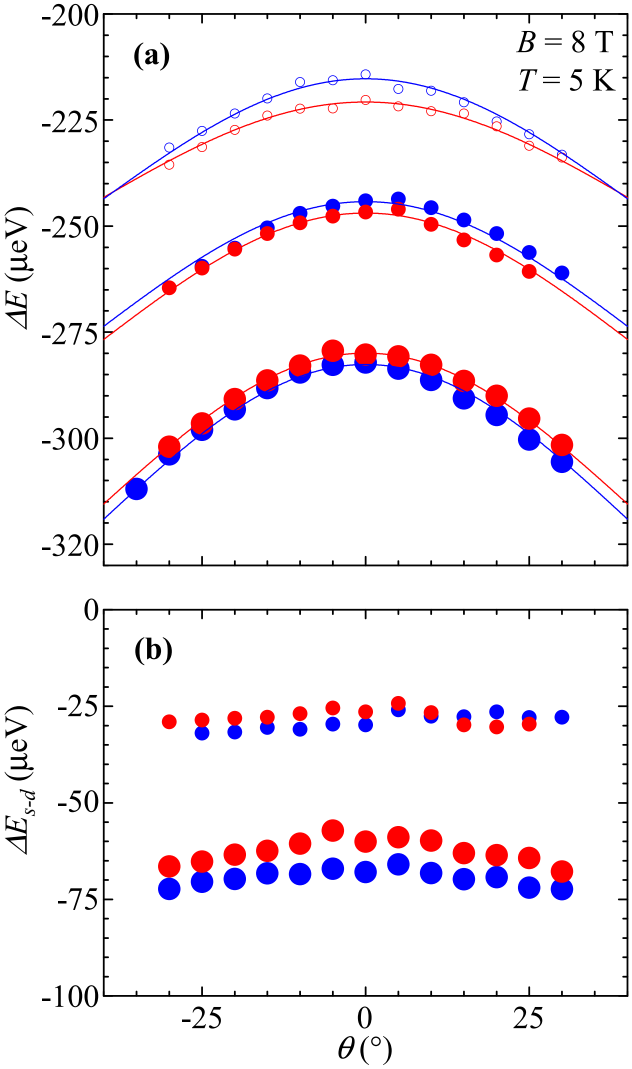

Figure 5.13: Angle dependence of ΔE and ΔE_{s-d} for a series of 5-nm (100) GaAs/$\mathrm{In_{0.2}Ga_{.8}As}$ QWs doped with Mn. The data plotted in the figure refers to a control sample with no Mn-doping (open circles) and to two samples with Mn-doping (solid circles); larger points indicate increasing $\bar{x}$. Red data are measured with the sample rotated by 90° in plane (about the sample growth direction $\hat{x}'$) with respect to blue data. (a) shows ΔE as a function of θ for the three samples along with fits to the data (lines) assuming an isotropic $N_0\alpha$ and an anisotropic g-tensor $\overleftrightarrow{g_e}$. In (b) we plot ΔE_{s-d} as a function of the angle θ for the two QWs with Mn doping.

eV for the 5-nm wide QWs shown in figure 5.13 (in the $\mathrm{Al}_{0.4}\mathrm{Ga}_{0.6}\mathrm{As}$/GaAs system $E_{gap} = 1.64$ eV for 5-nm wide QWs). Since E_{gap} is smaller for the QWs than for the bulk GaAs substrate, these samples are transparent to laser excitation resonant with the QW absorption. Thus we are able to use time-resolved FR rather than time-resolved KR, which we use for the $\mathrm{Al}_{0.4}\mathrm{Ga}_{0.6}\mathrm{As}$/GaAs QWs, to measure electron spin dynamics. The experimental geometry in transmission is more flexible than in reflection, allowing us to easily measure ν_L as a function of θ.

These measurements are shown in figure 5.13a along with fits assuming an anisotropic g-factor $\overleftrightarrow{g_e}$ and an isotropic *s*-*d* exchange $N_0\alpha$. Data is shown for three 5-nm QWs: one with no Mn-doping and two others with two different levels of Mn-doping (the exact value of $\bar{x}$ is not specified). Two orientations are also shown: the orientation labeled in red refers to a sample rotated 90° in plane (about the sample growth direction $\hat{x}'$) with respect to the orientation labeled in blue. The data thus allow us to determine all the spatial components of $\overleftrightarrow{g_e}$ and to ascertain whether $N_0\alpha$ is the same in all directions, i.e. isotropic. From the fits shown in figure 5.13 we find the three components of the 5-nm (100) $\mathrm{GaAs/In}_{0.2}\mathrm{Ga}_{.8}\mathrm{As}$ QWs g-factor as: $g_{x'} = -0.46 \pm 0.02$, $g_{y'} = -0.47 \pm 0.02$, and $g_{z'} = -0.60 \pm 0.02$. We also find, as shown in figure 5.13b, that ΔE_{s-d} (and thus $N_0\alpha$) is constant within the measurement error as function of the angle θ and the in plane orientation of the sample. We therefore conclude that within our experimental error, the *s*-*d* exchange energy $N_0\alpha$ is isotropic in $\mathrm{GaAs/In}_{0.2}\mathrm{Ga}_{.8}\mathrm{As}$ QWs. Due to the qualitative similarity of the $\mathrm{GaAs/In}_{0.2}\mathrm{Ga}_{.8}\mathrm{As}$ QWs to the $\mathrm{Al}_{0.4}\mathrm{Ga}_{0.6}\mathrm{As}$/GaAs QWs, it is likely that $N_0\alpha$ is also isotropic in this system and indeed in all GaAs-based heterostructures.

5.7 Attempted determination of the *p*-*d* exchange coupling

5.7.1 Measurement of polarized Photoluminescence

Since hole spin lifetimes are very short in GaAs QWs ($<$ 10 ps), we rely on measurements of PL to shed light on the *p*-like valence band and its magnetic coupling to Mn-bound *d* electrons, $N_0\beta$. In addition, because recombination happens near impurities, PL can reveal important information on defects and magnetic doping. Polarization-resolved PL is measured as a function of B in the Faraday geometry with PL collected normal to the sample surface. The excitation laser is linearly polarized and focused to a spot 100 μm in diameter with an energy set above the QW absorption energy. While PL is seen to quench with increasing Mn doping, as seen in figure 5.14, QWs with $\bar{x} = 0$ or with small x emit PL, whose energy dependence is well fit by two Gaussians (figure 5.15). The emission energy of the narrower, higher-energy Gaussian peak tracks the B dependence expected for the Zeeman splitting in a QW, indicating that this peak is due to heavy hole exciton recombination. On the other hand, the wider, lower-energy Gaussian is likely due to donor-bound exciton emission from shallow donors in the QWs. These shallow donors may be interstitial Mn centers, since the emission linewidth increases as the calculated Mn_{int} increases. Though the lower energy Gaussian is the result of Mn-doping, it is also present in some non-magnetic samples grown with a cold Mn cell (figure 5.15) perhaps due to an impurity level of Mn_{int} ($\leq 10^{15}$ cm^{-3}).

In addition to quenching the PL, increased Mn-doping broadens the low-energy emission peak. Figure 5.14 shows the zero field PL emission at $T = 5$ K for 7.5-nm wide QWs of varying Mn-doping. The effect of increasing Mn-

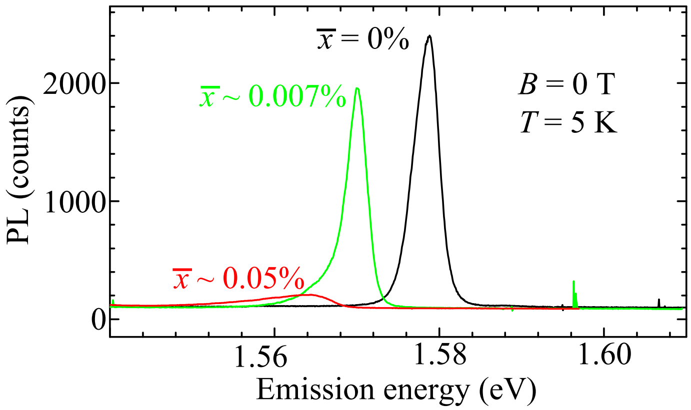

Figure 5.14: PL plotted as a function of emission energy for a set of 7.5-nm QWs with varying Mn-doping; the samples are excited with 1 W/cm^2 at 1.722 eV. Samples with $\bar{x} > 0.13\%$ showed no PL.

doping is qualitatively identical for all QWs of varying width: $w = 3.0$, 5.0, 7.5, and 10.0 nm. As doping increases, the PL broadens in energy, red shifts, and decreases in intensity, eventually quenching. The decreasing intensity of the PL with increasing Mn-doping parallels the degradation in KR signal with Mn-doping. The degradation of these two optical signals, each with distinct physical origins, i.e. emission and absorption, reflects the increasing density of crystalline defects with Mn-doping.

5.7.2 The Zeeman splitting

The splitting in the polarized emission energy of the higher energy Gaussian, $\Delta E_{PL} = E_{\sigma^+} - E_{\sigma^-}$, is measured in all the non-magnetic samples. For small fields ($B < 2$ T), ΔE_{PL} depends linearly on field with the slope giving the out-of-plane heavy hole exciton g-factor (g_{ex}). The extracted values of g_{ex} agree within the experimental error with previously published values [64]. At higher

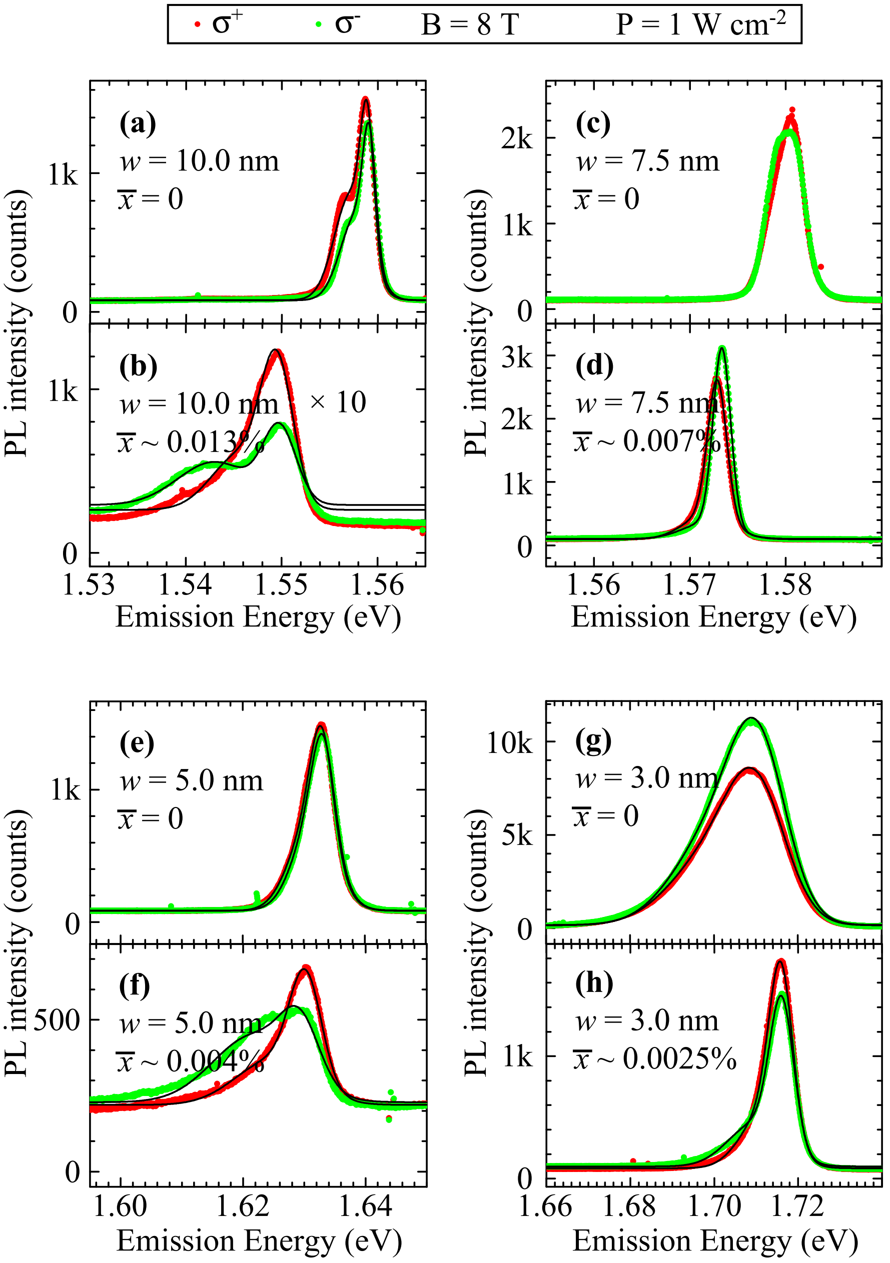

Figure 5.15: Polarization-resolved PL for QWs of varying w and $\bar{x}$ at $T = 5$ K. 2-Gaussian fits to the data are shown as black lines and the higher energy Gaussian is attributed to the heavy hole exciton in the QW. The excitation energy is set to 1.722 eV for (a)-(f) and 2.149 eV for (g) and (h).

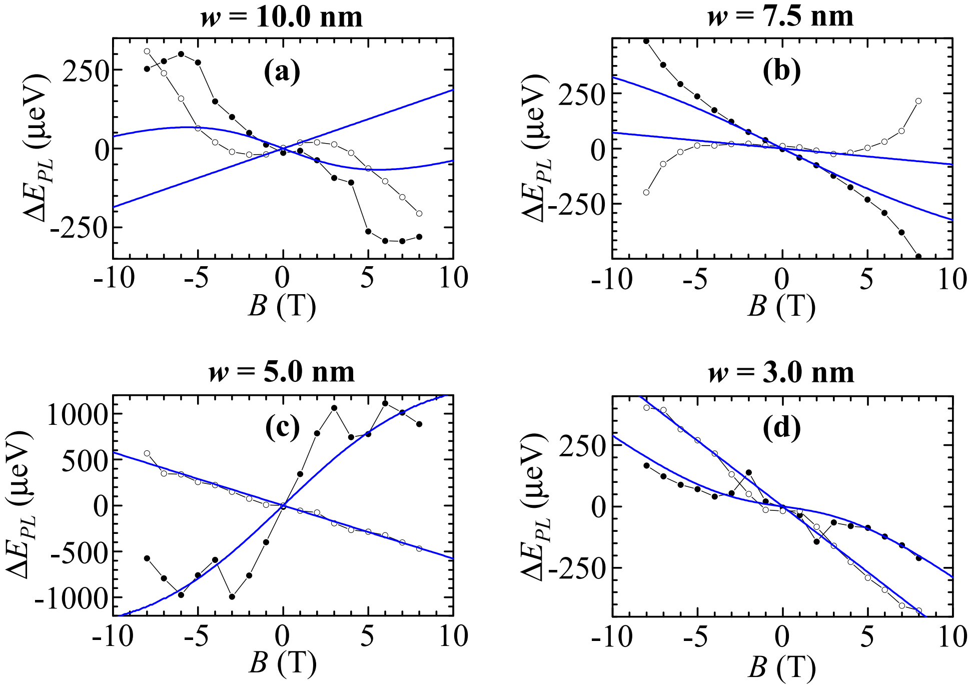

Figure 5.16: Polarized emission splitting (ΔE_{PL}) as a function of B at $T = 5$ K for QWs of varying w and $\bar{x}$. Data from QWs with $\bar{x} = 0$ are shown as open circles, while data from QWs with $\bar{x} \sim 0.013\%$ in (a), $\bar{x} \sim 0.007\%$ in (b), $\bar{x} \sim 0.004\%$ in (c), and $\bar{x} \sim 0.0025\%$ in (d) are shown as filled circles. Fits to ΔE_{PL} for $|B| < 2$ T appear as blue lines.

fields, ΔE_{PL} deviates from linearity, particularly in the wider QWs as shown in figure 5.16a and b where it reverses sign in both the 10-nm and the 7.5-nm QWs for $\bar{x} = 0$ at $|B| \sim 5$ T.

In Mn-doped samples, ΔE_{PL} results from both the Zeeman splitting (ΔE_{gex}) and the *sp-d* exchange splitting (ΔE_{sp-d}):

$$\Delta E_{PL} = \Delta E_{gex} + \Delta E_{sp-d} = -\frac{1}{\hbar} g_{ex} \mu_B B + \bar{x} N_0 (\alpha - \beta) \langle \Xi_z \rangle. \tag{5.13}$$

Using the measurements of g_{ex} from the $\bar{x} = 0$ samples and the previously extracted values of $\langle \Xi_z \rangle$ and $N_0\alpha$ at $T = 5$ K (figure 5.8), we fit the measured ΔE_{PL} to equation 5.13. In the 10-nm QW for low fields we estimate

$N_0\beta = -0.85 \pm 0.38$ eV using the fits shown in figure 5.16a as blue lines. As figure 5.16a makes clear, this model breaks down at high fields where nonlinearities dominate ΔE_{PL}.

As shown in figure 5.16b at high fields in the 7.5-nm QWs, similar nonlinear behavior in ΔE_{PL} contributes to the large uncertainty in our estimates of $N_0\beta$. Further complicating the determination of $N_0\beta$ are the widely differing values extracted for samples of different widths. Using fits shown in figure 5.16, we find $N_0\beta = -2.9 \pm 1.5$, $+24.5 \pm 1.8$, and $+4.3 \pm 0.4$ eV for QWs with $w = 7.5$, 5.0, and 3.0 nm, respectively. Such disagreement between samples indicates the incompleteness of our model for the valence band; the mixing of valence band states may be contributing to the problematic extraction of the *p*-*d* exchange coupling especially for small w [64]. Clearly, more work is necessary for the determination of $N_0\beta$ in GaMnAs QWs and its dependence on w. Previous measurements in bulk GaMnAs provide little guidance with one report suggesting positive *p*-*d* exchange for low $\bar{x}$ (paramagnetic) [115], and others finding negative *p*-*d* exchange for much larger $\bar{x}$ (ferromagnetic) [112, 113, 114]. PL measurements in recently grown InGaAs QWs, discussed in section 5.6.2, may be fruitful since strain in these samples causes large splittings between the HH and LH bands. The large separation of the LH band may reduce the mixing of valence band states, simplifying the PL behavior.

5.7.3 The Luminescence polarization

We compare the PL polarization spectra of the 7.5-nm QW with $\bar{x} \sim 0.007\%$ with the well-known Mn-acceptor emission line in bulk GaAs at 1.4 eV (figures 5.17a and b) [151]. PL polarization is defined here as $(I_{\sigma+} - I_{\sigma-})/(I_{\sigma+} + I_{\sigma-})$. The bulk Mn-acceptor line, shown in figure 5.17b, is measured in the same sample, resulting from the unintentional doping of Mn in the 300-nm GaAs buffer layer grown below the QW structure; the SIMS profiles in figure 5.2 show that the Mn concentration in this layer is less than 1×10^{16} cm^{-3}. The polarization of this peak demonstrates a paramagnetic (Brillouin function) field dependence, shown in figure 5.17d, following the magnetization of the substitutional Mn acceptors in the bulk GaAs. The low-energy peak in the QW PL polarization coincides with the low-energy PL peak which we assigned to emission from excitons bound to interstitial Mn donors. Its polarization is plotted in figure 5.17c (solid points) and demonstrates similar paramagnetic (Brillouin function) behavior with field and temperature to that of the bulk Mn-acceptor line.

The polarization of the bulk Mn-acceptor line is proportional to the spin-polarization of local Mn^{2+} moments since the PL from this line results from conduction band electrons recombining with holes trapped on substitutional Mn acceptors. The spin of these holes is coupled to the local Mn^{2+} spin [152]. We postulate a similar mechanism for the low-energy polarization feature in the QW PL in which holes in the valence band of the QW recombine with electrons bound to interstitial Mn donors. The clear Brillouin-like field dependence indicates that the recombinant polarization originates around isolated paramagnetic Mn impurities in the lattice, i.e. either substitutional Mn acceptors or interstitial Mn donors. The Brillouin-like behavior is inconsistent with coupled Mn centers such as interstitial-substitutional pairs, which couple antiferromagnetically and which are unlikely to be present in samples with such low Mn content [117]. The ~ 20 meV redshift of the polarization peak from the main QW peak does not match the 110 meV binding energy of the substitutional acceptor. While there is an excited state of the substitutional Mn acceptor with a binding energy of 26 meV [153], recombination from this excited state is unlikely when each acceptor is filled with, at most, one hole and given that PL usually originates

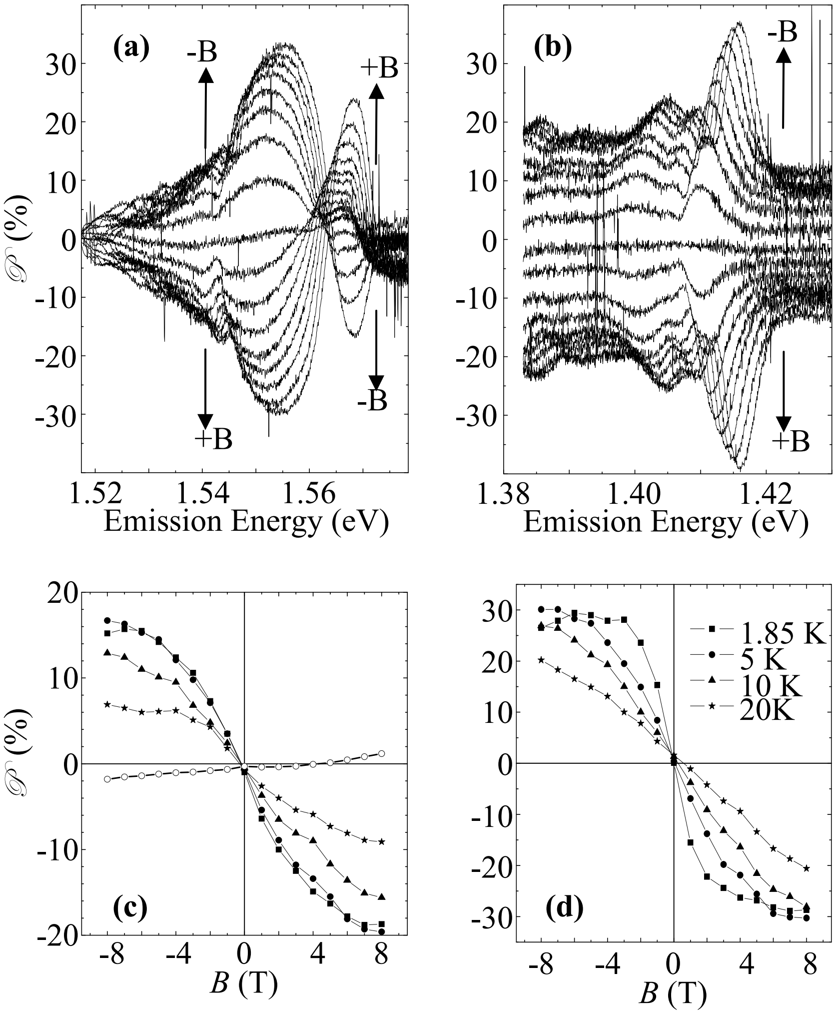

Figure 5.17: PL polarization spectra for a 7.5-nm GaMnAs QW with an 1.72 eV excitation at 1.0 mW (a) near the QW emission peaks (∼1.6 eV) and (b) at the bulk Mn-acceptor line for GaMnAs (∼1.4 eV), which results from unintentional Mn-doping in the 300-nm thick GaAs buffer layer. The spectra are plotted as a function of emission energy for different magnetic fields from -8 to +8 T at 1 T intervals. (c) The PL polarization integrated over a single emission peak as a function of B for the high energy (∼1.57 eV at T = 5 K, open circles) and low energy (∼1.55 eV at several temperatures, filled symbols) peaks, and (d) for the bulk Mn-acceptor line peak plotted for several temperatures.

from the lowest available energy levels. Rather, we assume that the recombination originates from the interstitial Mn donor and the valence band in the QW. Comparison to the experimentally measured interstitial Mn donor binding energy is not possible since it has not been reported. The postulated coupling of the electron spin to interstitial Mn spin results in polarized emission which follows the magnetization of interstitial Mn within the QW. These measurements open the possibility of indirectly measuring the magnetization of the Mn impurities in the QWs using polarization-resolved magneto-PL.

The high-energy feature in the QW PL polarization involves recombination of electrons and holes bound to the QW, but delocalized relative to the Mn states. Due to the exchange interactions in both the valence and conduction band, the spin splitting, and thus the resulting polarization, should have a Brillouin function field dependence equation. For the small values of $\bar{x}$ studied here, however, these effects are not resolvable. As shown in figure 5.17c, this polarization has a weaker field dependence (open circles) with an opposite sign compared to the polarization of the low-energy peak (solid points).

5.8 Theoretical Analysis

5.8.1 An antiferromagnetic *s*-*d* coupling?

The difference in behavior of the exchange couplings for the conduction and valence bands in II-VI DMS is rooted in the nature of exchange interactions between localized spins on impurity sites and the spins of band electrons:

$$H_{\mathrm{ex}} = -\frac{1}{\hbar^2} J \mathbf{S} \cdot \Xi, \tag{5.14}$$

where we have re-written equation 2.45 in its simplified two-particle form. Two mechanisms contribute to the value of J: (1) a normal (direct) exchange mechanism originating from the interaction potential between band and *d*-shell electrons proportional to the inverse of their separation; and (2) a resonant scattering mechanism due to hybridization between the band and *d*-shell electrons occurring when the *d*-level is close to a band edge [154, 155]. The first mechanism results in a positive (ferromagnetic) exchange and the second in a negative (antiferromagnetic) exchange. In general both mechanisms contribute to the total exchange J. In II-VI DMS, the resonant scattering mechanism does not contribute to the conduction band exchange which is dominated by the normal exchange. Thus a positive exchange is measured: $N_0\alpha = 0.22$ eV. In contrast, since the localized *d*-level falls within the valence band in these systems, the resonant scattering mechanism dominates the exchange for the valence band resulting in a negative interaction energy: $N_0\beta = -0.88$ eV.

The above reasoning makes the extrapolation of our measurements to a bulk GaMnAs exchange of $N_0\alpha = -23 \pm 8$ meV (discussed in section 5.6) surprising. The value has a much smaller magnitude and most importantly the opposite sign than values predicted by *s*-*d* exchange theories in DMS. Since direct exchange should dominate in the conduction band, the $N_0\alpha$ is expected to be positive. We must therefore consider that some of the assumptions which are valid in II-VI do not apply in GaMnAs. For instance, theoretical efforts are currently underway treating the effects of a possible hybridization between *s*-like conduction band states and an excited state of the Mn shell electrons [156]. Such a hybridization could lead to a resonant scattering contribution in the conduction exchange coupling, explaining the measurement of a negative $N_0\alpha$. It is also possible that the smaller band-gap energy in GaMnAs compared to II-VI systems and the correspondingly stronger admixture of valence band states to the conduction band explains the measured negative *s*-*d* exchange.

5.8.2 Kinetic exchange

In II-VI DMS nanostructures, increasing confinement results in the reduction in strength of the *s*-*d* exchange interaction between conduction electrons and electrons localized in the *d* shell of Mn impurities [150]. This reduction is due an enhancement of the electron kinetic energy by the dimensional quantization of states in a confined system. For conduction band states the dependence of the exchange coupling on carrier kinetic energy results in a decrease in the magnitude of the exchange energy for an increase in the kinetic energy [157]. Though theoretical models of kinetic exchange based on these principles replicate the qualitative features of the data in II-VI materials, their predictions fall short by a factor of ~ 5 [158].

A more complete model also takes into account the effects of the admixture of valence band states to the conduction band states [150]. For states with non-zero **k**, the *p*-like orbitals of the valence band admix to the Bloch functions of the conduction band. Due to the dominance of the resonant scattering mechanism in the valence band, these states contribute a negative energy to the total exchange as discussed in section 5.8.1. As electron kinetic energy (and thus **k**) increases and the admixture of valence band states becomes stronger, so does the negative contribution to the exchange energy. This negative shift in $N_0\alpha$ with increasing E_e contrasts the simple reduction in magnitude predicted for pure conduction band states. Therefore, depending on the degree of the admixture, a positive conduction band exchange constant can decrease and even become negative with increasing kinetic energy. Predictions made by this model agree quantitatively with the experimental data available in II-VI DMS.

Though there are a number of important differences between GaMnAs and the II-VI systems to which the theory of kinetic exchange has been applied, the

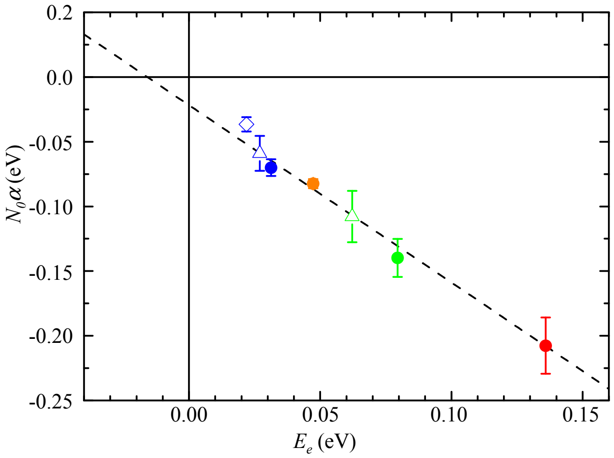

Figure 5.18: The *s*-*d* exchange coupling plotted as a function of confinement energy including data from samples with different QW depths. Blue, orange, green, and red symbols correspond to QWs with $w = 10.0$, 7.5, 5.0, and 3.0 nm, respectively. Solid cirles, open triagles, and open diamonds correspond to QWs with barriers containing 40, 20, and 10% Al, respectively.

model which includes the admixture of valence band states into the conduction band reproduces the general features shown by our measurements. As evident from figure 5.11b, $N_0\alpha$, which we measure to be negative in all our experiments, becomes more negative with increasing kinetic energy E_e, just as predicted by the model of Merkulov et al. The earlier model of Bhattacharjee et al., which ignores the aforementioned admixture of states, predicts a reduction in $|N_0\alpha|$ with increasing E_e and proves to be inconsistent with our findings. The quasi-linear dependence of $N_0\alpha$ on E_e also mimics the finding in the II-VI QWs (the slopes differ only by a factor of ~ 1.2) [150].

Experimental efforts are currently underway to make more detailed measurements of the dependence of $N_0\alpha$ on E_e in GaMnAs and InGaMnAs QWs [159]. We are also making measurements of $N_0\alpha$ as a function of E_e in GaMnAs QWs by varying the QW depth instead of the QW width. Such measurements provide further insight on the nature of the dependence and its functional form. Preliminary results shown in figure 5.18 show that measurements of $N_0\alpha$ in GaAs/AlGaAs samples with lower barriers (10% and 20% Al) follow the same dependence shown in figure 5.11b.

5.9 Conclusion

In summary, we demonstrate the growth of III-V GaMnAs heterostructures in which coherent electron spin dynamics and PL can be observed. By lowering the substrate temperatures during growth, sharper Mn profiles and higher Mn concentrations are attained, however optical signals eventually quench ($T_{sub} <$ 400°C) likely due to incorporation of defects by Al gettering, such as oxygen. Optical signals are also seen to quench for $\bar{x} > 0.13\%$. The exchange induced spin splitting in the conduction band in the GaMnAs QWs matches the traditional paramagnetic DMS picture and allows for the determination of the *s*-*d* exchange parameter via time-resolved electron spin spectroscopy. Surprisingly the measured *s*-*d* exchange coupling is antiferromagnetic in GaMnAs QWs, a result not predicted by current DMS theories. In particular, this result points to the limited understanding of the *s*-*d* exchange interaction in this important material system [46]. No evidence of long-range Mn spin coupling is observed, but negative effective Curie temperatures indicate spin heating of the Mn sublattice by photoexcitation. Electron spin lifetimes in the QWs increase for the lowest Mn dopings compared with undoped samples indicating the dominance of the Dyakanov-Perel mechanism over spin-flip scattering in this regime. The ability to magnetically dope III-V and maintain sensitive optical properties opens the door for more complex structures to be used in the study of both free carrier and magnetic ion spin at fast time scales, a technology which was previously limited to II-VI DMS.

Strong evidence is presented of a direct relation between the conduction band exchange constant and the electron kinetic energy due to one-dimensional quantum confinement in GaMnAs QWs. It is a quantitatively similar effect and has the same sign as what was reported for II-VI DMS QWs [150]. The *s*-*d* exchange coupling is antiferromagnetic in the QWs and extrapolates to -23 ± 8 meV in the limit of infinitely wide wells, indicating that antiferromagnetic $s-d$ exchange could be a bulk property of GaMnAs. While confinement is found to alter the *s*-*d* exchange energy, measurements suggest that the interaction remains isotropic regardless of reduced degrees of freedom.

Chapter 6

Electron spin transfer and coherence in coupled quantum wells

6.1 Introduction

During the course of our investigations into semiconductor heterostructures amenable to localization and control of electron spins in the conduction band, we researched the possibility of using GaAs-based coupled quantum well (CQW) structures. While the consequences of experiments on dynamic nuclear polarization and Mn doping in these CQWs were not promising, we gained a detailed knowledge of the electron spin dynamics in these canonical systems.

In this chapter we investigate the spin dynamics of optically excited electrons confined in asymmetric CQWs through time-resolved Faraday rotation (FR) experiments. The inter-well coupling is shown to depend on applied electric field and barrier thickness. We observe three coupling regimes: independent spin precession in isolated quantum wells, incoherent spin transfer between single-well states, and coherent spin transfer in a highly coupled system. Relative values of the inter-well tunneling time, the electron spin lifetime, and the Larmor precession period appear to govern this behavior.

In section 6.2 we give a brief background followed by a description of the properties of the CQW samples in section 6.3. Then, in section 6.4 we discuss the electron spin dynamics in the conduction band. Finally, we include a brief account of our attempts to extend previous experiments on localized nuclear polarization and Mn-doping to CQW structures in section 6.5.

6.2 Background

The possibility of developing spin-based electronic devices has focused recent interest on the study of carrier spin dynamics in semiconductor nanostructures. In this vein, electrical control of electron spin precession and relaxation rates has been achieved in a number of quantum well (QW) systems [15, 16, 160]. The accessibility of spatially direct and indirect excitonic states with the application of an external electric field make CQW systems [161] attractive for the study of electron spin dynamics. Extensive research has been devoted to indirect electron-hole pairs in CQWs [162, 163, 164, 165] and to carrier tunneling between coupled wells [166, 167, 168]. Here, time resolved FR experiments [85] on specifically engineered CQWs reveal the effect of inter-well tunneling on electron spin coherence. Since the electron g-factor depends strongly on quantum well width [63], electron spins in wells of unequal widths precess at different rates. When such wells are coupled through a tunneling barrier, spin precession rates are observed to either switch or tune continuously as a function of applied electric field.

6.3 Coupled quantum well samples

6.3.1 Sample structure

The sample structure consists of a pair of undoped GaAs QWs with $\mathrm{Al}_{0.33}\mathrm{Ga}_{0.67}\mathrm{As}$ barriers grown by molecular beam epitaxy [169] on top of a low temperature $\mathrm{Al}_{.33}\mathrm{Ga}_{.67}\mathrm{As}$ back gate structure [102], which is 1.3 μm from the surface. The sample structure is similar to that of the parabolic quantum wells discussed in chapter 4 and is shown schematically in figure 6.1 (see appendix A.2 for the exact sample structure). A Ni/Ge/Au/Ni/Au pad is annealed to contact the back gate, while a semi-transparent 1-mm^2 layer of Ti/Au deposited on the sample surface acts as the front gate. Applying a voltage U_g across the gates creates a uniform electric field in the QWs up to 30 kV cm^{-1} with negligible leakage current (less than 50 μA). A positive value of U_g corresponds to a positive voltage at the front gate with respect to the back gate. Different samples are grown with varying well widths w and well separations d. Here we shall discuss 6 such samples: sample 7-2-10 consists of a 10-nm QW grown on top of a 7-nm QW separated by a 2-nm barrier. Other samples include 7-6-10, 7-20-10, 8-4-8, 8-2-8, and 5.7-3.8-7.7 using the same naming convention. Experiments are performed at 5 K in a magneto-optical cryostat with an applied magnetic field B (along $\hat{z}$) in the plane of the sample and with the laser propagation parallel to the growth direction ($\hat{x}||\hat{x}'$, i.e. $\theta = 0°$).

6.3.2 Photoluminescence

Figures 6.2a, b, and c show photoluminescence (PL) measurements as a function of U_g and detection energy E_d for samples 7-20-10, 7-6-10, and 7-2-10, respectively. Samples 7-20-10 and 7-6-10 in figures 6.2a and b show two dis-

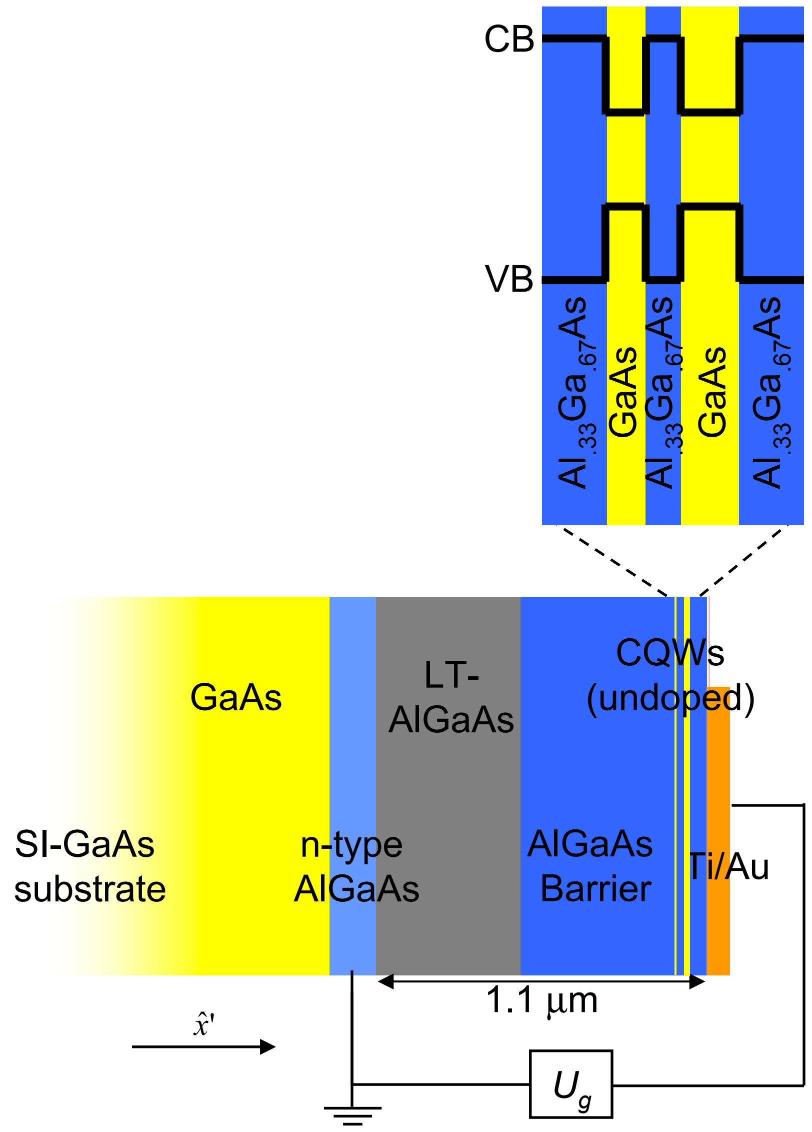

Figure 6.1: A schematic diagram of gated GaAs/$Al_{0.33}Ga_{0.67}As$ CQWs with a more detailed view in the inset.

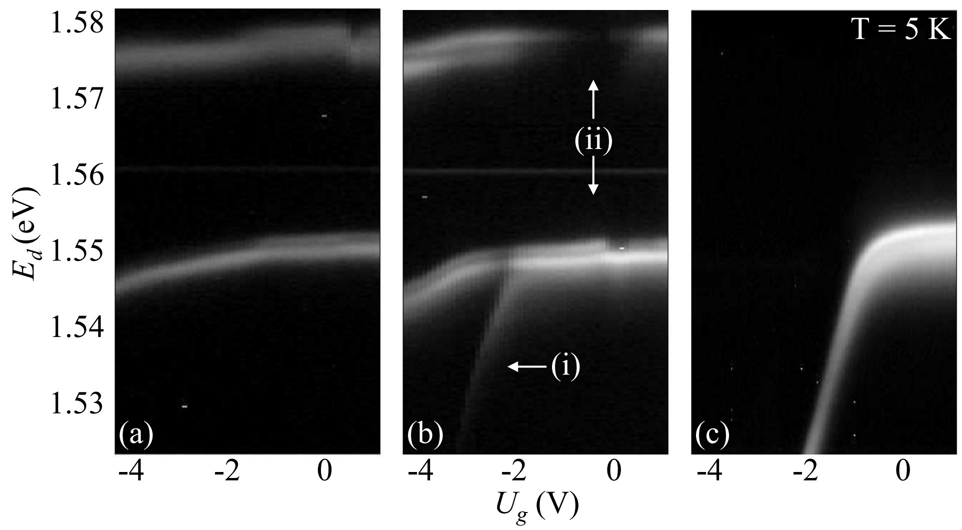

Figure 6.2: PL intensity plotted on a logarithmic grayscale as a function of U_g and E_d. A CW HeNe laser emitting at 1.96 eV is used to excite carriers at $B = 0$ T. (a) PL from sample 7-20-10 shows two Stark shifted peaks corresponding to the 7- and 10-nm QWs without evidence of inter-well coupling. (b) PL from sample 7-6-10 (i) reveals a strongly Stark shifted indirect exciton peak, and (ii) shows the quenching of the 7-nm well PL peak and the corresponding greater intensity in the 10-nm well peak. (c) Sample 7-2-10 shows a single PL peak which is strongly Stark shifted.

tinct PL peaks each with FWHM of 2-3 meV centered around 1.54 and 1.57 eV corresponding to emission from the 10-nm- and 7-nm-wide wells, respectively. The red-shift observed for each peak for $U_g < -2.0$ V agrees well with the Stark shift expected in QWs of similar thicknesses [170]. Figure 6.2b, however, shows evidence of coupling between the two wells in the form of (i) a strongly Stark shifted indirect exciton peak appearing below $U_g = -2.0$ V, and (ii) a quenching of the higher energy PL peak together with an increase in the emission intensity of the lower energy peak around $U_g = 0.0$ V [162, 171]. These features confirm that sample 7-6-10 with its 6 nm barrier between QWs is indeed a coupled system with a tunneling time τ shorter than the recombination lifetime $T_{\text{e-h}}$, while sample 7-20-10 with its much wider 20-nm barrier contains two uncoupled QWs with otherwise identical characteristics. Figure 6.2c shows a single PL peak for sample 7-2-10 with a strong Stark shift at negative voltages indicating an even shorter value of τ. $T_{\text{e-h}}$ has been measured to be of order 1 ns in similar structures [167], while τ is found to be as short as 1 ps for GaAs CQWs with 2.5 nm $Al_{0.2}Ga_{0.8}As$ barriers [172].

6.4 Electron spin Dynamics

6.4.1 Time-resolved Faraday rotation measurements

Time-resolved FR measurements are performed in a magnetic field in order to examine carrier spin dynamics in CQWs. The measurement, which monitors small rotations in the linear polarization of laser light transmitted through a sample, is sensitive to the direction of spin polarization of electrons in the conduction band as discussed in section 2.6.2. By tuning the laser energy E_L near the resonant absorption energy of different conduction band states, the polarization dynamics of these states can be selectively investigated. A 76-MHz Ti:Sapphire laser produces 250-fs pulses which are split into pump and probe with a FWHM of 8 meV and an average power of 2.0 mW and 100 μW, respectively. The linearly polarized probe is modulated by an optical chopper at $f_1 = 940$ Hz and the circular polarization of the pump is varied by a photoelastic modulator at $f_2 = 55$ kHz. Both beams are focused to an overlapping 50-μm spot on the semi-transparent front-gate. Thus, polarized electron spins are injected and precess in a perpendicular field B. The time evolution of the spins is well described by the expression for FR as a function of pump-probe delay,

$$\theta_F\left(\Delta t\right) = \theta_\perp e^{-\Delta t/T_2^*}\cos\left(2\pi\nu_L\Delta t+\phi\right), \tag{6.1}$$

where $\theta_\perp$ is proportional to the total spin injected perpendicular to the applied field, T_2^* is the inhomogeneous transverse spin lifetime, Δt is time delay between the pump and probe pulses, and ϕ is a phase offset. The Larmor frequency $\nu_L = g_e\mu_B B/h$ depends on the magnetic field B and the effective conduction band Landé g-factor g_e where μ_B is the Bohr magneton and h is Planck's constant. It is important to note that our measurement is insensitive to hole spins due to their rapid spin relaxation (faster than 5 ps) in GaAs/Al$_x$Ga$_{1-x}$As QWs [173].

Figure 6.3a shows FR measured in sample 7-6-10 at an applied magnetic field $B = 6$ T as a function of both Δt and the gate voltage U_g. Two distinct precession frequencies appear, as highlighted by the line-cuts at constant U_g shown in figure 6.3b, with a sharp transition between the two occurring around $U_g = -2$ V, i.e. at the same voltage as the onset of the indirect excitonic peak in figure 6.2b. There is an accompanying 10-fold drop in the FR amplitude $\theta_\perp$ as a function of voltage, as well.

The voltage dependent shift of ν_L in sample 7-6-10 is due to a change in the measured g-factor as shown in the inset to figure 6.3b. Here, the precession frequency, obtained by fitting equation 6.1 to data similar to that shown in figure 6.3a, is plotted as a function of B for two fixed voltages: $U_g = 0.0$ V and $U_g = -4.0$ V. The linear dependence of both distinct precession frequencies on B demonstrates the presence of two independent g-factors ($|g_e| = 0.052 \pm .001$ and $|g_e| = 0.193 \pm .005$) whose relative weight can by controlled by U_g.

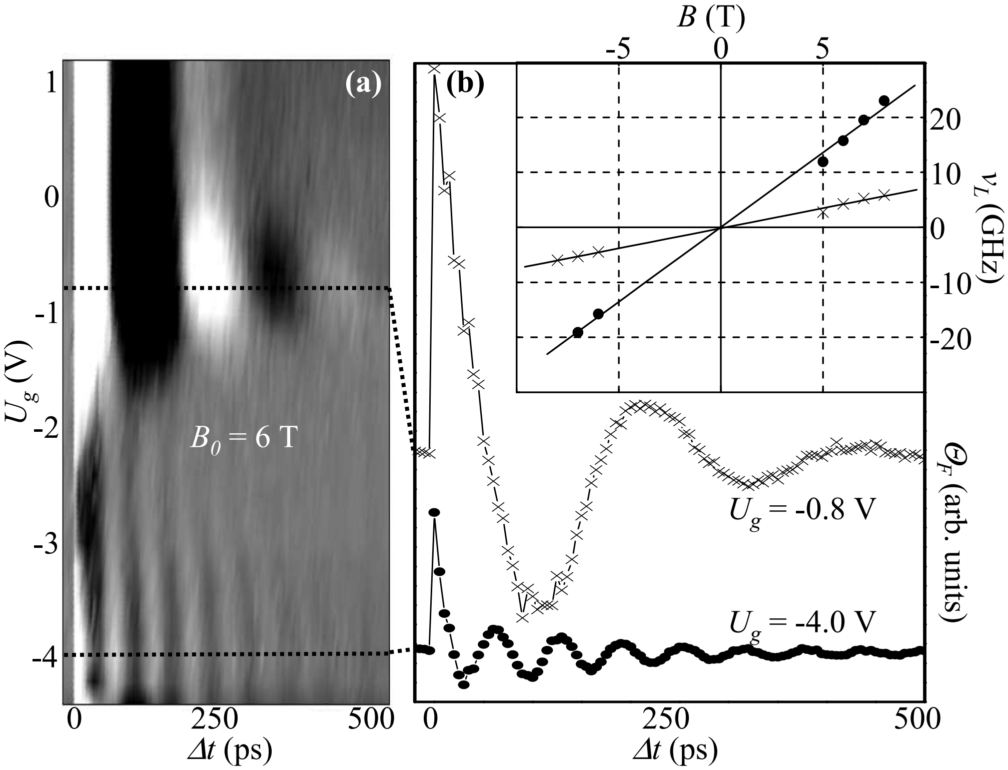

Figure 6.3: Dependence of time-resolved FR data on U_g and B in sample 7-6-10. (a) FR plotted in a grayscale as a function of U_g and Δt for $B = 6$ T and $E_L = 1.57$ eV. Note the appearance of only two precession frequencies and the sharp transition between the two. (b) Line cuts of the time resolved FR data shown in (a) for $U_g = -0.8$ V and $U_g = -4.0$ V. Inset: ν_L plotted as a function of B for two gate voltages U_g. Data taken at $U_g = 0.0$ V are shown as crosses and data taken at $U_g = -4.0$ V are shown as filled circles. The solid lines are linear fits to the data.

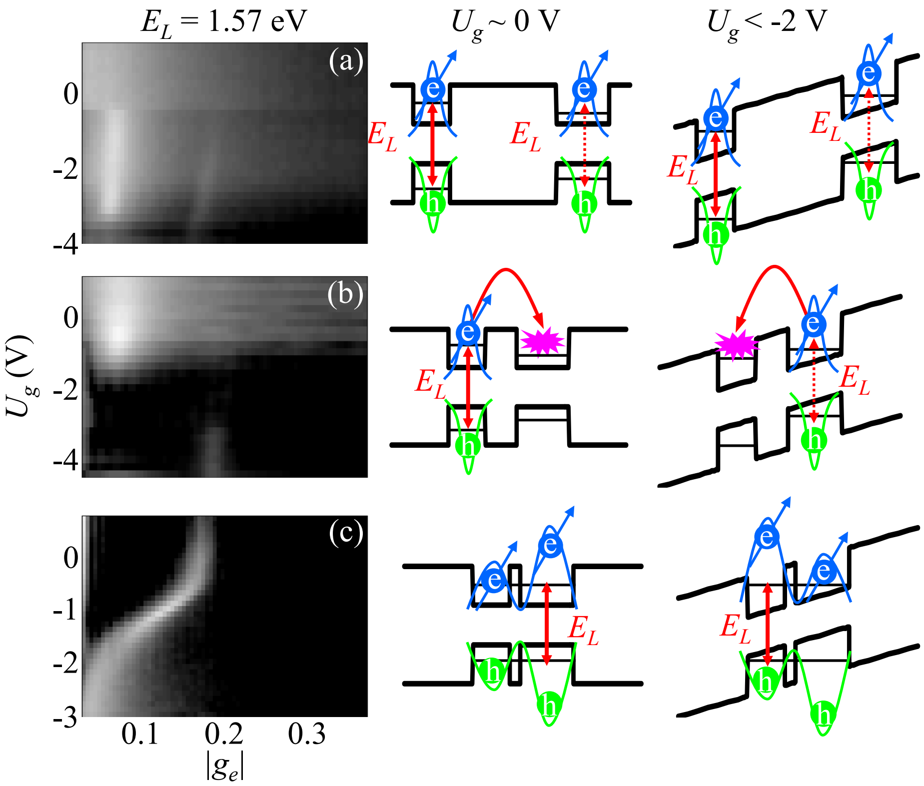

Figure 6.4: Dependence of g-factor on U_g and d. (a) Fourier transform of time resolved FR data measured in sample 7-20-10 plotted on a logarithmic grayscale as a function of $|g_e|$ and U_g at $B = 6$ T and $E_L = 1.57$ eV. Note the presence of two g-factors with a weak dependence on U_g. Schematic band diagrams are shown in the middle and on the right for U_g close to zero and for negative U_g, respectively. Electron spin is represented by blue arrows, while holes are shown without spin to illustrate the rapid hole spin relaxation (less than 5 ps) in these systems. The thick red arrow indicates resonant excitation and detection of FR, while the thin dotted arrow refers to weaker, off-resonant FR. (b) Similar data is shown for sample 7-6-10 where switching between two g-factors is observed as a function of U_g. Panels on the right illustrate the destructive effect of incoherent tunneling on the spin coherence of the lower energy conduction electron state. (c) Continuous tuning of the g-factor is observed in sample 7-2-10 and the panels to the right schematically depict the electron ground states extending over both QWs.

6.4.2 The effects of inter-well coupling

The dependence of the g-factor on U_g is explored in greater detail in figure 6.4 for three samples with varying well separation d: 7-20-10, 7-6-10, and 7-2-10. FR data taken at $B = 6$ T as a function of Δt and U_g (as shown in figure 6.3a are Fourier transformed. Grayscale plots show the logarithm of the Fourier amplitude as a function of U_g and of g-factor $|g_e|$ (extracted from the precession frequency ν_L). Measurements are performed at a laser energy $E_L = 1.57$ eV resonant with the 7-nm well absorption. Figure 6.4a shows the presence of the same two g-factors in sample 7-20-10, $|g_e| = 0.05$ and $|g_e| = 0.19$, as shown in figure 6.3. Experimental and theoretical literature confirms that these values of g_e correspond to the 7- and 10-nm-wide wells, respectively [63]. Since E_L is resonant with the 7-nm well absorption and detuned from the 10-nm well absorption by 20 meV, the Fourier amplitude of the $|g_e| = 0.05$ oscillations is observed to be an order of magnitude larger than the $|g_e| = 0.19$ oscillations, which correspond to the 10-nm well. Both g-factors show a weak dependence on U_g corresponding to slightly increased penetration of the electron wave function into the barriers for $U_g < -2.0$ V [174, 175]. As shown schematically in the center and right panels of figure 6.4a, the inter-well tunneling time τ in this uncoupled sample is much longer than either the transverse spin lifetime T_2 or the recombination time $T_{\text{e-h}}$.

The effect of reducing d to 6 nm and thus introducing inter-well coupling is shown in figure 6.4b. Here, a distinct switching behavior is observed between the 7- and 10-nm well g-factors as a function of U_g. Near $U_g = 0$ V, spin polarized electrons are excited and detected in the 7-nm well, however, in contrast with the $d = 20$ nm case, spin precession in the 10-nm well is not observed, even at a reduced amplitude. This behavior can be understood qualitatively from the center panel of figure 6.4b. Since the conduction band ground state of the 10-nm well is energetically lower then that of the 7-nm well, and because d is sufficiently small that $\tau < T_{\text{e-h}}$, electrons tunnel from the 7-nm well into the 10-nm well. In the process of electron transfer, the energy mismatch is compensated by acoustic phonon emission [176]. Assuming that τ is shorter than T_2 but longer than a spin precession period $1/\nu_L$, spin transfers incoherently. Because ν_L is unequal in the two wells, the incoherent tunneling randomizes the electron spin polarization in the 10-nm well, thereby destroying its spin coherence and quenching its FR signal. This picture is corroborated by the fact that in figure 6.2b, around U_g = 0 V no significant PL is found from the 7-nm well while PL from the 10-nm well is increased, indicating that electrons excited in the 7-nm QW tunnel into the 10-nm QW before recombination. For $U_g < -2.0$ V, spin precession from the 7-nm well disappears and precession from the 10 nm well emerges. In this case, as shown in the right panel of figure 6.4b, the applied electric field has raised the 10 nm well ground state energy above the 7-nm ground state energy causing the incoherent tunneling to change directions. As a result, spin coherence in the 7-nm well is destroyed and its corresponding FR signal disappears. The amplitude of the 10-nm FR signal remains small due to the detuning of E_L. We can further conclude that near $U_g = -2.6$ V, where figure 6.2b shows that the electron ground state energy levels of the 10-nm and 7-nm wells are degenerate, incoherent tunneling occurs in both directions, resulting in the destruction of spin coherence in both wells as shown in figure 6.4b.

Reduction of d to 2-nm results in the smooth tuning of g_e as a function of U_g between the 10- and 7-nm values. In figure 6.4c, the g-factor is shown to change from $|g_e| = 0.19$ near $U_g = 0$ V to $|g_e| = 0.05$ for $U_g < 0$ V. As shown schematically in the right panels of figure 6.4c, this behavior corresponds to a system in which τ is shorter than $1/\nu_L$ resulting in an electron spin wave function which effectively spans both quantum wells. As an electric field is applied across the structure, the relative amplitude of the wave function in each well is altered. Since the measured g-factor is a weighted average over the full electron wave function amplitude [15, 42], g_e is observed to tune continuously between the two single-well values. Near $U_g = 0$ V, the electron wave function amplitude is almost completely contained within the 10-nm well resulting in $|g_e| = 0.19$. For $U_g < 0$ V, $|g_e|$ approaches 0.05 as the wave function amplitude shifts to the 7-nm well.

The three regimes of interwell coupling represented by the samples with 20-, 6-, and 2-nm barriers are depicted in the schematic energy diagram of figure 6.5 [177]. In the first case, the conduction electrons are described by isolated single well states and interwell coupling is negligible as indicated by the lack of anti-crossing behavior. In the intermediate case, inelastic tunneling, assisted by phonons or defect states, dominates. As a result, spin coherence is disrupted in the QW into which electrons are flowing. Finally, in the highly coupled case, the electron eigenstate has an envelope function which spans the CQW structure, resulting in an averaged effective g-factor; in other words the electron spin reversibly tunnels between QWs many times over the course of a single spin precession. Calculations based on our structural parameters and the simple model of Dzyubenjo and Yablonskii yield tunneling times of $\tau \simeq 0.1$ ps for $d = 2$ nm [178].

Also note that our picture is corroborated by time-resolved FR measurements performed at a laser energy $E_L = 1.54$ eV resonant with the 10-nm well absorption. In the case of samples 7-20-10 and 7-6-10, we observe only oscillations at $|g_e| = 0.19$, corresponding to the 10-nm-wide well, regardless of the value of U_g. For sample 7-2-10, however, we observe the same smooth tuning of g_e as a function of U_g at $E_L = 1.54$ eV as we observe at $E_L = 1.57$ eV. This

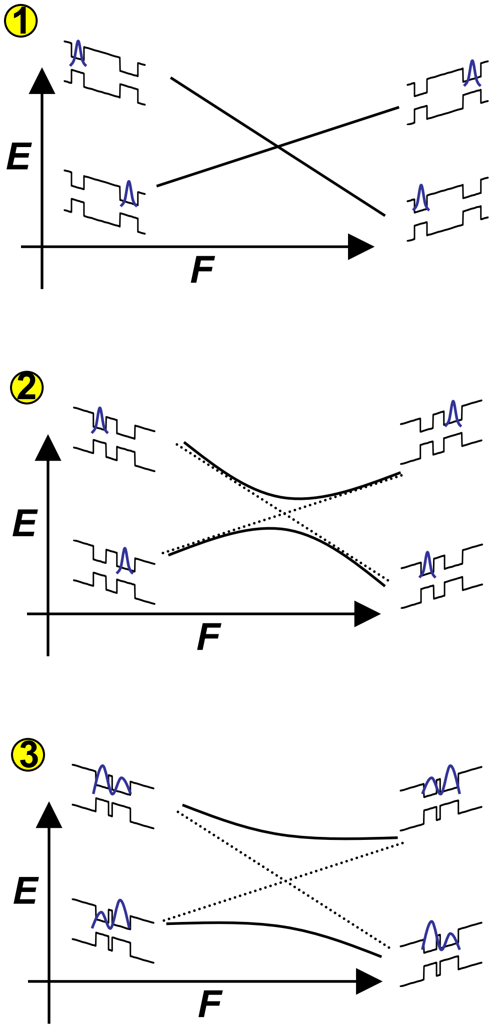

Figure 6.5: Three types of CQW structures are shown schematically: in the first, the conduction electrons are in isolated single well states; in the second, electron states are more coupled and tunneling is allowed; and in the third, the electron eigenstates have envelope functions spanning both QWs in the CQW structure. E is energy and F represents electric field across the CQWs

behavior is consistent with the three regimes, which we show schematically in figure 6.4. In sample 7-6-10, electrons tunnel inelastically from the higher energy well to the lower energy well, while in sample 7-2-10, the electron spin wave function spans both quantum wells resulting in reversible tunneling between wells.

6.4.3 Dependence of the g-factor on well width

In order to confirm the role of quantum well width and to rule out electron-hole exchange in causing the voltage dependence of the observed g-factor [179], experiments were done on three more structures. Figure 6.6a shows the Fourier transform of FR data taken at $B = 6$ T and $E_L = 1.58$ eV plotted as a function of $|g_e|$ and U_g (similar to grayscale plots in figure 6.4) for sample 8-4-8. The data indicate that spin oscillations occur at a single frequency corresponding to $|g_e| = 0.105 \pm .005$ with no measurable dependence on U_g. This g-factor corresponds to the expected value of g_e for an 8-nm wide GaAs QW. In addition, the lack of voltage dependence is expected in our model for a symmetric CQW structure; in particular, we find no evidence for a second excitonic g-factor. Data from sample 8-2-8 in figure 6.6b show a g-factor with a small dependence on U_g centered around the expected g_e for an 8-nm QW. The weak tuning is likely due to the significant portion of the electron envelope function which is pulled into the barrier in this highly coupled system. A similar Fourier transform is plotted in figure 6.6c for sample 5.7-3.8-7.7. Here we observe continuous tuning of g_e as a function of U_g as seen in the highly coupled sample 7-2-10. In this case, $|g_e|$ is observed to tune from 0.09 through 0 to 0.035 as U_g is varied from $+1.0$ V to -2.0 V. Since GaAs/Al$_x$Ga$_{1-x}$As quantum wells are predicted to have negative g-factors for w greater than 6 nm and positive values of g_e for smaller values

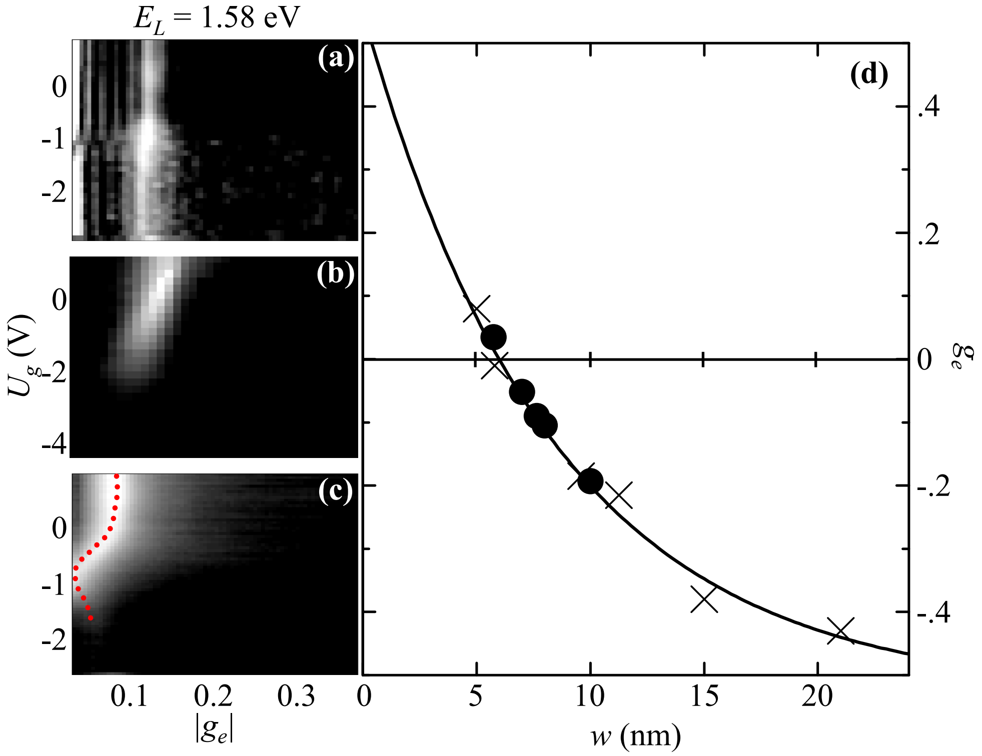

Figure 6.6: Dependence of g on QW width w. (a) Fourier transform of time resolved FR data measured in sample 8-4-8 plotted in a logarithmic grayscale as a function of $|g_e|$ and U_g at $B = 6$ T and $E_L = 1.58$ eV. Note that the g-factor, $|g_e| = 0.105$, has no observable dependence on U_g. (b) Similar data is plotted for sample 8-2-8 showing a very small change in g-factor as a function of U_g. Sample 5.7-3.8-7.7 in (c) shows continuous tuning from $|g_e| = 0.09$, via $|g_e| = 0$ around $U_g = 0$ V, and to $|g_e| = 0.035$. The red dots map the peak position of the Fourier transform in order to guide the eye. (d) g_e is shown as a function of w. Data drawn from work by Snelling et al. [63] is plotted as crosses and a fit to this data is shown as a solid line to guide the eye. Values of g_e extracted from FR data of our 5 samples for different w are plotted as filled circles.

of w [63], we can conclude that this sample shows tuning of the g-factor from -0.09 through 0 to 0.035.

Experimental data taken from work by Snelling et al. [63] showing g_e as a function of w are plotted as crosses in figure 6.6d. A fit to their data is shown as a black line in order to guide the eye. Values of g_e extracted from FR data of our 5 samples and correlated to the well widths are plotted as filled circles in figure 6.6d. From our samples we obtain g-factors of 0.038, -0.052, -0.065, -0.105, and -0.193 for well widths of 5.74, 7, 7.65, 8, and 10 nm, respectively. The sign of the g-factors was not explicitly measured, though an educated guess was made for the purposes of this plot. Figure 6.6d shows close agreement of our g-factor data with previous measurements of g_e as a function of quantum well width.

6.5 Localized moments in coupled quantum wells

The possibility of registering the conduction electron envelope function in one or the other QW in a CQW system makes it an attractive structure for the study of interactions between localized moments and conduction band electrons. Using a dynamic nuclear polarization (DNP) procedure similar to that described for parabolic quantum well (PQW) structures in section 4.4, we attempt to create nuclear polarization profiles in CQWs localized in one or the other QW depending on the gate voltage U_{pol} used during the DNP process. Such measurements do not conclusively demonstrate our ability to controllably polarize nuclei in one well or the other, mostly due to the low nuclear polarizations achieved and the short T_2^* of the electrons in the CQWs. Both of these effects contribute to a poor signal-to-noise ratio in our measurements compared to analogous measurements in PQWs.

CQW structures are also grown with spatially selective Mn-doping, i.e. with Mn-doping in one of the two wells, in the other, or in both. While some of these samples showed the presence of *s*-*d* coupling between electrons in the CQW conduction band and the Mn impurities, none of the structures showed the g_e tuning properties as a function of U_g observed in non-magnetic CQWs and described in section 6.4. It is likely that, even for low Mn-doping concentrations, the dipolar field due to the loosely bound holes and the ionic cores of the A^0 centers screens the externally applied electric field. In this case, changes in U_g do not affect the electron envelope function position, effectively pinning it in one of the two CQWs. Similar effects are observed in InGaMnAs/GaAs CQWs as in the GaMnAs/AlGaAs CQWs. While working GaAs-based CQW devices with Mn-doping may not be possible due to the electric charge of Mn impurities, similar structures may be possible in II-VI materials such as ZnMnSe, where Mn is electrically neutral [180].

6.6 Conclusion

The experimental data show electron spin precession in a fixed perpendicular magnetic field for CQW systems at low temperature. The effective g-factor of these structures is seen to depend both on which well electrons occupy and on the strength of tunneling between wells. Spin-resolved measurements reveal two distinct regimes of inter-well coupling, resulting in either the abrupt switching or the continuous tuning of g_e as a function of an applied electric field. Since the width of each QW determines the g-factor of electrons confined therein, future CQW structures may be engineered to switch between a variety of precession rates, including positive and negative rates and even $g_e = 0$, as observed in figure 6.6c.

Chapter 7

Conclusion

The main impetus behind our research into the coupling of mobile band electron spin and fixed moments is to gain a clearer understanding of these interactions, especially as the number of spins involved decreases an the dimensionality of the system is reduced. The study of ever smaller systems with ever fewer degrees of freedom has long been a trend in condensed matter physics, where the ultimate goal is to attain a fully quantum mechanical regime in which to do experiments.

The inherent disorder of solid state systems as compared with, for instance, trapped atomic gases, has always been a limitation in the application of pure quantum mechanics in the their description. Conversely, the same isolation and purity which makes atomic systems so spectroscopically clean and such nice models of quantum mechanics, makes them difficult to address, hard to couple, and virtually impossible to scale into useful devices. With advances in the design of semiconductor heterostructures, in the processing of sub-micron features, and with the increasing sensitivity of measurement techniques, single-electron condensed matter systems have been achieved; systems approximating artificial hydrogen atoms have been demonstrated, e.g. in single electron gate-defined quantum dots. The fundamental advantage in recreating such atomic systems in a semiconductor is the inherent control and accessibility afforded by the solid state. For instance, gate voltages can be used to alter quantum states of the system while advanced processing techniques allow for the scalable patterning of arrays of a given device.

Such atom-like devices could be used in the future to deepen our understanding of mesoscopic physics and quantum mechanics in general, a result which is already happening. Furthermore, they present the ideal medium in which to apply quantum mechanics to tackle technological applications, whether in the form of quantum computation or some other method of harnessing the behavior of quantum states.

The research presented in this volume, represents a step forward in understanding and developing controllable spin interactions in solid state systems. While none of the work discussed deals with single spin dynamics, the reduction of dimensionality and its effect on spin interactions is a central theme. The work on electronic-nuclear spin coupling in chapter 3 looks toward the detection and manipulation of small number of nuclear spins in solid state systems. In chapter 4 the patterning of a nano-scale nuclear polarization profile provides a proof of concept that the contact hyperfine interaction can be used to manipulate semiconductor nuclear spin in a spatially controllable way. As dimensionality and the numbers of nuclear spins decrease, similar results should be possible, e.g. in quantum wires and quantum dots. Measurements of the *s*-*d* coupling in chapter 5 and its dependence on confinement also focus on the role of reducing dimensionality. Indeed, the extension of the research towards the coupling of band electrons to single Mn centers in low-dimensional structures is ongoing. Furthermore, work on heterostructures and the control of carrier spin within them is relevant to future systems with fewer dimensions and with electron occupation numbers approaching 1. Hybrid systems combining the control of the parabolic quantum wells of chapter 4 or the coupled quantum wells of chapter 6 with gate defined quantum dot geometries present a intriguing opportunity for building devices with exquisite control of single charges and spins.

Appendix A

Sample structures

A.1 Parabolic quantum wells

Table A.1 shows an example of the parabolic quantum well (PQW) structures used in the experiments described in chapter 4. The first samples investigated

Table A.1: The layers in a typical PQW structure are listed here as they are grown on top of an (001) semi-insulating GaAs substrate from bottom to top. SL stands for superlattice and LT stands for low-temperature.

thickness (nm)	layer description
5	GaAs
50	$Al_{0.4}Ga_{0.6}As$
100	PQW 40% to 7% to 40%
350	$Al_{0.4}Ga_{0.6}As$
7.2	$6 \times 0.6/0.6$ GaAs/AlAs SL
485.6	LT-grown GaAs
7.2	$6 \times 0.6/0.6$ GaAs/AlAs SL
200	GaAs
50	n-GaAs ($n = 2 \times 10^{18}$ cm^{-3})
50	GaAs
80	$20 \times 2/2$ GaAs/AlAs SL
50	GaAs

Table A.2: The layers in a typical 7-6-10 CQW device are listed here as they are grown on top of an (001) semi-insulating GaAs substrate from bottom to top.

thickness (nm)	layer description
7.5	GaAs
50	$Al_{0.33}Ga_{0.67}As$
10	GaAs QW (CQW)
6	$Al_{0.33}Ga_{0.67}As$ barrier (CQW)
7	GaAs QW (CQW)
350	$Al_{0.33}Ga_{0.67}As$
500	LT-grown $Al_{0.33}Ga_{0.67}As$ structure
200	digital $Al_{0.13}Ga_{0.87}As$
200	n-$Al_{0.13}Ga_{0.87}As$ ($n = 4 \times 10^{18}$ cm^{-3})
1000	$Al_{0.33}Ga_{0.67}As$ etch stop layer
300	GaAs

were grown by D. C. Driscoll and are the same ones samples used in experiments on g-factor tuning and g-tensor modulation resonance by other members of the Awschalom lab [15, 16, 57]. Later samples with the same fundamental characteristics were grown by R. C. Myers.

A.2 Coupled quantum wells

We list the layers of a typical coupled quantum well (CQW) device discussed in chapter 6 in table A.2. R. C. Myers grew all of these samples.

A.3 Etch stop layers

Etch stop layers are often incorporated into both PQW and CQW samples in order to facilitate time-resolved Faraday rotation (FR) measurements which require transmission of the probe through the sample structure. The transmission geometry is preferred to the reflection geometry (time-resolved Kerr rotation) in

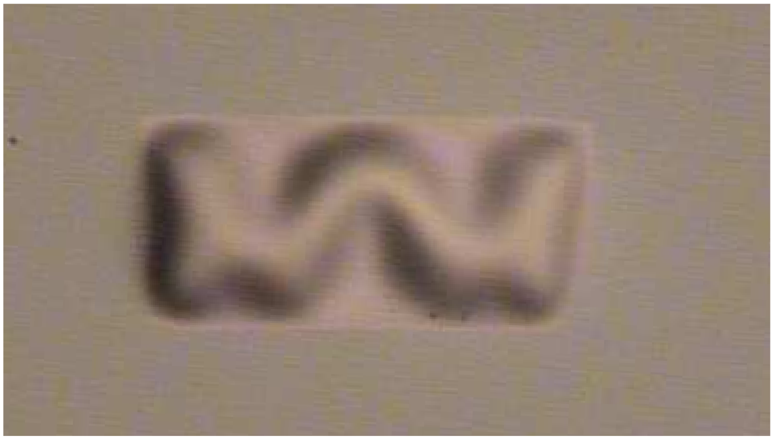

Figure A.1: A photograph taken with an optical microscope of a rectangular etched window in a CQW sample. The inhomogeneous "bubbling out" of the sample due to strain mismatching in the growth layers is clearly observable. The etched window is about 300 μm × 100 μm and ~ 1 μm thick.

measurements requiring a non-zero angle θ between the sample surface and the applied magnetic field. The geometry of the cryostat makes it difficult to collect a reflected probe from an angled sample. Therefore, in most measurements involving a non-zero nuclear polarization, the samples must be measured in the transmission geometry. This requirement behooves us to etch a window into the back of the sample removing the GaAs substrate, whose band-gap energy is smaller than the GaAs/AlGaAs QW's bandgap. The spray etch procedure described in section B.8 and the incorporation of an AlGaAs etch stop layer in the growth make this selective removal of the substrate possible.

If the experimental conditions do not require $\theta \neq 0°$, then the reflection geometry is preferred and measurement can be done with $\theta \simeq 0°$. Samples whose substrates have been etched away are very fragile as the material left behind in the window is ~ 1 μm thick. In addition, strain built into the sample structure causes these windows to "bubble out" as shown in figure A.1 making the sample surface inhomogeneous. Strain and the effective angle of incidence of the laser can vary across the sample window. In order to obtain consistent and reproducible results, great care must be taken to stabilize the position of the laser spot on the sample. Unetched samples measured in the reflection geometry do not present these challenges.

Further details on the growth of these an all the other samples described in this dissertation, especially the Mn-doped QWs described in chapter 5, can undoubtedly be found in the upcoming thesis of the grower, R. C. Myers [127].

Appendix B

Sample processing

B.1 Introduction

In order to take full advantage of the control over the carrier envelope functions afforded by semiconductor heterostructures, it is often necessary to tilt the bands by applying an external electric field. In this section we will cover a simple process used to make devices in which an electric field can be applied across quantum wells (QWs) along the confinement direction. In particular, we use this process in the preparation of the parabolic quantum well (PQW) and coupled quantum well (CQW) structures discussed in chapters 4 and 6.

The following process is meant for samples designed using the same principles as those discussed in appendix A. A low-temperature (LT) barrier of GaAs or AlGaAs about 500-nm thick must separate the QW structure from the n-doped layer acting as the back-gate. This layer acts as conduction barrier [102] preventing current from flowing from the n-doped back-gate to the Ti/Au front-gate deposited onto the sample surface. A brief outline of the process follows. First, we etch away the QW layer from a region of the sample onto which we deposit back-gate pads. We then anneal the sample so that these pads spike down and contact the n-doped back-gate layer, which lies about 1 μm below the surface. Next we evaporate a transparent layer of Ti/Au onto the QW region of the sample to serve as a front-gate. If the sample is to be used in the transmission geometry, an additional polishing, lithography, and spray-etching step must be completed at this point. Finally, we mount the sample and contact it either using a manual indium-bonding procedure or using a wire-bonder. All of the aforementioned steps are described for students with a rudimentary knowledge of clean-room techniques and should be fairly obvious for anyone with extensive processing experience.

B.2 Etching a mesa

Before starting the process, we cleave a few pieces (usually 2 or 3, just in case) of the sample for processing; typical samples are no larger than 5 mm $\times$ 6 mm. Depending on the application of the device, different amounts of the QW structure are to be etched away. In the case of DC operation, the capacitance of the device is irrelevant, and so we process large front-gate and and back-gate pads, making them easy to contact, as shown in figures B.1 and B.2a. For such devices, we typically etch away the QW layer from half of the sample surface. To do so, we spin and develop photoresist (usually 4110, see table B.1) and then use a wet-etch to etch down just above the back-gate ($\sim$ 200 nm above the n-doped region, meaning etching down $\sim$ 1 μm). Etching too far results in the depletion of the n-doped layer; not etching far enough will prevent the back-gate pads from contacting the n-doped layer during the anneal. We use a wet-etch consisting of H_2SO_4:H_2O_2:H_2O (1:8:80), whose etch rate is 6–10 nm s^{-1} depending on the Al concentration of the structure (AlGaAs etches faster in this solution than GaAs). It is a good idea to calibrate the etch rate for each

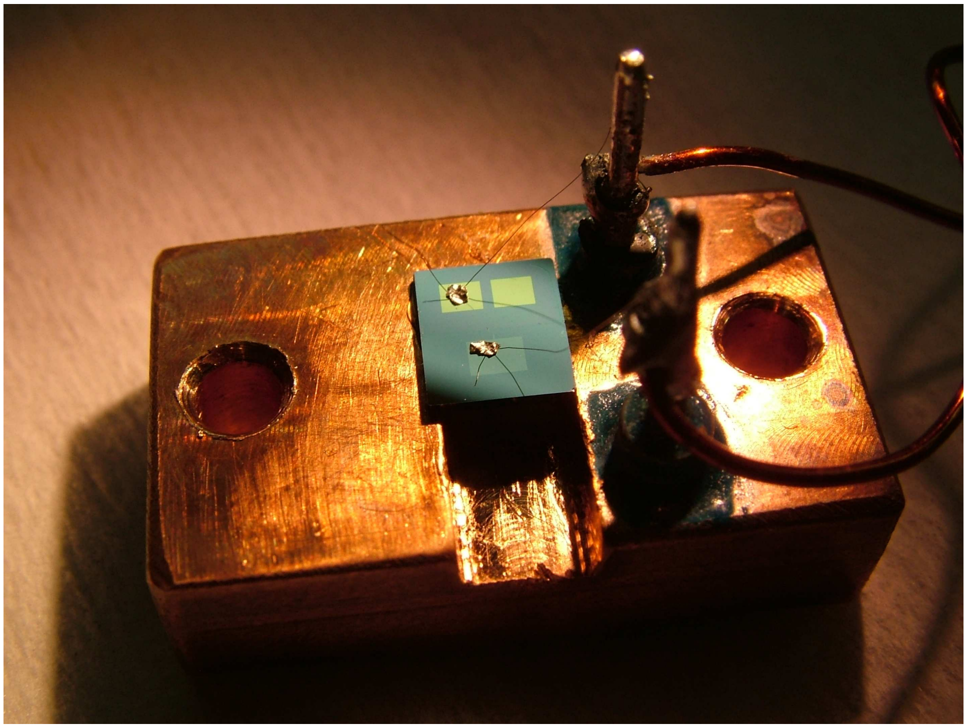

Figure B.1: A photograph of a CQW sample wired to its sample mount. The front-gate is visible as the lighter rectangular region on the bottom of the sample. The two back-gate pads appear above it as two gold squares. Thin gold wire connects the two external pins to the indium blobs stuck onto the sample contacts.

sample structure, using the Dektak to measure the etched depth.

For RF applications, a large capacitance is undesirable as it will result in a low impedance ($Z = \frac{i}{\omega C}$) and thus small RF voltages across the QW structure. In this case, we strive to make the overlap area of the front-gate and the back-gate as small as possible, as shown in figure B.2b. These devices require a two-step etch, leaving a thin strip of QW layer in the middle of the sample, a region etched down to just above the back-gate layer ($\sim 1\ \mu$m deep) on one side, and a region etched through the back-gate layer ($\sim 1.5\ \mu$m deep) on the other. The same general photolithography techniques and wet-etch solution are used with these devices as with the DC devices.

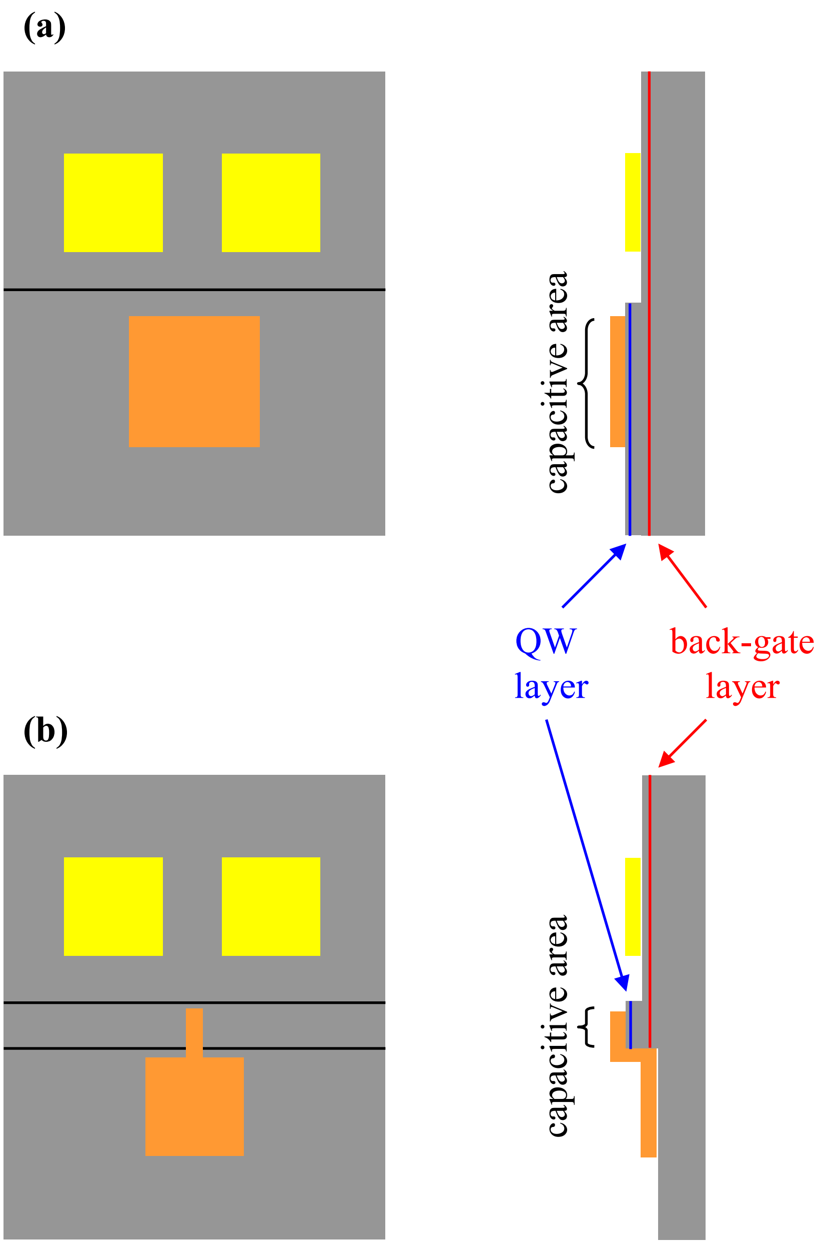

Figure B.2: A diagram showing the final sample structure for the application of (a) DC and (b) RF electric fields across a QW structure. On the right are diagrams of the sample viewed from above, with black lines indicating changes in sample height, yellow squares indicating the back-gate pads, and orange region representing the semi-transparent front-gate. On the left are cross-sectional views of the side of the sample showing the QW and back-gate layers as blue and red regions, respectively. Thicknesses of the metal and semiconductor layers are not to scale.

Table B.1: Developing 4110 photoresist (positive).

step	description
1	Spin at 5 kHz for 40 s
2	Soft bake (90–100°) for 1 min
3	Expose (positive) for 15 s at 7.5
4	Develop in 4:1 AZ400K:H_2O for 1 min

Table B.2: Developing 5214 photoresist (negative).

step	description
1	Spin at 5 kHz for 40 s
2	Soft bake (90–100°) for 1 min
3	Expose (negative) for 15 s at 7.5
4	Hard bake (110–120°) for 2 min
5	Flood expose for 1 min at 7.5
6	Develop in 4:1 AZ400K:H_2O for 1 min

B.3 Evaporating back-gate pads

After confirming the success of the etching procedure using the Dektak, we are ready to evaporate the back-gate pads. We typically evaporate two adjacent pads so that after annealing we can check that they have made and ohmic contact to the n-doped back-gate layer by measuring the resistance across the pads. Once again, using photoresist (usually 5214, see table B.2) and a mask, we pattern two back-gate pads of the desired size, typically 1.5 mm $\times$ 1.5 mm. Once the resist is developed and the the whole sample surface, save the pad area, is covered in resist, we are ready to deposit.

Using electron-beam deposition, we put down the following layer structure from bottom to top: 5 nm of Ni, 25 nm of Ge, 65 nm of Au, 20 nm of Ni, and 500 nm of Au.

B.4 Annealing the sample

Once the back-gate pads have been evaporated, we anneal the sample such that the metal in the pads spikes down into the n-doped layer and forms an ohmic contact with the back-gate. The procedure is usually done on the strip annealer, but can also be done using the rapid thermal annealer. For the strip annealer, we load the sample and pump down the chamber. We then flow forming gas such that the pressure equilibrates to 1 Torr. We adjust the temperature set-point to 420°C and as the temperature rises past 350°C, we start a timer. After timing for 1 minute, we reset the set-point to 21°C and wait until the temperature slowly drops below 100°C. At this point, we vent the chamber and remove the sample. To confirm that the back-pads have spiked down into the n-doped layer, we measure the resistance across the pads, which should be less than 100 Ω (it is typically 10–20 Ω).

B.5 Evaporating a front-gate

At this point we pattern more resist (5214, see table B.2) onto the sample to define the front-gate area as shown in figure B.2. The shape and alignment of the particular front-gate design depends on the application of the device. A simple square area about 1.7 mm × 1.7 mm in size suffices for most DC applications.

Using electron-beam deposition, we put down 5 nm of Ti followed by 3 nm of Au. A number of other combinations work in the range of 2–10 nm of Ti and 3–5 nm of Au. Thicker metal layers have lower resistances, but are also less transparent than thin layers. Before depositing Ti, it is important remove the oxide on the surface of the source. This can be accomplished by doing a predeposition for a few seconds with the deposition shutter closed. Once the pressure in the electron-beam chamber begins to drop dramatically, the oxide layer has been removed. We now can begin depositing Ti onto the sample.

When depositing Ti/Au on sample with an RF gate structure as shown schematically in figure B.2b, we mount the sample at a $\sim 30^\circ$ angle such that we deposit an electrically continuous semi-transparent film across the $\sim 1.5\ \mu$m deep step on the sample surface, as shown on the right side of figure B.2b. A custom-made aluminum “angle jig” should be available for this purpose in one of the group boxes in the clean room.

B.6 Polishing the sample

For optical experiments requiring the transmission of light through the sample, e.g. Faraday rotation or absorption, we must etch away the GaAs substrate from a small window in the front-gate area. Note that this is necessary for GaAs/AlGaAs QWs, but not for InGaAs/GaAs QWs where the band-gap energy of the QW is lower than that of the substrate. If a window is not required, we can skip directly to mounting and contacting the sample discussed in section B.9.

In order to minimize the amount of material which we have to etch away, we polish the sample down, from the substrate side, to a thickness of 150–250 μm. Polishing the sample further makes it extremely fragile and difficult to handle; leaving more material makes the subsequent spray-etch lengthy, exaggerating the effects of its anisotropy.

Before taking the sample out of the clean-room for polishing, we spin some thick photoresist (4210) on the front side of the sample to protect its surface. We develop the resist without exposing it, such that the entire surface is protected. Note that we have noticed that failure to develop the resist, results in permanent residue on the sample surface which can interfere with optical experiments. At this point we wax the sample, face-down (i.e. the contacts and the protective resist facing down), onto a piece of a glass slide, which we cut slightly larger than the size of the sample. This step protects the front of the sample during the subsequent process and makes its handling easy even after it has been polished down and is extremely fragile. Care must be taken in pressing the sample down and in moving it around to squeeze out as much wax as possible from between the sample and the glass slide. For the rest of the process to go smoothly, the sample must be waxed flat to the glass slide.

We next wax the glass slide and sample flat to one of the polishing chucks found in the sample processing area. This polishing chuck is then screwed onto the bottom of our custom-made polishing rig. Then we hand polish the sample using 9-μm Fibrmet discs from Buehler (part number: 69-3271). We place the disks on a flat glass surface and flow de-ionized water as we polish. We take care to use smooth circular or figure-eight motions as we polish off no more than ~ 25 μm (one tick on the polishing rig) of material at a time. Checking the progress of the polish by measuring the sample height regularly is recommended.

Once we attain the desired thickness (no thinner than 100 μm), we finish the surface by polishing on a 8” Chemomet wheel from Buehler (part number: 40-7918) with a mixture of bleach and 0.05-μm abrasive powder from Buehler (part number: 40-6301-016). There are no exact proportions for the bleach mixture, but it should look “milky”. To achieve a nice mirror-finish, we advance the polishing rig 75–100 μm (3–4 ticks) from its last position and polish the sample with slow and smooth motions. We do *not* press down on the top of the polishing rig as we did during the coarse polishing, simply letting the weight of the polishing rig provide pressure on the sample. Finishing the sample usually takes some practice in order to consistently produce a clean mirror finish. Note that some care should be taken to avoid getting bleach on one's clothes as it will permanently ruin them.

A smooth mirror finish on the back of the sample is important so that the photoresist which is subsequently spun on this surface flows smoothly and covers the sample uniformly. If the surface is rough, small holes and gaps form in the resist, which during the spray etch result in unintentional holes through the sample. These holes compromise the structural integrity of the sample and cause it to become extremely fragile and susceptible to breakage, especially during the bonding procedure.

B.7 Defining the measurement window

Once the sample has been polished and cleaned, it should be brought back to the clean-room, still attached to the glass slide. Here we use photoresist (usually 5214, see table B.2) to pattern the back surface of the sample (the side which we have just polished) with a small window, usually 300 μm × 300 μm (due to the anisotropy of the spray etch these dimensions will typically result in a window which is about 100 μm × 200 μm). In order to align this window behind the front-gate of the sample, we use the infrared (IR) mask aligner. This aligner allows the user to shine a light through the sample and to look at the IR light transmitted through it. In this way, we are able to align the mask used for patterning the small window directly above the already patterned Ti/Au front-gate on the other side of the sample. Care should be taken in this process not to crush the sample between the mask and the glass slide, as it is very fragile at this point. Once the resist has been patterned and developed, we take the sample out of the clean-room for the final time and prepare for the spray-etch.

B.8 Spray-etching the sample

To spray-etch the sample, we first wax it and its glass slide to a “T”-shaped rig made of glass slides in order to suspend the sample in a beaker over the spray-etching solution and in front of the spray-etcher nozzle. The spray-etcher consists of two perpendicular glass nozzles joined together and it operates on the Venturi principle: flowing pressurized nitrogen gas through the top tube sucks up etchant through the bottom tube, whose intake is dipped into the etchant solution, and delivers it onto the sample surface in a powerful spray [116]. The etchant solution used is NH_4OH:H_2O_2 (7:250). Care should be taken in aligning patterned window on the back of the sample with the etcher nozzle in order to achieve a speedy and uniform etch. During the spray-etch, we shine a bright light onto the back of the sample (the side being etched) and set up a telescope focused on the front of the sample aimed at the expected position of the window. Once the substrate has been etched and we reach the AlGaAs stop-etch, light will transmit through the newly etched window in the sample. After seeing this transmission, we wait no more than 5 to 10 seconds to stop the spray-etch and rinse the sample off in de-ionized water. Depending on the thickness of the sample, the strength of the etchant, and the composition of the layers preceding the stop-etch layer, the spray etch can take anywhere between 20 and 60 minutes. It is therefore, very important to carefully watch and time the first sample etched.

After the spray-etch, we heat the sample and the “T”-shaped rig on a hot plate to separate them and then we place the sample attached to its glass slide in a beaker of acetone for lift-off. After soaking for 20–30 minutes, the sample will either lift-off on its own or will easily slide off the glass slide. Extra care should be taken in handling the sample at this point, as the window is very fragile. After cleaning, the sample is ready to be mounted and contacted.

Sometimes the sample can be slid off of the glass slide by simply heating it on a hot plate and pushing it off with a pair of tweezers, though this is not recommended as it often results in a shattered sample window. Also, we avoid the use of the sonicator to aid in lift-off as the vibrations result in a shattered window.

B.9 Contacting the sample

We affix the sample to its mount using either rubber cement or GE varnish. In both cases, as little adhesive as possible should be used in order to avoid getting residue on the windows of the sample space in the cryostat, as described in section C.4.2. Using a conservative amount of adhesive also prevents an excess from covering the sample surface. Once the adhesive has dried and fully cured, we are ready to contact the sample.

If we have mounted the sample to a chip carrier, at this point we can use the wire-bonder to contact the sample to the carrier. Once bonded, the chip carrier is simply mounted into its slot on the sample mount. This scheme is preferred for samples with RF applications, which have small gates and pads patterned on the surface. Contacting small regions is often only possible using the wire-bonder, which gives the user more precision and control in the contacting process than manual indium-bonding does.

While the indium-bonding process is inherently “sloppier” than wire-bonding, it is also faster and easier. Learning to use the wire-bonder efficiently requires time and patience and is not always worth the effort, especially for samples used in DC experiments where the contact pads can be quite large. For such samples, indium-bonding is the preferred contacting scheme. In this process we use a

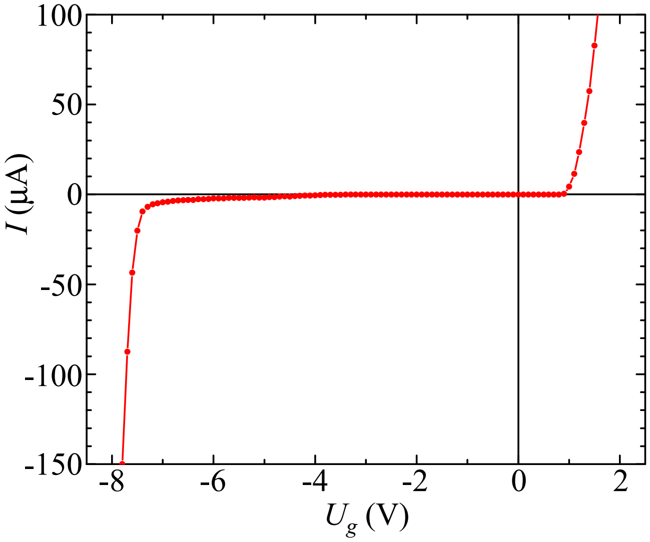

Figure B.3: A typical I/V curve for a CQW structure taken at $T = 5$ K. PQW samples have similar I/V characteristics. For the voltage ranges used during experiments $I < 10\ \mu$A.

microscope to look at the sample surface and we contact thin gold wires to the sample by pressing them down onto the contacts with small blobs of indium metal. If the sample surface is clean, the indium sticks to the contacts and the wire, providing a robust electrical connection. We typically use thin gold wire with a diameter of 0.001” and pure indium in this process. On the other end, the gold wires are soldered onto large pins on the sample mount using conventional solder. A sample contacted using this method is shown in figure B.1, where the pins, wires, indium blobs, and contacts are all clearly visible. For samples with etched windows, special care should be taken not to put excessive pressure on the sample as this will result in a shattered window or a broken sample.

Once the sample pads have been contacted, the connection should be tested at room temperature and then again in the cryostat at the operating temperature, e.g. $T = 5$ K. A typical I/V curve from a CQW structure with indium-bonded contacts is shown in figure B.3.

Appendix C

Operation of an Oxford Spectromag

C.1 Introduction

Magneto-optical cryostats are used to impose large magnetic fields (up to 8 or 9 T) and low temperatures (down to 1.5 K or even 350 mK using the helium 3 insert) on a sample while providing optical access to it. In order to do so, these systems use a split-coil superconducting magnet rather than a simple solenoid. In the Awschalom lab, this instrument, and specifically the Oxford Spectromag model (see figure C.1), has been a work-horse in a number of optical measurements of spin dynamics in semiconductors. There are several Spectromag systems in the lab; in this section we cover some important maintenance and trouble-shooting techniques which students running these systems should know. This appendix is by no means a complete reference on the Spectromag, but should serve as a supplementary resource to the manual [181] and other literature available on the subject. Detailed instructions on cooling the system down and on the helium transfers can be found elsewhere and are not covered here.

C.2 Installation

Installing a Spectromag system can be either a short and painless process or a long drawn-out drama. In order to ensure the former scenario, there are several steps which can be taken. First, the Oxford instruction manual has a detailed section on the installation procedure which should be followed carefully. Additional precautions which should be taken in order to ensure a smooth installation and to avoid future problems are covered in this section.

Note that once the system is open, gloves should be used at all times while working on it in order to prevent the accumulation of hand grease in the vacuum space. While Oxford is notorious for shipping cryostats whose vacuum spaces are covered in a film of pump oil, there is no reason to add to the mess. In fact, it is a good idea to clean as much of the oil from the vacuum space as possible using acetone, isopropyl alcohol, and methanol before proceeding with the first cool-down. Oil left in the system may end up coating windows in the system.

C.2.1 Re-doing the indium seal

During the first stages of the installation, the tail of the system is removed and the shipping bungs are removed. This is an ideal time to familiarize oneself with the innards of the the cryostat and most importantly for re-doing the indium seal at the bottom of the variable temperature insert (VTI). While these seals are tight during testing in England, they can loosen in transit and cause a leak during cool-down. It is wise to simply re-do the seal before going any further.

The indium seal in question is at the bottom of the VTI, between the VTI and the capillary leading to the needle valve (NV) and the helium bath. The two

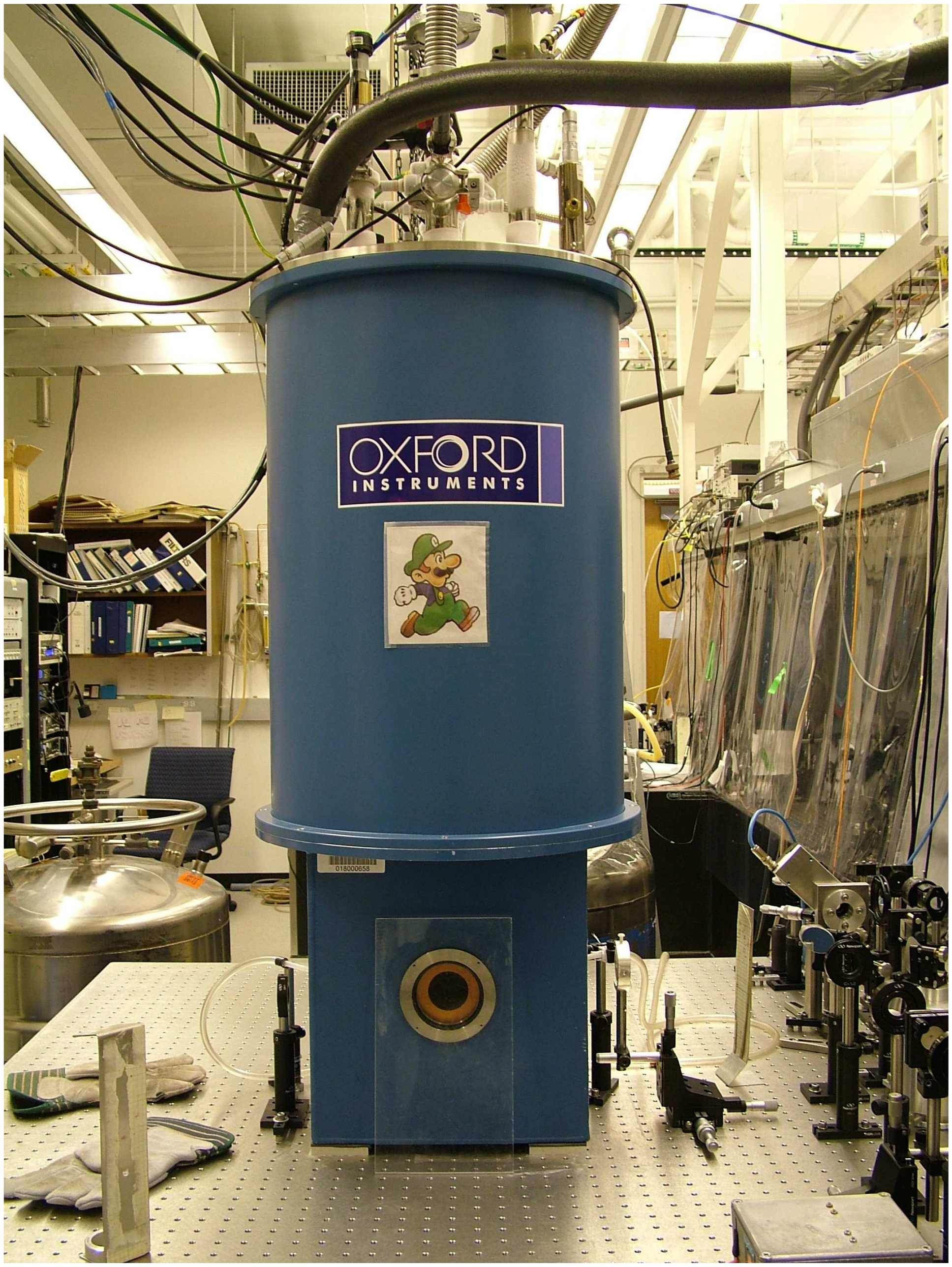

Figure C.1: A photograph of Luigi, one of the Oxford Spectromags in the Awschalom Lab.

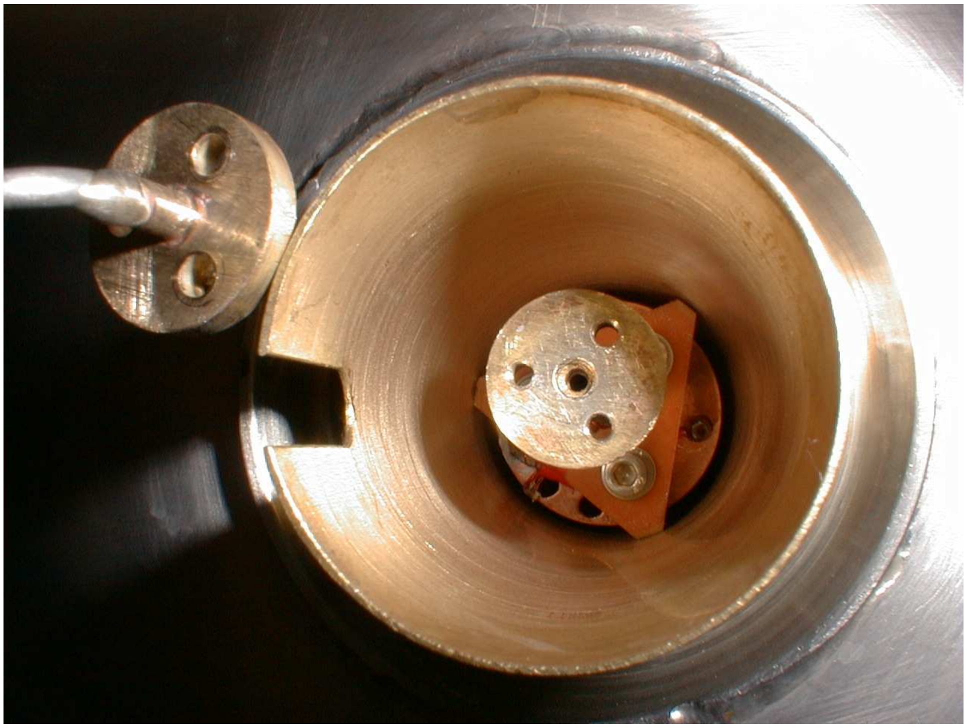

Figure C.2: A view from below the Spectromag of the two flanges involved in the indium seal. The flange in the center leads to the bottom of the VTI, while the flange on the left leads to a capillary attached to the NV assembly. Indium residue is visible on the center flange.

flanges between which the seal must be made are shown in figure C.2.

In order to undo the original seal, unscrew the bolts holding it together and then use a small flat-head screw-driver to pry apart the flanges. Special care must be taken in this process in order not to damage the soft brass flanges and cause a permanent leak. Sometimes the flanges have holes for "jacking screws" in which case the removal should be straightforward. We carefully remove the indium from the flanges using a small wooden stick taking care not to scratch the flange surface. Scratches, especially radial ones, can cause leaks in the seal.

Once the old seal has been removed and minimal indium residue remains, we can make a new seal. In order to do so, we use thin indium wire, which is usually provided along with the spare parts for a new Spectromag, and wrap it in a circle around the raised lip in the center of the flange. It is sufficient to simply overlap the ends of the wire rather than twisting it. We then make sure that the indium is short enough that it does not protrude from the edges of the flanges. Also, we apply a light coat of silicone vacuum grease on the wire before assembly in order to make the indium o-ring peel off more conveniently next time. Carefully screwing the bolts back in with the indium o-ring in place, we re-seal to flanges. Though tightening firmly, we take care not to distort the brass flanges or to strip the screws. The seal should be leak-checked at room temperature before proceeding with the cool-down.

C.2.2 Re-entrant tubes

As mentioned in section C.2, Oxford has a tendency to ship cryostats whose vacuum spaces are covered in a film of oil. While a significant amount of oil can be cleaned up during the first opening, it will always stick around, usually hiding in the super-insulation where we cannot easily clean it. The oil's presence rears its ugly head shortly after the first cool-down in the form of an opaque annular film which forms on the four nitrogen windows as shown in figure C.3. These windows are attached to the nitrogen shield shown in figure C.4 and are therefore held at 77 K when the cryostat is cold. Acting as cold-traps for the pump oil, the windows accumulate more and more oil as the cryostat stays cold, eventually obscuring the optical path to the sample. This phenomenon has been observed in several of Oxford's latest Spectromags despite our alerting them to the problem. Note that we have never observed oil to condense on any of the other two sets of windows in the system: neither the outer windows nor the VTI windows, even though the latter are also generally quite cold.

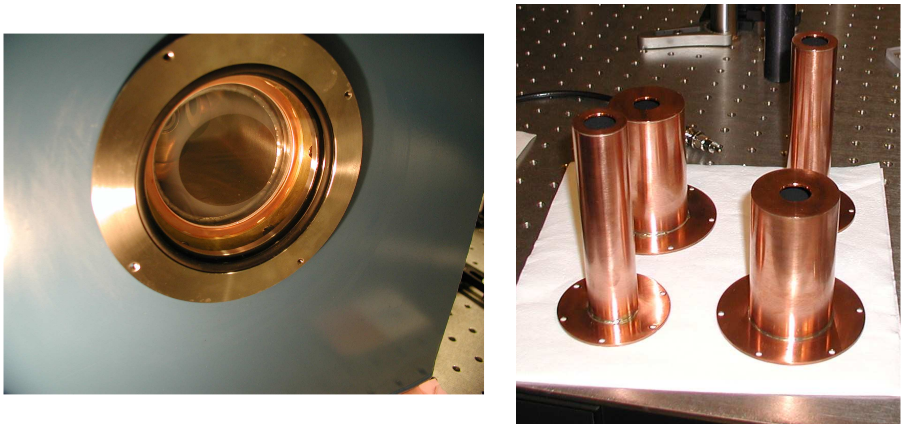

Figure C.3: In the left panel is a photograph of an annular oily residue which tends to build up on the nitrogen windows several days after cooling the system down. The re-entrant tubes shown in the right panel are installed in place of the nitrogen windows to solve this problem.

To fix this problem we replace the nitrogen windows with copper re-entrant tubes, shown in figure C.3. While this installation cuts down on the ease of optical access to the sample, it has been the only successful strategy at fighting the oil condensation. The tubes present a large area of copper at 77 K which acts as a cold trap for the oil and essentially pumps it from the vacuum space. They also serve as effective thermal radiation shields, keeping the cryostat's boil-off rates normal.

The tubes should be requested from Oxford before installation of the system as they have to be custom made for it. In screwing the tubes to the nitrogen shield, care must be taken not to cause a touch between them and the magnet casing causing a thermal short between the helium and nitrogen spaces. As Oxford is likely to ship crooked and asymmetrical tubes, there are preferred orientations for the tubes. Even if a touch does not occur at room temperature, it may develop upon cooling down as different components contract. Since the re-entrant tubes protrude into the magnet casing with very little space between them and the casing, they should be prime suspects in any investigation of a

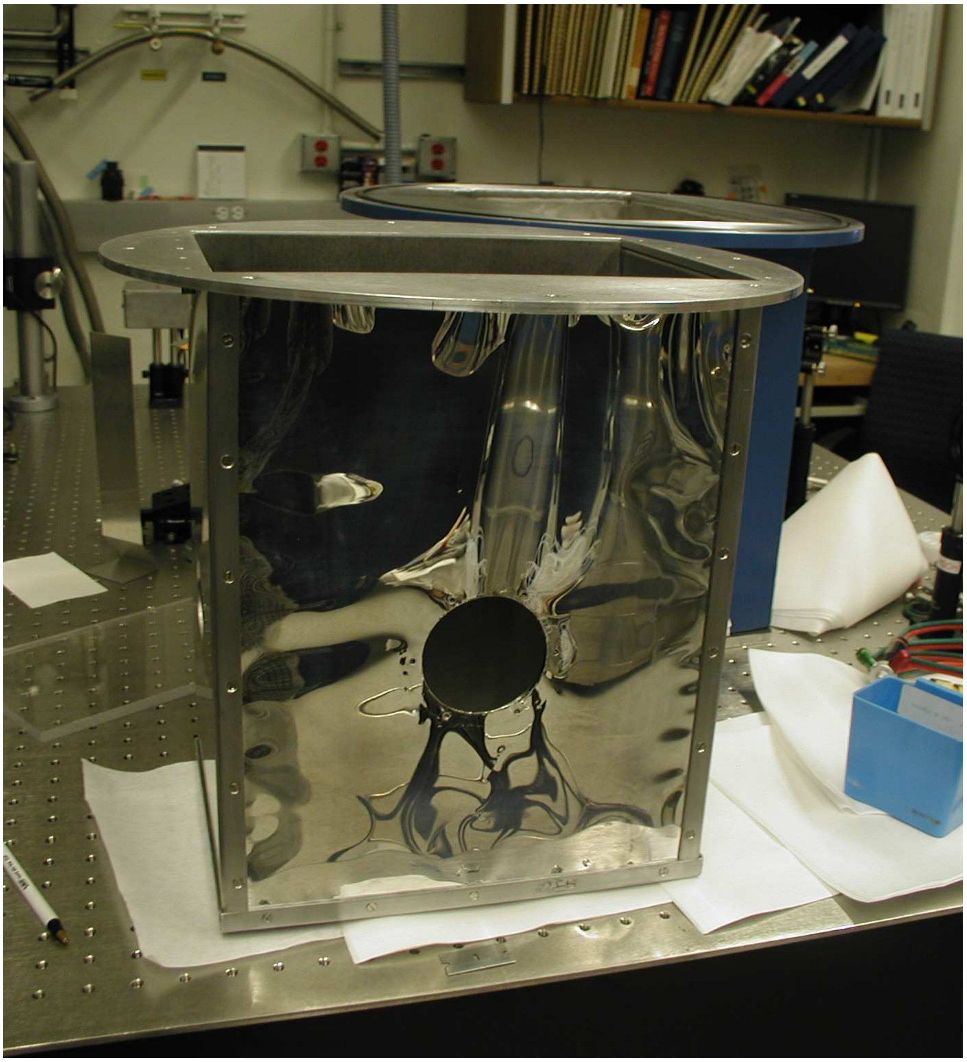

Figure C.4: The nitrogen shield is shown here once it has been unbolted from the tail and the nitrogen windows have been removed.

touch. Often the only way to solve these types of problems is to continue trying new orientations and configurations of the re-entrant tubes until there is no longer a touch.

C.2.3 Manifold design

Before running the system, we must prepare a gas-handling system to interface with the cryostat. This apparatus is typically mounted on a wall near the cryostat and is connected to it through a series of over-head bellows (typically flexible metal tubing from American Boa Inc.). A design for a system with a lambda space is shown in figure C.5. Systems without lambda spaces require only two, rather than three, independent outlet ports. The manifold must be welded together by the machine shop and carefully cleaned and leak checked before use. A full manifold design, complete with Swagelok input fittings is shown in figure C.6.

Along with preparing a manifold, it is also essential to build a respectable break-out box in order to have orderly access to the handful of resistances and heaters which must be monitored and used during the course of cooling down and operating the system.

C.2.4 Setting up the power supply

Before first ramping up the magnet, we must install the magnet power supply. We carefully follow the installation instructions, setting all of the appropriate parameters and break-points in the supply's memory.

Setting the correct maximum current is critically important. Each system has a maximum current, i.e. magnetic field, which it can support before quenching (more on this subject in section C.7). For Spectromag systems this is 7-8 T

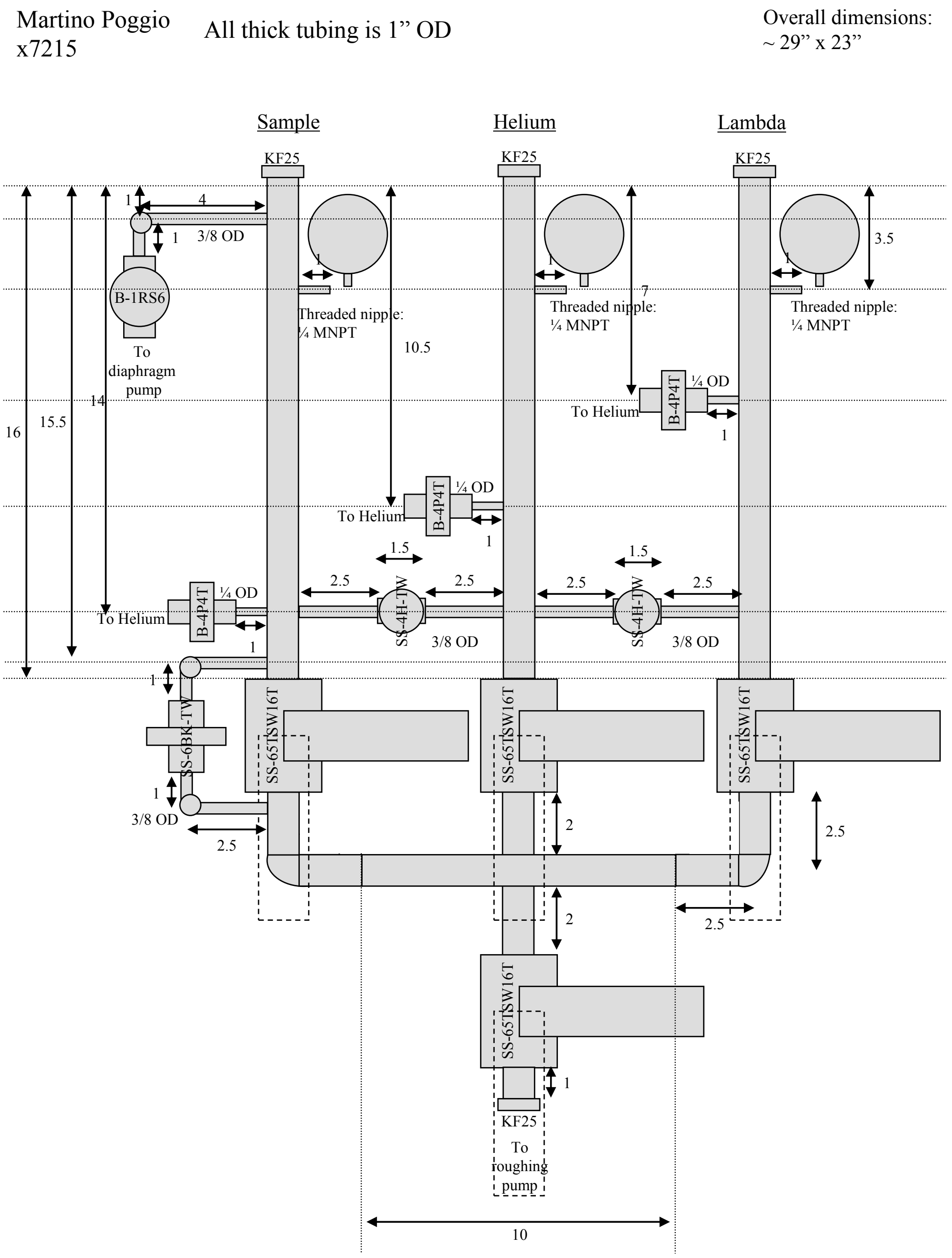

Figure C.5: A design for a gas handling manifold for a Spectromag system. All dimensions are in inches and part numbers refer to valves readily available from Ventura Valve and Fitting Co.

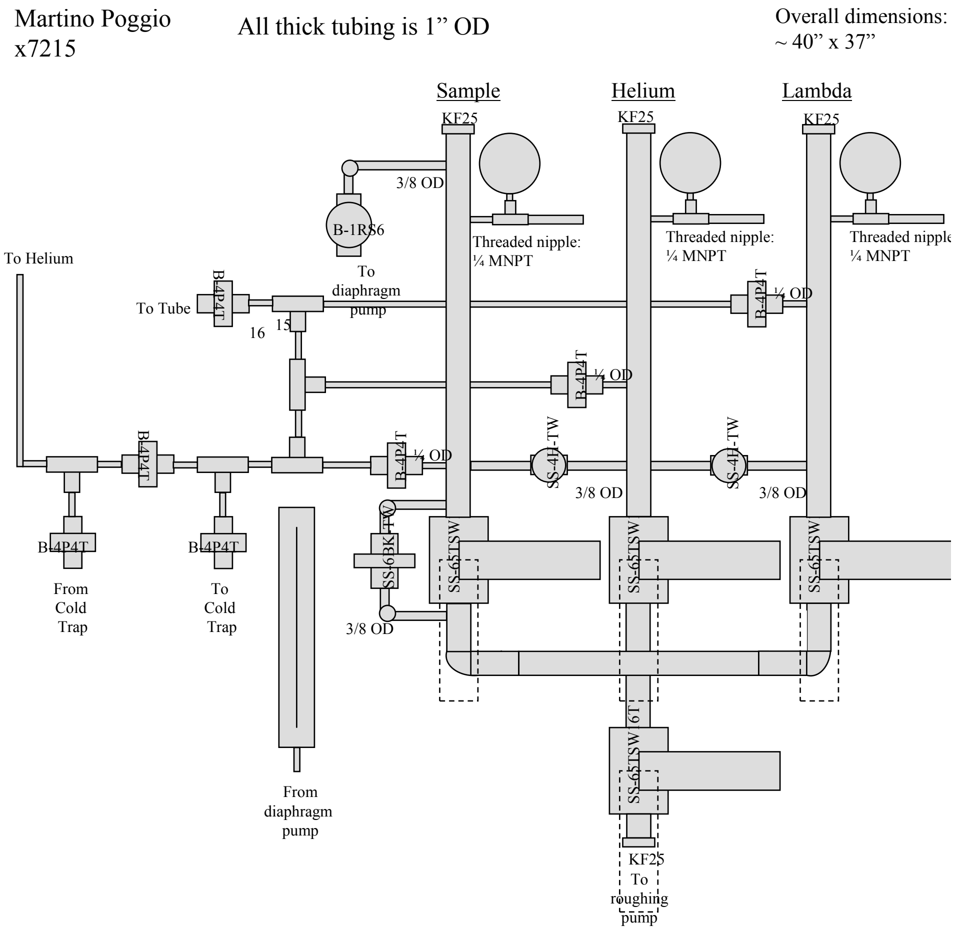

Figure C.6: A full design for an assembled gas handling manifold.

depending on the magnet; before changing the power supply settings, this value should be double-checked in against the value listed in that system's manual. If the maximum current in the power supply is set above this threshold, it is very likely that at some point during its operation, through some manual, programming, or unforeseen computer error, the magnet will quench. Under the wrong circumstances, quenches can damage a split-coil system beyond repair, so they should be avoided at all costs. A correct setting of the maximum current will prevent either the user or the computer from ramping the magnet beyond its critical field.

In systems with a lambda fridge there are two maximum currents: the maximum current achievable under normal operation and that achievable when the lambda fridge is cold, e.g. 8 and 9 T, respectively. Since the small boost in magnetic field is rarely worth the effort and risk of using the lambda fridge, the lower current should be set as the power supply's maximum. This current is easily changed if the user eventually wants to use the lambda fridge to go to the true maximum field. Having the maximum set beyond the critical current for normal operation, however, voids the benefit of this safety feature and will eventually lead to a quench.

C.2.5 Condensation

Despite the carefully controlled humidity in the lab and the thermal isolation of the inside of the Spectromag from it outer components, certain surfaces on the Spectromag remain cold enough to often be covered in water condensation. This mist can be especially annoying when it accumulates on the outer windows as it can interfere with optical measurements. This problem is easily solved by setting up a permanent spray of filtered nitrogen gas to dry out each window.

Despite the filtration, particles are inevitably sprayed onto the windows along with the nitrogen. Over time residue builds up and it is therefore a good idea to periodically check the state of the windows and to clean them.

Another trouble spot is the top of the cryostat (see figure C.7), through which the cold nitrogen and helium boil-off gases pass on their way out of the system. Condensation from the fittings shown in figure C.7 drips onto the top flange of the cryostat and seeps into the welds on this flange. This process causes the welds to rust and eventually to leak. While these leaks can be repaired by opening the system and re-welding the seals from the inside with the help of a skilled welder, it is far easier to prevent them. In order to do so, we stop the water condensation from accumulating on the top plate. Wrapping absorptive paper or cloth "collars" (we have found that clean-room wipes work best) around all the tubes leading cold gas out of the system is an easy and effective solution for the problem. Some extra wiping will be required during times of extreme condensation, e.g. transfers, cool-downs, superfluid runs, and periods of extended field ramping. Further protection can be added by covering the offending welds with a lining of aquarium sealant, though it is our experience that this material will peel away over time, exposing the welds.

C.3 Day to day care

C.3.1 Monitoring cryogen boil-off rates

Keeping a good record of the cryogen boil-off rates is an important part of the day-to-day attention required by a Spectromag system. Having the computer automatically monitor the levels and keeping a log of their values is the easiest way to achieve this task. This log makes changes in the boil-off rates easy to

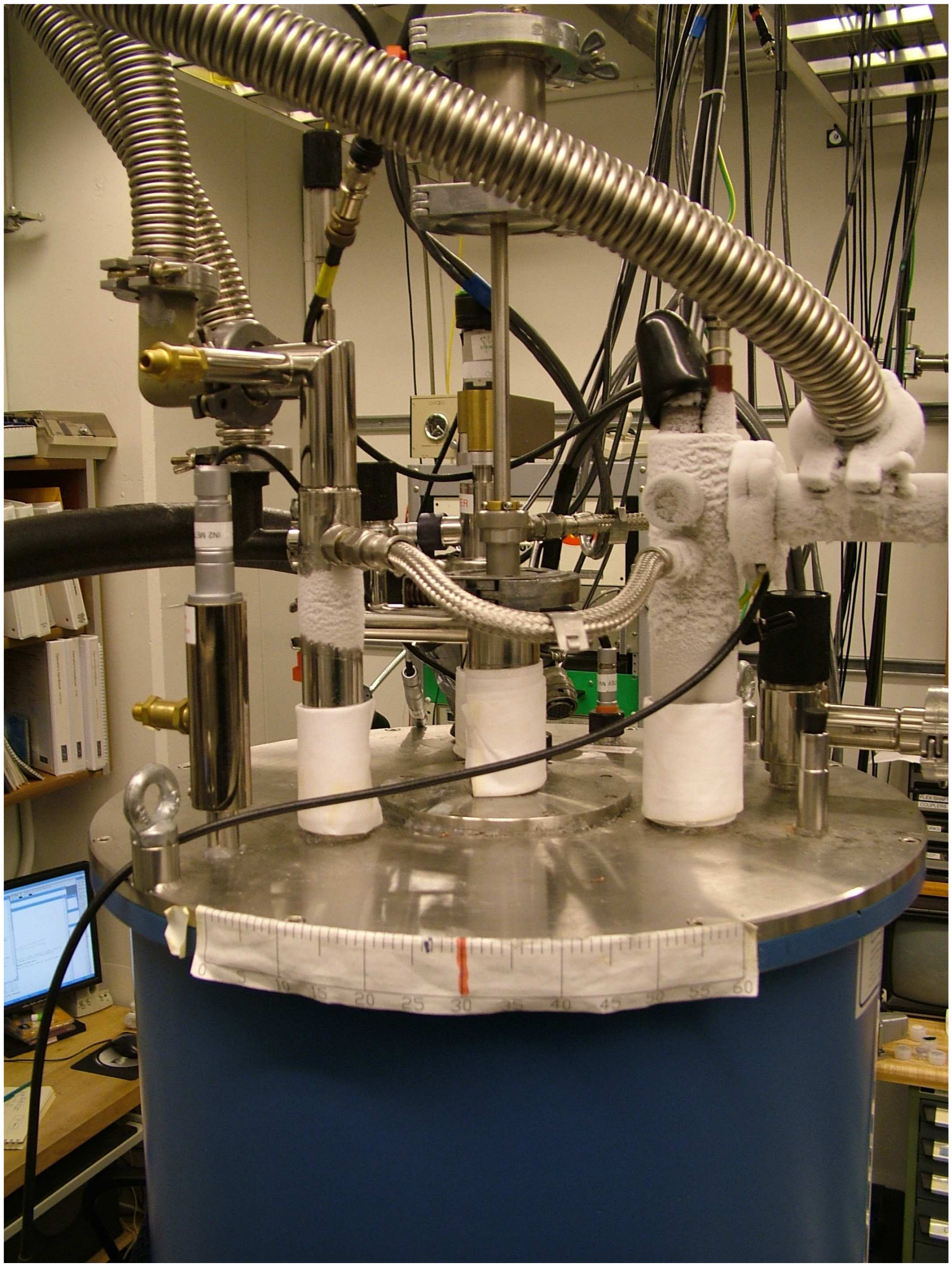

Figure C.7: A view of the top of a Spectromag. Note the ice and condensation present on the exit port from the helium bath (a transfer has recently been completed). Also note the “collars” fitted to each port susceptible to condensation.

spot and makes the analysis of the system's long term stability straightforward. In the case of a touch or leak in the system, the nitrogen and helium boil-off can provide important information distinguishing between the two. For instance, in the case of a touch between two parts in contact with the nitrogen and helium spaces, respectively, a specific signature will be left in the boil-off data: the nitrogen rate will drop while the helium rate will rise.

C.3.2 Transferring helium

Helium transfers are required in Spectromag systems every 2-4 days depending on the intensity with which the system is being used. While this procedure is routine and should be common knowledge among students in the lab, there are couple of important things to keep in mind.

When cooling the cryostat down for the first time, the transfer stick which goes into the cryostat should be fitted with the end-piece with the hole directed straight down. This will channel helium into the magnet space cooling the system down more efficiently. Using the end-piece with holes on the side directs helium away from the magnet and into the helium space, making the initial cool-down extremely slow. If helium liquid is simply dumped in at the top of the system, it will evaporate long before it reaches the magnet at the bottom. The fitting with the holes in the side is used in typical transfers, but is only necessary for transfers performed with the magnet persistent at a non-zero magnetic field. In this case, it is important to direct the flow of incoming helium liquid away from the magnet in order not to cause vibrations in the windings which could result in a quench. Special care should be taken when transferring at high field including the use of low pressures and slow transfer speeds in order to minimize perturbations of the magnet. Unless absolutely necessary, i.e. there is not enough helium in the bath to support ramping the magnet down to zero field, these types of transfers should be avoided. Despite the risks, safe transfers have been made in the lab with the magnet persistent at 8 T.

Also, a filter should always be fitted to the end-piece on the transfer stick which dips into the storage dewar. These dewars of helium often contain ice particles which should be kept out of the Spectromag system. The accumulation of ice particles will eventually cause the clogging of the NV and in larger quantities can cause more serious problems. The transfer sticks available in the lab should all be fitted with 10-μm mesh filters for this purpose.

After starting a transfer, sometimes the gas at the bottom of the system can form a relatively static plug inhibiting the flow of helium. In this case, we notice that despite a full storage dewar with an overpressure, the helium level in the cryostat does not rise and little gas is emitted from the blow-off port. A snug fit between the bottom of the transfer line and the Spectromag's inlet cone is usually to blame. Simply sliding the transfer line up by a half inch releases the trapped gas (at this point we notice a plume emitted from the blow-off port) and the transfer will proceed normally.

It is also important not to be distracted during a transfer, lest the system overfill. Such a mishap can potentially lead to the freezing of the large diameter o-ring seal between the cryostat body and the top flange, making the vacuum jacket soft and turning the Spectromag in question into an ice cube.

C.3.3 Loading and unloading samples

Loading and unloading samples should be done with care. Every time the VTI is opened to the air while the systems is cold, we give water and air the opportunity to enter the sample space. If we are not careful, the ice will cover the inside of

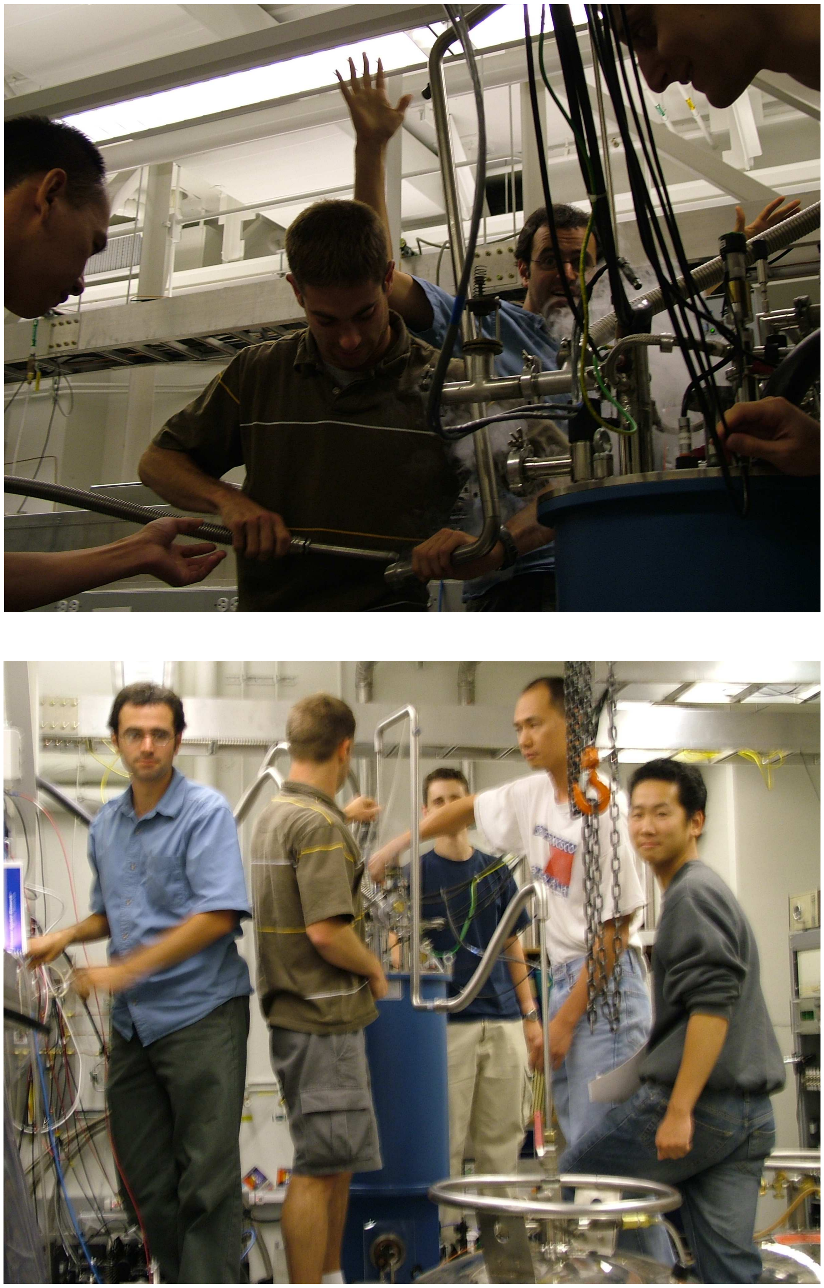

Figure C.8: How not to transfer helium.

the VTI windows and cause serious problems with our optical measurements. This ice can also result in the clogging of the NV.

For this reason, the probe stick should be removed and inserted into the VTI carefully *and* quickly. An overpressure of helium gas passed through a cold-trap (a coil of copper tubing dipped into an open-mouth dewar of liquid nitrogen) should be applied to the sample space. Even with these precautions taken, air or water can accumulate in the VTI over time. Therefore, it is a good policy to minimize the number of times samples are loaded and unloaded from a cold system.

C.3.4 The switch heater

The superconducting magnet in the Spectromag system is energized through a persistent mode switch, known as the switch heater. When heated, this small length of superconducting wire, which is wrapped with a heater wire, reverts to its highly resistive normal state. The power supply is connected across this length of wire and thus can be used to increase or decrease the current flowing to the magnet when the switch heater is on.

This component is essential to the operation of the system and is impossible to replace. In most systems Oxford includes a spare switch heater in case the primary one should fail. Nevertheless, it is vitally important not to destroy the switch heater. Such an event typically occurs when one forgets to turn the switch heater off after ramping the magnet. Given a sufficient amount of time, all of the helium in the system will boil away and without anywhere to dissipate its heat, the switch heater will burn itself out. This process will take at most one day since the helium boil-off rate is about 4 times the normal rate with the switch heater on. In order to avoid such a course of events it is important to always check the status of the switch heater before leaving the cryostat for an extended period of time. It is also important to write programs controlling the magnet power supply which under no circumstance leave the switch heater on after running.

C.4 Cleaning the VTI windows

C.4.1 Ice on the windows

In most cases, a layer of white cyrstaline residue on the VTI windows is ice from impurities which entered the system during the loading and unloading of samples. Usually this ice consists of air (mostly nitrogen) and is easily removed by heating the VTI above 77 K, the boiling temperature of of nitrogen. This type of ice is easily identified upon passing 63 K, the freezing temperature of nitrogen, when the crystalline residue liquefies. If this liquefaction does not occur, the ice probably consists of water and in this case the VTI must be heated to 300 K and kept there until the water has evaporated. Care must be taken not to heat the VTI at its maximum current for more than 10-15 minutes without a short break, as the heater may burn itself out. In both the case of nitrogen and water ice, it is important to thoroughly pump on the VTI while it is warm in order to remove the offending gas from the VTI before cooling back down.

If the formation of ice becomes a chronic problem, rearing its head every time the VTI is cooled down, chances are that there is a leak in one of the sample stick's o-rings: either the o-ring sealing the stick to the VTI or, more likely, the o-ring forming the seal to the vertically sliding probe stick. Leaks of this kind must be fixed before we proceed with measurements.

Figure C.9: The bottom of a VTI window cleaner with lens paper in place.

C.4.2 Other detritus on the windows

If the procedures discussed in section C.4.1 are not effective, the residue on the windows is not ice; a variety of different contaminants could be responsible including particles out-gassing from GE varnish, rubber cement, or other adhesives used to affix samples to the probe. To prevent contaminants from making their way into the VTI, use as little adhesive as possible to affix samples and allow adhesives, especially GE varnish, to fully dry and cure before inserting them into the VTI.

In order to clean existing detritus from the windows, we wait until the system has warmed up and then use a long rod fitted with a custom-made lens paper holder (shown in figure C.9) to wipe the windows clean from the inside. This is a two person job with one person holding the cleaning rod and another directing operations while looking at the windows from the outside. Special care should be taken not to scratch the windows or to put unnecessary pressure on them. We do *not* use solvents as they can compromise the Ecobond seals around the VTI windows and cause permanent leaks. Such a disaster would require the replacement of the VTI windows.

C.5 Needle valve problems

C.5.1 Over-tightening the needle valve

The NV is a typical source of problems during the day-to-day operation of a Spectromag system. First, it is very important not to over-tighten the NV when closing it. As seen in figure C.10, the NV makes a steel on brass seal which can easily be made to leak by over tightening. Since brass is a soft metal, one must be very careful not to tighten beyond “finger-tight.” For Spectromag systems equipped with a motorized NV, we highly recommend the use of this system in place of manually opening and closing the valve. Cryostats in the lab with motorized controllers have remained leak tight far longer than those without. Note that a leaky NV is not the end of the world; it simply results in a slightly shorter helium hold time and the inability to completely seal off the VTI from the helium space.

C.5.2 Ice in the needle valve

The most common problem encountered with NVs is their clogging with nitrogen ice floating around in the helium space. This tends to occur after several months of keeping a system cold, when enough ice particles have accumulated to cause a problem. Oxford, anticipating this problem, provides us with access to a NV heater and a NV resistor for monitoring its temperature. These components are mounted to a small copper block which is bolted to the brass NV housing shown from below in figure C.11.

The main symptom of a clogged NV is the lack of liquid helium flow into

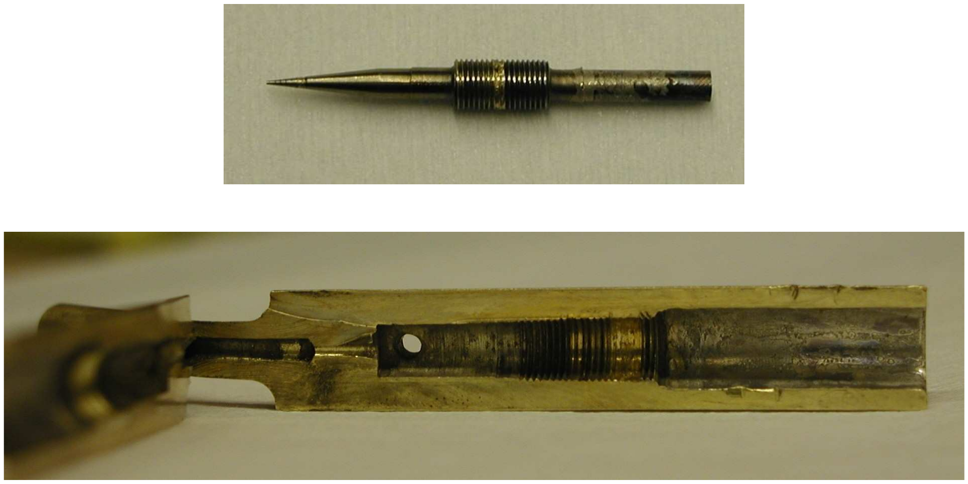

Figure C.10: A photograph of the inside of a NV. This particular NV has been removed and cut open after it seized. Residue from the seizure is still visible in the threads. The exit path at the bottom of the NV housing leads to the VTI, while the hole drilled in the side leads to the helium bath.

VTI. Typically, the NV will turn freely despite the lack of flow. If the NV has seized or is difficult to turn, this may still be a simple problem with nitrogen ice. It is likely, however, that more serious problems exist as discussed in section C.5.3.

Once the problem has been diagnosed as a clogged NV, we proceed to heating it using the NV heater. To do so we connect a small current supply to the heater and pass no more than 100 mA through it. At the same time we heat the VTI using the VTI heater. We continue heating until both the VTI sensor and the NV resistor indicate temperatures above 77 K. At this point, we pump on the VTI and open and close the NV looking to see if the flow of helium starts. It often takes few iterations of heating and pumping and a good deal of opening and closing of the NV before a clog works itself out. It may even take 10 to 20 minutes of sustained NV and VTI temperatures above 77 K to melt a clog. If the clog consists of water rather than nitrogen or oxygen, it will be virtually impossible to unclog the NV without warming the whole system up. Since the NV is always in contact with he liquid helium bath, there is no way of heating it up to sufficiently high temperatures to melt water ice. Though this outcome is always a possibility, it is rare.

Note that care must be taken not to pass too much current for too much time through either the NV heater or the VTI heater. Burning one of these heaters out is a major headache and should be avoided at all costs. Generally we use currents under 100 mA for no longer than 10-15 minutes at a time. We must allow several minutes in between heating cycles for heat to dissipate away from the heaters preventing permanent damage.

C.5.3 A seized needle valve

A seized NV is a far more serious problem than a clogged NV. It has only occurred once in the Awschalom lab to date and required an extended intervention to repair. This rare occurrence was likely due to a design flaw in the NV which somehow became unthreaded and started to slowly chew away at the brass threads of its housing until it seized. When such a disaster occurs it is obvious as the NV does not budge at all no matter how hard one tries to turn it.

The NV itself is a threaded piece of steel with a conical tip as shown in figure C.11 which is welded to the end of a long and hollow steel tube. This tube sits in a snug cylindrical shaft and extends out to the outside of the cryostat where it is attached to a motorized NV controller or a simple manual knob. In fact, the NV can be inspected for damage (if it's not seized) by fully unscrewing it from its brass housing and pulling it out of its cylindrical shaft. Note, this should *only* be done when the system is warm.

The NV housing is the threaded brass piece with an inlet and outlet port.

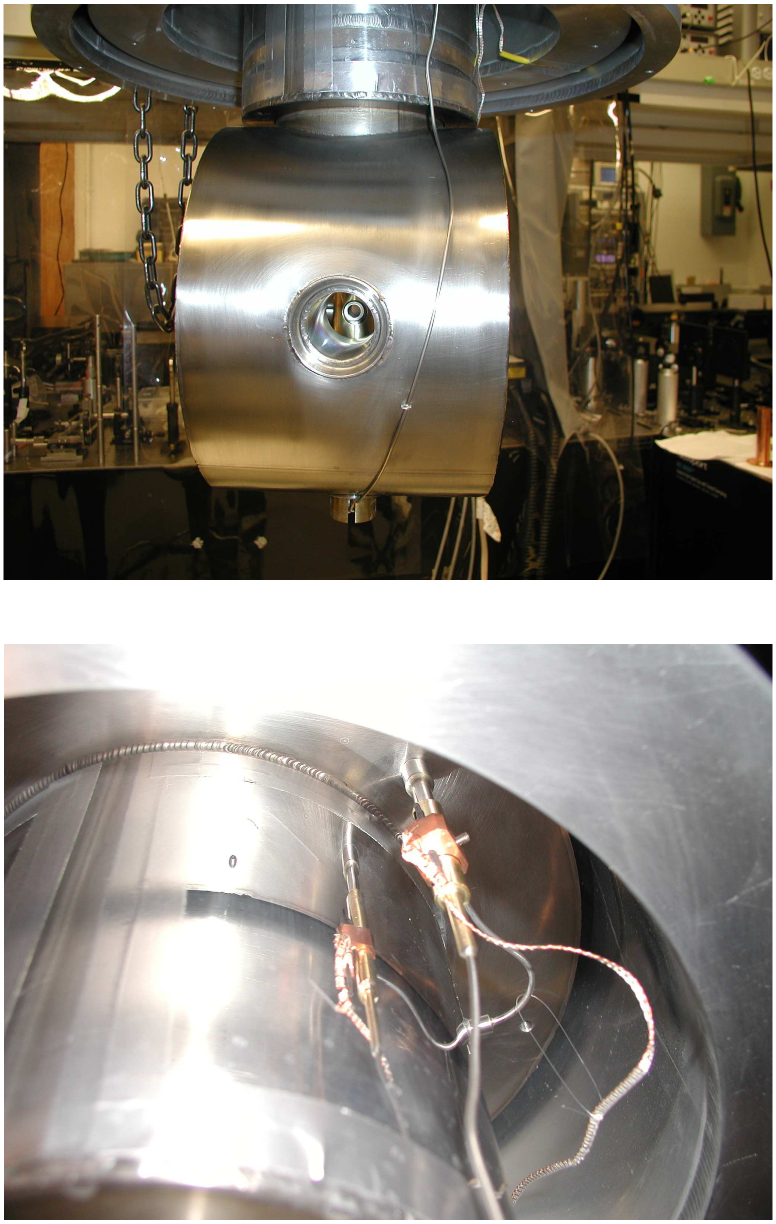

Figure C.11: On top is a photograph of the magnet with the cryostat's tail removed. The small tube is the capillary carrying liquid helium from the NV to the VTI. On the bottom is a photograph of the NV housing from below. Wires leading the NV heater and resistor are visible. Here, the tail of the cryostat has been removed and we are looking up toward the cryogen spaces from below. The NV is still in place.

The housing from the seized NV was cut open and is shown in figure C.11. In order to remove the seized NV, the NV had to be turned hard enough to break the steel tube from the NV tip. The shaft was then removed and the NV housing was heated with an acetylene torch until it could be detached from the tubes to which it was soldered. A new NV tip was then welded to the steel shaft, making sure to center it along the axis of the tube before attachment. Meanwhile a new NV housing was machined by Oxford and installed by our skilled machinists using the torch. This delicate procedure is complicated by the awkward position of the NV in the cryostat and by the fact that its input and output connections have to hold vacuum. Furthermore, we had to be careful not to heat the exposed surfaces near the NV too much, lest we cause other damage to the cryostat. We covered all surfaces near the NV housing with a protective coating of tin foil in order to avert any possible damage due to the torch. Once in place, the new NV worked perfectly and the system continues to show no signs of damage.

C.6 Touches and leaks

C.6.1 Touches

Touches and leaks in a Spectromag system can cause a lot of headaches for students resulting in months of lost time. Therefore it is important to work methodically to determine the exact cause of the touch or leak and to address it appropriately.

Touches are more common than leaks, as leaks tend to be caught before cool-down during the compulsory leak checks. The most common type of touch is between the nitrogen shield (or the re-entrant tubes which are attached to it) and the magnet housing. Such a touch is easily diagnosable as it is characterized by a drop off in the nitrogen boil-off rate and a simultaneous increase in the helium boil-off rate. These touches are usually fixed by warming the system up and making small adjustments in how the nitrogen shield is attached to the tail of the cryostat. In typical Oxford fashion, there is quite a bit of slop in how the nitrogen shield can be set with respect to the magnet housing. We find that altering the configuration slightly, just enough to maximize the space between the shield and the housing, usually fixes the problem, though it may take a few iterations.

Touches can also happen between the VTI and the magnet housing. This problem should be characterized by a drop in the equilibrium VTI temperature and a rise in the helium boil-off rate. The insertion of a ring of Teflon spacers around the VTI, between it and the magnet housing, can provide an easy solution.

A touch between any of the cold surfaces and the outer housing of the cryostat will have an obvious cooling effect on the outside of the system. Such touches should be rare as there is quite a bit of space between the inner and outer surfaces.

C.6.2 Leaks

The most common Spectromag leaks are caught in the early leak-checking phases of a cool-down and tend to be leaks through the o-ring seal of an outer window. An o-ring which is either cracked or has some dust or hair on it will cause a leak. A more serious kind of leak can develop on the top flange of the cryostat due to water condensation causing rust in one of the welds. Such an occurrence can be prevented as discussed in section C.2.5 and can be fixed by a having a skilled welder re-do the weld from the inside. Another common leak occurs in the indium seal below the VTI and is easily fixed by following the directions in section C.2.1, unless permanent damage has been done to the flanges.

A particularly hard leak to diagnose occurs in the o-ring inside the valve used from pumping the outer vacuum jacket. Since the leak-checker is connected through this valve, such a leak will elude identification by this procedure. Though tricky to catch, this problem is easily fixed by cleaning or replacing the valve's o-ring.

Leaks have also been known to develop through the epoxy seals of the VTI windows. Leaks in this area are usually the result of a violent quench or other stress put on the windows. In the past, bumping the windows in the process of cleaning them or forcing a sample probe without enough clearance past them has lead to leaky seals. To fix this problem the cryostat must be warmed-up, the VTI removed, and new windows must be epoxied in place.

Slow leaks can also develop and may not be apparent until the cryostat has been cold for many months and the boil-off rates start to slowly rise. These types of leaks can sometimes be ignored as they can be offset adequately by the cryo-pumping action of the cold surfaces in the cryostat. Eventually, however, when the surfaces are saturated, the cryostat will go soft. While a couple of these types of leaks have been identified, it is still unclear what their origin is.

C.7 Quenches

When a large amount of current is passing through a superconducting magnet and a small region of the superconductor becomes normal, heat will be generated. If this heat cannot be dissipated more quickly than it is generated, the normal region will propagate throughout the material in an avalanche fashion.

Once this process starts, there is no way to stop it: the magnet is quenching. If this occurs during the operation of a Spectromag, the best thing to do is to open all available release valves in order to let all the high pressure gas flow from the system as freely as possible. These events are usually the result of large forces imposed on the magnet windings, large amplitude vibrations, or the surpassing of the critical current. In all cases something causes an element of the winding wire to move within the applied magnetic field, converting some electromagnetic energy into heat and providing a starting point for the quench. The best protection against a quench is attentiveness and preventive measures such as those described in section C.2.4. In addition, it is important to keep any magnetic objects far from the stray fields of the magnet and to be careful not to bump the system while it is energized.

Quenches can result in a number of very serious consequences for the system including the damage of the magnet windings (very serious) or the VTI. Sometimes, however, lady luck has smiled on students and a quench has left the system unharmed.

A related problem can occur if by some human, computer, or power grid problem, the magnet power supply no longer “knows” at which current the magnet is persisting. Due to UCSB’s notoriously flaky power grid, it is a good idea not to run experiments requiring copious magnet ramping during periods of inclement weather, e.g. high winds or heavy rain. In case of such a loss of the field setpoint, it is important to be aware at all times what the field of the magnet is, even if only roughly. If the power supply and the magnet do not have matching currents when the switch heater is turned on, all the excess current will be released as heat in the helium bath through a pair of diodes. If the currents are extremely different, enough heat could be dumped to cause a quench in the system. If, however, the currents are close, not much besides a large waste of liquid helium is likely to occur. It is therefore important to keep track of the magnet action mentally and perhaps in the form of an automatic computer log.

C.8 Probe design

While Oxford ships each Spectromag system with a generic probe stick, we often need to make our own in order to accommodate the specific needs of our experiment. An example of a probe design popular in the lab is shown in figures C.13-C.25 and in a photograph in figure C.12. Four probes based on this original design have been made so far. The design's fundamental innovation with respect to earlier probes is that it incorporates a semi-rigid coaxial line for transmitting radio frequency (RF) voltages to the sample in addition to traditional DC signals sent via twisted pairs. It is also designed such that a wide variety of mounts can be made and used with it including RF coils (as shown in figures C.15-C.17) and chip carriers. As long as these mounts are designed properly (for this particular design, holding the sample 0.297" from their base), the sample will sit on the probe stick's axis of rotation. This design feature allows the user to rotate the sample with respect to the applied magnetic field without changing the position of the sample's center line; such a feature is convenient for preserving the alignment of optical experiments regardless of sample angle and should be considered in future probe stick designs.

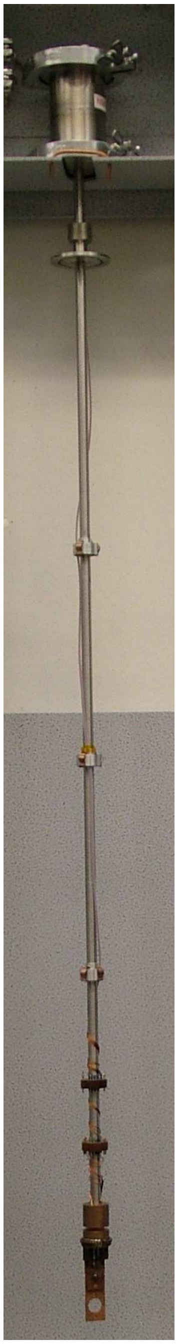

Figure C.12: An RF probe for Spectromag (model F2001).

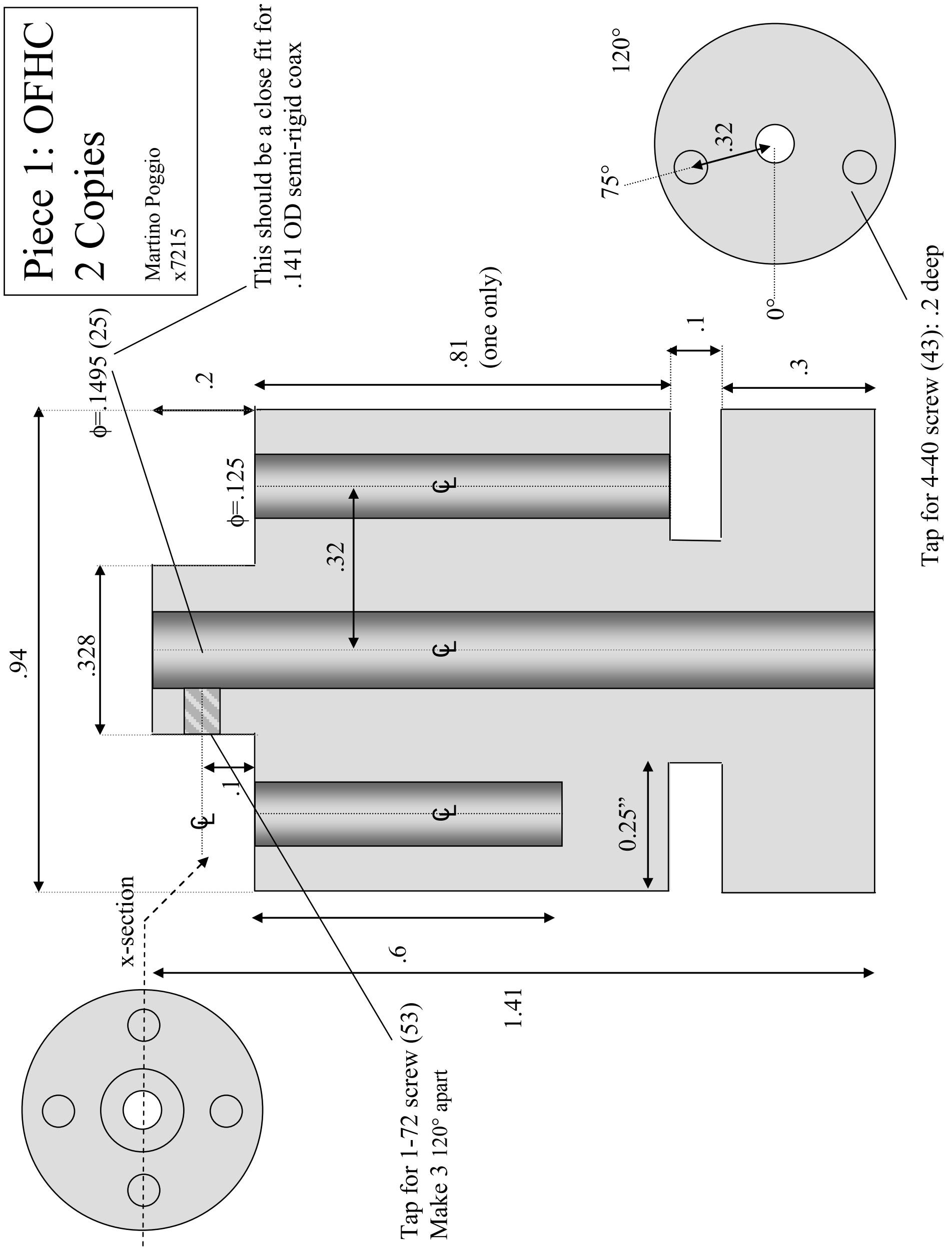

Figure C.13: Design for the temperature stage at the bottom of an RF probe (model F2002) for a 25-mm bore Oxford Spectromag.

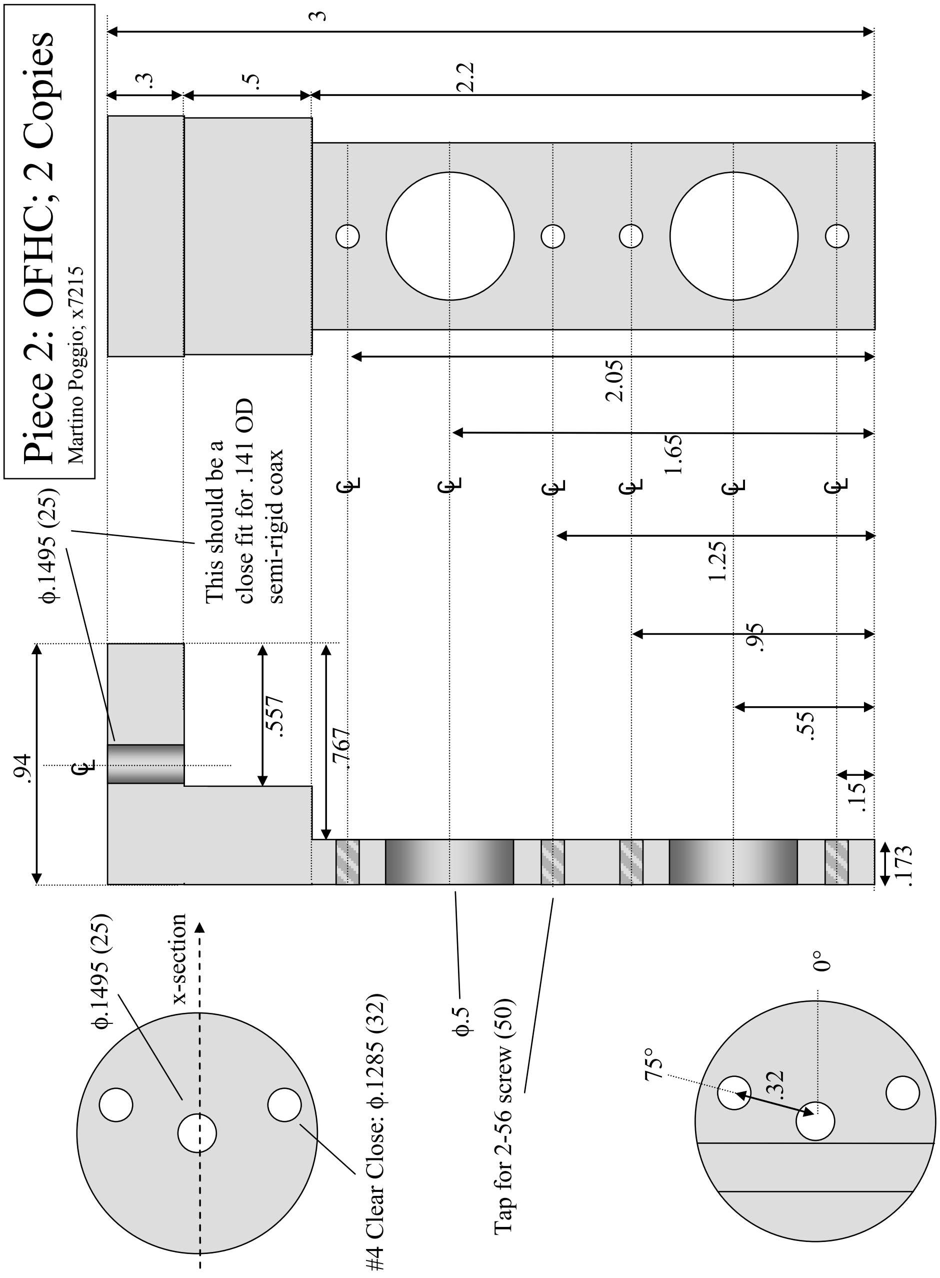

Figure C.14: Design for the sample stage at the bottom of an RF probe (model F2002) for a 25-mm bore Oxford Spectromag. Springs from Majr Products Corp. (part number: 5250-02R75-BC) should be braised to the upper perimeter of this part for stability.

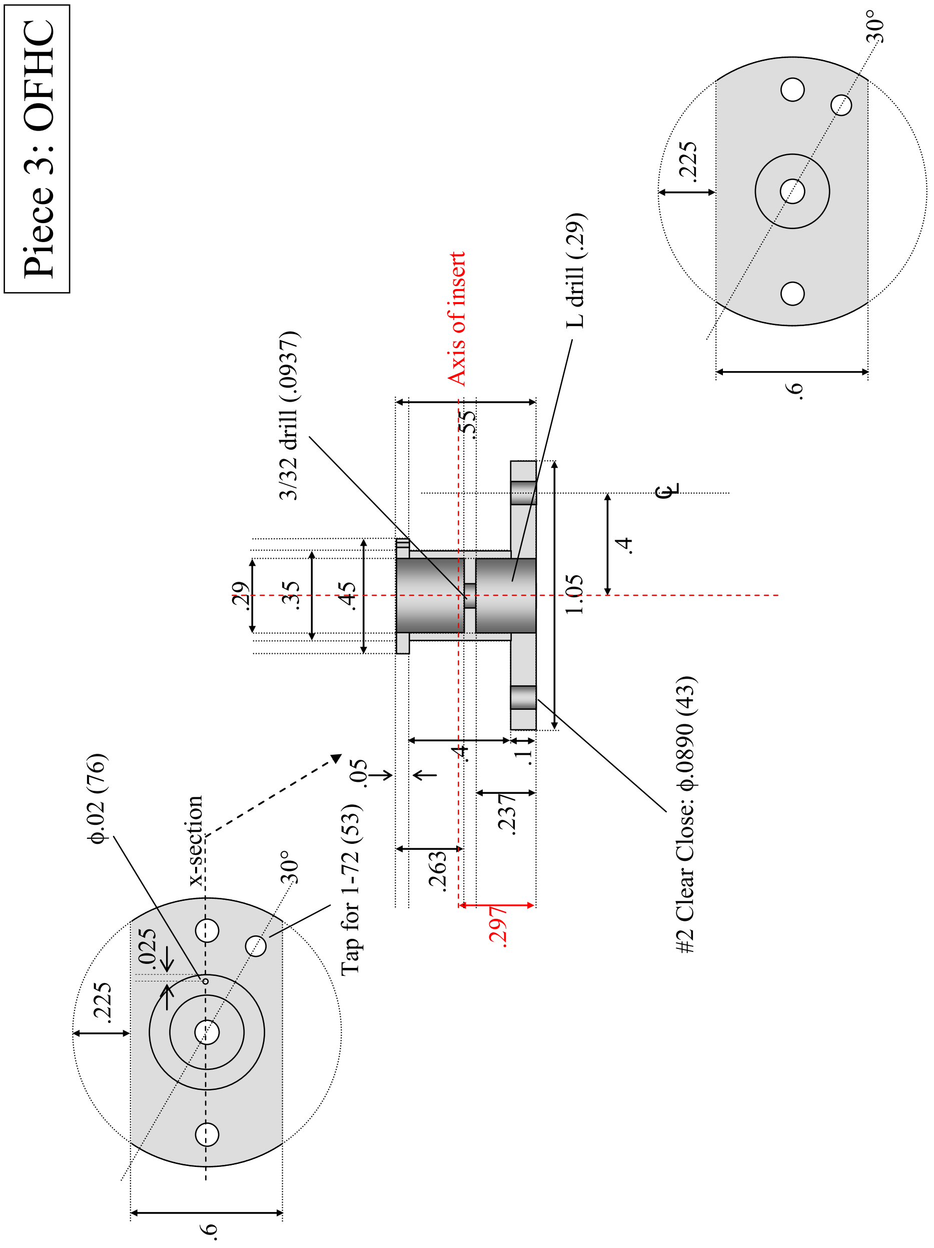

Figure C.15: Design for an solenoidal RF coil and sample holder to be used with probe model F2002.

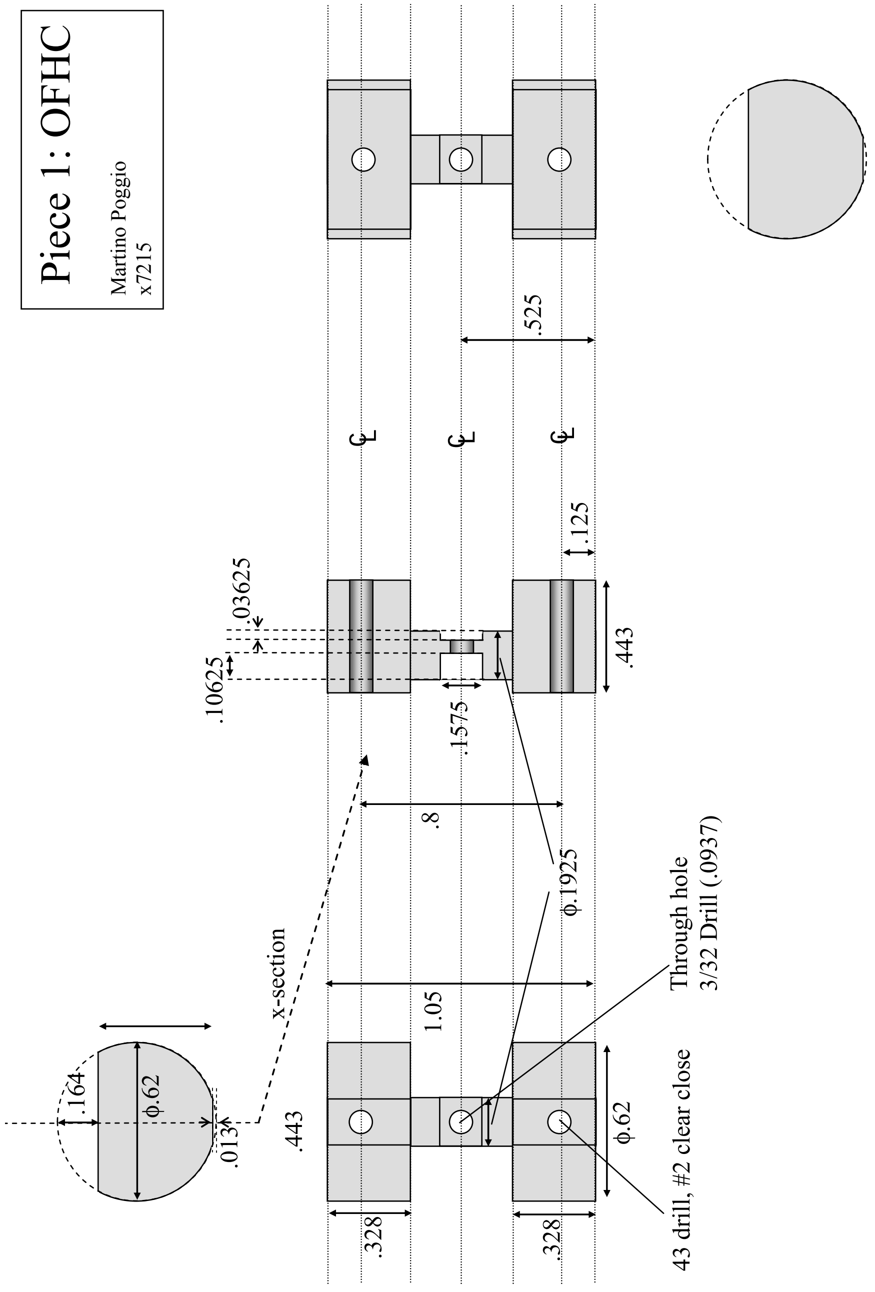

Figure C.16: Design for an Helmholtz RF coil and sample holder to be used with probe model F2002.

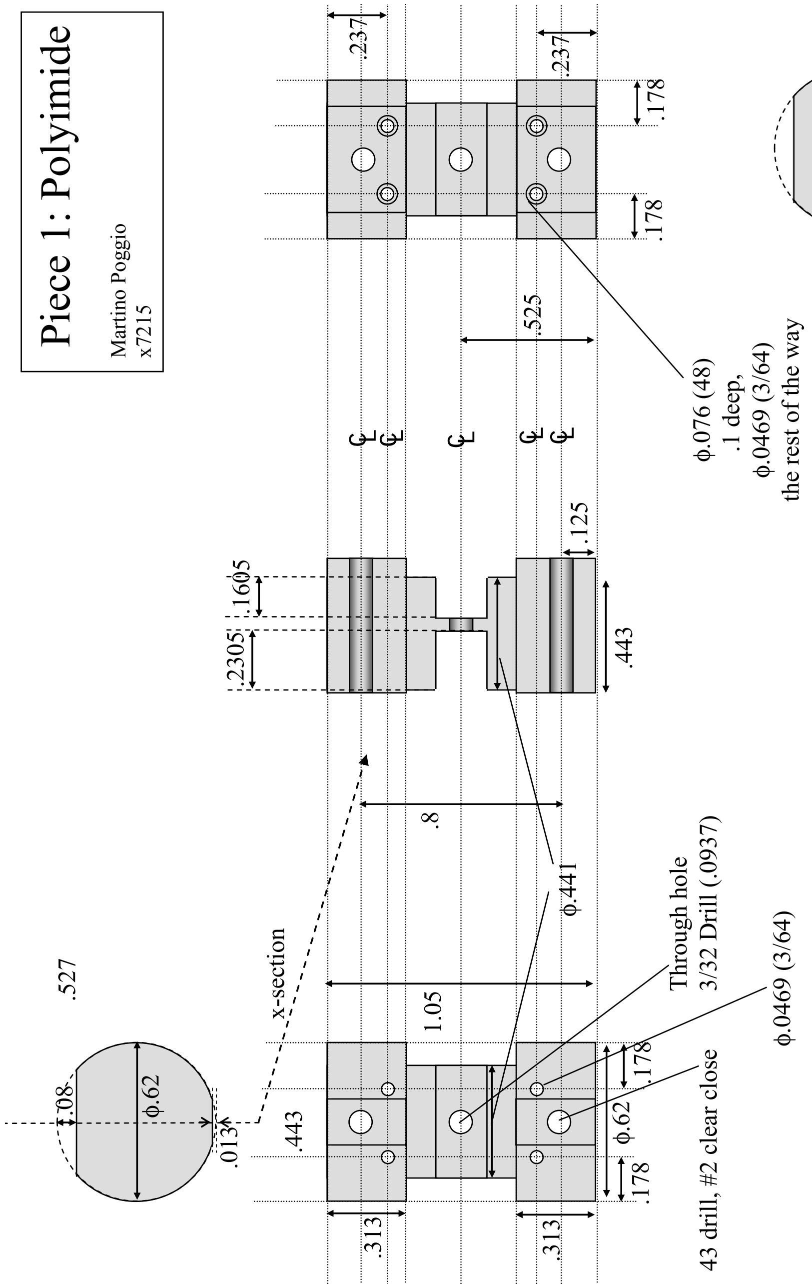

Figure C.17: Design for an Helmholtz RF coil and sample holder with electrical pins to be used with probe model F2002.

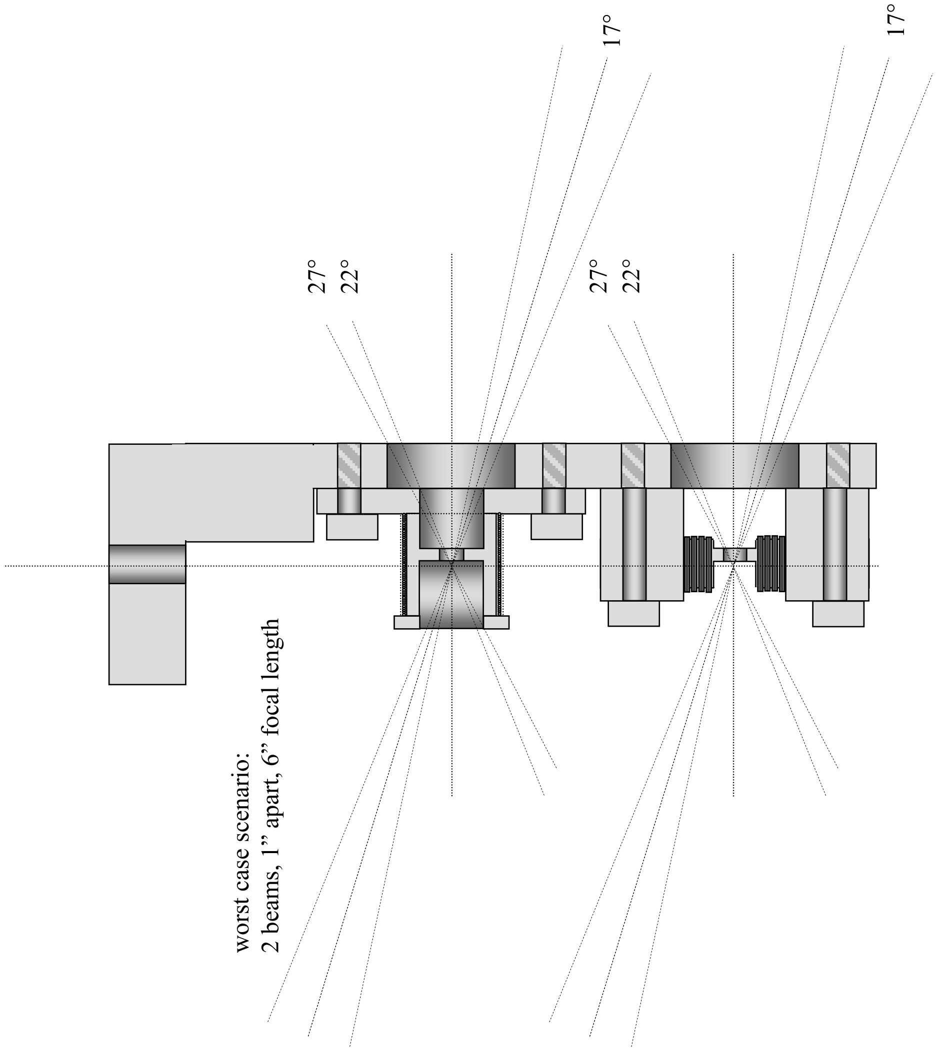

Figure C.18: A schematic drawing of the bottom of an assembled sample probe showing some estimates for the maximum angles of transmission for pump and probe beams.

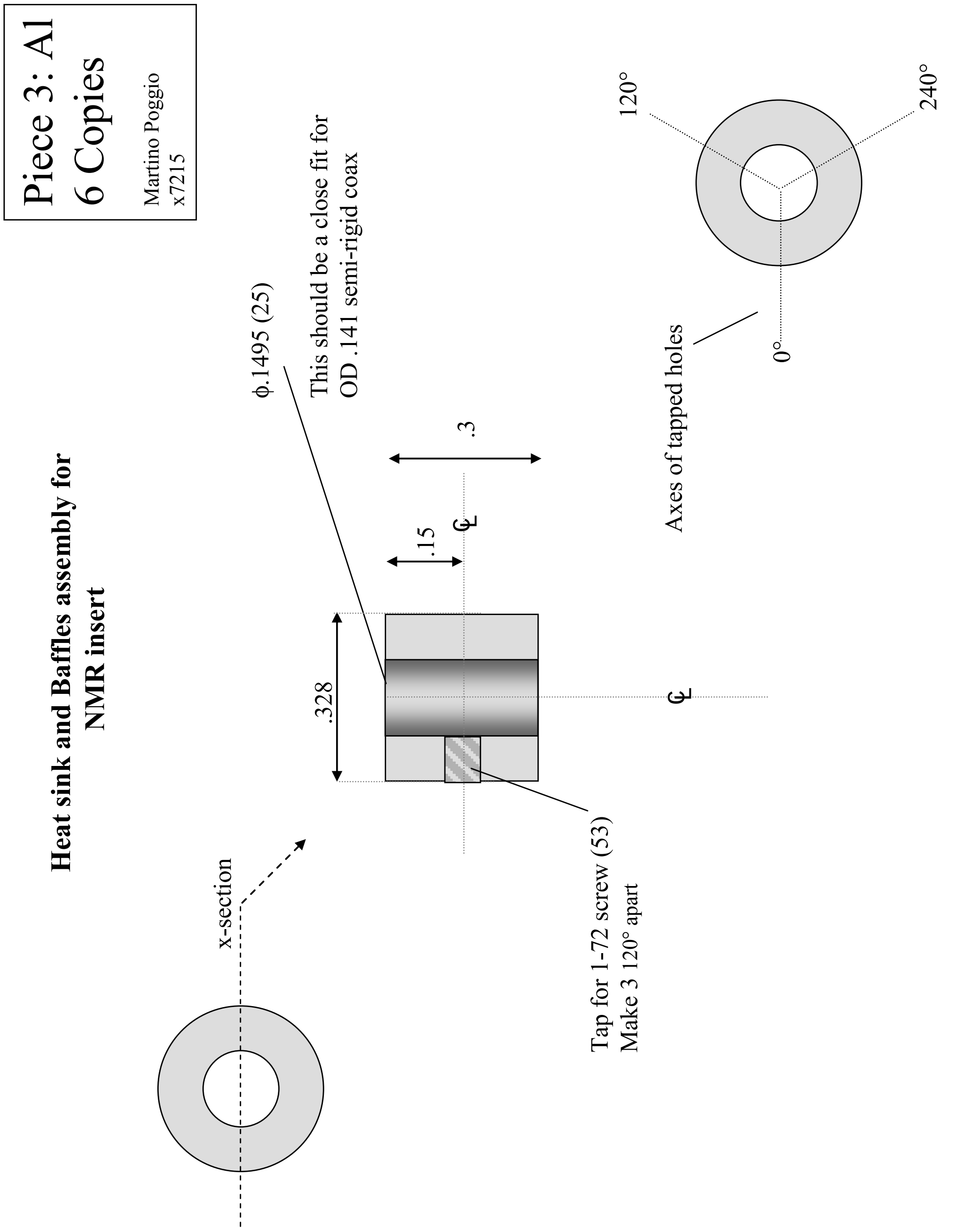

Figure C.19: A design for a heat sink and baffles mounting assembly. These pieces serve both as mounting fixtures for the baffles on the outside of the probe tube and as thermal anchors for the semi-rigid coax passing through their center.

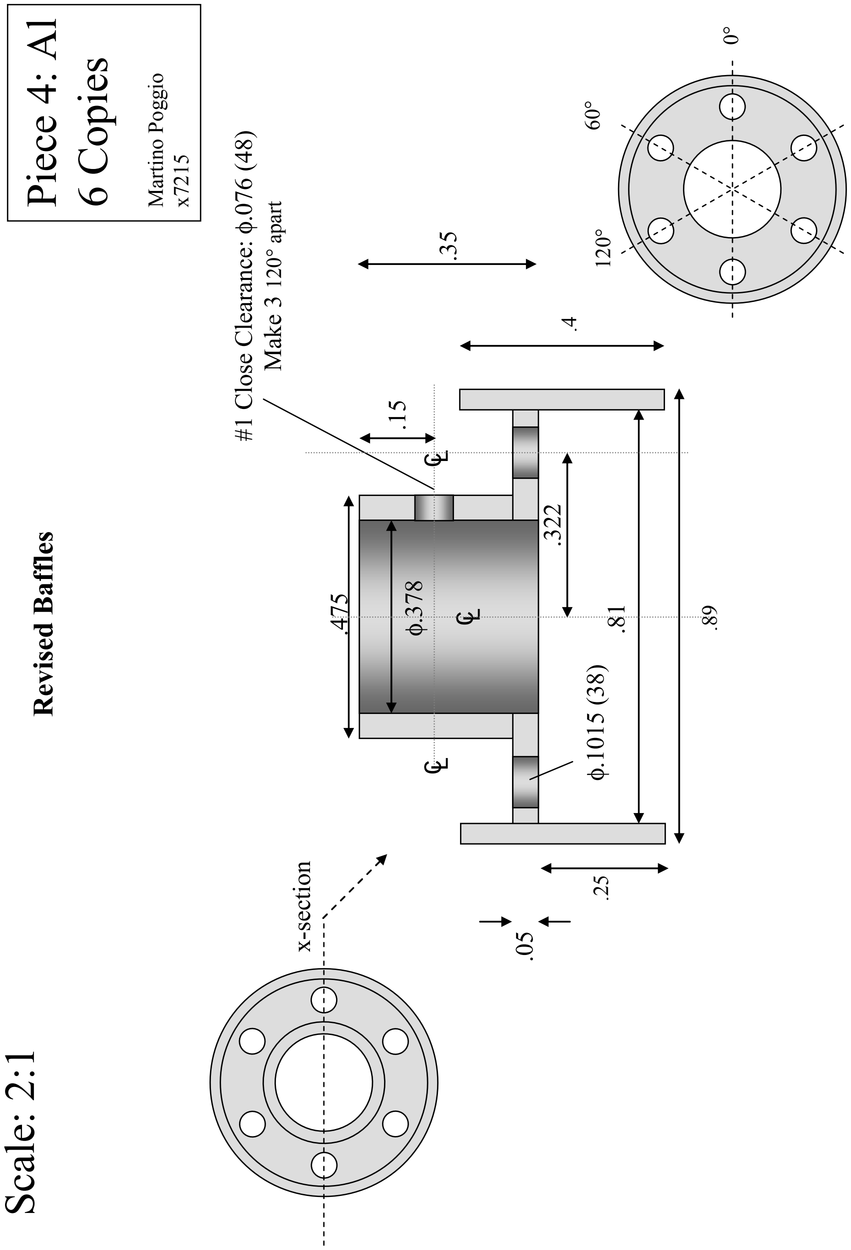

Figure C.20: A design for the baffles of a Spectromag probe to be used with the pieces shown in C.19. Springs from Majr Products Corp. (part number: 5240-19D42-BD) should be fixed to outside of this part for stability.

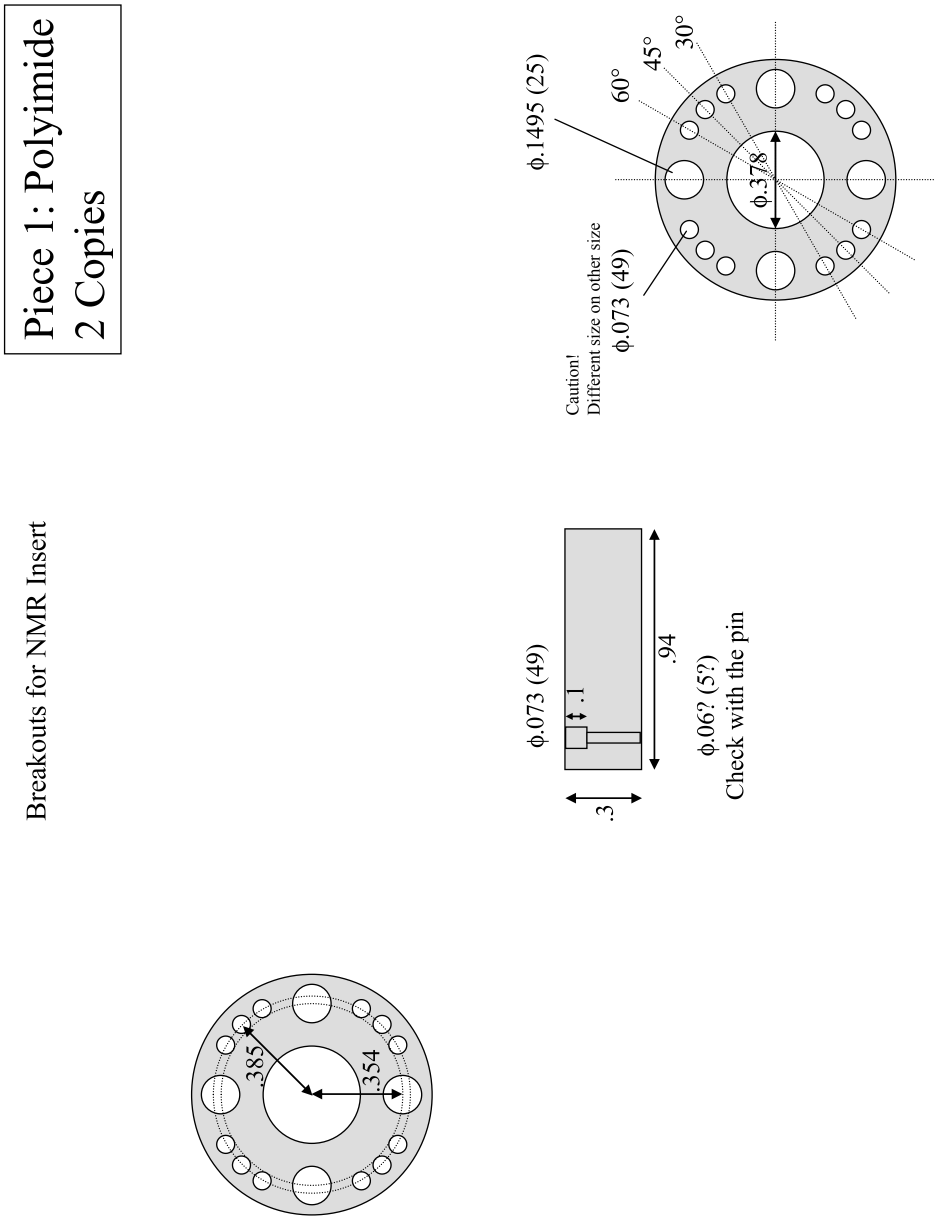

Figure C.21: A design for an electrical break-out of a Spectromag probe.

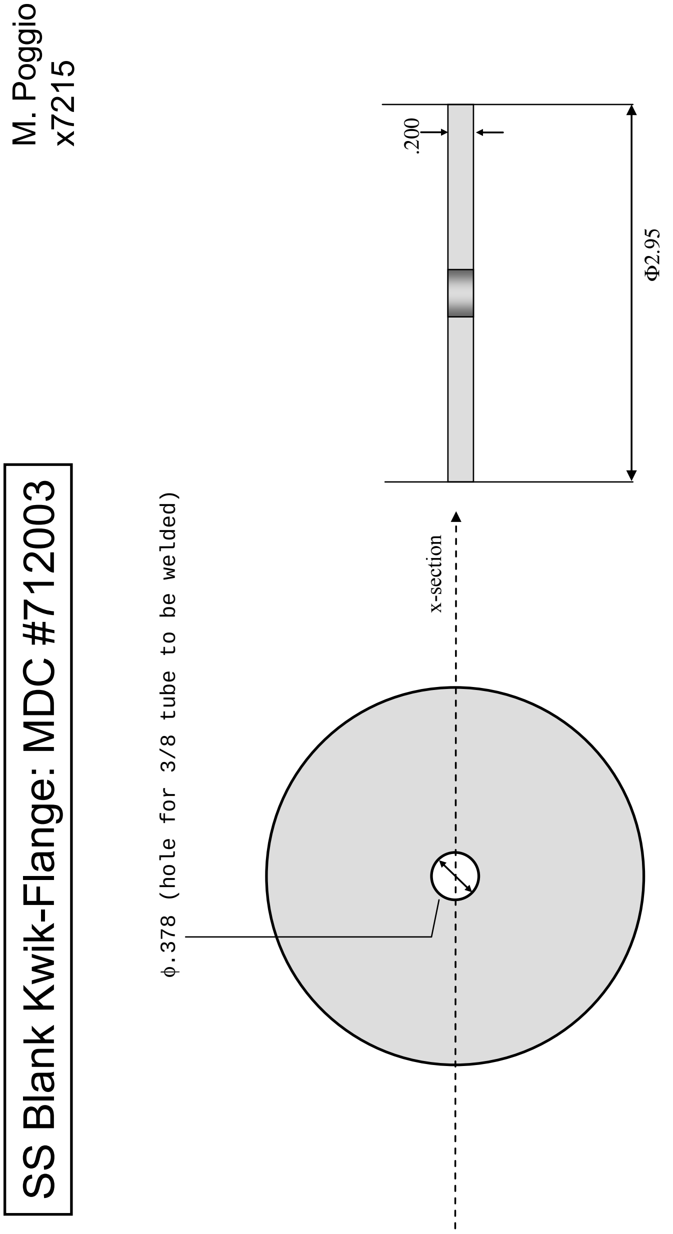

Figure C.22: The bottom plate of the top part of a Spectromag probe; this part is outside the cryostat at room temperature. It is machined from a standard Kwik-Flange component.

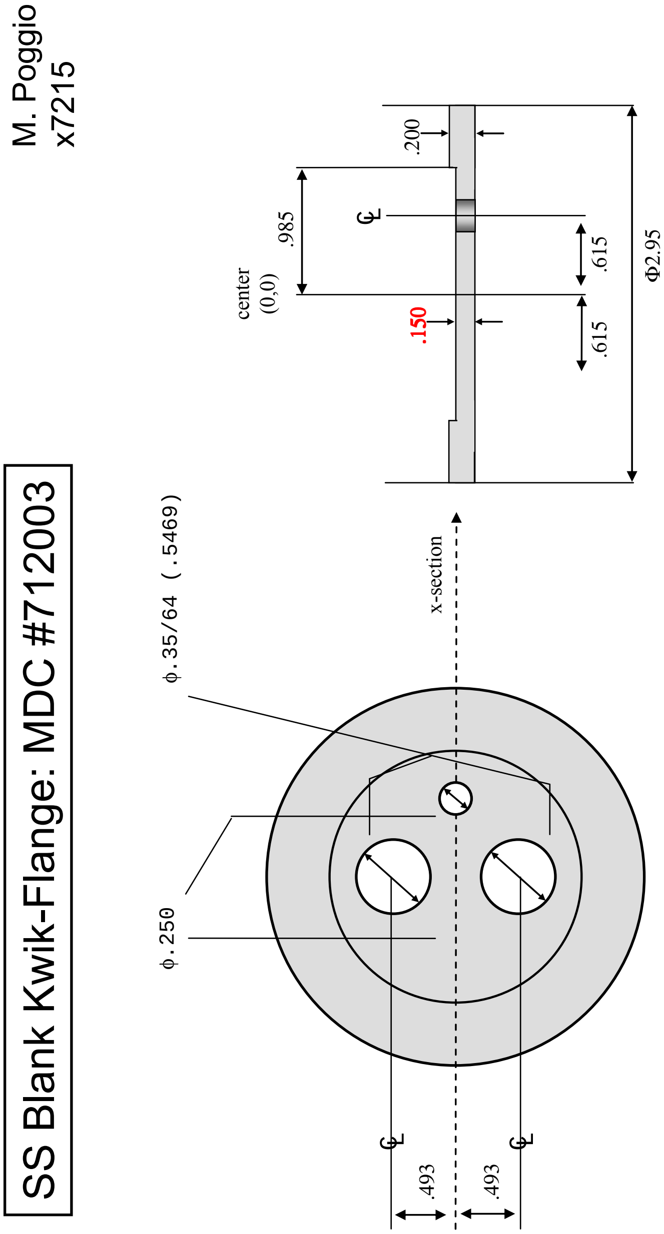

Figure C.23: The top plate of the top part of a Spectromag probe; this part is outside the cryostat at room temperature. It is machined from a standard Kwik-Flange component.

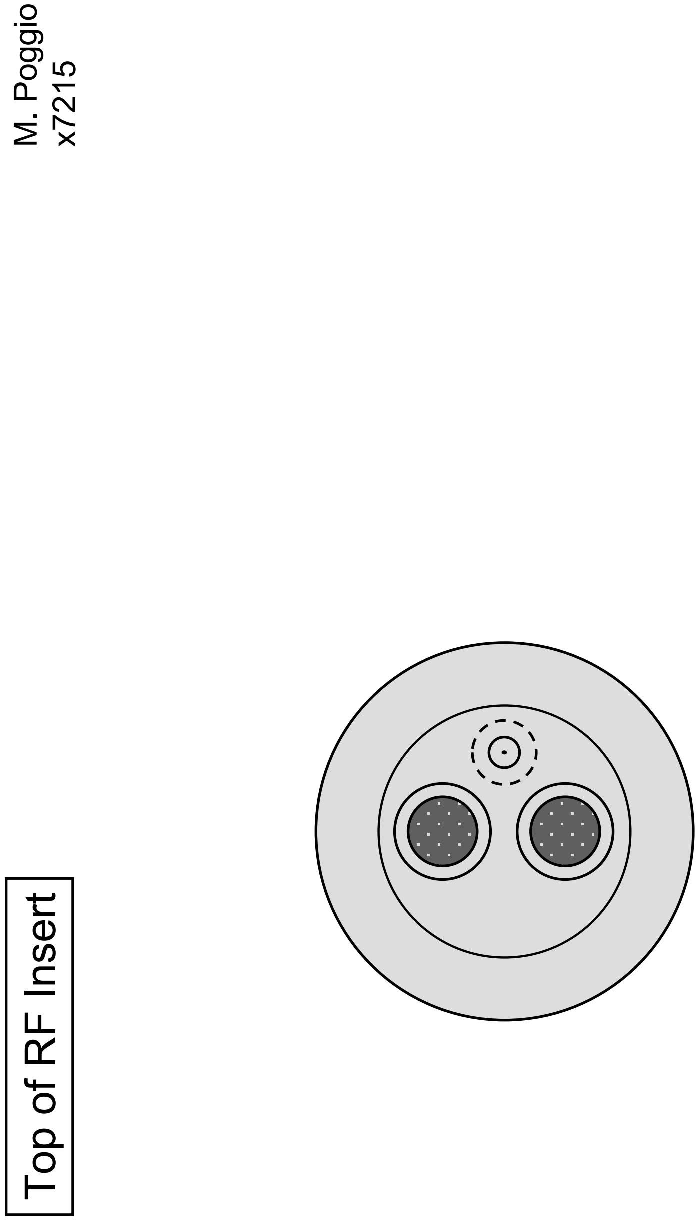

Figure C.24: A view from above of the top part of a Spectromag probe; this part is outside the cryostat at room temperature. It is machined from a standard Kwik-Flange component and includes schematics of the Fischer and SMA plugs which feed through it.

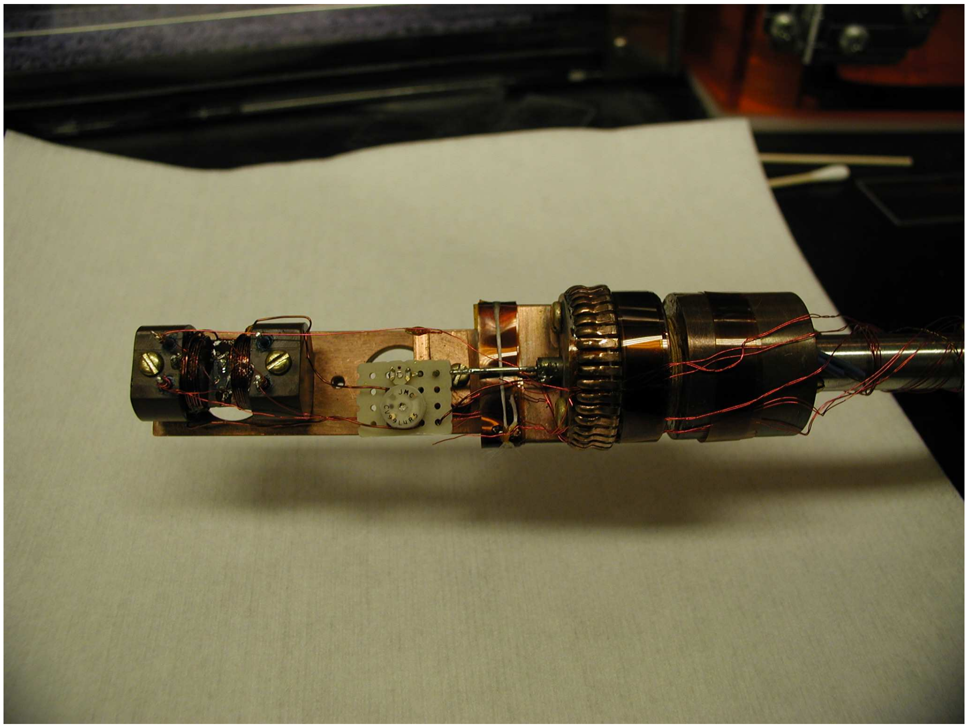

Figure C.25: A photograph of the bottom of an RF probe (model F2002) for a Spectromag. The sample is wired with electrical contacts, temperature sensors, and an impedance matched RF coil mounted to the bobbin whose design is shown in figure C.17. The variable capacitors used for impedance matching are visible on the small breadboard near the end of the semi-rigid coax.

Appendix D

Coupling RF radiation to an NMR coil

D.1 Introduction

The optical nuclear magnetic resonance (NMR) experiments described in chapter 3 involve the creation of a radio frequency (RF) magnetic field with an amplitude of order one gauss at the position of the sample inside a magneto-optical cryostat. RF voltages are transmitted from an RF source down into the cryostat through a transmission line connected to an NMR coil. A number of challenges present themselves in coupling RF fields efficiently to a sample coil since the characteristic length l of the apparatus (the cryostat is about 1.3 m tall) is on the order of the wavelength of the necessary RF radiation (e.g. for $\nu = 50$ MHz, $\lambda = 6$ m). In this limit, simple notions of circuits and circuit elements break down; these assumptions are only valid for $\lambda \gg l$. We must think of our signals in terms of transmitted and reflected waves and carefully consider the geometry of our experimental setup. Fortunately, our task is significantly easier than the design of a conventional NMR coil, which in addition to creating RF electromagnetic fields, also must be able to detect them.

D.2 NMR probe design

D.2.1 The transmission line

The large temperature difference between the sample (typically at $T = 5$ K) and the exterior of the cryostat ($T = 300$ K) forces us to use a semi-rigid stainless steel coax to couple RF radiation from our source to the NMR coil near the sample. Since stainless steel is a poor thermal conductor, it does not transport a significant amount of heat into the cryostat, allowing us to adequately cool the sample. This type of coax, however, is an efficient RF attenuator which severely limits the amplitude of the magnetic fields produced at the sample position. As a compromise, we use a semi-rigid coaxial cable with a stainless steel outer conductor and a beryllium-copper inner conductor, which has slightly worse thermal, but significantly better conductive properties than its stainless steel counterpart. In order to couple as much RF to the bottom of the cryostat as possible, we also choose the largest diameter coax which we can fit in our probe design, $d = 0.141$”.

In order to minimize heat gradients in the semi-rigid coax, we also carefully design the probe stick such that throughout its length it provides thermal contact between the coax and the gas in the VTI. This task is accomplished by thermally anchoring the coax to the sample stage and to all of the baffles, whose design is shown in figures C.19 and C.20.

D.2.2 The coil

Care must also be taken in the design of the coil. In order to achieve an RF field $\mathbf{B_1}$ perpendicular to both the applied magnetic field $\mathbf{B}$ and the the laser propagation direction, as required by the experiments in chapter 3, we choose a Helmholtz coil configuration. Using the Biot-Savart law we find that for such a split-coil configuration the magnetic field at the center of the coil is maximized for

$$r = \frac{d}{\sqrt{2}}, \tag{D.1}$$

where r is the radius of the coils and d is the distance between their centers. With the distance d fixed by the size of our sample, we use this simple relation to solve for the appropriate r.

Typical Helmholtz coil parameters are easily inferred from the bobbin designs shown in figures C.16 and C.17. One successful coil had $d = 0.158$" and $r = 0.096$" and consisted of two coils made from 4 turns each of 22 AWG magnet wire. Its inductance and resistance were measured at 0.24 μH and 0.63 Ω, respectively [182].

D.2.3 Impedance matching

In order to couple RF radiation into the coil while minimizing losses due to reflections and interference, we must impedance match the coil to the to the transmitter electronics. This is usually achieved by transforming the coil impedance to a standard impedance such as 50 Ω, which is the characteristic impedance of most transmission lines and RF electronics. We can transform the coil impedance by including low-loss reactive elements (capacitors) in the circuit and by tuning their impedance to achieve a 50 Ω total impedance.

Two matching schemes are typically used [183]. In the resonant-coax scheme,

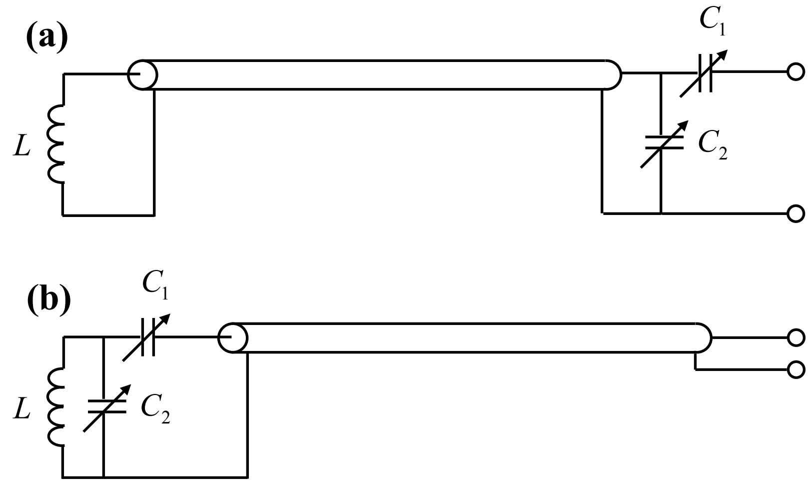

Figure D.1: A schematic representation of the two typical coil matching schemes. (a) shows the resonant-coax scheme and (b) the matched-load scheme. L is the inductance of the coil, and C_1 and C_2 are the capacitances of the tuning capacitors.

shown in figure D.1a, the coil is connected directly to the coax at the bottom of the cryostat and the matching capacitors are connected at the top of the probe stick outside the cryostat. The coax is therefore included in the resonant circuit. This scheme has the advantage that the matching capacitors are easily tuned to optimize the circuit's performance. Unfortunately, however, the inclusion of the coax in the resonant circuit has a strong attenuating effect and makes the maximum achievable RF magnetic field at the sample quite small.

In a second scheme, the matched-load scheme, shown in figure D.1b, the matching capacitors are connected to the coil at the bottom of the cryostat and the whole circuit is in turn connected to the semi-rigid coax. Here, the coax is not part of the resonant circuit and its attenuating effects are significantly reduced in comparison with the resonant-coax scheme. The drawback here is that the matching network is near the sample and is therefore both at low temperature and very difficult to access for circuit optimization purposes.

In both cases, the impedance of the load to be matched is the total impedance of the first capacitor with capacitance C_1 in series with the parallel capacitance and inductance of the second capacitor and the coil, C_2 and L, respectively. In the case of the resonant-coax scheme, the basic circuit is the same, though we must also account for the capacitance of the coax in parallel with C_2. For convenience, we will absorb the coax capacitance into C_2 for the following analysis. Therefore the total impedance of the load can be expressed as,

$$Z = \frac{1}{i\omega C_1} + R_{C_1} + \frac{\left(\frac{1}{i\omega C_2} + R_{C_2}\right)(i\omega L + R_L)}{\frac{1}{i\omega C_2} + R_{C_2} + i\omega L + R_L}, \tag{D.2}$$

where R_{C_1}, R_{C_2}, and R_L are the resistances associated with the two tuning capacitors and the coil, respectively. Simplifying this expression we have,

$$Z = \frac{\left(\frac{L}{C} + R_C R_L + R_{C_1} R_{C_2} - \frac{1}{\omega^2 C_1 C_2}\right) + i\left(\omega L R_C - \frac{R_L}{\omega C} - \frac{R_{C_2}}{\omega C_1} - \frac{R_{C_1}}{\omega C_2}\right)}{R_{C_2} + R_{C_L} + i\left(\omega L - \frac{1}{\omega C_2}\right)}, \tag{D.3}$$

where $C = \frac{C_1 C_2}{C_1 + C_2}$ and $R_C = R_{C_1} + R_{C_2}$. Since we use low-loss elements, all of the resistances R_L, R_{C_1}, and R_{C_2} should be small and to first order all terms containing a resistance can be ignored. In this case, the total impedance will be completely real (resistive) only when,

$$-\frac{\omega L^2}{C} + \frac{L}{\omega C_1 C_2} + \frac{L}{\omega C C_2} - \frac{1}{\omega^3 C_1 C_2^2} = 0. \tag{D.4}$$

Solving this equation results in $\omega = \pm\sqrt{\frac{1}{LC_2}}\,, \pm\sqrt{\frac{1}{L(C_1+C_2)}}$. The first pair of roots correspond to the resonance of the tank circuit containing L and C_2 and to first order has a total resonant impedance $Z = \frac{L}{C_2(R_{C_2}+R_L)}$. The second pair of roots correspond to a lower frequency with a lower impedance Z which is more complicated to express, but is also completely resistive as shown graphically in figure D.2.

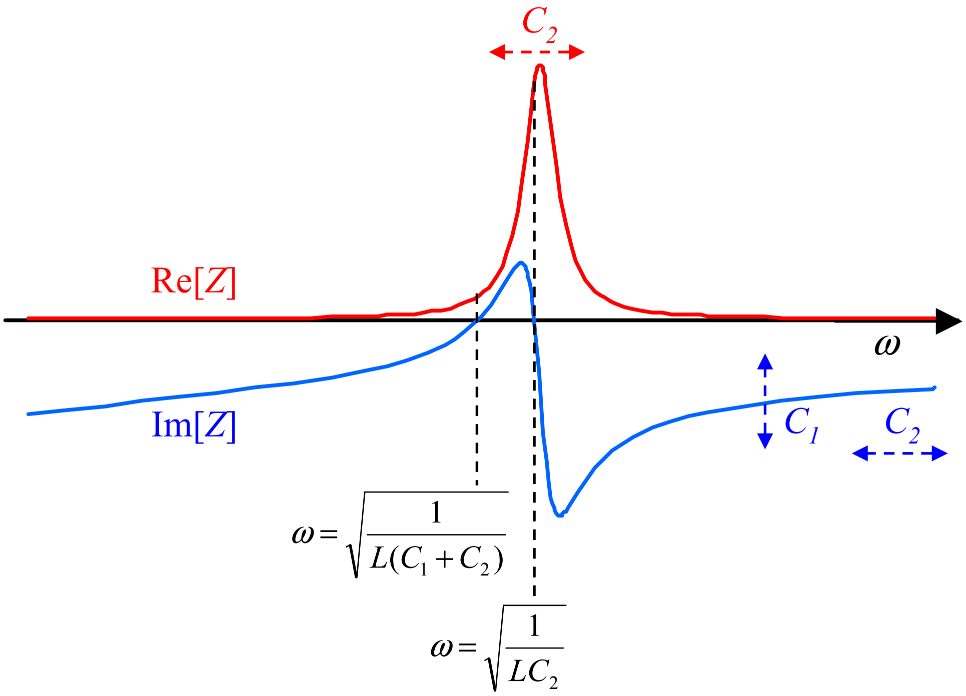

Figure D.2: The real and imaginary impedance of a matched-load circuit or resonant-coax circuit shown in figure D.1. The red and blue curve show the real and imaginary parts, respectively, of the total impedance Z as a function of angular frequency ω, with the black line indicating zero-impedance. The labeled dotted lines indicate the resonant angular frequencies at which the total impedance is completely real, i.e. resistive. As shown by the dashed arrows, changing C_2 tends to move both $Re[Z]$ and $Im[Z]$ along the ω axis, while changing C_1 only has the effect of moving $Im[Z]$ along the impedance (vertical) axis. By a judicious choice of C_1 and C_2 we can set the impedance at the desired $\omega = \sqrt{\frac{1}{l(C_1+C_2)}}$ to $Z = 50\ \Omega$.

It is important to note that at $\omega = \sqrt{\frac{1}{LC_2}}$, the impedance and the frequency are completely independent of C_1. Therefore, in tuning the circuit we set C_2 such that $\sqrt{\frac{1}{LC_2}}$ is slightly higher than the desired operating frequency and its impedance is also higher than the desired 50 Ω. As it turns out, changing C_1 only affects the imaginary part of Z without changing the real part. Therefore, by tuning C_1 we are then able to set the frequency $\sqrt{\frac{1}{L(C_1+C_2)}}$ at which Z again becomes completely resistive. In this way we can choose any real value for Z lying on the right side of the peak in figure D.2a. With the appropriate choice of C_1 and C_2, we can set a resistive impedance of 50 Ω at the desired frequency.

In practice, we match the circuit by tuning a pair of variable capacitors while looking at the reflected power from the circuit as a function of drive frequency. In this process we make use of an RF reflectometer which is described in detail in section D.3.2. A dip in the reflected power, corresponding to a peak in the transmitted power, occurs at the $Z = 50\ \Omega$ matching condition. Tuning the circuit is very simple in the resonant-coax scheme since it can be done from outside the cryostat while the sample is cold. In the matched-load scheme, tuning must be done outside the cryostat at room temperature where we can access C_1 and C_2. The subsequent cool-down results in some degradation of the matching efficiency mostly due to the thermal contraction of the circuit elements. Detailed study of the changes in the capacitances of the variable capacitors as a function of temperature, however, make this change predictable: for our variable capacitors (purchased from Newark and made by Johanson Manufacturing, Series: 9400 and Seal-Trim, 0.25-100 pF), capacitances increase by a factor of ~ 1.3 when cooled down from 300 K to 5 K. Therefore, we can achieve excellent matching even in the matched-load scheme. This fact, coupled with the higher transmitted powers of the matched-load scheme in comparison with the resonant-coax scheme, make it the more attractive option. We use this method to impedance match the coils used in most of the experiments described in chapter 3. A photograph of a coil matched using the matched-load scheme is shown in figure C.25.

Examples of capacitances used in the our matching circuits are: $C_1 = 5.03$ pF and $C_2 = 39.7$ pF to achieve a resonance of 48.7 MHz in conjunction with the coil described in section D.2.2.

D.3 Measurement methods

D.3.1 Measuring capacitance

In order to measure capacitance, we simply need a lock-in amplifier with a current input. We then connect one lead of the capacitance to be measured to the internal oscillator of the lock-in and the other to the current input as shown in figure D.3. Since the current measured will be,

$$I = \frac{V}{R + \frac{1}{i\omega C}} = \frac{V}{R^2 + \frac{1}{\omega^2 C^2}} \left(R + i \frac{1}{\omega C} \right), \tag{D.5}$$

where V and ω are the voltage and angular frequency, respectively, of the internal oscillator, and R and C are the resistance and capacitance associated with the capacitive element being measured. If the element is not lossy, it should be easy to choose a sufficiently small ω such that $\frac{1}{\omega C} \gg R$. Then,

$$\lim_{\frac{1}{\omega C} \gg R} I = i\omega C V. \tag{D.6}$$

Therefore, the lock-in amplifier will measure a current at angular frequency ω with a 90° phase shift from the driving voltage and an amplitude proportional to the capacitance C. In this way we measure the capacitance of our circuit

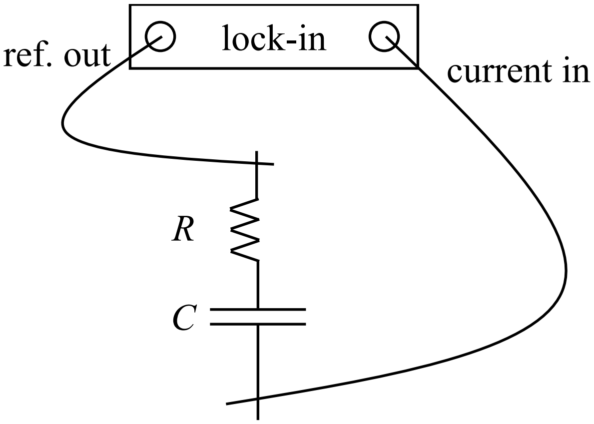

Figure D.3: A schematic representation of a simple method for measuring an unknown capacitance.

elements typically using values for V and $2\pi\omega$ of 100 mV and 100 Hz, respectively.

D.3.2 An RF reflectometer

A simple RF relfectometer can be assembled using a directional coupler and a oscilloscope. The configuration shown in figure D.4 saves us the need of using an expensive and cumbersome network analyzer to impedance match our circuits. The directional coupler can be purchased from Mini-Circuits (part number ZFDC-20-4). In this configuration the signal sent the oscilloscope corresponds to the RF voltage reflected by the circuit in question. By writing a simple computer program which sweeps the source frequency and fits the amplitude of the reflected voltage, we can obtain a reliable reflectance spectrum from most circuits.

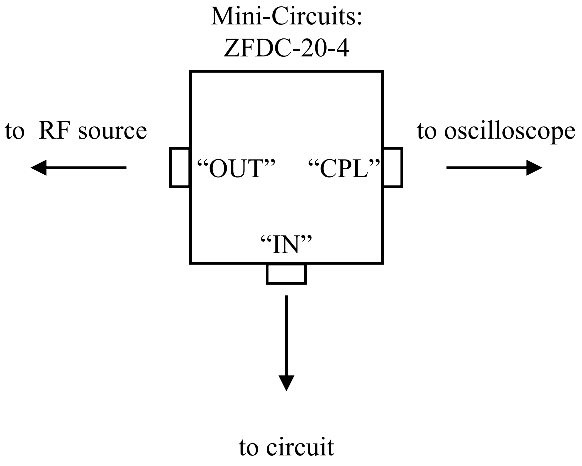

Figure D.4: A schematic representation of an RF reflectometer.

Appendix E

Nuclear gyromagnetic ratios for relevant isotopes

Table E.1: Nuclear gyromagnetic rations for relevant isotopes [184].

isotope	S	$\frac{\gamma_N}{2\pi}$(MHz/T)	quadrupole moment (m^2)	abundance (%)
^{69}Ga	$3/2$	10.257	0.178×10^{-28}	60.11
^{71}Ga	$3/2$	13.032	0.112×10^{-28}	39.89
^{75}As	$3/2$	7.317	0.3×10^{-28}	100
^{27}Al	$5/2$	11.135	0.4193×10^{-28}	100
^{115}In	$9/2$	9.364	1.16×10^{-28}	95.7
^{113}In	$9/2$	9.344	1.14×10^{-28}	4.3
^{29}Si	$1/2$	8.490	$-$	4.67
^{55}Mn	$5/2$	10.575	0.55×10^{-28}	100
^{9}Be	$3/2$	6.005	$-$	100
^{167}Er	$7/2$	1.235	-2.83×10^{-28}	22.95
^{121}Sb	$5/2$	10.226	-0.53×10^{-28}	57.3
^{123}Sb	$7/2$	5.538	-0.68×10^{-28}	42.7

References

[1] G. E. Uhlenbeck, *Nature* **117**, 264 (1926).

[2] W. Pauli, *f. Physik* **41**, 81 (1927).

[3] L. D. Laudau, E. M. Lifshitz, *Quantum Mechanics* (Butterworth-Heinemann, Oxford, 1997).

[4] W. Gerlach, O. Stern, *Z. Phys.* **9**, 349 (1922).

[5] B. Friedrich, D. Herschbach, *Physics Today* **56**, 53 (2003).

[6] W. Pauli, *Science* **103**, 213 (1946).

[7] M. N. Baibich, J. M. Broto, A. Fert, F. Nguyen Van Dau, F. Petroff, P. Eitenne, G. Creuzet, A. Friederich, J. Chazelas, *Phys. Rev. Lett.* **61**, 2472 (1988).

[8] G. Binasch, P. Grunberg, F. Saurenbach, W. Zinn, *Phys. Rev. B* **39**, 4828 (1989).

[9] J. Barnas, A. Fuss, R. E. Camley, P. Grunberg, W. Zinn, *Phys. Rev. B* **42**, 8110 (1990).

[10] D. D. Awschalom, D. Loss, N. Samarth, eds., *Semiconductor Spintronics and Quantum Computation* (Springer-Verlag, Berlin, 2002).

[11] J. M. Kikkawa, D. D. Awschalom, *Phys. Rev. Lett.* **80**, 4313 (1998).

[12] J. M. Kikkawa, D. D. Awschalom, *Nature* **397**, 139 (1999).

[13] I. Malajovich, J. M. Kikkawa, D. D. Awschalom, J. J. Berry, N. Samarth, *J. Appl. Phys.* **87**, 5073 (2000).

[14] I. Malajovich, J. J. Berry, N. Samarth, D. D. Awschalom, *Nature* **411**, 770 (2001).

[15] G. Salis, Y. Kato, K. Ensslin, D. C. Driscoll, A. C. Gossard, D. D. Awschalom, *Nature* **414**, 619 (2001).

[16] Y. Kato, R. C. Myers, D. C. Driscoll, A. C. Gossard, J. Levy, D. D. Awschalom, *Science* **299**, 1201 (2003).

[17] Y. Kato, R. C. Myers, A. C. Gossard, D. D. Awschalom, *Nature* **427**, 50 (2004).

[18] Y. K. Kato, R. C. Myers, A. C. Gossard, D. D. Awschalom, *Phys. Rev. Lett.* **93**, 176601 (2004).

[19] Y. K. Kato, R. C. Myers, A. C. Gossard, D. D. Awschalom, *Science* **306**, 1910 (2004).

[20] T. Fujisawa, D. G. Austing, Y. Tokura, Y. Hirayama, S. Tarucha, *Nature* **419**, 278 (2002).

[21] J. M. Elzerman, R. Hanson, L. H. W. van Beveren, B. Witkamp, L. M. K. Vandersypen, L. P. Kouwenhoven, *Nature* **430**, 431 (2004).

[22] J. R. Petta, A. C. Johnson, J. M. Taylor, E. A. Laird, A. Yacoby, M. D. Lukin, C. M. Marcus, M. P. Hanson, A. C. Gossard, *Science* **309**, 2180 (2005).

[23] G. Lampel, *Phys. Rev. Lett.* **20**, 491 (1968).

[24] E. Brun, R. J. Mahler, H. Mahon, W. L. Pierce, *Phys. Rev.* **129**, 1965 (1963).

[25] F. Meier, B. P. Zakharchenya, eds., *Optical Orientation* (Elsevier, Amsterdam, 1984).

[26] S. E. Barrett, R. Tycko, L. N. Pfeiffer, K. W. West, *Phys. Rev. Lett.* **72**, 1368 (1994).

[27] A. I. Ekimov, V. I. Safarov, *JETP Lett.* **15**, 179 (1972).

[28] V. K. Kalevich, V. D. Kul'kov, V. G. Fleisher, *Sov. Phys. Solid State* **22**, 703 (1980).

[29] V. K. Kalevich, V. D. Kul'kov, V. G. Fleisher, *Sov. Phys. Solid State* **23**, 892 (1981).

[30] V. K. Kalevich, *Sov. Phys. Solid State* **28**, 1947 (1986).

[31] M. Eickhoff, B. Lenzman, G. Flinn, D. Suter, *Phys. Rev. B* **65**, 125301 (2002).

[32] J. M. Kikkawa, D. D. Awschalom, *Science* **287**, 473 (2000).

[33] R. K. Kawakami, Y. Kato, M. Hanson, I. Malajovich, J. M. Stephens, E. Johnston-Halperin, G. Salis, A. C. Gossard, D. D. Awschalom, *Science* **294**, 131 (2001).

[34] K. R. Wald, L. P. Kouwenhoven, P. L. McEuen, N. C. van der Vaart, C. T. Foxon, *Phys. Rev. Lett.* **73**, 1011 (1994).

[35] J. H. Smet, R. A. Deutschmann, F. Ertl, W. Wegscheider, G. Abstreiter, K. von Klitzing, *Nature* **415**, 281 (2002).

[36] J. M. Taylor, C. M. Marcus, M. D. Lukin, *Phys. Rev. Lett.* **90**, 206803 (2003).

[37] H. Ohno, *Science* **281**, 951 (1998).

[38] Y. Ohno, R. Terauchi, T. Adachi, F. Matsukura, H. Ohno, *Phys. Rev. Lett.* **83**, 4196 (1999).

[39] H. Ohno, D. Chiba, F. Matsukura, T. Omiya, E. Abe, T. Dietl, Y. Ohno, K. Ohtani, *Nature* **408**, 944 (2000).

[40] D. Chiba, M. Yamanouchi, F. Matsukura, H. Ohno, *Science* **301**, 943 (2003).

[41] M. Poggio, , D. D. Awschalom, *Appl. Phys. Lett.* **86**, 182103 (2005).

[42] M. Poggio, G. M. Steeves, R. C. Myers, Y. Kato, A. C. Gossard, D. D. Awschalom, *Phys. Rev. Lett.* **91**, 207602 (2003).

[43] P. Schewe, J. Riordon, B. Stein, *Physics News Update* **662**, 2 (2003).

[44] R. C. Myers, M. Poggio, N. P. Stern, A. C. Gossard, D. D. Awschalom, *Phys. Rev. Lett.* **95**, 017204 (2005).

[45] M. Poggio, R. C. Myers, N. P. Stern, A. C. Gossard, D. D. Awschalom, cond-mat/0503521.

[46] C. Sliwa, T. Dietl, cond-mat/0505126.

[47] M. Poggio, G. M. Steeves, R. C. Myers, N. P. Stern, A. C. Gossard, D. D. Awschalom, *Phys. Rev. B* **70**, 121305 (2004).

[48] C. Cohen-Tannoudji, B. Diu, F. Laloe, *Quantum Mechanics* (John Wiley & Sons, New York, 1977).

[49] E. Merzbacher, *Quantum Mechanics* (John Wiley & Sons, New York, 1998).

[50] H. L. Anderson, ed., *A Physicist's Desk Reference* (American Istitute of Physics, New York, 1989).

[51] E. L. Hahn, *Phys. Rev.* **80**, 580 (1950).

[52] J. C. Phillips, *Bonds and Bands in Semiconductors* (Academic Press, New York, 1973).

[53] J. M. Luttinger, W. Kohn, *Phys. Rev.* **97**, 869 (1955).

[54] E. O. Kane, *J. Phys. Chem. Solids* **1**, 249 (1957).

[55] E. Hecht, *Optics* (Addison-Wesley, Reading, Massachusetts, 1990).

[56] C. Hermann, C. Weisbuch, *Phys. Rev. B* **15**, 823 (1977).

[57] Y. K. Kato, *Electrical Manipulation of Electron Spin Coherence in Nonmagnetic Semiconductors*, Ph.D. dissertation, University of California, Santa Barbara (2005).

[58] P. Pfeffer, W. Zawadzki, *Phys. Rev. B* **41**, 1561 (1990).

[59] W. Zawadzki, S. Klahn, U. Merkt, *Phys. Rev. B* **33**, 6916 (1986).

[60] G. Bastard, *Wave Mechanics Applied to Semiconductor Heterostructures* (Les Editions de Physique, Paris, 1988).

[61] O. Madelung, *Semiconductors: Data Handbook* (Springer-Verlag, Berlin, edn. 3, 2004).

[62] J. H. Davies, *The Physics of Low-Dimensional Semiconductors* (Cambridge University Press, Cambridge, United Kingdom, 1998).

[63] M. J. Snelling, G. P. Flinn, A. S. Plaut, R. T. Harley, A. C. Tropper, R. Eccleston, C. C. Phillips, *Phys. Rev. B* **44**, 11345 (1991).

[64] M. J. Snelling, E. Blackwood, C. J. Mcdonagh, R. T. Harley, C. T. B. Foxon, *Phys. Rev. B* **45**, 3922 (1992).

[65] B. Kowalski, P. Omling, B. K. Meyer, D. M. Hofmann, C. Wetzel, V. Harle, F. Scholz, P. Sobkowicz, *Phys. Rev. B* **49**, 14786 (1994).

[66] A. Malinowski, D. J. Guerrier, N. J. Traynor, R. T. Harley, *Phys. Rev. B* **60**, 7728 (1999).

[67] A. Malinowski, R. T. Harley, *Phys. Rev. B* **62**, 2051 (2000).

[68] G. Salis, D. D. Awschalom, Y. Ohno, H. Ohno, *Phys. Rev. B* **64**, 195304 (2001).

[69] A. Abragam, *Principles of Nuclear Magnetism* (Oxford University Press, Oxford, 1961).

[70] D. J. Griffiths, *Am. J. Phys,* **50**, 698 (1982).

[71] J. K. Furdyna, J. Kossut, eds., *Semiconductors and Semimetals* (Academic Press, San Diego, 1988), vol. 25, chap. 5, p. 183.

[72] J. J. Sakurai, *Modern Quantum Mechanics* (Addison-Wesley, Reading, Massachusetts, 1994).

[73] C. Zener, *Phys. Rev.* **81**, 440 (1951).

[74] C. Zener, *Phys. Rev.* **82**, 403 (1951).

[75] C. Zener, *Phys. Rev.* **83**, 229 (1951).

[76] S. V. Vonsovskii, E. A. Turov, *Zh. Eksp. Teor. Fiz* **24**, 419 (1953).

[77] T. Kasuya, *Progr. Theor. Phys.* **16**, 58 (1955).

[78] E. Abrahams, *Phys. Rev.* **98**, 387 (1955).

[79] K. Yosida, *Phys. Rev.* **106**, 893 (1957).

[80] A. H. Mitchell, *Phys. Rev.* **105**, 1439 (1957).

[81] M. Faraday, *Philos. Trans. R. Soc. London* **136**, 1 (1846).

[82] D. J. Hilton, C. L. Tang, *Phys. Rev. Lett.* **89**, 146601 (2002).

[83] T. Amand, X. Marie, P. LeJeune, M. Brousseau, D. Robart, J. Barrau, R. Planel, *Phys. Rev. Lett.* **78**, 1355 (1997).

[84] J. A. Gupta, *Coherence and Manipulation of Spin States in Semiconductor Nanostructures*, Ph.D. dissertation, University of California, Santa Barbara (2002).

[85] S. A. Crooker, D. D. Awschalom, J. J. Baumberg, F. Flack, N. Samarth, *Phys. Rev. B* **56**, 7574 (1997).

[86] D. Paget, G. Lampel, B. Sapoval, V. I. Safarov, *Phys. Rev. B* **15**, 5780 (1977).

[87] D. Paget, *Phys. Rev. B* **25**, 4444 (1982).

[88] G. Salis, D. T. Fuchs, J. M. Kikkawa, D. D. Awschalom, Y. Ohno, H. Ohno, *Phys. Rev. Lett.* **86**, 2677 (2001).

[89] D. Rugar, R. Budakian, J. Mamin, B. W. Chui, *Nature* **430**, 329 (2004).

[90] J. A. Sidles, *Phys. Rev. Lett.* **68**, 1124 (1992).

[91] J. A. Sidles, J. L. Garbini, K. J. Bruland, D. Rugar, O. Zuger, S. Hoen, C. S. Yannoni, *Rev. Mod. Phys.* **67**, 249 (1995).

[92] M. N. Leuenberger, D. Loss, M. Poggio, D. D. Awschalom, *Phys. Rev. Lett.* **89**, 207601 (2002).

[93] X. Marie, J. Amand, T. Barrau, P. Renucci, P. LeJeune, V. K. Kalevich, *Phys. Rev. B* **61**, 11065 (2000).

[94] D. J. Guerrier, R. T. Harley, *Appl. Phys. Lett.* **70**, 1739 (1997).

[95] W. Hanle, *Z. Phys.* **30**, 93 (1924).

[96] R. R. Parsons, *Phys. Rev. Lett.* **23**, 1152 (1969).

[97] C. Weisbuch, *Proc. XIXth Congress Ampere*, H. Brunner, K. H. Hausser, D. Schweitzer, eds. (Heidelberg, 1976).

[98] I. Tifrea, M. E. Flatte, *Phys. Rev. Lett.* **90**, 237601 (2003).

[99] N. A. Gershenfeld, I. L. Chuang, *Science* **275**, 350 (1997).

[100] W. Desrat, D. K. Maude, M. Potemski, J. C. Portal, Z. R. Wasilewski, G. Hill, *Phys. Rev. Lett.* **88**, 256807 (2002).

[101] R. C. Miller, A. C. Gossard, D. A. Kleinman, O. Munteanu, *Phys. Rev. B* **29**, 3740 (1984).

[102] K. D. Maranowski, J. P. Ibbetson, K. L. Campman, A. C. Gossard, *Appl. Phys. Lett.* **66**, 3459 (1995).

[103] D. A. B. Miller, D. S. Chemla, T. C. Damen, A. C. Gossard, W. Wiegmann, T. H. Wood, C. A. Burrus, *Phys. Rev. Lett.* **53**, 2173 (1984).

[104] D. A. B. Miller, D. S. Chemla, T. C. Damen, A. C. Gossard, W. Wiegmann, T. H. Wood, C. A. Burrus, *Phys. Rev. B* **32**, 1043 (1985).

[105] Y. Chuliang, Y. Qing, *Phys. Rev. B* **37**, 1364 (1988).

[106] C. Weisbuch, C. Hermann, *Phys. Rev. B* **15**, 816 (1977).

[107] M. Paillard, X. Marie, P. Renucci, T. Amand, A. Jbeli, J. M. Gerard, *Phys. Rev. Lett.* **86**, 1634 (2001).

[108] W. Lau, J. T. Olesberg, M. E. Flatte, cond-mat/0406201.

[109] I. Tifrea, M. Poggio, M. E. Flatte, D. D. Awschalom, unpublished.

[110] C. P. Slichter, *Principles of Magnetic Resonance* (Springer-Verlag, Berlin, edn. 3, 1990).

[111] G. Burkard, D. Loss, D. P. DiVincenzo, *Phys. Rev. B* **59**, 2070 (1999).

[112] F. Matsukura, H. Ohno, A. Shen, Y. Sugawara, *Phys. Rev. B* **57**, 2037(R) (1998).

[113] J. Okabayashi, A. Kimura, O. Rader, T. Mizokawa, A. Fujimori, T. Hayashi, M. Tanaka, *Phys. Rev. B* **58**, 4211 (1998).

[114] M. A. Zudov, J. Kono, Y. H. Matsuda, T. Ikaida, N. Miura, H. Munekata, G. D. Sanders, Y. Sun, C. J. Stanton, *Phys. Rev. B* **66**, 161307 (2002).

[115] J. Szczytko, W. Mac, A. Stachow, A. Twardowski, P. Becla, J. Tworzydklo, *Solid State Commun.* **99**, 927 (1996).

[116] S. A. Crooker, *Ultrafast Optical Studies of Coherent Spin Dynamics in Magnetic Quantum Structures*, Ph.D. dissertation, University of California, Santa Barbara (1997).

[117] K. M. Yu, W. Walukiewicz, T. Wojtowicz, I. Kuryliszyn, X. Liu, Y. Sasaki, J. K. Furdyna, *Phys. Rev. B* **65**, 201303 (2002).

[118] J. Masek, F. Maca, *Phys. Rev. B* **69**, 165212 (2004).

[119] J. Kreissl, W. Ulrici, M. El-Metoui, A. M. Vasson, A. Vasson, A. Gavaix, *Phys. Rev. B* **54**, 10508 (1996).

[120] J. Schneider, U. Kaufmann, W. Wikening, M. Baeumler, *Phys. Rev. Lett.* **59**, 240 (1987).

[121] M. Baeumler, B. K. Meyer, U. Kaufmann, J. Schneider, *Mater. Sci. Forum* **38–41**, 797 (1989).

[122] J. Szczytko, W. Mac, A. Twardowski, F. Matsukura, H. Ohno, *Phys. Rev. B* **59**, 12935 (1999).

[123] J. Szczytko, A. Twardowski, K. Swiatek, M. Palczewska, M. Tanaka, T. Hayashi, K. Ando, *Phys. Rev. B* **60**, 8304 (1999).

[124] R. Bleekrode, J. Dieleman, H. J. Vegter, *Phys. Lett.* **2**, 355 (1962).

[125] N. Almeleh, B. Goldstein, *Phys. Rev.* **128**, 1568 (1962).

[126] M. Linnarsson, E. Janzen, B. Monemar, M. Kleverman, A. Thilderkvist, *Phys. Rev. B* **55**, 6938 (1997).

[127] R. C. Myers, Ph.D. dissertation, University of California, Santa Barbara (2006).

[128] E. Johnston-Halperin, J. A. Schuller, C. S. Gallinat, T. C. Kreutz, R. C. Myers, R. K. Kawakami, H. Knotz, A. C. Gossard, D. D. Awschalom, *Phys. Rev. B* **68**, 165328 (2003).

[129] R. C. Myers, A. C. Gossard, D. D. Awschalom, *Phys. Rev. B* **69**, 161305 (2004).

[130] R. C. Myers, A. C. Gossard, D. D. Awschalom, unpublished.

[131] K. Wagenhuber, H. P. Tranitz, M. Reinwald, W. Wegscheider, *Appl. Phys. Lett.* **85**, 1190 (2004).

[132] C. A. Evans Jr., *Anal. Chem.* **44**, 67A (1972).

[133] A. Benninghoven, *Surface Sci.* **35**, 427 (1973).

[134] H. W. Werner, H. A. M. DeGrefte, *Surface Sci.* **35**, 458 (1973).

[135] A. M. Nazmul, S. Sugahara, M. Tanaka, *J. Cryst. Growth* **251**, 303 (2003).

[136] T. Ishitani, R. Shimizu, *Appl. Phys.* **6**, 241 (1975).

[137] T. Ishitani, R. Shimizu, H. Tamura, *Appl. Phys.* **6**, 277 (1975).

[138] N. P. Stern, R. C. Myers, M. Poggio, A. C. Gossard, D. D. Awschalom, unpublished.

[139] K. Akimoto, M. Kamada, K. Taira, M. Arai, N. Watanabe, *J. Appl. Phys.* **59**, 2833 (1986).

[140] T. Achtnich, G. Burri, M. A. Py, M. Ilegems, *Appl. Phys. Lett.* **50**, 1730 (1987).

[141] G. Snider, Poisson solver (http://www.nd.edu/∼gsnider).

[142] S. C. Erwin, A. G. Petukhov, *Phys. Rev. Lett.* **89**, 227201 (2002).

[143] L. X. Zhao, C. R. Staddon, K. Y. Wang, K. W. Edmonds, R. P. Campion, B. L. Gallagher, C. T. Foxon, *Appl. Phys. Lett.* **86**, 071902 (2005).

[144] H. Raebiger, A. Ayuela, R. M. Nieminen, *J. Phys.: Condens. Matter* **16**, L457 (2004).

[145] S. A. Crooker, J. J. Baumberg, F. Flack, N. Samarth, D. D. Awschalom, *Phys. Rev. Lett.* **77**, 2814 (1996).

[146] J. Fabian, S. Das Sarma, *J. Vac. Sci. Technol. B* **17**, 1708 (1999).

[147] Y. G. Semenov, *Phys. Rev. B* **67**, 115319 (2003).

[148] D. Keller, D. R. Yakovlev, B. Konig, W. Ossau, T. Gruber, A. Waag, L. W. Molenkamp, A. V. Scherbakov, *Phys. Rev. B* **65**, 035313 (2002).

[149] B. E. Larson, K. C. Hass, H. Ehrenreich, A. E. Carlsson, *Phys. Rev. B* **37**, 4137 (1988).

[150] I. A. Merkulov, D. R. Yakovlev, A. Keller, W. Ossau, J. Heurts, A. Waag, G. Landwehr, G. Karczewski, T. Wojtowicz, J. Kossut, *Phys. Rev. B* **83**, 1431 (1999).

[151] P. W. Yu, Y. S. Park, *J. Appl. Phys.* **50**, 1097 (1979).

[152] A. Petrou, M. C. Smith, C. H. Perry, J. M. Worlock, J. Warnock, R. L. Aggarwal, *Solid State Commun.* **55**, 865 (1985).

[153] B. Lakshmi, G. Favrot, D. Heiman, *Proc. SPIE* **5359**, 290 (2004).

[154] B. Coqblin, C. F. Ratto, *Phys. Rev. Lett.* **21**, 1065 (1968).

[155] A. K. Bhattacharjee, G. Fishman, B. Coqblin, *Physica* **117B & 118B**, 449 (1983).

[156] T. Dietl, private communication.

[157] A. K. Bhattacharjee, *Phys. Rev. B* **41**, 5696 (1990).

[158] A. K. Bhattacharjee, *Phys. Rev. B* **58**, 15660 (1998).

[159] M. Poggio, R. C. Myers, N. P. Stern, A. C. Gossard, D. D. Awschalom, unpublished.

[160] O. Z. Karimov, G. H. John, R. T. Harley, W. H. Lau, M. E. Flatte, M. Henini, R. Airey, *Phys. Rev. Lett.* **91**, 246601 (2003).

[161] R. Dingle, A. C. Gossard, W. Wiegmann, *Phys. Rev. Lett.* **34**, 1327 (1975).

[162] Y. J. Chen, E. S. Koteles, B. S. Elman, C. A. Armiento, *Phys. Rev. B* **36**, 4562 (1987).

[163] M. N. Islam, R. L. Hillman, D. A. B. Miller, D. S. Chemla, A. C. Gossard, J. H. English, *Appl. Phys. Lett.* **50**, 1098 (1987).

[164] T. Fukuzawa, E. E. Mendez, J. M. Hong, *Phys. Rev. Lett.* **64**, 3066 (1990).

[165] L. V. Butov, L. S. Levitov, A. V. Mintsev, B. D. Simons, A. C. Gossard, D. S. Chemla, *Phys. Rev. Lett.* **92**, 117404 (2004).

[166] G. Bastard, C. Delalande, R. Ferreira, H. W. Liu, *Journal of Luminescence* **44**, 247 (1989).

[167] A. Alexandrou, J. A. Kash, E. E. Mendez, M. Zachau, J. M. Hong, T. Fukuzawa, Y. Hase, *Phys. Rev. B* **42**, 9225 (1990).

[168] V. B. Timofeev, A. V. Larionov, A. S. Ioselevich, J. Zeman, G. Martinez, J. Hvam, K. Soerensen, *JETP Lett.* **67**, 613 (1998).

[169] A. C. Gossard, *IEEE J. Quant. Electron.* **22**, 1649 (1986).

[170] H. J. Polland, L. Schultheis, J. Kuhl, E. O. Gobel, C. W. Tu, *Phys. Rev. Lett.* **55**, 2610 (1985).

[171] T. B. Norris, N. Vodjdani, B. Vinter, C. Weisbuch, G. A. Mourou, *Phys. Rev. B* **40**, 1392 (1989).

[172] H. G. Roskos, M. C. Nuss, J. Shah, K. Leo, D. A. B. Miller, A. M. Fox, S. Schmitt-Rink, K. Kohler, *Phys. Rev. Lett.* **68**, 2216 (1992).

[173] T. C. Damen, L. Via, J. E. Cunningham, J. Shah, L. J. Sham, *Phys. Rev. Lett.* **67**, 3432 (1991).

[174] E. L. Ivchenko, A. A. Kiselev, M. Willander, *Solid State Commun.* **102**, 375 (1997).

[175] H. W. Jiang, E. Yablonovitch, *Phys. Rev. B* **64**, 041307(R) (2001).

[176] T. Takagahara, *Phys. Rev. B* **31**, 6552 (1985).

[177] R. Ferreira, G. Bastard, *Rep. Prog. Phys.* **60**, 345 (1997).

[178] A. B. Dzyubenko, A. L. Yablonskii, *Phys. Rev. B* **53**, 16355 (1996).

[179] I. Y. Gerlovin, Y. K. Dolgikh, S. A. Eliseev, V. V. Ovsyankin, Y. P. Efimov, I. V. Ignatiev, V. V. Petrov, S. Y. Verbin, Y. Masumoto, *Phys. Rev. B* **69**, 035329 (2004).

[180] I. Lawrence, S. Haacke, H. Mariette, W. W. Ruhle, H. Ulmer-Tuffigo, J. Cibert, G. Feuillet, *Phys. Rev. Lett.* **73**, 2131 (1994).

[181] Oxford Instruments, Oxford, *Operator's Handbook: Spectromag System* (2001).

[182] Y. J. Jiang, *J. Magn. Reson.* **142**, 386 (1999).

[183] D. E. MacLaughlin, *Rev. Sci. Inst.* **60**, 3242 (1989).

[184] Webelements (http://www.webelements.com).

Physical Constants

Speed of light	c	2.99792458	$\times 10^{8}$	m s^{-1}
Dielectric constant	ε_0	8.8541878	$\times 10^{-12}$	F m^{-1}
		8.8541878		fF mm^{-1}
Magnetic permeability	μ_0	4π	$\times 10^{-7}$	T m A^{-1}
		12.5663706		mT μm mA^{-1}
Planck constant	h	6.62606876(52)	$\times 10^{-34}$	J s
		4.13566727(16)	$\times 10^{-15}$	eV s
		4.13566727(16)		meV ps
	$\hbar = h/(2\pi)$	1.054571596(82)	$\times 10^{-34}$	J s
		6.58211889(26)	$\times 10^{-16}$	eV s
		658.211889(26)		μeV ps
Electronic charge	e	1.602176462(63)	$\times 10^{-19}$	C
Free electron mass	m_e	9.10938188(72)	$\times 10^{-31}$	kg
Bohr magneton	$\mu_{\mathrm{B}} = e\hbar/2m_e$	57.88381749(43)		μeV T^{-1}
Boltzman constant	k_B	86.17342(15)		μeV K^{-1}
	h/e^2	25.812807572(95)		kΩ
	$\hbar/\mu_{\mathrm{B}}$	11.37125914(94)		ps T
	hc/e	1239.84185(68)		eV nm
	e/h	2.41798948(88)	$\times 10^{14}$	Hz eV^{-1}
		0.241798948(88)		GHz $\mu\mathrm{eV}^{-1}$